

Exploring the Luminescence Dynamics of Lanthanide-Doped Nanoparticles: Exploiting the
Temporal Dimension for Diverse Applications

Steven Maurizio

A Thesis
in
The Department
of
Chemistry and Biochemistry

Presented in Partial Fulfillment of the Requirements
for the Degree of Doctor of Philosophy (Chemistry) at
Concordia University
Montréal, Québec, Canada

March 2024

© Steven Maurizio, 2024

CONCORDIA UNIVERSITY
SCHOOL OF GRADUATE STUDIES

This is to certify that the thesis prepared

By: Steven Maurizio

Entitled: Exploring the Luminescence Dynamics of Lanthanide-Doped Nanoparticles:
Exploiting the Temporal Dimension for Diverse Applications

and submitted in partial fulfillment of the requirements for the degree of

Doctor Of Philosophy (Chemistry)

complies with the regulations of the University and meets the accepted standards with respect to originality and quality.

Signed by the final examining committee:

_____ Chair
Dr. William Bukowski

_____ External Examiner
Dr. Claudia Wickleder

_____ Arms-Length Examiner
Dr. Ayse Turak

_____ Examiner
Dr. Rafik Naccache

_____ Examiner
Dr. Ashlee Howarth

_____ Thesis Supervisor
Dr. John Capobianco

Approved by

_____ Dr. Louis Cuccia, Graduate Program Director

March 18, 2024

_____ Dr. Pascale Sicotte, Dean (Faculty of Arts and Science)

ABSTRACT

Exploring the Luminescence Dynamics of Lanthanide-Doped Nanoparticles: Exploiting the Temporal Dimension for Diverse Applications

Steven Maurizio, Ph.D.
Concordia University, 2024

Lanthanide luminescence at the nanoscale has garnered considerable attention over the last few decades, with research on ternary fluoride nanoparticles focusing heavily on upconversion and to a lesser extent on radioluminescence. However, these nanomaterials have not yet been implemented commercially. This is likely, in part, due to the overwhelming emphasis on demonstrating potential applications, rather than understanding the fundamental mechanisms that drive these luminescence phenomena. As a result, the forbidden nature of the lanthanide 4f-4f transitions has hindered the widespread implementation of such nanoparticles.

To shed light on the complex nature of lanthanide-doped upconverting nanoparticles, studies on co-doped Yb^{3+} and Tm^{3+} nanoparticles were completed with varying host composition (including LiYF_4 , NaGdF_4 , and BaYF_5) and activator dopant concentration (ranging from 0.1 to 2.0 mol%). The interionic spacing and site symmetry of the lanthanide ions was deemed to play an integral role in the relative intensity of each Tm^{3+} emission, indicating that different combinations are optimal for different applications. With the addition of an active shell doped with Tb^{3+} , the energy transfer across the core/shell interface was evaluated next, establishing that a radiative energy transfer mechanism from the $^1\text{D}_2$ excited state of Tm^{3+} was most prominent.

Influences known to affect the upconversion efficiency of nanomaterials were then evaluated on $\text{LiLuF}_4:\text{Eu}^{3+}$ radioluminescent nanoparticles. The results herein indicated that a greater material density and effective atomic number improved the efficiency of the radioluminescence process, while varying the dopant concentration was not as influential, when compared to direct ultraviolet excitation. Furthermore, the addition of Gd^{3+} as a sensitizer or employing core/shell structures did not prove advantageous to the radioluminescence intensity.

While luminescence lifetimes are measured to evaluate nonradiative energy transfer efficiencies between spectroscopically active species, proof-of-concepts herein demonstrate that

they can also be employed to add a temporal component to various applications. These include upconversion nanothermometry, particle velocimetry, and covert information storage, all taking advantage of the long-lived excited state decay times of various lanthanide ions.

Acknowledgements

It goes without saying that putting up with me is no easy feat, so anyone that has stuck with me through this journey deserves more than a brief mention in the acknowledgement section of a thesis... But for now, it'll have to do. While my approach to expressing gratitude is not for the faint of heart (consisting of snarky remarks or constant attitude), I truly am thankful for all the support, whether scientific or emotional, that those around me have provided.

First and foremost, to my mother, father, and let's throw my brother in there for extra credit. Thank you for the loving, supportive, and motivating home environment that has allowed me to grow into the person I am today. I would not have progressed this far academically if I didn't have you behind me, constantly nagging about the importance of education.

To Etienne, my better half. It seems that, more often than not, I come home complaining about something, and you listen to it all with open ears. You do an amazing job of simmering me down when things get out of hand, and I can't imagine how I would have made it this far without you by my side.

To Professor Capobianco, the roller coaster I have put you through these last six years is more than any supervisor should have to endure, but you took it in stride and have molded me into a determined researcher. You taught me to think independently, articulate myself properly, and enthusiastically justify my research, and for that I am grateful. I like to think that our constant bickering is built out of passion for the game, and while things have gotten heated, it's always been for the good of science. Perhaps one day we will stop arguing, but I think Ferrari has a better shot at winning a championship before that day comes. Thank you for taking me under your wing, and I hope my time as your student has at least been joyful and entertaining.

To my supervisory committee members, Professors Ashlee Howarth and Rafik Naccache. Thank you for the added perspective you've provided when I needed it. I appreciate the efforts you've made to direct my research, whether that be reassurance in a decision I've made, or the slap in the face I needed when pursuing a tangent that wasn't in my best interest. My thesis is immensely more structured and grounded thanks to your feedback these last few years.

To my Arm's Length Examiner, Professor Ayse Turak, and my External Examiner, Professor Claudia Wickleder, I appreciate you taking the time to review and scrutinize my thesis, and I look forward to our future discussions.

To Dr. Gabi Mandl, words cannot describe how grateful I am to have met you and gone through this journey alongside you. Picking each other up when we were down and knocking us down a few pegs when we were over eager, the duality that we shared allowed us both to progress and grow. I appreciate everything I've learned from you, and I can't wait to see what the world has in store for us.

To Professor Gabriella Tessitore, it has been an honor to stand by your side through these many years. Sharing a desk and spending numerous late nights has been instrumental in my development. You taught me to be thorough in my experiments, question everything I read, and cover every angle when making assertions. I am a better scientist because of you, and I can only aspire to reach your level of knowledge and wisdom.

To the other labmates that have worked with me throughout my time as a student. It takes a village to accomplish what we have done, and my contributions to science are better because of the people surrounding me. I am grateful to all of you for providing a caring and insightful lab environment that others can only dream of.

Finally, to the colleagues and collaborators that have contributed to the research presented in this thesis. I appreciate the effort and time you've taken to help improve our understanding of lanthanide luminescence, and I look forward to what comes next in this field.

"The only true wisdom is in knowing you know nothing."

– Socrates

Table of Contents

List of Figures	xi
List of Tables	xvii
List of Abbreviations	xviii
List of Symbols	xix
Chapter 1. Introduction	1
1.1. Lanthanides	1
1.1.1. 4f Electronic States	2
1.1.2. Electronic Transitions and Selection Rules.....	3
1.2. Luminescence	4
1.2.1. Photoluminescence.....	5
1.2.2. Upconversion Luminescence	6
1.2.3. Radioluminescence	11
1.3. Energy Transfer	14
1.3.1. Lanthanide Energy Transfer Mechanisms	16
1.4. Nanoscience	17
1.4.1. Photoluminescent and Upconverting Lanthanide-doped Nanomaterials	18
1.4.2. Nanoscintillators and Radioluminescent Nanomaterials.....	20
Chapter 2. Statement of the Problem	22
2.1. Academic Research on Lanthanide-doped Luminescent Nanoparticles	22
2.2. Research Project Objectives.....	28
Chapter 3. Experimental Methods	31
3.1. Reagents.....	31
3.2. Nanoparticle Synthesis.....	31
3.2.1. LiREF ₄	31
3.2.2. NaREF ₄	32

3.2.3. Ba _{1-x} RE _x F _{2+x}	34
3.2.4. CsMnCl ₃	35
3.3. Physical Characterization.....	35
3.3.1. Powder X-ray Diffraction	35
3.3.2. Transmission Electron Microscopy	36
3.3.3. Inductively Coupled Plasma – Mass Spectrometry	37
3.3.4. Zeta Potential	37
3.4. Spectroscopic Characterization.....	37
3.4.1. Absorption Spectroscopy	37
3.4.2. Excitation Spectroscopy.....	37
3.4.3. Emission Spectroscopy	38
3.4.4. Luminescence Lifetimes	39
3.4.5. Upconversion Quantum Yields.....	39
3.5. Proof-of-Concepts.....	40
3.5.1. NIR-triggered photoisomerization	40
3.5.2. Upconversion Lifetime Nanothermometry	40
3.5.3. Particle Velocimetry	41
3.5.4. Covert Information Storage	41
Chapter 4. Tm ³⁺ -doped Upconverting Nanoparticles	43
4.1. Effect of Activator Concentration on LiYF ₄ :Yb ³⁺ ,Tm ³⁺ UCNPs.....	43
4.1.1. Proof-of-Concept: NIR-Triggered Photoisomerization	52
4.2. Effect of Activator Concentration on Ba _{1-x} Y _x F _{2+x} :Yb ³⁺ ,Tm ³⁺ UCNPs.....	54
4.3. Effect of Host Composition on Yb ³⁺ ,Tm ³⁺ UCNPs	66
4.4. Proof-of-Concept: NIR Nanothermometry Using Upconversion Lifetimes	67
Chapter 5. Tm ³⁺ and Tb ³⁺ co-doped Upconverting Nanoparticles	74
5.1. Tm ³⁺ → Tb ³⁺ ET Across Core/Shell Interface in NaGdF ₄ UCNPs.....	78
5.2. Proof-of-Concept: Time-Resolved Color Tuning for Particle Velocimetry	87

Chapter 6. Er ³⁺ -doped and Ho ³⁺ -doped Upconverting Nanoparticles	93
6.1. Spectroscopy of Yb ³⁺ ,Er ³⁺ and Yb ³⁺ ,Ho ³⁺ Co-doped LiYF ₄ UCNPs	93
6.2. Proof-of-Concept: Covert Information Storage Using Time-Resolved Imaging.....	98
6.2.1. Photoluminescent Nanoparticles	99
6.2.2. Upconverting Nanoparticles	103
Chapter 7. Eu ³⁺ -doped Radioluminescent Nanoparticles	108
7.1. Effect of Material Density on LiREF ₄ :Eu ³⁺ RLNPs	108
7.2. Effect of Activator Concentration on LiLuF ₄ :Eu ³⁺ RLNPs	114
7.3. Effect of Adding a Gd ³⁺ Sensitizer to LiLuF ₄ :Eu ³⁺ RLNPs	121
7.4. Influence of Nanoparticle Architecture on LiLuF ₄ :Eu ³⁺ RLNPs	125
Chapter 8. Conclusions and Future Directions	131
8.1. Conclusions.....	131
8.1.1. Lanthanide Luminescence Mechanisms and Optimizations	131
8.1.2. Demonstrated Applications Using Luminescence Lifetimes	133
8.2. Future Directions	135
References	138
Appendix 1: Trivalent Lanthanide Energy Levels.....	151
Appendix 2: Nanomaterial Crystallography	152

List of Figures

Figure 1.1 Energy level diagram depicting the interaction that dictate the position of lanthanide excited states.	2
Figure 1.2 Energy level diagram depicting traditional fluorescence.	6
Figure 1.3 Energy level diagram depicting ground and excited state absorption.	7
Figure 1.4 Energy level diagram depicting energy transfer upconversion.	8
Figure 1.5 Energy level diagram depicting cooperative luminescence.	9
Figure 1.6 Energy level diagram depicting cooperative sensitization.	10
Figure 1.7 Schematic representation of the three processes that dictate the efficiency of radioluminescence in wide band-gap materials.	13
Figure 1.8 Energy level diagrams depicting different energy transfer phenomena.	14
Figure 1.9 Energy level diagrams depicting different energy transfer mechanisms.....	17
Figure 1.10 Schematic representation of a doped material.	19
Figure 2.1 Energy level diagram depicting ETU between Yb^{3+} and Er^{3+}	23
Figure 2.2 Energy level diagram depicting ETU between Yb^{3+} and Ho^{3+}	23
Figure 2.3 Energy level diagram depicting ETU between Yb^{3+} and Tm^{3+}	24
Figure 2.4 Absorption spectra of relevant biological tissues and media, depicting the biological windows.	25
Figure 2.5 Energy level diagram depicting energy transfer between Nd^{3+} and Yb^{3+}	26
Figure 4.1 TEM micrographs, particle size distributions and PXRD diffractograms of $\text{LiYF}_4:25\%\text{Yb}^{3+},x\%\text{Tm}^{3+}$ UCNPs.	45
Figure 4.2 Upconversion emission spectra of $\text{LiYF}_4:25\%\text{Yb}^{3+},x\%\text{Tm}^{3+}$ UCNPs.....	46
Figure 4.3 Upconversion emission spectrum from Figure 4.2, normalized to the $^1\text{G}_4 \rightarrow ^3\text{H}_6$ transition, and an energy level diagram depicting the CR mechanisms described in Reference 145.....	48
Figure 4.4 Upconversion emission spectrum from Figure 4.2, normalized to the $^1\text{D}_2 \rightarrow ^3\text{F}_4$ transition, and an energy level diagram depicting the proposed CR mechanism.	49
Figure 4.5 Upconversion lifetime profiles of $\text{LiYF}_4:25\%\text{Yb}^{3+},x\%\text{Tm}^{3+}$ UCNPs.....	50
Figure 4.6 NIR emission spectrum of $\text{LiYF}_4:25\%\text{Yb}^{3+},x\%\text{Tm}^{3+}$ UCNPs.....	52

Figure 4.7 Reaction scheme depicting the UV/blue-sensitized photoisomerization of azopropOH; and the absorption spectra of the <i>trans</i> - and <i>cis</i> - isomers of azopropOH, overlapping the upconversion emission spectrum of LiYF ₄ :25%Yb ³⁺ ,0.24%Tm ³⁺	53
Figure 4.8 Absorption spectrum of <i>trans</i> -azopropOH after continuous 976 nm irradiation, in solution with LiYF ₄ :25%Yb ³⁺ ,x%Tm ³⁺ UCNPs.	54
Figure 4.9 TEM micrograph of synthesized barium yttrium fluoride nanoparticles.	55
Figure 4.10 PXRD diffractogram of synthesized barium yttrium fluoride nanoparticles.	56
Figure 4.11 PXRD diffractograms of Ba _{1-x} Y _x F _{2+x} nanoparticles, with the calculated unit cell parameter <i>a</i> as a function of Ba ²⁺ concentration.....	57
Figure 4.12 Excitation and emission spectra, and luminescence lifetimes of BaYF ₅ :20%Eu ³⁺ nanoparticles.	58
Figure 4.13 Upconversion emission spectra of BaYF ₅ :25%Yb ³⁺ ,x%Tm ³⁺	60
Figure 4.14 Ratios of integrated emission intensities from Figure 4.13 as a function of Tm ³⁺ concentration.....	61
Figure 4.15 Upconversion lifetimes of the emissions at 475 and 802 nm from BaYF ₅ :25%Yb ³⁺ ,x%Tm ³⁺ UCNPs.....	63
Figure 4.16 Upconversion QYs of the emissions at 475 and 802 nm from BaYF ₅ :25%Yb ³⁺ ,x%Tm ³⁺ UCNPs.....	65
Figure 4.17 Upconversion emission spectra of BaYF ₅ , NaGdF ₄ , and LiYF ₄ UCNPs doped with Yb ³⁺ and Tm ³⁺	66
Figure 4.18 TEM micrographs and upconversion emission spectra, under 976 nm excitation of core/shell NaYF ₄ :20%Yb ³⁺ ,x%Tm ³⁺ /NaYF ₄ UCNPs.	69
Figure 4.19 Upconversion lifetime profiles of core/shell NaYF ₄ :20%Yb ³⁺ ,x%Tm ³⁺ /NaYF ₄ UCNPs under pulsed 976 nm excitation.	71
Figure 4.20 Single exponential decay times plotted as a function of temperature in water and DMF, from the lifetime profiles in Figure 4.19.	72
Figure 5.1 Tb ³⁺ energy level diagram.	74
Figure 5.2 Upconversion emission spectra of LiYF ₄ :25%Yb ³⁺ ,0.2%Tm ³⁺ , LiYF ₄ :25%Yb ³⁺ ,0.2%Tm ³⁺ ,15%Tb ³⁺ , and LiYF ₄ :25%Yb ³⁺ ,15%Tb ³⁺ nanoparticles.	75
Figure 5.3 Photoluminescence emission spectra of LiYF ₄ :25%Yb ³⁺ ,0.2%Tm ³⁺ ,15%Tb ³⁺ and LiYF ₄ :25%Yb ³⁺ ,15%Tb ³⁺ nanoparticles.	76

Figure 5.4 NIR luminescence spectra of $\text{LiYF}_4:25\%\text{Yb}^{3+},0.2\%\text{Tm}^{3+}$ and $\text{LiYF}_4:25\%\text{Yb}^{3+},0.2\%\text{Tm}^{3+},15\%\text{Tb}^{3+}$ nanoparticles, with an energy level diagram depicting the ET process from excited Yb^{3+} to the lower excited states of Tb^{3+} .	77
Figure 5.5 TEM micrographs of nanoparticles comprising core-only $\text{NaGdF}_4:49\%\text{Yb}^{3+},1\%\text{Tm}^{3+}$ and core/shell $\text{NaGdF}_4:49\%\text{Yb}^{3+},1\%\text{Tm}^{3+}/\text{NaGdF}_4:x\%\text{Tb}^{3+}$, with the corresponding particle size distributions.....	79
Figure 5.6 PXRD diffractograms and HAADF STEM micrographs of core/shell $\text{NaGdF}_4:49\%\text{Yb}^{3+},1\%\text{Tm}^{3+}/\text{NaGdF}_4:x\%\text{Tb}^{3+}$ UCNPs.	80
Figure 5.7 Upconversion emission spectra of $\text{NaGdF}_4:49\%\text{Yb}^{3+},1\%\text{Tm}^{3+}/\text{NaGdF}_4:x\%\text{Tb}^{3+}$ core/shell nanoparticles.....	81
Figure 5.8 Excitation spectra of $\text{NaGdF}_4:49\%\text{Yb}^{3+},1\%\text{Tm}^{3+}/\text{NaGdF}_4:20\%\text{Tb}^{3+}$ core/shell nanoparticles overlapping the upconversion emission spectra recorded in Figure 5.7.....	82
Figure 5.9 Upconversion lifetimes, under pulsed 976 nm excitation, of $\text{NaGdF}_4:49\%\text{Yb}^{3+},1\%\text{Tm}^{3+}/\text{NaGdF}_4:x\%\text{Tb}^{3+}$ core/shell nanoparticles.....	84
Figure 5.10 Energy level diagram depicting the ET mechanisms from Tm^{3+} to Tb^{3+} across the core/shell interface.	85
Figure 5.11 Upconversion luminescence lifetime of the ${}^3\text{H}_4 \rightarrow {}^3\text{H}_6$ transition of Tm^{3+} , under pulsed 976 nm excitation, of $\text{NaGdF}_4:49\%\text{Yb}^{3+},1\%\text{Tm}^{3+}/\text{NaGdF}_4:x\%\text{Tb}^{3+}$ core/shell nanoparticles, with an energy level diagram depicting the indirect depopulation of the ${}^3\text{H}_4$ state of Tm^{3+} through CR mechanisms influenced by ET to Tb^{3+}	86
Figure 5.12 Upconversion luminescence spectra of core/shell nanoparticles comprising $\text{NaGdF}_4:49\%\text{Yb}^{3+},x\%\text{Tm}^{3+}/\text{NaGdF}_4:10\%\text{Tb}^{3+}$	87
Figure 5.13 Upconversion luminescence lifetimes, digital photographs, and normalized time-resolved emission spectra of $\text{NaGdF}_4:49\%\text{Yb}^{3+},1\%\text{Tm}^{3+}/\text{NaGdF}_4:20\%\text{Tb}^{3+}$ UCNPs under pulsed 976 nm excitation.....	88
Figure 5.14 Digital photographs and intensity profiles in a rectangular area of flowing UCNPs in a microcapillary.	89
Figure 5.15 Upconversion luminescence lifetimes of the Tm^{3+} emission at 450 nm and the Tb^{3+} emission at 543 nm from $\text{NaGdF}_4:49\%\text{Yb}^{3+},1\%\text{Tm}^{3+}/\text{NaGdF}_4:20\%\text{Tb}^{3+}$ core/shell UCNPs, under pulsed 976 nm excitation.	90

Figure 5.16 Digital photographs and the corresponding experimental and theoretical particle velocities of $\text{NaGdF}_4:49\%\text{Yb}^{3+},1\%\text{Tm}^{3+}/\text{NaGdF}_4:20\%\text{Tb}^{3+}$ core/shell UCNPs in toluene.	92
Figure 6.1 TEM micrographs of $\text{LiYF}_4:x\%\text{Yb}^{3+},2\%\text{Er}^{3+}$ UCNPs with their corresponding particle size distributions.	94
Figure 6.2 Upconversion emission spectra and luminescence lifetimes of $\text{LiYF}_4:x\%\text{Yb}^{3+},2\%\text{Er}^{3+}$ UCNPs.	95
Figure 6.3 TEM micrographs of $\text{LiYF}_4:20\%\text{Yb}^{3+},x\%\text{Ho}^{3+}$ UCNPs, with their corresponding particle size distributions.	96
Figure 6.4 Upconversion emission spectra and luminescence lifetimes of $\text{LiYF}_4:20\%\text{Yb}^{3+},x\%\text{Ho}^{3+}$ UCNPs.	97
Figure 6.5 Eu^{3+} energy level diagram.	100
Figure 6.6 TEM micrographs and PXRD diffractograms of $\text{LiYF}_4:20\%\text{Eu}^{3+}$ and CsMnCl_3 photoluminescent nanoparticles.	101
Figure 6.7 Photoluminescence emission spectra, luminescence lifetimes, and time-resolved spectra of $\text{LiYF}_4:20\%\text{Eu}^{3+}$ and CsMnCl_3 nanoparticles.	102
Figure 6.8 Digital photographs under ambient lighting and pulsed 355 excitation of the completed print consisting of $\text{LiYF}_4:20\%\text{Eu}^{3+}$ nanoparticles forming the “Eu” symbol, masked using CsMnCl_3 nanoparticles.	103
Figure 6.9 TEM micrograph of $\text{LiYF}_4:20\%\text{Yb}^{3+},0.5\%\text{Ho}^{3+}$ UCNPs.	104
Figure 6.10 Upconversion emission spectra and luminescence lifetimes of citrate-capped $\text{LiYF}_4:18\%\text{Yb}^{3+},2\%\text{Er}^{3+}$ and $\text{LiYF}_4:20\%\text{Yb}^{3+},0.5\%\text{Ho}^{3+}$ UCNPs.	105
Figure 6.11 Digital photographs under continuous wave and pulsed 976 nm excitation, consisting of a QR code printed using $\text{LiYF}_4:20\%\text{Yb}^{3+},0.5\%\text{Ho}^{3+}$ UCNPs, masked with $\text{LiYF}_4:18\%\text{Yb}^{3+},2\%\text{Er}^{3+}$ UCNPs.	106
Figure 7.1 TEM micrographs of $\text{LiYF}_4:20\%\text{Eu}^{3+}$, $\text{LiY}_{0.5}\text{Lu}_{0.5}\text{F}_4:20\%\text{Eu}^{3+}$, and $\text{LiLuF}_4:20\%\text{Eu}^{3+}$ nanoparticles with their corresponding particle size distributions.	109
Figure 7.2 PXRD diffractograms of $\text{LiYF}_4:20\%\text{Eu}^{3+}$, $\text{LiY}_{0.5}\text{Lu}_{0.5}\text{F}_4:20\%\text{Eu}^{3+}$, and $\text{LiLuF}_4:20\%\text{Eu}^{3+}$ nanoparticles.	110
Figure 7.3 Radioluminescence emission spectra, under X-ray excitation, of $\text{LiYF}_4:20\%\text{Eu}^{3+}$, $\text{LiY}_{0.5}\text{Lu}_{0.5}\text{F}_4:20\%\text{Eu}^{3+}$, and $\text{LiLuF}_4:20\%\text{Eu}^{3+}$ nanoparticles.	112

Figure 7.4 Linear attenuation coefficient of each nanoparticle composition and the Mini-X X-ray source emission spectrum.	112
Figure 7.5 Photoluminescence emission spectra, under 355 nm excitation, of $\text{LiYF}_4:20\%\text{Eu}^{3+}$, $\text{LiY}_{0.5}\text{Lu}_{0.5}\text{F}_4:20\%\text{Eu}^{3+}$, and $\text{LiLuF}_4:20\%\text{Eu}^{3+}$ nanoparticles.	114
Figure 7.6 TEM micrographs of $\text{LiLuF}_4:x\%\text{Eu}^{3+}$ nanoparticles, with their corresponding particle size distributions.	115
Figure 7.7 Radioluminescence emission spectra under X-ray excitation, and photoluminescence emission spectra under 355 nm excitation, of $\text{LiLuF}_4:x\%\text{Eu}^{3+}$ nanoparticles.	116
Figure 7.8 Photoluminescence lifetimes recorded under pulsed 355 nm excitation of $\text{LiLuF}_4:x\%\text{Eu}^{3+}$ nanoparticles.	117
Figure 7.9 Radioluminescence emission spectra under X-ray excitation, photoluminescence emission spectra under 355 nm excitation, and luminescence lifetimes under pulsed 355 nm excitation, of $\text{LiLuF}_4:x\%\text{Dy}^{3+}$ nanoparticles.	119
Figure 7.10 Radioluminescence emission spectra under X-ray excitation, photoluminescence emission spectra under 355 nm excitation, and luminescence lifetimes under pulsed 355 nm excitation, of $\text{LiLuF}_4:x\%\text{Sm}^{3+}$ nanoparticles.	120
Figure 7.11 TEM micrographs of $\text{LiLuF}_4:10\%\text{Gd}^{3+}$, $\text{LiLuF}_4:20\%\text{Eu}^{3+}$, and $\text{LiLuF}_4:10\%\text{Gd}^{3+},20\%\text{Eu}^{3+}$ nanoparticles, with their corresponding size distributions.	122
Figure 7.12 Radioluminescence emission spectra, under X-ray excitation, of $\text{LiLuF}_4:10\%\text{Gd}^{3+}$, $\text{LiLuF}_4:20\%\text{Eu}^{3+}$, and $\text{LiLuF}_4:10\%\text{Gd}^{3+},20\%\text{Eu}^{3+}$ RLNPs.	123
Figure 7.13 Schematic representation of the population dynamics of Eu^{3+} excited solely <i>via</i> electron/hole recombination or through QC with Gd^{3+}	124
Figure 7.14 Reference PXRD patterns for LiYF_4 , LiEuF_4 , and LiLuF_4 , used to calculate the theoretical material densities as a function of Y^{3+} or Eu^{3+} dopant concentration.	126
Figure 7.15 TEM micrographs of core-only $\text{LiLuF}_4:20\%\text{Eu}^{3+}$, core/shell $\text{LiLuF}_4:20\%\text{Eu}^{3+}/\text{LiLuF}_4$, core/shell $\text{LiLuF}_4:20\%\text{Eu}^{3+}/\text{LiLuF}_4:10\%\text{Y}^{3+}$, and core/shell $\text{LiLuF}_4:20\%\text{Eu}^{3+}/\text{LiLuF}_4:20\%\text{Eu}^{3+}$ nanoparticles, with their corresponding particle size distributions and photoluminescence lifetimes under pulsed 355 nm excitation.	127
Figure 7.16 Photoluminescence emission spectra under 355 nm excitation, and radioluminescence emission spectra under X-ray excitation, of core-only $\text{LiLuF}_4:20\%\text{Eu}^{3+}$,	

core/shell $\text{LiLuF}_4:20\%\text{Eu}^{3+}/\text{LiLuF}_4$, core/shell $\text{LiLuF}_4:20\%\text{Eu}^{3+}/\text{LiLuF}_4:10\%\text{Y}^{3+}$, and core/shell $\text{LiLuF}_4:20\%\text{Eu}^{3+}/\text{LiLuF}_4:20\%\text{Eu}^{3+}$ nanoparticles..... 128

List of Tables

Table 1.1 SLJ selection rules for lanthanide electronic transitions.....	4
Table 3.1 Measured power densities with varying pulse width.	39
Table 4.1 ICP-MS results for the experimental dopant concentrations of Yb ³⁺ and Tm ³⁺ in LiYF ₄ UCNPs.	44
Table 4.2 Single exponential fitting of the decay components in Figure 4.5.....	51
Table 4.3 ICP-MS results depicting the experimental Ba ²⁺ :Y ³⁺ ratio to determine x in synthesized Ba _{1-x} Y _x F _{2+x} nanoparticles.	57
Table 4.4 Reported CR mechanisms between Tm ³⁺ ions in nanoparticles.	62
Table 4.5 Single exponential decay times from the curves in Figure 4.15.	64
Table 4.6 Linear and Arrhenius fitting from the trends observed in Figure 4.20.	72
Table 5.1 ICP-MS results for the experimental composition of the NaGdF ₄ core/shell UCNPs studied.	78
Table 5.2 Upconversion decay times and corresponding energy transfer efficiencies derived from Figure 5.7 and Figure 5.9.	85
Table 6.1 Transition probabilities of Er ³⁺ and Ho ³⁺ , reported in LaF ₃ from Reference 206 and 207.....	98
Table 7.1 Unit cell parameters and Z_{eff} calculations for the synthesized RLNP compositions..	111
Table 7.2 Theoretical transmitted X-ray energy of each nanoparticle composition, using Figure 7.4 and Equation 1.3.	113
Table 7.3 Relative luminescence intensity and Eu ³⁺ efficiency of the studied nanoparticle compositions, using the calculated differences in volume occupied by the core and shell.	129

List of Abbreviations

azopropOH	3-(4-phenylazophenoxy)propanol
CR	Cross-Relaxation
DMF	Dimethylformamide
EM	Energy Migration
ESA	Excited State Absorption
ET	Energy Transfer
ETU	Energy Transfer Upconversion
FRET	Förster Resonance Energy Transfer
GSA	Ground State Absorption
HAADF	High-Angle Annular Dark-Field
IC	Internal Conversion
ICP-MS	Inductively Coupled Plasma – Mass Spectrometry
ISC	Intersystem Crossing
NIR	Near- Infrared
PIV	Particle Imaging Velocimetry
PXRD	Powder X-ray Diffraction
QC	Quantum Cutting
QR	Quick Response
QY	Quantum Yield
RE	Rare-earth
RLNP	Radioluminescent Nanoparticle
STEM	Scanning Transmission Electron Microscopy
TEM	Transmission Electron Microscopy
UCNP	Upconverting Nanoparticle
UV	Ultraviolet

List of Symbols

Φ	Luminescence Quantum Yield
μ	Linear Attenuation Coefficient
ρ	Material Density
Z_{eff}	Effective Atomic Number
E	Photon Energy
A	Material Atomic Mass (Section 1.2) Microcapillary Cross-Section Area (Section 5.2)
I_0, I	Initial and Final Emission Intensities
x	Material Thickness
η	Overall Radioluminescence Efficiency
β	Conversion Efficiency
S	Energy Transfer Efficiency
Q	Activator Quantum Efficiency (Section 1.2) Microfluidic Flow Rate (Section 5.2)
R_0	Förster Distance
h	Reduced Planck Constant
τ_0	Donor Excited State Lifetime
c	Speed of Light
$J(W)$	Spectral overlap integral between the emission band of the donor and the absorbance band of the acceptor
n	Refractive Index (Section 1.3) Number of photons (Section 3.4)
N'	Avogadro's Number (molecules/mmol)
W_0	Energy of the donor transition
E_{FRET}	FRET efficiency
$R_{DA} \& r$	Distance between the donor and acceptor species
k_{ET}	Dexter Energy Transfer Efficiency
J	Normalized spectral overlap integral between the emission band of the donor and the absorbance band of the acceptor

L	Sum of ionic radii of the donor and acceptor species
h	Planck Constant
λ	Wavelength of Light
d	Interatomic lattice spacing
θ	Reflection angle determined <i>via</i> PXRD
abc	Unit cell lattice parameters
hkl	Miller Indices for a given crystallographic plane
P	Excitation Powder Density
$\langle n_s \rangle$	Rate of Phonons
ω	Energy of Phonon
k	Boltzmann Constant
T	Temperature
τ & τ_{decay}	Excited State Decay Time
k_r	Radiative Relaxation Rate
k_{FRET}	Nonradiative Energy Transfer Rate
$k_{h.ph.}$	Host Phonon Relaxation Rate
$k_{s.ph.}$	Solvent Phonon Relaxation Rate
τ_0	Theoretical Decay Time at 0 K
C	Quenching Rate Constant
ΔE	Energy gap between the emitting and next lowest energy level
S_R	Relative Thermal Sensitivity
E_{ET}	Total Energy Transfer Efficiency
v_P	Particle Velocity
u	Axial Fluid Velocity
ξ_{min}, ξ	Minimum and Average energy required to produce one electron hole pair
E_i	Ionization Energy
$\langle E_{kin} \rangle$	Generated Kinetic Energy of an electron or hole
K	Energy loss fraction due to phonon quenching

Chapter 1. Introduction

1.1. Lanthanides

The lanthanide series consists of fourteen elements from cerium to lutetium, so named due to their similar physical and chemical properties to lanthanum. Derived from the ancient Greek “lanthanein”, which roughly translates to “to escape notice”, the lanthanides were initially discovered in 1794 when Johan Gadolin isolated “yttria”, which contained a mixture of lanthanide oxides.¹ With the final discovery of lutetium in 1907 and Henry Moseley’s studies on atomic numbers in 1913, the full lanthanide series was realized. The inclusion of scandium, yttrium, and lanthanum constitutes the well-known “rare-earth” (RE) elements, despite their comparable natural abundance to other common elements. For example, the terrestrial abundance of cerium is similar to nickel or copper, and even the rarest RE elements (thulium and lutetium) are still orders of magnitude greater in abundance than gold.² It is likely that this misleading nomenclature is owed to their late discovery and difficult separation, since isolating each element is resource intensive. Regardless, RE elements have found widespread uses in many industries, including catalysis, car manufacturing, and telecommunications, owing to their unique chemical, magnetic, and optical properties.³⁻⁵

The general electronic configuration of the lanthanides in their elemental form is $[\text{Xe}]6s^25d^14f^x$, where x follows the series from 1 for cerium to 14 for lutetium.⁶ However, the lanthanides are generally found and mined in their trivalent oxidation state, with an electronic configuration of $[\text{Xe}]4f^x$, since their lowest ionization energies correspond to the electrons in the outermost 6s and 5d orbitals. Some of the lanthanides can also exist in other oxidation states, such as Ce^{4+} , which possesses no valence electrons, or Eu^{2+} , which configures as $[\text{Xe}]4f^7$. In all instances, a unique property amongst the lanthanides is the shielding of valence electrons from the outer, fully occupied 5s and 5p orbitals, which overwhelmingly minimizes external influences on the 4f electrons.⁷ This implies that certain aspects of the lanthanides, such as their optical properties, are minimally affected by the environment, and are characteristic to each element.

1.1.1. 4f Electronic States

Unlike p or d orbitals, which are degenerate before external electric forces act on them, the f orbitals in a given lanthanide have different energies, even when considering a free ion, as depicted in **Figure 1.1**.^{8,9} The primary forces that dictate the energy of different electron configurations are Coulombic interactions between the electrons and the nucleus of the ion. This is because of how close the 4f orbitals are to the nucleus, resulting in spectroscopic terms that are generally separated by 10^4 cm^{-1} .^{10,11} Secondly, spin-orbit coupling between the angular momenta of an electron and its orbit dictate the position of spectroscopic levels within a term, which can influence the position of a level by up to $\pm 10^3 \text{ cm}^{-1}$. These influences result in a series of characteristic electronic ground and excited states that are unique to each lanthanide, depicted in Appendix 1.

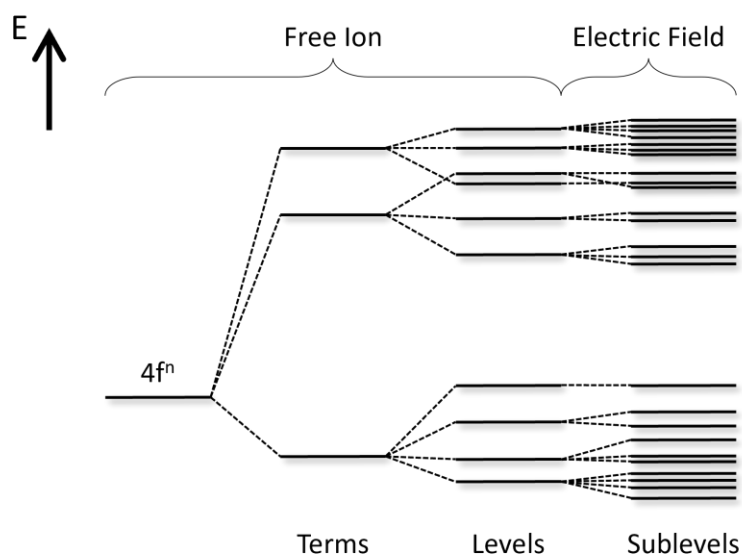


Figure 1.1 Energy level diagram depicting the Coulombic interactions (Terms), spin-orbit coupling (Levels) and crystal field effects (Sublevels) that dictate the position of lanthanide excited states.

In order to make sense of the different 4f electronic excited states, the Russell-Saunders coupling scheme is used to label each 4f level with a $^{2S+1}L_J$ term symbol.^{7,12} The $2S+1$ term is the spin multiplicity and is obtained from the sum of all electron spins ($\pm 1/2$ each). The L term is determined using the sum of the angular momentum quantum numbers of the occupied orbitals, which is then correlated to a letter following the same convention (0=S, 1=P, 2=D, 3=F, 4=G, and

so on). Finally, the J term describes the spin-orbit coupling of a given state and is obtained from the previous terms ($S+L, S+L-1, S+L-2 \dots |S-L|$).

Interestingly, while the previously discussed shielding from the 5s and 5p orbitals prevents drastic changes in the energy of 4f electronic levels, there is still an observed Stark effect that can dictate the position of individual sublevels by $\approx 10^2 \text{ cm}^{-1}$.⁸ This process is not characteristic of the ion, but rather its environment, when a lanthanide is used as a metal center of a complex or a dopant in a material. The number and magnitude of these sublevels are a consequence of the symmetry and polarizability of the ion's coordination sphere.

1.1.2. Electronic Transitions and Selection Rules

Lanthanide luminescence stems from electronic transitions that originate from the valence electrons of the ions. This can either be intraconfigurational 4f-4f transitions, which occur between 4f electronic states, as mentioned above, or from interconfigurational 4f-5d transitions. The probability of such transitions, however, are not devoid of the selection rules that govern other luminescent molecules, complexes, and materials.¹³ Firstly, the spin selection rule states that an electronic transition may not undergo a change in spin multiplicity, meaning no electron in the configuration may change spin. Secondly, the Laporte selection rule states that an electronic transition may not take place between two states of equal parity, meaning the orbitals responsible for the transition must originate from different azimuthal quantum numbers (for example, $d \rightarrow p$, $f \rightarrow d$, etc.).

It is apparent that the lanthanide 4f-4f transitions are forbidden by the Laporte selection rule, and in many instances the spin selection rule. However, they are still observed with relative ease in many systems.⁷ As mentioned previously, when an electric field acts on the lanthanide ions, a Stark effect is observed to generate sublevels of different 4f electronic states. Interestingly, the ligand or crystal field that drives this process is also responsible for a phenomenon known as j-mixing, where the electric field acts on the empty 5d orbitals of the lanthanide ions.¹⁴ This causes distortions in the 5d wavefunction, which in turn mixes with the internal 4f wavefunction, and gives the 4f orbitals some 5d character, thus alleviating the Laporte selection rule. Transitions facilitated through this mechanism are known as induced electric dipole transitions, which are

subject to different restrictions than traditional electric dipole transitions, as arranged in **Table 1.1**.^{15,16}

In some instances, lanthanide transitions originate from magnetic dipole transitions, which are weaker in intensity, but are subject to more lenient selection rules than electric dipole transitions. One such example is the $^5D_0 \rightarrow ^7F_1$ emission of Eu^{3+} , which occurs with a transition probability that is independent of the ion's environment.¹⁷ In contrast, the interconfigurational 4f-5d transitions are highly dependent on the environment of the ion.¹⁸ This is because they involve the population of the 5d orbitals, which are highly influenced by the electric field surrounding the ion. Examples include the ultraviolet (UV) emissions from Ce^{3+} or the broad-spanning visible emission from Eu^{2+} .^{19,20}

Table 1.1 SLJ selection rules for lanthanide electronic transitions.

Dipole Transition	<i>S</i>	<i>L</i>	<i>J</i>
Electric	$\Delta S = 0$	$ \Delta L \leq 0$	
		$L = 0 \leftrightarrow L' \neq 0$	$J = 0 \leftrightarrow J' \neq 0$
		$L' = 0 \leftrightarrow L \neq 0$	$J' = 0 \leftrightarrow J \neq 0$
Induced Electric	$\Delta S = 0$	$ \Delta L \leq 6$	$ \Delta J \leq 6$
		$L = 0 \therefore \Delta L = 2,4,6$	$J = 0 \therefore \Delta J = 2,4,6$
		$L' = 0 \therefore \Delta L = 2,4,6$	$J' = 0 \therefore \Delta J = 2,4,6$
Magnetic	$\Delta S = 0$	$\Delta L = 0$	$J = 0 \leftrightarrow J' \neq 0$
			$J' = 0 \leftrightarrow J \neq 0$

1.2. Luminescence

Since lanthanide luminescence requires a radiative relaxation of an ion from a higher energy excited state to a lower energy state or ground state, a sufficient source of energy is required to populate these excited states. For example, cathodoluminescence involves electron bombardment on a substrate that generates light, and was commonly used industrially in red-emitting, Eu^{3+} -based cathode ray tubes.²¹ More recently, photon-sensitized lanthanide

luminescence has become more commonplace as it is considerably more practical, having uses in anti-counterfeiting, telecommunication, and medical imaging applications.²²

There are two independent properties that influence the capabilities of lanthanide luminescence: the absorption cross-section and the quantum yield (QY) of the system. When exposed to a source of photons with an energy resonant with the initial excitation, the absorption of a photon is the first step, the efficiency of which is conventionally reported as the absorption cross-section, in units of cm^2/ion .²³ Once an ion is in an excited state, there are multiple relaxation pathways that it may follow, including both radiative and nonradiative. This percentage of excited ions that relax radiatively is reported as the luminescence QY (Φ), as described in Equation 1.1:²⁴

$$\Phi = \frac{\text{Number of photons emitted}}{\text{Number of photons absorbed}} * 100 \quad (1.1)$$

1.2.1. Photoluminescence

Fluorescence from organic molecules is the most commonly encountered form of photoluminescence, where higher energy irradiation is converted to lower energy emissions.²⁵ However, fluorescence relies on allowed singlet-singlet transitions between molecular orbitals, while photoluminescence from lanthanides occur from transitions between the intrinsic orbitals of the ion. Photoluminescent lanthanide ions are excited using higher energy light to directly populate the excited states, followed by an internal conversion to the emitting level. This internal conversion is typically achieved through phonon-assisted relaxation, where the vibrational modes from the ion's environment bridge the energy gap from the initial excited state to the emitting state.²⁶ Finally, the ion relaxes radiatively, to a lower energy state or the ground state, generating a photon (**Figure 1.2**).

An industrial example of lanthanide photoluminescence is in modern optical telecommunications, which have improved considerably in recent years, as Er_2O_3 -doped optical fibers are now the standard in signal amplification. Exploiting the ${}^4\text{I}_{13/2} \rightarrow {}^4\text{I}_{15/2}$ emission of Er^{3+} at 1550 nm, which can be excited using 980 nm irradiation, this near-infrared (NIR) emission band enables the necessary amplification to transmit information signals around the planet.^{27,28} As a more tangible example, europium-doped materials, such as oxides and oxysulfides, are commonly employed by governments and different industries as anti-counterfeiting tools.^{22,29} By printing

these materials in patterns only visible *via* photoluminescence under UV excitation, distinguishing real vs counterfeit goods, currencies, and documents is much easier.

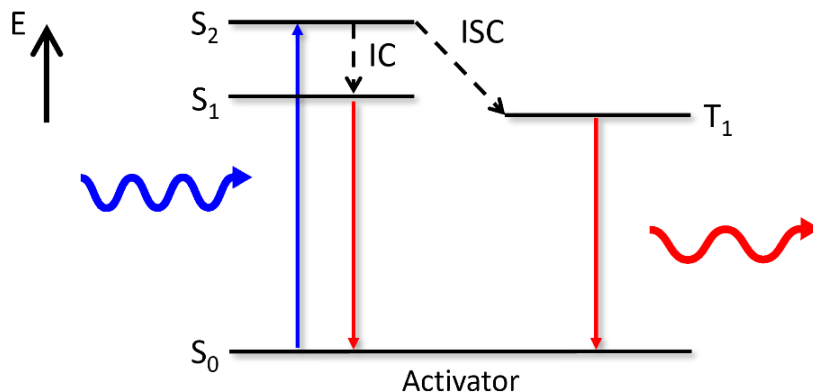


Figure 1.2 Energy level diagram depicting traditional fluorescence. IC: Internal conversion, ISC: Intersystem crossing.

1.2.2. Upconversion Luminescence

First postulated by Bloembergen in 1958 and studied by Auzel in the 1960s, upconversion is a non-linear luminescence process where multiple excitation photons can sequentially populate higher excited states of a luminescent ion, resulting in emissions of higher energy than the incident excitation source.^{30,31} In contrast to photoluminescence, this is facilitated through intermediate excited states with relatively long lifetimes (hundreds of microseconds to milliseconds), which stems from the low transition probabilities due to the forbidden nature of lanthanide 4f-4f transitions. This allows the absorption of another photon, rather than radiative relaxation back to the ground state. The result is the population of higher energy states that can then relax radiatively to generate photons that are of higher energy than the incident photons being absorbed. While many different upconversion mechanisms are observed, the phenomena mentioned herein are those pertinent to the research in this thesis.

The simplest upconversion mechanism is ground/excited state absorption (GSA/ESA), where a single ion (known as an activator) completes the entire absorption and emission process.³¹ This is achievable when the activator ion has “ladder-like” excited states that can each be populated *via* the absorption of photons of the same wavelength, as depicted in **Figure 1.3**. The efficiency of GSA/ESA is dependent on the absorption cross-section of each absorption transition involved, as well as the lifetime of each intermediate excited state, since the sequential absorption steps must be more probable than the relaxation of the ion back to the ground state.³² The most common example of lanthanide GSA/ESA is from Er^{3+} , where sequential absorptions of 976 nm photons can produce emissions in the green and red regions of light.³¹

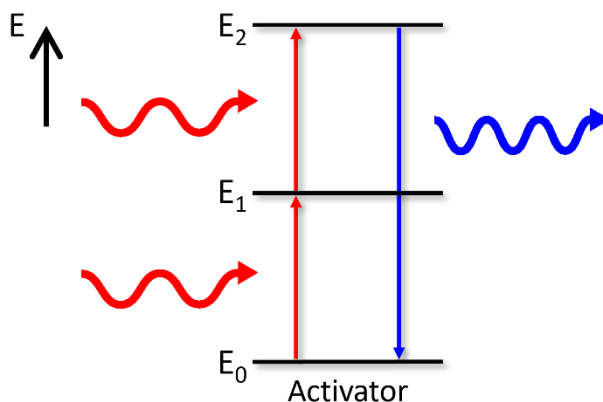


Figure 1.3 Energy level diagram depicting upconversion luminescence *via* ground and excited state absorption.

When multiple activator ions are in close proximity to each other, there is the potential for energy transfer (ET) between them in a manner that is destructive to the luminescence efficiency, known as concentration quenching. This, consequently, limits the efficiency of GSA/ESA since activator ions must be sufficiently spaced to avoid ET. To circumvent this limitation, a second ion that has an excited state resonant with the activator ion’s ladder-like levels is introduced, which is the basis for energy transfer upconversion (ETU).^{33,34} This sensitizer ion (sometimes referred to as the donor ion) which ideally has a higher absorption cross-section than the activator, can absorb the incident excitation photons and transfer that energy nonradiatively to the activator ion (often referred to as the acceptor ion), as depicted in **Figure 1.4**. When this ET process occurs more than once, between one or more sensitizers to a single activator, ETU is achieved, with improved upconversion luminosity than GSA/ESA by more than an order of magnitude.

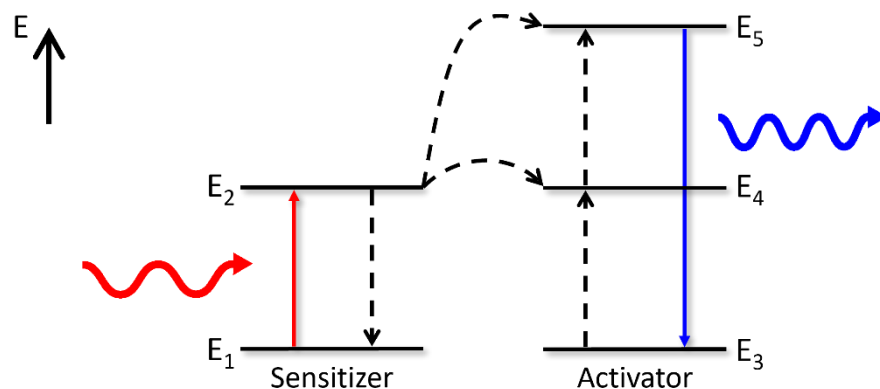


Figure 1.4 Energy level diagram depicting upconversion luminescence *via* energy transfer upconversion.

The most common sensitizer in lanthanide ETU is Yb^{3+} , which has the highest absorption cross-section in the NIR region, at 976 nm, from the ${}^2\text{F}_{5/2} \leftarrow {}^2\text{F}_{7/2}$ transition. When this ion is paired with Er^{3+} , Tm^{3+} , or Ho^{3+} as the activator ion, upconversion luminescence in the UV, visible, or higher-energy NIR regions is observed.³⁵

Cooperative upconversion mechanisms have also been studied to a lesser extent, which are more complex and therefore less efficient than traditional GSA/ESA and ETU. Cooperative luminescence from Yb^{3+} is the most rudimentary example, which involves the dimerization of two ions, as depicted in **Figure 1.5**.^{36,37} Upon the coupling of their angular momenta, the resulting dimer possesses multiple excited states and resembles a ladder-like structure that can undergo GSA/ESA. Similarly, if a third Yb^{3+} ion is in close proximity, ETU between this monomer and a neighboring dimer is also possible.

Other lanthanide ions that do not possess resonant excited states, and therefore cannot achieve conventional upconversion, can still undergo cooperative sensitization; however, there are several possible mechanisms that drive this process. Dimerization between Yb^{3+} and Tb^{3+} has been observed, shown in **Figure 1.6a**, following a similar approach to Yb^{3+} dimers that undergo GSA/ESA.³⁸ Simultaneous energy transfer from two Yb^{3+} ions to either Tb^{3+} or Eu^{3+} has also been observed, shown in **Figure 1.6b**.^{39,40} The distinction between which mechanism prevails is likely dependent on the host composition and the interionic spacing.

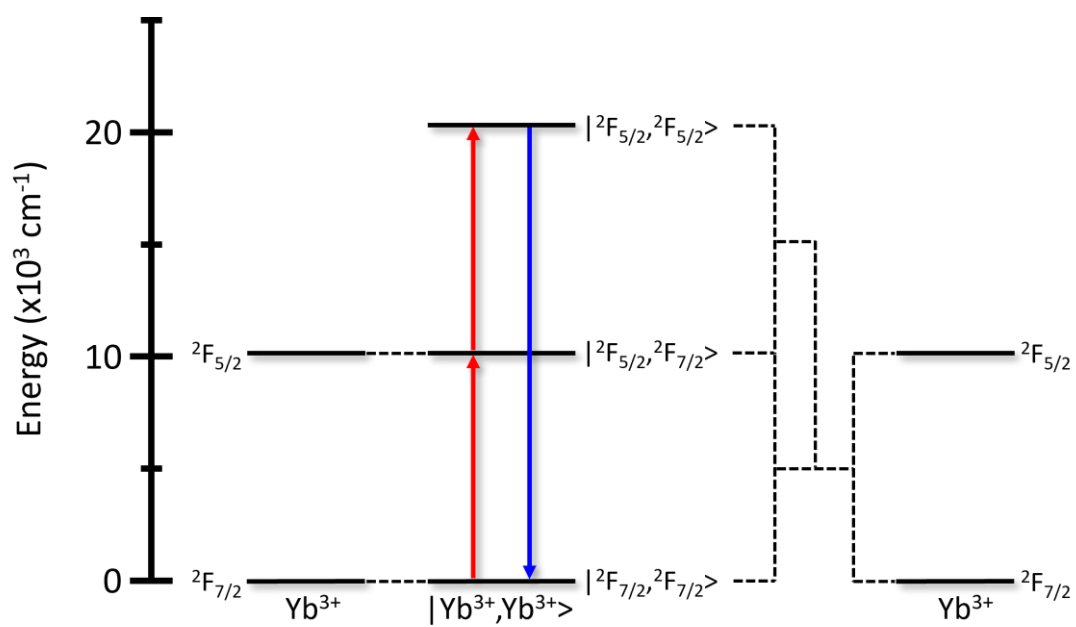


Figure 1.5 Energy level diagram depicting upconversion luminescence *via* cooperative luminescence from the dimerization of Yb³⁺ ions.

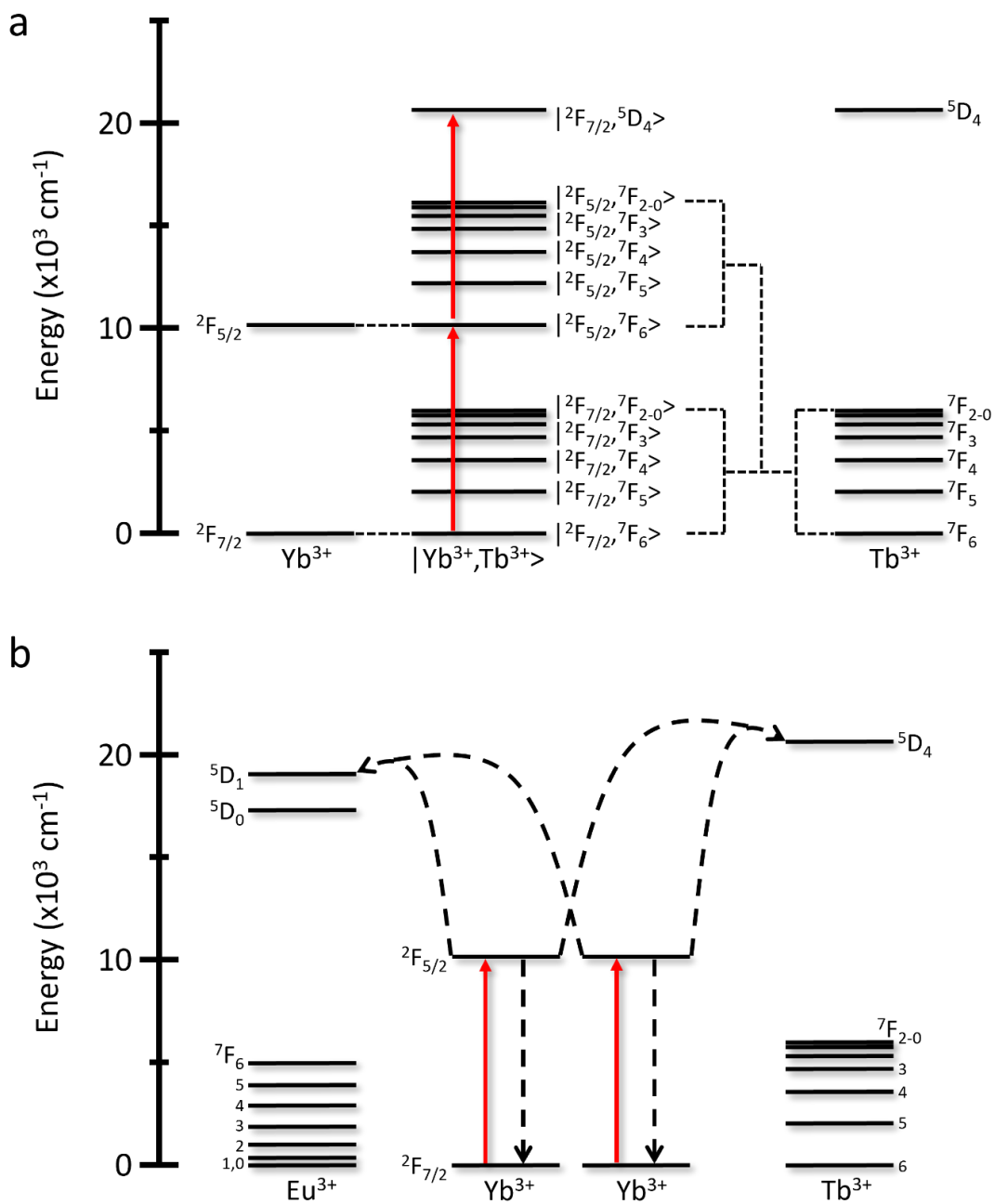


Figure 1.6 Energy level diagram depicting upconversion luminescence *via* cooperative sensitization either (a) from the dimerization of Yb^{3+} and Tb^{3+} ions, or (b) through simultaneous energy transfer from multiple Yb^{3+} ions to a single activator ion.

1.2.3. Radioluminescence

While upconversion uses lower energy excitation to generate higher energy emissions, some materials and molecules luminesce upon excitation with high-energy ionizing radiation. The irradiation consists of either high-energy photons (X-ray or gamma) or other particles with enough energy to ionize atoms, and the nature of the interaction is dependent on the energy of the incident particles.^{41,42} Scintillators, which are a specific branch of radioluminescent materials that rely on band-gap or allowed transitions, have found widespread industrial use in radiation detectors and medical imaging.^{43,44} However, more recently, radioluminescence from forbidden 4f-4f lanthanide transitions has been studied in more detail, showing promising results for use in X-ray mediated photodynamic therapy and biomedical imaging.⁴⁵ To this end, for the sake of brevity, the following discussion focuses on X-ray-sensitized radioluminescence materials.

Generally speaking, “lower energy” X-rays (up to several hundred keV) interact with materials predominantly through the photoelectric effect, where atoms will eject inner shell electrons upon irradiation.⁴² This process can lead to various secondary effects, since the newly generated electron vacancy needs to be filled, which occurs through the generation of secondary X-rays or Auger electrons, resulting in a propagation of energy through the material. X-rays with energies between 0.5 and 5 MeV interact *via* Compton scattering, where the photons collide and release valence shell electrons.⁴⁶ Similar to the photoelectric effect, the vacancy can then propagate through a given material. Finally, for high energy X-rays (≥ 10 MeV), the light-matter interaction occurs *via* pair production, where the photon is absorbed by a nucleus and generates an electron/positron pair that propagates through a material, dissipating the energy through Coulombic interactions with neighbouring nuclei and electrons. In many instances of all three effects, the energy provided by one single X-ray photon exceeds the energy of the transition, thus the interactions are inelastic, and a cascade of processes occurs until all the energy is deposited.

The attenuation of ionizing radiation by a material, specifically in relation to the photoelectric effect, can be quantified using a linear attenuation coefficient (μ), depicted in Equation 1.2:

$$\mu = \frac{\rho Z_{eff}^4}{E^3 A} \quad (1.2)$$

Where the density of the material (ρ) and its effective atomic number (Z_{eff}) improve the attenuation as they increase, whereas increasing the energy of the incident X-rays (E) and the atomic mass of the material (A) decrease the probability for photoelectric attenuation of a material.⁴⁷ This influence on incident X-rays can be described using a modified version of Beer's law (Equation 1.3):

$$I = I_0 e^{-\mu x} \quad (1.3)$$

Where I_0 and I are the initial and final X-ray intensities, and x is the thickness of the material.⁴⁸

Once the energy from X-ray irradiation is attenuated by a material, luminescence may follow if the conditions are appropriate. With specific interest in wide band-gap materials, the overall radioluminescence efficiency (η) can be quantified using Equation 1.4:

$$\eta = \beta S Q, \quad \text{where } 0 \leq \eta, \beta, S, Q \leq 1 \quad (1.4)$$

Which is a product of the efficiency of each individual stage that converts the absorbed energy into emitted photons by the material, as illustrated in **Figure 1.7**.⁴⁹

Firstly, the conversion efficiency (β) describes the conversion of the absorbed energy into band-gap transitions, where electrons are promoted from the valence band to the conduction band of a crystal, leaving a hole in its place. These electron/hole pairs can then propagate throughout the lattice of the material. This stage is dependent on the band-gap energy of the material, where smaller band-gaps (such as those in semiconductor materials) can generate more electron/hole pairs per absorbed X-ray photon, while insulators with larger band gaps generate fewer electron/hole pairs per absorbed X-ray photon of the same energy. Secondly, these electron/hole pairs can recombine on luminescent centers incorporated throughout the lattice of a material, transferring the energy and ultimately populating their respective excited states. This is referred to as the energy transfer efficiency (S), and the mechanism through which this process occurs is still poorly understood, with speculation that it follows a charge transfer or dipole coupling, as described in Section 1.3. Finally, with the excitation of luminescent centers, the activator quantum

efficiency (Q) determines the number of emitted photons, following the principle described in Section 1.2.

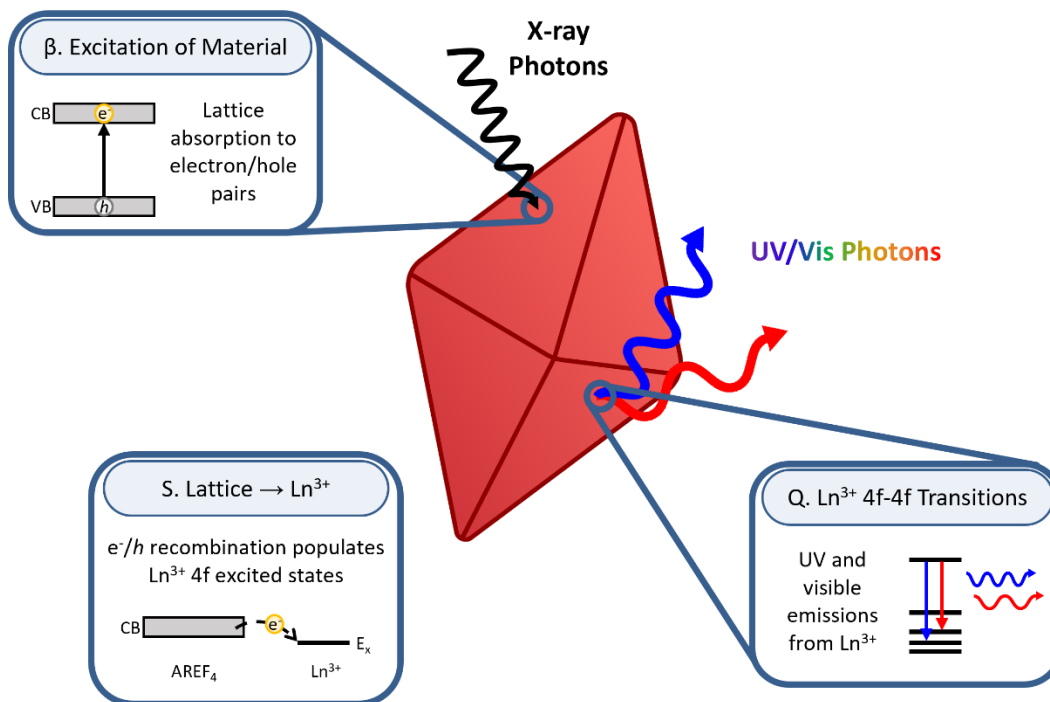


Figure 1.7 Schematic representation of the three processes (β , S , and Q) that dictate the efficiency of radioluminescence in wide band-gap materials.

When considering radioluminescent materials for study, with the intent on a particular application, there are other properties that researchers need to consider.⁴⁹ A luminescent center that produces emissions at the desired wavelength, with maximal light yield (typically described as number of emitted photons per MeV of energy absorbed), are primary considerations. For repeated and long-term use, the material in question must be chemically stable and possess high resistance to radiation damage. For applications where the radioluminescence emissions are meant to detect ionizing radiation, the decay time of the material must be fast, as to give temporal resolution to the measurement. Finally, given the climate in today's society, the price tag to produce this material must be low enough that the problem being solved is cost-effective.

Commonly used radioluminescent materials that employ trivalent lanthanide ions as luminescent centers include $(Y,Gd)_2O_3:Eu^{3+}$ or $Gd_2O_2S:Pr^{3+},Ce^{3+},F^-$ as computed tomography detectors, and $(Y,Lu)_2SiO_5:Ce^{3+}$ to improve the temporal resolution of positron emission tomography.⁵⁰⁻⁵² Outside of the medical field, radioluminescent materials used in electron

microscopy detectors ($\text{Gd}_2\text{O}_2\text{S}:\text{Tb}^{3+}$ or $\text{Y}_3\text{Al}_5\text{O}_{12}:\text{Ce}^{3+}$) and in gamma ray spectroscopy to study the atmospheric composition of distant planets and star systems ($\text{Cs}_2\text{LiYCl}_6:\text{Ce}^{3+}$ or $\text{SrI}_2:\text{Eu}^{3+}$) are now the industrial standard.^{22,53,54}

1.3. Energy Transfer

As mentioned briefly in the previous sections, lanthanide luminescence is often dependent on the transfer of energy from one ion to another, or in the instance of radioluminescence, from the host material to a luminescent center. This ET can occur through a few different phenomena, as illustrated in **Figure 1.8**.

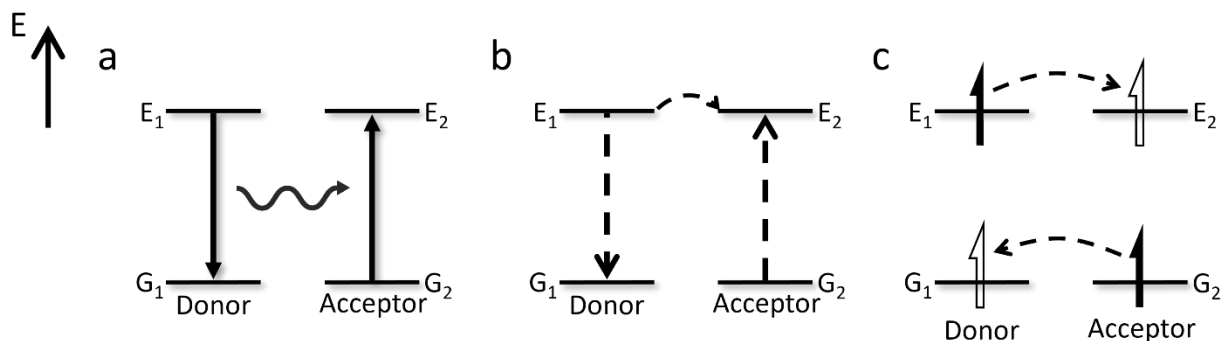


Figure 1.8 Energy level diagrams depicting energy transfer *via* (a) reabsorption of light, (b) FRET, and (c) Dexter energy transfer.

The simplest approach to ET is the reabsorption of light emitted from one ion by another, sometimes referred to as radiative energy transfer. The initially excited ion emits independently, and those emitted photons may be absorbed by an adjacent ion. Because this process involves the emission of a photon by the sensitizer in any direction, it is widely seen as detrimental to improving lanthanide luminescence. For example, in ETU, the sensitizer absorbs the excitation light and must transfer that energy to the activator ion. However, if the sensitizer emits *via* photoluminescence instead, and that energy is re-absorbed by the activator, the overall process is less efficient than the activator absorbing the incident photons through GSA/ESA, since there are fewer steps in the mechanism. The sole advantage to radiative ET is the independence to atomic distance between the two ions involved, since the emission from the sensitizer and the absorption from the activator are separate events.⁵⁵

The more sought-after ET mechanism in lanthanide luminescence is Förster Resonance Energy Transfer (FRET) between the sensitizer and activator ions.⁵⁶ If the two ions are sufficiently close together, their individual Coulombic interactions can facilitate a coupling of their angular momenta, leading to dipole-dipole interactions that result in nonradiative ET between them. The Förster distance (R_0 , Equation 1.5) between any two spectroscopically active species (ions, fluorescent molecules, complexes, etc.) is used to quantify the efficiency of this process, and is considered the distance at which FRET is 50% efficient:

$$R_0 = \sqrt[6]{\frac{3\hbar\tau_0c^2J(W)}{4\pi^3n^2N'^2W_0^2}} \quad (1.5)$$

Where \hbar is the reduced Planck constant, τ_0 is the excited state lifetime of the sensitizer, c is the speed of light, $J(W)$ is the spectral overlap integral between the emission band of the sensitizer and the absorption band of the acceptor, n is the refractive index of the medium, N' is Avogadro's number in molecules/mmol, and W_0 is the energy of the donor's transition in wavenumbers. As expected, the greater the spectral overlap between the two species, the more efficient FRET will be. Similarly, the longer the donor remains in its excited state, the more probable FRET is since the donor is less likely to relax. This is why FRET between the metastable excited states of lanthanide ions is so prevalent. In a practical sense, the FRET efficiency (E_{FRET}) can be determined using Equation 1.6:

$$E_{FRET} = \frac{1}{1 + \left(\frac{r}{R_0}\right)^6} \quad (1.6)$$

Where r is the distance between the donor and acceptor. This sixth-power distance dependence is seen as the primary limiting factor in FRET, since the donor and acceptor species will likely have relatively long distances between them. These can either be ions in a crystalline material or molecules dispersed in a solvent or other medium.

The Dexter energy transfer model is the other mechanism through which luminescent species may transfer energy between electronic states.⁵⁷ In contrast to FRET, which still involves the electronic transitions (excitation and relaxation) of the component species, Dexter energy transfer describes an electron transfer from the excited donor to the acceptor's orbital configuration. For charge compensation, an electron from the ground state configuration of the

acceptor is transferred back to the donor ion, restoring its ground state configuration. Since this mechanism involves a physical interaction between the two species, the distance dependency is exponential, as observed in Equation 1.7:

$$k_{ET} \propto J * \exp\left(\frac{-2R_{DA}}{L}\right) \quad (1.7)$$

Where k_{ET} is the rate of Dexter energy transfer, J is the normalized spectral overlap integral between the emission band of the donor and the absorbance band of the acceptor, R_{DA} is the distance between the donor and acceptor, and L is the sum of the donor and acceptor van der Waals radii.⁵⁸ This exponential dependence on distance, coupled with the previously discussed shielding effects on the valence 4f electrons of the lanthanide ions, overwhelmingly minimizes any Dexter energy transfer from occurring.

1.3.1. Lanthanide Energy Transfer Mechanisms

As mentioned previously, the long-lived 4f-4f excited state lifetimes of the lanthanides make them highly susceptible to nonradiative ET, and the many states that most of them possess enable numerous possible mechanisms (**Figure 1.9**). Most commonly and efficiently, when the energy gaps between the donor and acceptor are resonant, ET can occur. A common example of this is the first ETU step between Yb^{3+} and Er^{3+} , as discussed in Section 1.2.2, where the Yb^{3+} : $^2\text{F}_{5/2} \rightarrow ^2\text{F}_{7/2}$ and Er^{3+} : $^4\text{I}_{11/2} \leftarrow ^4\text{I}_{15/2}$ transitions are almost perfectly resonant.⁵⁹ However, there are many instances where the donor and acceptor have slightly mismatched energies, and are reliant on “phonon-assisted” energy transfer. This employs vibrational modes of the medium, whether that be from the solvent, ligands, lattices, etc., to bridge the energy difference and facilitate ET.⁶⁰ A known example is the first ETU step between Yb^{3+} and Tm^{3+} , where the Yb^{3+} : $^2\text{F}_{5/2} \rightarrow ^2\text{F}_{7/2}$ and Tm^{3+} : $^3\text{H}_5 \leftarrow ^3\text{H}_6$ transitions differ in energy by approximately 1650 cm^{-1} , which still occurs through phonon-assisted ET.⁶¹

When multiple of the same ion are present in proximity, there is also the possibility that energy from one may transfer to another. If this ET occurs from the same states of both the donor and acceptor ions, it is referred to as energy migration (EM).⁶² This process is very efficient, since the same states from the same ion have truly perfect resonance, and likely occurs multiple times, essentially migrating the initially absorbed energy throughout the medium. If two identical ions

are in different excited states, ET between them can occur if resonant states are present. This is appropriately named cross-relaxation (CR) since it involves populating an excited state of one ion while relaxing a neighboring ion to a lower energy state. An example of this between Er^{3+} ions involves the ${}^4\text{F}_{7/2} \rightarrow {}^4\text{F}_{9/2}$ and ${}^4\text{F}_{9/2} \leftarrow {}^4\text{I}_{11/2}$ transitions, which results in both ions populating the red-emitting ${}^4\text{F}_{9/2}$ level.⁶³

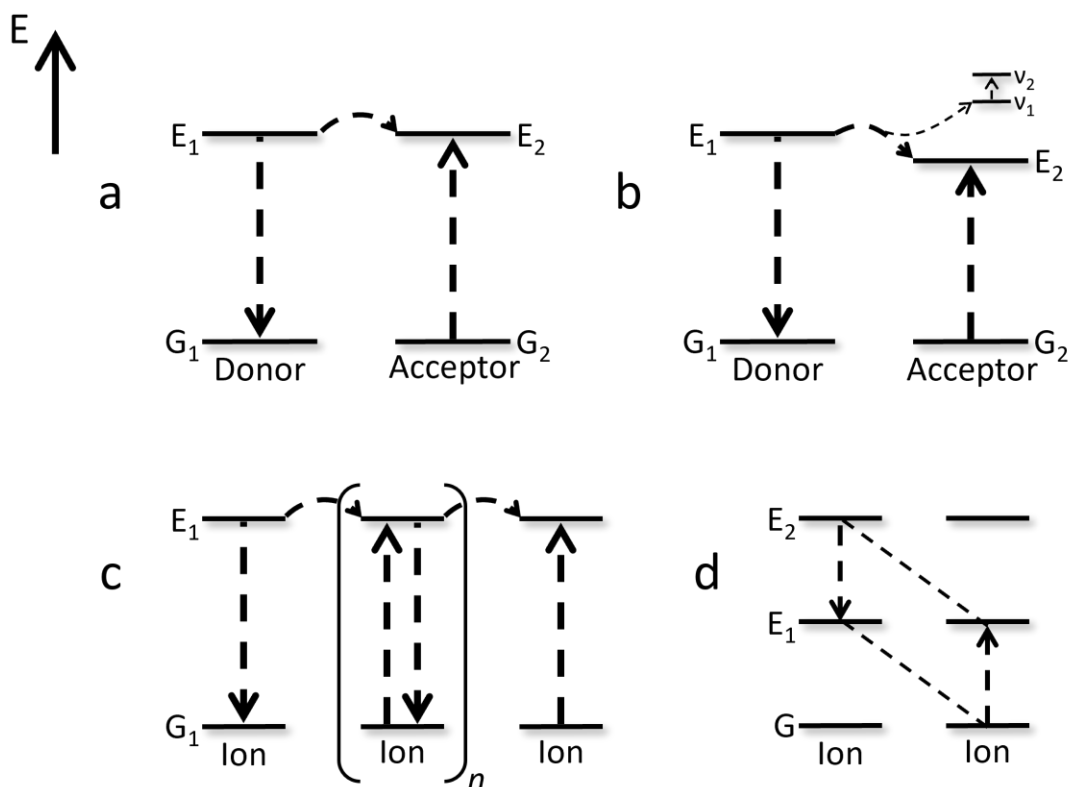


Figure 1.9 Energy level diagrams depicting energy transfer mechanisms *via* (a) ideal energy transfer, (b) phonon-assisted energy transfer, (c) energy migration, and (d) cross-relaxation.

1.4. Nanoscience

As the name suggests, nanoscience is the study of all things at the nanoscale, whether that be intermolecular or interatomic forces, physicochemical and optical properties of inorganic nanomaterials, or subcellular interactions, to name a few of the many topics currently being studied.^{64–66} While it is generally confined to molecules, materials, or other forms of matter with at least one spatial dimension ≤ 100 nm, this definition is more of a suggestion; in reality it is as dynamic and adaptable as the field itself. Originally conceptualized in 1959 by Richard Feynman,

who envisioned an entire field of research driven by the manipulation of individual atoms and molecules, it was not until the late 1970s and 1980s that nanoscience was popularized.^{64,67,68} New obstacles and considerations have emerged as nanoscience continues to expand and develop, such as the increased dominance of non-covalent interactions between molecules and forces that would otherwise be negligible. Therefore, comparing single crystal and bulk materials to nanomaterials has been integral to lanthanide-doped nanoparticles.

One principal characteristic of nanoparticles is their high surface area-to-volume ratios, which imparts them with unique properties, such as colloidal stability. Moreover, nanoparticles can contain atoms situated on the surface with unoccupied valence orbitals, resulting in partial charges that increase their reactivity.⁶⁴ These, or other functional groups coordinated to the surface, have enabled nanoparticle use in a myriad of applications, including heterogeneous catalysis and drug delivery.^{69,70} Furthermore, luminescent nanoparticles can even be used as imaging probes, exploiting their functional surface for targeting of specific cellular regions or organ systems.⁷¹

To this end, the co-precipitation nanoparticle synthesis technique is one of the most implemented protocols.⁷² This method relies on the nucleation of the nanoparticles using lanthanide halide salts in nonpolar solvents, slightly elevating the temperature to dissociate the reagents, followed by cooling the solution, which promotes the ionic bonding that forms the nanoparticles.⁷³ Further elevating the solution to temperatures exceeding 280 °C allows for Ostwald ripening that tunes their size, morphology, and crystal structure.^{74,75} Similarly, thermal decomposition protocols have been studied, which exploit lanthanide reagents that decompose at temperatures above 280 °C, leaving free ions in solution that then form ionic bonds.⁷² Other synthesis methods, such as solvo/hydrothermal or more elaborate ionic liquid-based techniques have also been explored, but to a lesser extent.

1.4.1. Photoluminescent and Upconverting Lanthanide-doped Nanomaterials

As mentioned in Section 1.1.2, the induced electric dipole transitions observed in lanthanide ions need a crystal or ligand field to distort the empty 5d orbitals, facilitating them despite their forbidden nature. This electric field is most often introduced by doping the lanthanides in inorganic crystalline materials. Traditionally, doping is defined as the addition of an impurity to a material to induce a change in the properties of that material.^{76,77} Therefore, the addition of

lanthanide ions to something otherwise spectroscopically silent imbues them with luminescence properties. Lanthanide-doped glasses are the perfect examples of such materials, including Er^{3+} green upconversion in $x\text{PbO}\cdot(1-x)\text{SiO}_2$, Eu^{3+} photoluminescence in $\text{M}(\text{PO}_3)_2$, or Nd^{3+} NIR upconversion in $x\text{AlF}_3\cdot(1-x)\text{MF}_2$ (where M are alkaline earth metals).⁷⁸⁻⁸⁰

The most commonly studied lanthanide-doped materials involve substituting host atoms with the “dopant”, occupying the same crystalline site, with its corresponding symmetry and coordination number. It can be argued that this does not constitute a doped material, but rather a new composition entirely, since the lanthanide ions are not impurities distorting the crystalline lattice (**Figure 1.10**). However, since they still introduce new properties to the material, the term “dopant” is used. The most common examples include lanthanide-doped oxides (Y_2O_3), oxysulfides ($\text{Y}_2\text{O}_2\text{S}$), and fluorides (YF_3 or AYF_x , where A is an alkali or alkaline earth metal).⁸¹⁻⁸⁴ In all instances, the lanthanides substitute Y^{3+} ions in the lattice of the material, and in many cases completely replace Y^{3+} , such as in $\text{Gd}_2\text{O}_2\text{S}$ or NaLuF_4 .^{85,86} Since the lanthanide ions occupy known crystalline sites within the material, the spectroscopic properties are more predictable and reproducible than amorphous or impure materials. This makes it easier to study, optimize, and implement upconverting nanoparticles for long-term, industrial use.

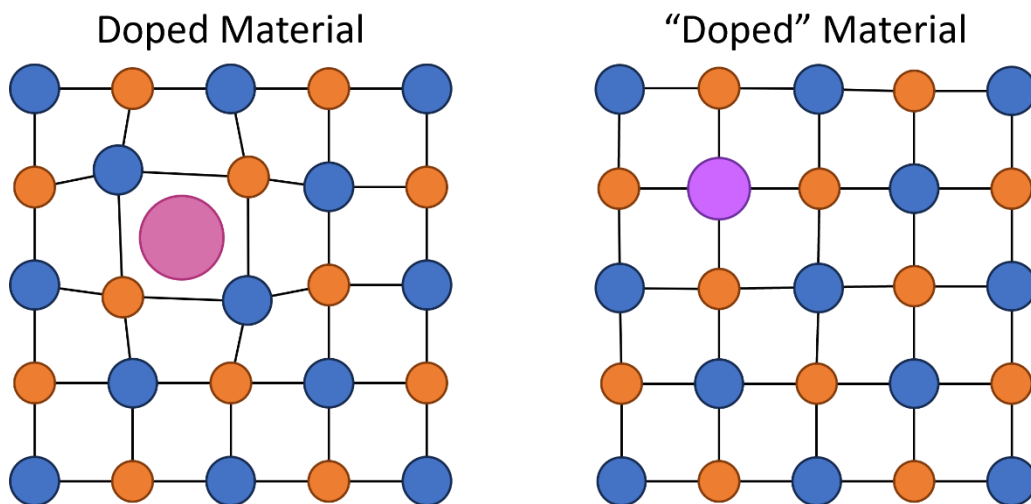


Figure 1.10 Schematic representation of a doped material, where (left) the impurity occupies interstitial space and thus distorts the crystallinity, or (right) the impurity is incorporated within the lattice with minimal distortions.

As mentioned previously, the benefit to nanomaterials is their adaptability to different applications otherwise unfeasible with bulk-scale materials. However, their nanoscale size leads to new hindrances in the luminescence efficiency of the lanthanide dopants. Most nanoparticles are synthesized using bottom-up approaches, which can cause defect formation near the surface of the nanoparticles, either through the introduction of vacancies in the unit cells or hydroxyl functional groups occupying anion sites.^{74,87} The latter introduces high energy phonons (exceeding 3000 cm^{-1}) which can bridge the energy gap and quench the excited states of the lanthanides, greatly limiting their efficiency.⁸⁸ Efforts have been made to minimize such quenching effects through core/shell architectures or functionalizing the nanoparticle surface, but these only curtail effects that are otherwise nonexistent at the bulk-scale.^{89,90}

1.4.2. Nanoscintillators and Radioluminescent Nanomaterials

Conventional lanthanide luminescence at the nanoscale, either through photoluminescence or upconversion, suffers primarily from increased nonradiative relaxation of their excited states when compared to bulk-scale materials. However, under ionizing irradiation, studying the excitation of the lanthanide luminescent centers is further complicated at the nanoscale. Since the principal interactions between X-ray photons and matter are inelastic, it can be assumed that a single X-ray photon would deposit energy to multiple nanoparticles before dissipating. This means, in colloidal nanoparticle dispersions, the changes in radioluminescence would not be linear with changing concentration. Similarly, the subsequent interactions from ejected Auger electrons and secondary X-rays would also change as a function of nanoparticle concentration, further complicating their study and potential use.⁹¹ Moreover, after the absorption of ionizing radiation, the generated electron/hole pairs can propagate freely throughout a nanoparticle. However, this distance can also exceed the length of a nanoparticle, as it has been approximated that the diffusion of hot electrons across an ionic crystal is about 100 nm .⁹² This means that excitons may propagate to the surface of the nanoparticle and recombine without transferring energy to a luminescent center, or may be ejected from the nanoparticle entirely, dissipating the energy into the environment.

A study comparing the relative efficiency of known scintillators at the bulk and nanoscale demonstrated exactly this concern.⁹³ For example, the commonly employed $\text{Bi}_4\text{Ge}_3\text{O}_{12}$ scintillator performs better at the nanoscale than a series of Pr^{3+} -doped $\text{Y}_3\text{Al}_5\text{O}_{12}$, while the latter perform

better as single crystals, and the reason for this is still not fully understood. This implies that well documented bulk materials with weak radioluminescence may not translate to nanoscintillators or radioluminescent nanomaterials. Similarly, strongly emitting radioluminescent materials may not carry over the same efficiency at the nanoscale and must be evaluated accordingly when choosing a material composition for any given application.

Chapter 2. Statement of the Problem

2.1. Academic Research on Lanthanide-doped Luminescent Nanoparticles

Since the turn of the millennium, lanthanide-doped upconverting nanoparticles (UCNPs) have gained considerable attention from the scientific community, owing to the versatility of upconversion luminescence and the functionality that comes from nanoparticles. Since the luminescence from UCNPs originate from inorganic crystalline materials, they are resistant to photobleaching and photoblinking, while also possessing high chemical stability and minimal toxicity.⁹⁴ This is paramount to their implication in biomedical applications, which have been at the forefront of UCNP research.⁹⁵ Research in solar energy conversion, information storage, and nanothermometry using UCNPs has also shown promise for future implementation.⁹⁶⁻⁹⁸ Despite their potential in these different areas of study, the major limitation is the inherently weak luminescence from the forbidden 4f-4f electronic transitions, coupled with the low quantum yields that arise from upconversion, since multiple excitation photons are required to generate one emitted photon. Therefore, while many studies focus on their potential uses, attention has also been placed on improving the luminescence efficiency of UCNPs.

Upconversion research at the nanoscale has been overwhelmingly focused on fluoride host nanoparticles.^{72,99,100} This is due to their generally simplistic synthesis protocols that generate reproducible, monodisperse, crystalline UCNPs with high functionalizing capabilities, colloidal stability and low phonon energies ($<400\text{ cm}^{-1}$). More specifically, UCNPs most often studied by researchers are comprised of the ternary NaYF₄ or NaGdF₄ host composition, doped with Yb³⁺ as the sensitizer, and either Er³⁺ or Tm³⁺ as the activator ion. According to Google Scholar, over one-third of the 3500 publications on UCNPs in 2022 make mention of these hosts, emphasizing its prominence in the field. As mentioned previously, ETU between Yb³⁺ and Er³⁺ converts 976 nm light into emissions in the green and red regions of light, as illustrated in **Figure 2.1**.¹⁰¹ ETU between Yb³⁺ and Ho³⁺ has also been studied for its green and red emissions as well, as depicted in **Figure 2.2**, although it is considerably less efficient than Er³⁺. ETU between Yb³⁺ and Tm³⁺ is particularly unique, since it converts NIR light to higher energy NIR, red, blue, and UV emissions, as illustrated in **Figure 2.3**.

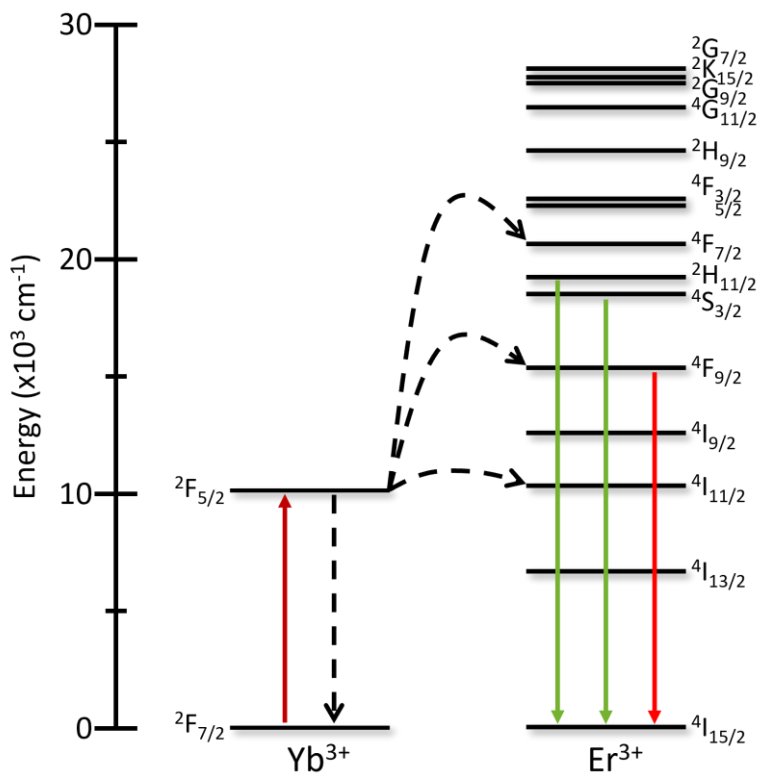


Figure 2.1 Energy level diagram depicting ETU between Yb^{3+} and Er^{3+} .

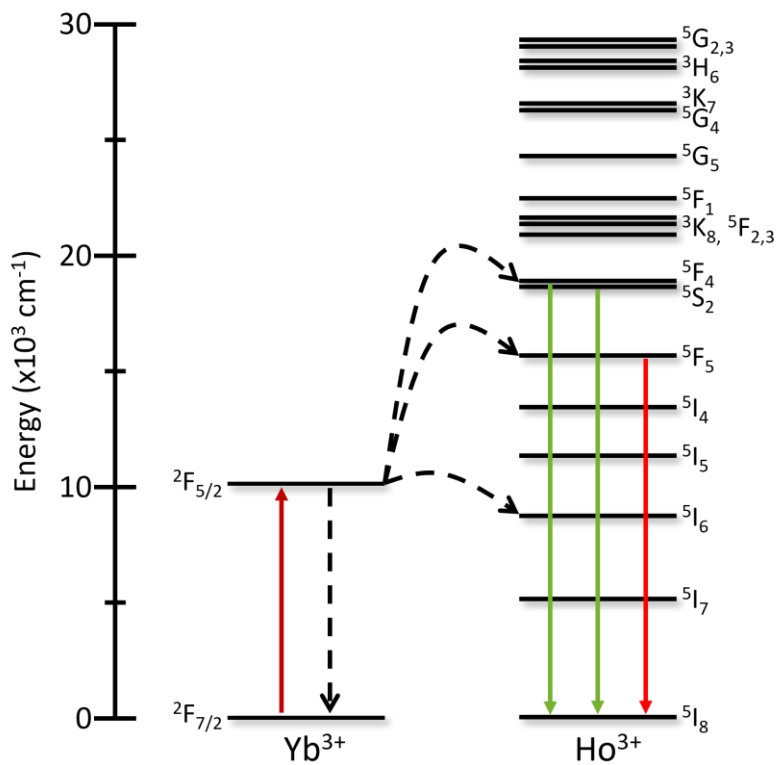


Figure 2.2 Energy level diagram depicting ETU between Yb^{3+} and Ho^{3+} .

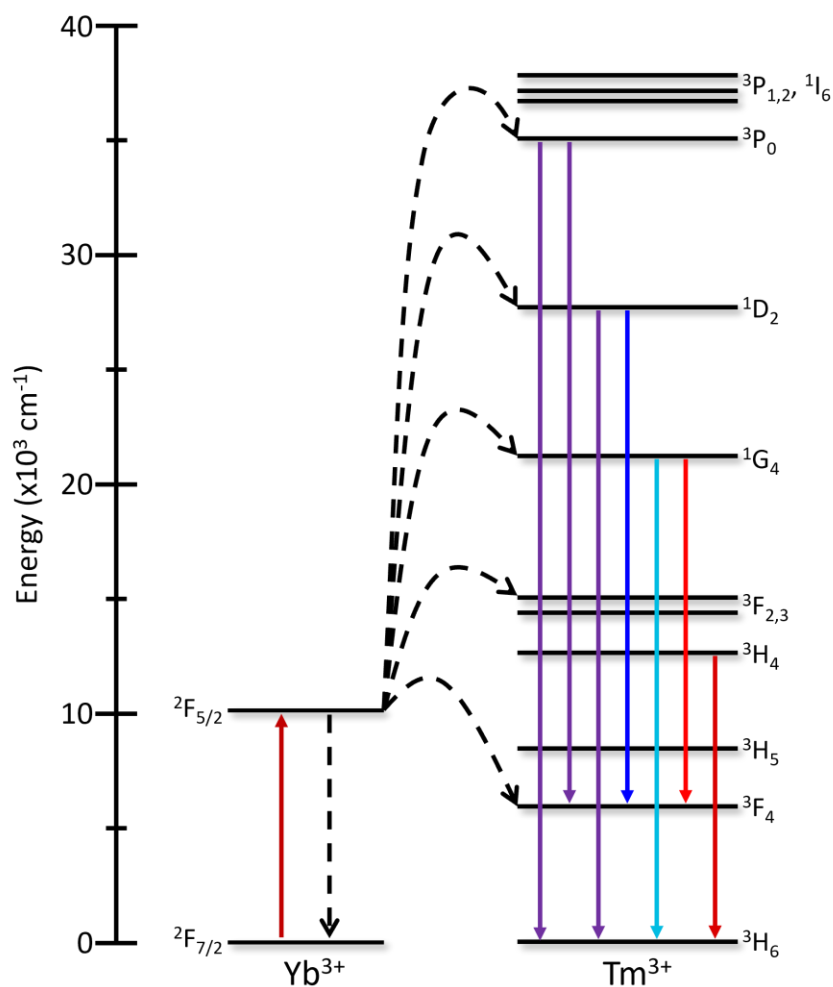


Figure 2.3 Energy level diagram depicting ETU between Yb^{3+} and Tm^{3+} .

As mentioned in Section 1.4.1, phonon quenching of the lanthanide excited states by the environment is one of the biggest challenges impeding the efficiency of UCNPs. To prevent the interaction between colloiddally-dispersed UCNPs and solvent molecules, the use of core/shell nanoparticles has been adopted. The simplest core/shell structure incorporates the sensitizer and activator ions in the core, with an inert shell to physically separate the lanthanide dopants from the vibrational modes of solvent molecules, such as $\text{NaYF}_4:\text{Yb}^{3+},\text{Er}^{3+}/\text{NaYF}_4$.¹⁰² In certain studies, the adoption of active shells has also proven effective at enhancing upconversion luminescence further, through the incorporation of Yb^{3+} ions in the shell. This allows for improved absorption of the incident 976 nm photons before energy transfer to the activator ions in the core.⁸⁹

Excitation at 976 nm, which lies on the fringe of the second biological window (1000 – 1500 nm, as depicted in **Figure 2.4**), has enabled the use of UCNPs for study in various biomedical applications, since incident light can penetrate tissues to greater depths than UV or visible light.^{95,103} For this reason, bioimaging using UCNPs has been studied *ad nauseam*, in both *in vitro* and *in vivo* settings, with emphasis on evaluating where nanoparticles accumulate subcellularly or how to target particular organs. For example, NaYF₄:Yb³⁺,Tm³⁺ nanoparticles have demonstrated use as bioimaging probes, due to the characteristic emission band from Tm³⁺ at 800 nm (³H₄ → ³H₆), which lies in the first biological window.¹⁰⁴ Photodynamic therapy using UCNPs has proven advantageous compared to traditional approaches, where the nanoparticles are employed in tandem with a photosensitizer to enable the production of reactive oxygen species under NIR irradiation. Photosensitizers such as Rose Bengal, which has an absorption band that overlaps with the green emissions of Er³⁺, and riboflavin, which absorbs between 300 – 500 nm, overlapping with the emission bands of Tm³⁺, have demonstrated reactive oxygen species generation under NIR irradiation, courtesy of sensitization from the UCNPs.^{105,106} Photo-assisted drug delivery has also been demonstrated through the coordination of a drug-derivative to the surface of UCNPs, with the intention of only releasing the drug in a target region that is exposed to NIR irradiation. For example, the UV emissions from LiYF₄:Yb³⁺,Tm³⁺ can cleave doxorubicin derivatives electrostatically linked to the nanoparticle surface.¹⁰⁷

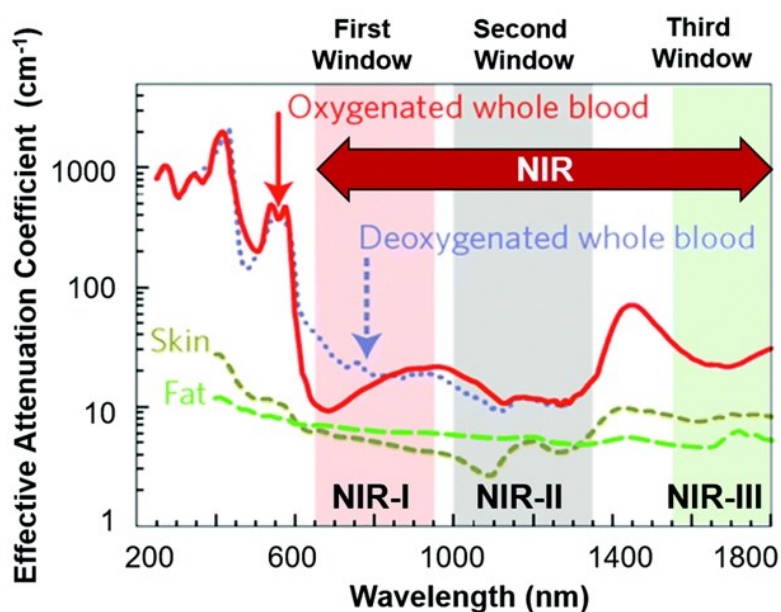


Figure 2.4 Absorption spectra of relevant biological tissues and media, illustrating the three optical windows. Reproduced from Reference 95 with permission from the Royal Society of Chemistry.

While 976 nm irradiation does lie on the edge of a biological window, a local absorption maximum of water exists at this wavelength, resulting in adverse heating effects that limit the viability of UCNPs excited at this wavelength.¹⁰⁸ To circumvent this problem, researchers have elected to use Nd^{3+} as a co-dopant, which absorbs 800 nm irradiation and transfers this energy to Yb^{3+} , as depicted in **Figure 2.5**.¹⁰⁹ Since this wavelength lies in the middle of the first biological window, there is minimal heating of aqueous environments, thus increasing the feasibility of UCNPs in biological settings. However, with the addition of another ET step in the upconversion process, the nanoparticles are less efficient, which introduces new limitations in their use. Similarly, the use of NIR dyes that absorb 800 nm light has been explored, since they rely on fluorescent molecules with higher absorption cross-sections than Nd^{3+} .¹¹⁰ However, under the conventional high excitation powers used for upconversion luminescence of nanomaterials, the photostability of these dyes is compromised, which prevents their use in any application that requires prolonged irradiation (exceeding thirty minutes) or stable emission intensities.¹¹¹

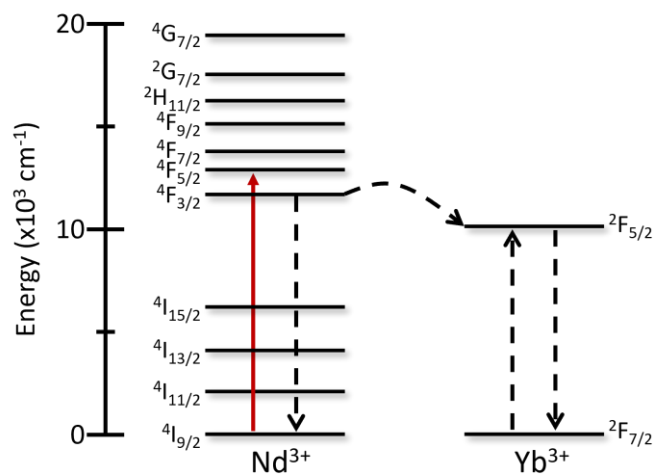


Figure 2.5 Energy level diagram depicting energy transfer between Nd^{3+} and Yb^{3+} , to further sensitize ETU.

The versatility of UCNPs extends beyond biological applications, as other industrial uses are also being explored. For example, by incorporating UCNPs in silicon-based solar cells, NIR light emitted by the sun can be absorbed *via* upconversion to visible light.^{96,112} This capacity to absorb approximately 50% of the solar spectrum that is otherwise ignored aims to improve energy harvesting capabilities and thus increasing the effectiveness of solar cells.¹¹³ Since lanthanide activator ions can range in emission wavelength across the entire visible spectrum, UCNPs have

been studied extensively for information storage and anti-counterfeiting applications. Their use in Quick Response (QR) codes dates back to 2012, where Meruga *et al.* printed overlapping nanoparticle compositions with Er^{3+} and Tm^{3+} as activators. This displayed different information simultaneously in green and blue light, respectively, that could be filtered and observed individually.¹¹⁴ Since then, many advancements have been explored to refine and sophisticate overlapping patterns with different emission colors that could be isolated individually using different band-pass filters or color channels.^{115,116}

Another interesting feature of lanthanide luminescence is the slew of radiative transitions that originate from each ion, many of which lie close together in energy. As a result, there are some excited states for a given ion that are thermally coupled, which means their relative population is dependent on the temperature of the nanoparticle. This allows for a direct correlation between the ratio of the radiative transitions from those states and the temperature of the nanoparticle's environment, allowing for spectroscopic temperature evaluations with high spatial resolution using UCNPs.¹¹⁷ This is particularly impressive with nanoparticles doped with Er^{3+} , since the $^2\text{H}_{11/2}$ and $^4\text{S}_{3/2}$ excited states responsible for the emissions at 525 and 545 nm, respectively, are only separated by a few hundred wavenumbers. Since this energy gap is easily bridged *via* phonons, which are temperature dependent, the emission ratio from these two states are an indication of the temperature of the UCNPs.¹¹⁸

Over the last couple decades, the radioluminescence properties and population mechanisms of lanthanide-doped binary and ternary fluoride nanoparticles have also been explored.^{119,120} These radioluminescent nanoparticles (RLNPs) benefit from the previously discussed functionality of fluoride nanoparticles, with wide band-gaps (exceeding 10 eV) that can facilitate higher energy lanthanide transitions.¹²¹ The latter property has been integral to the implementation of Pr^{3+} -doped NaLuF_4 nanoparticles for X-ray mediated photodynamic therapy, which relies on a radiative transition at 405 nm originating from the $^1\text{S}_0$ excited state.⁴⁵ This emission overlaps with the absorption band of an endogenous photosensitizer, protoporphyrin IX, that accumulates in cancer cells, thus proving an effective enhancement over conventional radiotherapy alone. X-ray bioimaging using Eu^{3+} -doped $\text{Ba}_{0.55}\text{Y}_{0.3}\text{F}_2$ nanoparticles has also proven effective in conjunction with image-guided radiotherapy, due to the unlimited depth penetration of ionizing radiation, and the characteristic red emissions from Eu^{3+} which lie on the edge of the first biological window.¹²²

Relying on the heavier Ba^{2+} cation allows for efficient X-ray attenuation *via* the photoelectric effect, improving the signal-to-noise of the resulting images.

Radioluminescent NaLuF_4 nanoparticles doped with Tb^{3+} have seen potential use as nanoscale storage phosphors, which can be implemented as a safety tool in radiation dosimetry.¹²³ Similarly, in radiation detection, where fast decay times are necessary to have high temporal resolution, the implementation of materials like $\text{LaF}_3:\text{Ce}^{3+}$ have been explored, due to the allowed 4f-5d interconfigurational transitions of Ce^{3+} .¹²⁴

2.2. Research Project Objectives

Bulk-scale lanthanide-doped phosphors are common in many areas of today's consumer-driven economy, including lighting devices, radiation detectors, lasers, anti-counterfeiting tools and telecommunication fibers.²² However, the pivot from bulk-scale to nanomaterials in biomedical or other industrial applications has been lackluster, with no company or organization explicitly implementing lanthanide-doped luminescent nanoparticles into commercial products. This begs the question of why, after two decades of study and thousands of research papers, has there been no commercial sector that has adopted these nanomaterials?

The greatest disadvantage of lanthanide luminescence is the weak emissions from the forbidden 4f-4f transitions, which hinders any application that requires strong emission intensities. This problem is further exacerbated with upconversion, since each step in the upconversion process has individual losses in efficiency. Furthermore, at the nanoscale, the prevalence of surface quenching is naturally greater with an increase in surface area-to-volume ratio. With these debilitating factors in mind, it becomes clear why limitations in the luminosity of UCNPs or RLNPs have inhibited their implementation. Recently, researchers have focused their attention on putting lanthanide-doped nanoparticles *to work*, rather than understanding in greater detail *how they work*, which is, to some extent, what has hindered their integration into everyday society.

The research presented herein aims to take a step back and study the fundamental mechanisms through which lanthanide luminescence occurs in nanomaterials, with the intent on improving their efficiencies by understanding the population and relaxation processes. This includes considerations that come from their nanoscale size and any consequence that stems from the synthesis of the nanoparticles.

While the choice to employ the NaREF₄ host composition appears trivial, given its overwhelming use throughout the literature, the effect the host composition has on the upconversion efficiency is not fully understood. Therefore, studies on NaGdF₄, LiYF₄, and BaYF₅ nanoparticles doped with Yb³⁺ and Tm³⁺ were carried out, to evaluate the relative and absolute upconversion intensities with varying crystalline site symmetry, coordination number, and interionic spacing. The Tm³⁺ activator ion, which emits in the UV, visible, and NIR regions, is susceptible to many different ET mechanisms, and is thus a good choice to probe the aforementioned variables. Similarly, the activator dopant concentration was also evaluated (ranging from 0.1 to 2 mol% Tm³⁺), to observe changes in the absolute and relative upconversion intensities with changing interionic spacing between Tm³⁺ ions within a nanoparticle lattice.

With greater understanding on the ET mechanisms and the ET efficiencies between lanthanides in UCNPs, the effect of core/shell structures were investigated. However, rather than the conventional inert or sensitizer-doped shell, an active shell doped with activator ions was studied, to evaluate ET from the core to the shell. This was completed using NaGdF₄ nanoparticles doped with Yb³⁺ and Tm³⁺ in the core, and Tb³⁺ doped in the shell. Mechanisms that drive Tm³⁺ → Tb³⁺ ET were studied using the characteristic green emissions of Tb³⁺ to provide insight on the interactions across the UCNP core/shell interface.

With a greater understanding of upconversion luminescence at the nanoscale, attention was also put into evaluating how the luminescence dynamics could be implemented in applications of these nanoparticles. Rather than using lifetime measurements exclusively to study ET, upconversion and photoluminescence decay times were used to measure temperature, evaluate the velocity of nanoparticles in a microfluidic flow, and temporally encrypt printed information. These studies aim to demonstrate that the forbidden nature of lanthanide luminescence is not exclusively a limitation, but rather can be exploited to the benefit of various techniques, both academically and commercially.

With decades of research on lanthanide luminescence at the nanoscale, the resources and devotion to upconversion have eclipsed the attention placed on RLNPs. This is likely due, in part, to the inherent danger of ionizing radiation, but also the complexity and ambiguity behind radioluminescence mechanisms, which limit their implementation in biological applications. Therefore, to gain a better understanding of radioluminescence at the nanoscale, variables that are

known to affect bulk-scale materials were assessed, as well as commonly explored variables that influence the efficiency of nanomaterials, to see if their influence is consistent in RLNPs. These variables include material density, the dopant concentration of the luminescent center, the addition of a possible sensitizer ion, and the effect of core/shell structures. Eu^{3+} -doped LiREF_4 nanoparticles were used throughout these experiments due to the efficient visible photoluminescence from Eu^{3+} .

The multifaceted work presented in this thesis aims to advance the current understanding of lanthanide luminescence at the nanoscale, *via* upconversion and radioluminescence, to improve the overall efficiency of these materials for future implementation. By considering variables that are overlooked at times, considerable improvements can be made without convoluted material functionalization or manipulation. Moreover, a new approach to various techniques can inspire a future path in exploiting the forbidden nature of lanthanide transitions, rather than solely looking to overcome it, and taking advantage of the temporal domain.

Chapter 3. Experimental Methods

3.1. Reagents

Rare-earth oxides were purchased of highest available purity from Alfa Aesar (Y_2O_3 : 99.99%, Tm_2O_3 : 99.997%, and Yb_2O_3 : 99.998%), Sigma Aldrich (Sm_2O_3 : 99.99%, Ho_2O_3 : 99.999%, and Er_2O_3 : $\geq 99.99\%$), or Chemicals 101 Corp. (Eu_2O_3 : 99.9%, Gd_2O_3 : 99.995%, Dy_2O_3 : 99.99%, and Lu_2O_3 : 99.999%). Hexahydrated rare-earth chlorides were purchased from Sigma Aldrich at the highest available purity ($\text{YCl}_3 \cdot 6\text{H}_2\text{O}$: 99.999%, $\text{GdCl}_3 \cdot 6\text{H}_2\text{O}$: 99.999%, $\text{TbCl}_3 \cdot 6\text{H}_2\text{O}$: 99.999%, $\text{TmCl}_3 \cdot 6\text{H}_2\text{O}$: 99.99%, and $\text{YbCl}_3 \cdot 6\text{H}_2\text{O}$: 99.998%). Trifluoroacetic acid (99%), sodium trifluoroacetate (98%), sodium hydroxide (99.99%), ammonium fluoride (99.99%), barium acetylacetonate ($\leq 100\%$), manganese(II) acetate tetrahydrate ($\geq 99\%$), and chlorotrimethylsilane ($\geq 98.0\%$) were purchased from Sigma Aldrich. Lithium trifluoroacetate ($\geq 97\%$) and cesium carbonate (99.9%) were purchased from Alfa Aesar. Technical grade oleic acid (90%), 1-octadecene (90%), oleylamine (70%), methyl benzoate (99%), toluene ($\geq 99.5\%$), and anhydrous ethylene glycol (99.8%) were purchased from Sigma Aldrich. Glacial acetic acid (99.7%) was purchased from ACP Chemicals. Trisodium citrate dihydrate ($\geq 99.0\%$) was purchased from BioShop Life Science Products.

3.2. Nanoparticle Synthesis

3.2.1. LiREF₄

LiYF_4 nanoparticles studied throughout this work were synthesized using a previously established one-pot thermal decomposition method.¹²⁵ In a 100 mL three-neck round-bottom flask, 1.25 mmol of rare-earth oxides (RE_2O_3) was added to 10 mL of 50% v/v aqueous trifluoroacetic acid, and refluxed for 16 h, dissolving the oxides and generating the rare-earth trifluoroacetate precursors. The precursors were then dried in the reaction flask at 60 °C by removing the stoppers and reflux condenser, followed by the addition of 2.5 mmol of lithium trifluoroacetate in 20 mL of oleic acid and 20 mL of 1-octadecene. This mixture was degassed for 30 min at 120 °C, under vacuum at approximately 10 mbar and stirring at 350 rpm. The vacuum was then substituted for an argon atmosphere, and the solution temperature was raised to 315 °C at a rate of 10 °C/min,

where it remained for 1 h. Once the reaction was complete, the solution was cooled to room temperature under ambient conditions and separated into two centrifuge tubes. 25 mL of ethanol was added to each tube to precipitate the nanoparticles, and the solutions were centrifuged at 4000 rpm for 15 min. The supernatants were discarded, and the pelleted nanoparticles were washed by dispersing them in 10 mL hexanes. After reprecipitating the samples in 35 mL of ethanol, the samples were centrifuged at 4000 rpm for 15 min. This was repeated twice more, and the completed nanoparticle samples were stored as a solid pellet with an ethanol blanket.

In Chapter 4, Y_2O_3 , Yb_2O_3 , and Tm_2O_3 were used to synthesize $\text{LiYF}_4:\text{Yb}^{3+},\text{Tm}^{3+}$ nanoparticles. In Chapter 6, Y_2O_3 , Eu_2O_3 , Yb_2O_3 , Er_2O_3 , and/or Ho_2O_3 were used to synthesize $\text{LiYF}_4:\text{Eu}^{3+}$, $\text{LiYF}_4:\text{Yb}^{3+},\text{Er}^{3+}$, and $\text{LiYF}_4:\text{Yb}^{3+},\text{Ho}^{3+}$ nanoparticles. Similarly, in Chapter 7, LiLuF_4 nanoparticles doped with Eu^{3+} , Gd^{3+} , Sm^{3+} or Dy^{3+} were synthesized using Lu_2O_3 instead of Y_2O_3 , with Eu_2O_3 , Gd_2O_3 , Sm_2O_3 , or Dy_2O_3 to achieve the reported dopants and concentrations.

In Chapter 7, LiLuF_4 core/shell nanoparticles were studied, following a modified shell growth procedure similar to the core-only nanoparticles.¹²⁶ 0.5 mmol of RE_2O_3 (consisting of Lu_2O_3 , Y_2O_3 , and/or Eu_2O_3) was dissolved in 10 mL of 50% v/v aqueous trifluoroacetic acid, refluxed for 16 h. The resulting trifluoroacetate precursors were dried and mixed with 1 mmol of lithium trifluoroacetate in 15 mL of oleic acid and 15 mL of 1-octadecene. The solution was degassed at 120 °C for 30 min, under vacuum at approximately 10 mbar and stirred at 350 rpm. Once complete, the vacuum was substituted for an argon atmosphere, and the solution temperature was raised to 300 °C for 1 h. The reaction solution was then cooled to room temperature under ambient conditions, separated into two centrifuge tubes and each mixed with 30 mL of ethanol to precipitate the nanoparticles. The solutions were then centrifuged at 4000 rpm for 15 min and the supernatants were discarded. Each sample was washed by dispersing them in 10 mL of hexanes, reprecipitating them in 35 mL ethanol, and centrifuging at 4000 rpm for 15 min. Once repeated twice more, the synthesized core/shell nanoparticles were stored as a solid pellet under an ethanol blanket.

3.2.2. NaREF_4

The NaGdF_4 core/shell nanoparticles studied in Chapter 4 and Chapter 5 were synthesized using a hybrid procedure. To synthesize the core nanoparticles, a previously reported co-

precipitation method was used.¹²⁷ 1 mmol of RECl₃•6H₂O, consisting of GdCl₃, YbCl₃, and TmCl₃ in their intended molar ratios, was mixed in 6 mL of oleic acid and 15 mL of 1-octadecene in a 100 mL three-neck round-bottom flask. This solution was degassed at 160 °C for 30 min, under vacuum and stirring at 350 rpm. The reaction was then cooled to 50 °C, switched from a vacuum to an argon atmosphere, followed by the addition of a 10 mL solution of 2.5 mmol NaOH and 4 mmol NH₄F in methanol, at a rate of 1 mL/min. Stirring at 50 °C continued for 30 min, followed by elevating the temperature to 68 °C and restoring the vacuum to evaporate the methanol. The temperature was further elevated to 90 °C for 10 min and 120 °C for 10 min to fully evaporate any residual methanol. The vacuum was once again substituted for an argon atmosphere, and the temperature was raised to 300 °C at a rate of 10 °C/min, where it remained for 2 h. The solution was cooled to room temperature under ambient conditions and washed following the same protocol described in Section 3.2.1.

To grow the shell, 1 mmol of RECl₃•6H₂O, consisting of GdCl₃ and TbCl₃ in their intended molar ratios, were combined in 6 mL of oleic acid and 8 mL 1-octadecene in a 50 mL three-neck round-bottom flask. This solution was degassed at 160 °C for 40 min, under vacuum and stirring at 350 rpm. The solution was cooled to 80 °C, followed by the addition of 1.25 mmol of sodium trifluoroacetate, and constant stirring for 5 min. The solution was then elevated to 100 °C, followed by the addition of 25 mg of core nanoparticles in 1 mL of hexanes. The solution was left at this temperature for 10 min to evaporate the hexanes, followed by an increase to 280 °C for 80 min, at a rate of 10 °C/min. Once complete, the solution was cooled to room temperature under ambient conditions and washed using the same protocol described in Section 3.2.1. The completed core/shell nanoparticles were stored as a solid pellet under an ethanol blanket.

In Section 4.4, core/shell nanoparticles of NaYF₄ were studied, synthesized using a hybrid co-precipitation/thermal decomposition technique as well.¹²⁷ To synthesize the core nanoparticles, 1 mmol RECl₃•6H₂O, consisting of YCl₃, YbCl₃, and TmCl₃ in their respective molar ratios, was dissolved in 7 mL of oleic acid and 15 mL of 1-octadecene in a 100 mL three-neck round-bottom flask. This solution was degassed at 160 °C for 1 h, under argon atmosphere and stirring at 350 rpm. The solution was then cooled to room temperature, followed by the addition of a solution consisting of 2.5 mmol NaOH and 4 mmol NH₄F dissolved in 10 mL of methanol. This solution was stirred for 30 min at room temperature before elevating the temperature to 100 °C to evaporate

the methanol. The solution was further raised to 300 °C for 1 h, at a rate of 10 °C/min. Once complete, the solution was cooled to room temperature under ambient conditions, precipitated using ethanol and isolated *via* centrifugation at 6000 rpm.

To grow the inert shell, 0.25 mmol of Y₂O₃ was added to 10 mL of a 50% v/v aqueous solution of trifluoroacetic acid, which was allowed to react under reflux for 16 h. Once complete and dried, the trifluoroacetate precursors were combined with 1 mmol of sodium trifluoroacetate, 10 mL of oleic acid, 10 mL of 1-octadecene, and half the batch of previously synthesized core nanoparticles. This solution was degassed at 120 °C for 30 min under an argon atmosphere, followed by elevating the temperature to 320 °C for 30 min. Once complete, the solution was cooled to room temperature under ambient conditions, precipitated with ethanol, and isolated *via* centrifugation at 6000 rpm. To render the nanoparticles colloiddally stable in aqueous solutions, a 10 mL dispersion of as-synthesized oleate-capped nanoparticles in hexanes was mixed with 10 mL of water at pH 2 using HCl. The solution was stirred vigorously to protonate the oleate ligands, rendering the nanoparticles oleate-free, which were dispersible in water.¹²⁸

3.2.3. Ba_{1-x}RE_xF_{2+x}

The Ba_{1-x}RE_xF_{2+x} nanoparticles studied in Section 4.2 were synthesized using a previously established thermal decomposition technique.¹²⁹ In a 100 mL three-neck round-bottom flask, 1.25 mmol RE₂O₃ (comprising Y₂O₃, Yb₂O₃, Tm₂O₃, and/or Eu₂O₃) was dissolved in 10 mL of a 50% v/v solution of aqueous trifluoroacetic acid under reflux for 16 h. Once dried, barium acetylacetonate (Ba(acac)₂•xH₂O) was added in varying quantities to achieve the desired Ba²⁺:RE³⁺ molar ratio. These reagents were mixed in 20 mL of oleic acid and 20 mL of 1-octadecene, and degassed at 120 °C for 30 min under vacuum and stirring at 350 rpm. Once complete, the vacuum was replaced with an argon atmosphere, and the solution temperature was increased to 300 °C at a rate of 10 °C/min. The solution was left to react for 1 h, and then cooled to room temperature under ambient conditions. The solution was separated into two centrifuge tubes, and the nanoparticles were precipitated by adding 35 mL of ethanol to each. After centrifugation at 4000 rpm for 15 min, the nanoparticle samples were washed using the protocol described in Section 3.2.1.

3.2.4. CsMnCl₃

Nanoparticles of CsMnCl₃ studied in Chapter 6 were synthesized using a previously reported solvothermal injection technique.¹³⁰ An excess of cesium carbonate was dissolved in glacial acetic acid, producing cesium acetate. In a 25 mL three-neck round-bottom flask, 1 mmol of this precursor was combined with 1 mmol of manganese(II) acetate tetrahydrate, in 2.5 mL of oleic acid, 10 mL of 1-octadecene, 0.5 mL of oleylamine, and 0.5 mL of acetic acid. This solution was degassed at 120 °C for 30 mins, under vacuum of approximately 10 mbar, and constant stirring at 350 rpm. The vacuum was then substituted for an argon atmosphere, and the solution temperature was increased to 200 °C. 400 μL of chlorotrimethylsilane was quickly added to the solution, and the reaction was allowed to proceed for 10 s. Once complete, the reaction vessel was submerged in an ice bath to halt the reaction, and the solution was transferred to a single centrifuge tube. The solution was centrifuged at 10000 rpm for 10 min, and the supernatants was discarded. To wash the nanoparticles, samples were dispersed in 10 mL of hexanes, followed by centrifugation at 10000 rpm for 10 min. This process was repeated twice more, and the samples were stored as a solid pellet covered in ethanol.

3.3. Physical Characterization

3.3.1. Powder X-ray Diffraction

As-synthesized, oleate-capped nanoparticle samples were fully dried in preparation for powder X-ray diffraction (PXRD).

In Chapter 4, samples of LiYF₄ nanoparticles were mounted on silica wafer sample stages, and the diffractograms were recorded using a Bruker D2 Phaser equipped with a LynxEye detector and a Cu source at a generation power of 30 kV and 10 mA. Measurements ranged from 10 – 90° 2θ, with a resolution of 0.01° and an integration time of 2 s. Samples of Ba_{1-x}Y_xF_{2+x} and NaGdF₄ nanoparticles (core-only and core/shell, including those studied in Chapter 5) were mounted on quartz plate sample holders, and diffractograms were recorded using a Scintag XDS-2000 diffractometer equipped with a Si(Li) Peltier-cooled solid-state detector, a Cu source with a generator power of 45 kV and 40 mA, divergent slits (2 mm and 4 mm), and receiving slits (0.5 mm and 0.2 mm). Measurements ranged from 10 – 90° 2θ, with a resolution of 0.02° and an

integration time of 2 s. Samples to measure high-resolution diffractograms of $\text{Ba}_{1-x}\text{Y}_x\text{F}_{2+x}$ nanoparticles were loaded onto zero-reflection quartz sample holders and recorded using a STOE Stadi P powder diffractometer equipped with a silicon strip detector and monochromator, and a Cu source with a generator power of 40 kV and 40 mA. Measurements ranged from $10 - 90^\circ 2\theta$, with a resolution of 0.01° . Diffractograms of NaYF_4 nanoparticles were recorded using a Rigaku Ultima IV equipped with a Cu source operating at 44 kV and 40 mA, from $10 - 60^\circ 2\theta$.

For LiYF_4 and CsMnCl_3 nanoparticles studied in Chapter 6, samples were loaded onto silicon wafer sample stages, and diffractograms were recorded using a Rigaku Miniflex, equipped with a Cu source operating at 40 kV and 15 mA. Measurements ranged from $10 - 90^\circ 2\theta$ with a resolution of 0.02° . Nanoparticle samples of LiREF_4 studied in Chapter 7 were loaded onto quartz plates and measured using a Scintag XDS-2000 equipped as stated above, from $10 - 80^\circ 2\theta$ and a step size of 0.02° .

Unit cell parameters throughout this research were calculated using the experimentally recorded PXRD diffractograms processed through the STOE WinXPOW software using Louër's algorithm.¹³¹

Z_{eff} values in Chapter 7 were calculated using the Auto- Z_{eff} software developed by the Medical Radiation Physics Research Group at RMIT University.¹³²

3.3.2. Transmission Electron Microscopy

As-synthesized oleate-capped nanoparticles were dispersed in hexanes or toluene at a concentration of 1 or 0.5 mg/mL, and dropped onto formvar/carbon film supported copper grids (300 mesh, 3 mm diameter) in preparation for transmission electron microscopy (TEM) analysis. Micrographs of LiYF_4 , NaGdF_4 , and $\text{Ba}_{1-x}\text{Y}_x\text{F}_{2+x}$ nanoparticles studied in Chapter 4 were recorded using a JEOL-JEM-2100F electron microscope operating at 200 kV, equipped with a Gatan charge-coupled device camera. Micrographs of NaYF_4 nanoparticles were recorded using a JEOL 2010 electron microscope, operating at 200 kV, coupled to a Gatan charge-coupled device camera. To evaluate the core/shell NaGdF_4 nanoparticles studied in Chapter 5, scanning transmission electron microscopy (STEM) micrographs were recorded using high-angle annular dark-field imaging (HAADF) from an FEI Titan 80-300 HB electron microscope. TEM micrographs presented in Chapter 6 and Chapter 7 were taken using a Talos L120C STEM operating at 120 kV.

3.3.3. Inductively Coupled Plasma – Mass Spectrometry

Nanoparticle composition analysis in Chapter 4 was completed using inductively coupled plasma – mass spectrometry (ICP-MS), from 1 mg/mL solutions of nanoparticles in hexanes or toluene. 100 μ L of this solution was mixed with 1 mL of concentrated HCl and 100 μ L of H₂O₂ in 150 mm test tubes. Tubes were covered and heated to 115 °C under reflux for 16 h. Once digested, samples were dried and dissolved in enough 5% aqueous HNO₃ to obtain approximately 5 ppm solutions. These samples were processed through an Agilent 7500ce ICP-MS, equipped with a quartz Scott-type spray chamber, off-axis Omega lens ion focus, and an octupole reaction system with a quadrupole mass spectrometer analyzer operating at 3 MHz.

3.3.4. Zeta Potential

Citrate-capped nanoparticles studied in Chapter 6 were dispersed in 70% v/v ethylene glycol in water at a concentration of 10 mg/mL. Zeta potential was recorded using a Malvern Zetasizer Nano ZSP at 25 °C.

3.4. Spectroscopic Characterization

3.4.1. Absorption Spectroscopy

Absorption spectra in Section 4.1.1., on 4.3×10^{-6} M solutions of 3-(4-phenylazophenoxy)propanol in toluene, were recorded using an Agilent Technologies Cary 5000 Series UV-Vis-NIR spectrophotometer, operating at a scan speed of 600 nm/s and a resolution of 1 nm.

3.4.2. Excitation Spectroscopy

Excitation spectra of powder samples of BaYF₅:Eu³⁺ nanoparticles presented in Section 4.2 were recorded using a Horiba Jobin Yvon Fluorolog 3-22 spectrometer, equipped with a 450 W xenon lamp dispersed using a double monochromator blazed at 330 nm (1200 grooves/mm) as the excitation source. The Eu³⁺ emission at 591 nm was isolated using a single monochromator (500 nm blaze, 1200 grooves/mm) and measured using a cooled Hamamatsu R928P photomultiplier tube. Spectra were plotted with a 0.5 nm step size and 2 s integration time.

Powder samples of core/shell $\text{NaGdF}_4:\text{Yb}^{3+},\text{Tm}^{3+}/\text{NaGdF}_4:\text{Tb}^{3+}$ nanoparticles in Chapter 5 were excited using a 150 W Xenon Arc lamp dispersed using an Oriel 77250 0.125 m monochromator (2400 grooves/mm). The resulting emissions were collected using a Jarrell-Ash Czerny-Turner 25-102 1 m double monochromator (1180 grooves/mm) coupled to a cooled Hamamatsu R943-02 photomultiplier tube, and processed using an SR400 Stanford Research Systems gated photon counter.

3.4.3. Emission Spectroscopy

NIR emission spectra of 1 mg/mL $\text{LiYF}_4:\text{Yb}^{3+},\text{Tm}^{3+}$ nanoparticle solutions in toluene presented in Chapter 4 were recorded under 976 nm irradiation using a Coherent 6-pin fiber-coupled F6 series laser diode operating at 42.9 W/cm^2 . Emissions were dispersed using a Spectral Products DK-240 monochromator (600 grooves/mm) and detected using a Spectral Products AD-131 InGaAs detector. Photoluminescence spectra of powder samples studied in Chapter 6 and Chapter 7 (LiREF_4 and CsMnCl_3) were recorded under 355 nm irradiation using a Spectra Physics Quanta-Ray INDI Nd:YAG laser operating at 760 mW/cm^2 and pulsed at a frequency of 10 Hz. Emissions were filtered through a Thorlabs FESH0750 visible bandpass filter and collected using a Princeton Instruments FERGIE BRX-VR UV-NIR spectrograph fitted with a 1200 grooves/mm grating blazed at 290 nm.

Upconversion emission spectra in Chapter 4 and Chapter 5 (1 mg/mL nanoparticle solutions in toluene of LiYF_4 , NaGdF_4 , or $\text{Ba}_{1-x}\text{Y}_x\text{F}_{2+x}$) were recorded under 976 nm irradiation from a Coherent 6-pin fiber-coupled F6 series laser diode operating at 42.9 W/cm^2 . Visible/NIR emissions (425 – 850 nm) were dispersed using a Jarrell-Ash Czerny-Turner 25-102 1 m double monochromator (1180 grooves/mm) and collected using a water-cooled Hamamatsu R943-02 photomultiplier tube. UV emissions (275 – 500 nm) were dispersed using an Oriel 77250 0.125 m monochromator (2400 grooves/mm) and detected with a Hamamatsu R4632 photomultiplier tube. Signals were processed through an SR440 Stanford Research Systems preamplifier and converted to quantifiable values using an SR400 Stanford Research Systems gated photon counter. Upconversion emission spectra of LiYF_4 nanoparticle powder samples in Chapter 6 were recorded under the same irradiation source and conditions, but emissions were collected using a Princeton Instruments FERGIE BRX-VR UV-NIR spectrograph fitted with a 1200 grooves/mm grating blazed at 290 nm.

Radioluminescence spectra of LiREF₄ nanoparticles in Chapter 7 were recorded on powder samples irradiated with an Amptek Mini-X uncollimated, unfiltered X-ray source fitted with a gold target, operating at 50 kV and 80 μ A. Emission spectra were recorded using a Princeton Instruments FERGIE BRX-VR UV-NIR spectrograph fitted with a 295 grooves/mm grating blazed at 550 nm.

3.4.4. Luminescence Lifetimes

Samples for photoluminescence lifetimes were irradiated using a Spectra Physics Quanta-Ray INDI Nd:YAG laser operating at 760 mW/cm² and pulsed at a frequency of 10 Hz. Samples for upconversion luminescence lifetimes were irradiated using a Coherent 6-pin fiber-coupled F6 series laser diode, operating at pulse widths and power densities presented in **Table 3.1**. Power densities were calculated by measuring the laser spot size using a modified Logitech C920x HD Pro Webcam, and the laser power was measured using a Thorlabs PM100D Power meter fitted with an S405C Thermal Power Head. For UV and visible lifetimes, emissions were isolated using an Oriel 77250 0.125 m monochromator (2400 grooves/mm) and detected with a Hamamatsu R4632 photomultiplier tube. For 800 nm luminescence lifetimes, emissions were isolated using a Jarrell-Ash Czerny-Turner 25-102 1 m double monochromator (1180 grooves/mm) and collected using a water-cooled Hamamatsu R943-02 photomultiplier tube.

Table 3.1 Measured power densities with varying pulse width.

Pulse Width (ms)	0.2	0.5	1	2	3	4
Power Density (W/cm²)	1	1.5	4	7	10	14

3.4.5. Upconversion Quantum Yields

QY measurements on solid samples of upconverting BaYF₅:Yb³⁺,Tm³⁺ nanoparticles studied in Section 4.2 were irradiated under the same continuous wave 976 nm irradiation conditions described in Section 3.4.3, with the exception of varying power densities from 0.3 – 4.8 W/cm². Emissions were collected using a modified Avantes AvaSphere-30-REFL integrating sphere that was fiber-coupled to a Thorlabs FOFMS/M-UV Filter Mount, fitted to an Avantes AvaSpec-ULS2048L spectrometer. Recorded emission spectra were intensity calibrated using a

CAL-ISP30 NIST calibrated lamp, converting arb.u. to W. Values were then converted to number of photons using the photon energy equation presented in Equation 3.1:

$$E = n \frac{hc}{\lambda} \quad (3.1)$$

Where E is the energy of a photon, n is the number of photons, h is the Planck constant, c is the speed of light, and λ is the wavelength of light. Using an undoped BaYF₅ sample as a reference to evaluate scattering, the upconversion spectra and laser line were compared to calculate the number of photons emitted and absorbed, respectively. Using Equation 1.1, these values are converted to a QY.

3.5. Proof-of-Concepts

3.5.1. NIR-triggered photoisomerization

3-(4-phenylazophenoxy)propanol was synthesized using a previously reported protocol.¹³³ 10 mmol 4-phenylazophenol was combined with 12 mmol of 3-bromopropanol in DMF at 75 °C for 6 h. The product was isolated in cold water and chloroform, washed with 1 M HCl and a saturated aqueous NaCl solution, and purified by silica column chromatography using a 1:6 ethyl acetate:dichloromethane solution as the mobile phase.

Solutions of 1 mg/mL LiYF₄:Yb³⁺,Tm³⁺ nanoparticles and 4.3 x 10⁻⁶ M 3-(4-phenylazophenoxy)propanol were prepared in hexanes, and irradiated using the 976 nm laser setup described in Section 3.4.3. Absorption spectra were recorded in 30 min intervals.

3.5.2. Upconversion Lifetime Nanothermometry

Upconversion luminescence lifetimes were recorded using the same setup described in Section 3.4.4. for 800 nm emissions. In a quartz cuvette, 1 mL of aqueous NaYF₄:Yb³⁺,Tm³⁺/NaYF₄ nanoparticle solutions (7 mg/mL) were positioned on a modified Glas-Col heating mantle, controlled using a J-KEM Scientific Model 210 temperature controller, with an uncertainty of ± 1 °C.

3.5.3. Particle Velocimetry

To observe the luminescence profiles of upconverting NaGdF₄:Yb³⁺,Tm³⁺/NaGdF₄:Tb³⁺ core/shell nanoparticles in Chapter 5, Molex TSP series Polymicro Flexible Fused Silica Capillaries with 75, 100, and 150 μm internal diameters were used, with a Coherent 6-pin fiber-coupled F6 series laser diode (operating at $\approx 10^4$ W/cm², and a beam diameter of 35 μm) positioned perpendicular to the capillaries at the beginning of the flow path. Nanoparticle solutions in toluene were passed through the capillaries using a Harvard Apparatus 11 Plus syringe pump and observed using an AO Instrument Company Series 60 light microscope focused with a viewing diameter of 1.5 mm. Blue or green upconverted emissions were isolated using a Thorlabs FB450 or a Thorlabs FES0600/Schott OG515 bandpass filter and recorded using the digital camera of a Google Pixel 3 smartphone. Once recorded, the images were processed using ImageJ, where a rectangular area in the center of each capillary/emission was plotted using the Plot Profile tool. This provides a quantifiable intensity as a function of distance, using the capillary's internal diameter as a reference length.

To measure the lifetimes of the NaGdF₄ core/shell nanoparticles for velocimetry calculations, an Oriel 77250 photomultiplier tube was positioned at the eyepiece of the optical microscope. Using the same setup described in Section 3.4.4., and the blue or green filters described above, the blue or green emission intensities as a function of time could be recorded from inside the capillaries.

3.5.4. Covert Information Storage

Ink solutions of UV-sensitized nanoparticles in Section 6.2.1 were produced using a previously reported formulation, slightly modified.¹³⁴ Oleate-capped CsMnCl₃ or LiYF₄:Eu³⁺ nanoparticles were dispersed in 10% v/v methyl benzoate in toluene at a concentration of 10 mg/mL. To generate the prints, packing tape was cut into the intended pattern on borosilicate glass slides, followed by drop-casting the pattern ink solution over top and allowing the toluene to evaporate. This was followed by removing the packing tape and drop-casting the mask ink solution on top, covering the entire print area.

For NIR-sensitized UCNPs in Section 6.2.2, as-synthesized oleate-capped upconverting nanoparticles were rendered hydrophilic using a previously reported ligand exchange protocol to

citrate.¹³⁵ 100 mg of oleate-capped nanoparticles were dispersed in 10 mL of hexanes and 10 mL of pH 2 water, resulting in a phase separation. After stirring at 1500 rpm for 1 h, the translucent organic phase became transparent, while the transparent aqueous phase became opaque, indicative of a phase transition. The aqueous phase was then isolated and centrifuged at 13300 rpm for 5 min, the supernatant was discarded, and the nanoparticles were dispersed in 2 mL of water. After a second centrifugation, the nanoparticles were dispersed in 4 mL of 0.1 M sodium citrate and stirred at 1000 rpm for 2 h. Samples were centrifuged again at 13300 rpm and washed/centrifuged in 2 mL of water, twice. Citrate-coated nanoparticles were stored in water until needed. To formulate inks, 50 mg of citrate-coated nanoparticles were dispersed in 1 mL of 70% v/v ethylene glycol in water. Solutions were loaded into a Canon PG-240 ink cartridge, which was installed into a Canon PIXMA MG3620 printer. The pattern (two layers) and the mask (two layers) were printed onto Domtar First Choice ColorPrint 28 lb. paper, which appeared transparent and otherwise clean once complete.

UV-sensitized prints were excited using a Spectra Physics Quanta-Ray INDI Nd:YAG laser (operating at 760 mW/cm^2 and pulsed at a frequency of 10 Hz), while NIR-sensitized upconverting prints were excited using a 976 nm CNI FC-W-980-80W diode laser fitted with a collimator to spread the emission beam (operating at a power density of 4.8 W/cm^2 and a pulse width of 500 μs controlled using a Koolertron DDS Signal Generator/Counter). Images were taken using the digital camera of a Samsung Galaxy S20 FE set to the Pro mode with a shutter speed of 1 ms. Slow motion videos were recorded using the same setup, with the camera set to the Super Slow-Mo mode.

Chapter 4. Tm³⁺-doped Upconverting Nanoparticles

The wide selection of emission wavelengths from Tm³⁺ has garnered considerable attention for the study of potential UCNP applications. These include emissions in the UV (290, 345, and 360 nm from the ³P₀ → ³H₆, ³F₄, and ¹D₂ → ³H₆ transitions, respectively), blue (450 and 475 nm from the ¹D₂ → ³F₄ and ¹G₄ → ³H₆ transitions, respectively), red (650 nm from the ¹G₄ → ³F₄ transition) and higher energy NIR (800 nm from the ³H₄ → ³H₆ transition) spectral regions. When in combination with Yb³⁺ as a sensitizer, these emissions can be sensitized using two to five incident 976 nm photons *via* ETU. Yb³⁺, Tm³⁺ co-doped UCNPs have demonstrated uses in bioimaging using the NIR emission at 800 nm, photodynamic therapy using the blue emissions, and photocatalysis using the UV emissions, each with varying success.^{104,136,137} The major limitations, however, lie in the inefficiency of the upconversion process, due in part to the slightly mismatched resonance between the Tm³⁺ excited states with Yb³⁺, as well as the many different possible CR mechanisms in Tm³⁺ owing to its many “ladder-like” excited states.

The trivial nature in choosing a host material has portrayed NaREF₄ nanoparticles as the “one-size-fits-all” composition throughout the literature, with little regard to the influence of host composition on the Tm³⁺ upconverted emission intensities and ratios. Moreover, Tm³⁺ is sensitive to many ET mechanisms, and thus its concentration within a nanoparticle composition is important. However, the commonly used activator dopant concentrations, which range from 0.5-2 mol% in fluoride nanoparticles, are explored with no real scrutiny into the effect of minor changes in this variable (± 0.1%). Therefore, the ensuing studies focus primarily on LiYF₄ and BaYF₅ UCNPs as alternative host materials. The effect of the Tm³⁺ dopant concentration on the upconversion emission intensities was evaluated in each host individually, followed by a relative comparison between hosts, including NaGdF₄.

4.1. Effect of Activator Concentration on LiYF₄:Yb³⁺, Tm³⁺ UCNPs

Since its first reported synthesis in 2009, the LiYF₄ nanoparticle host proved a promising alternative to the sodium ternary fluoride compositions.¹²⁵ Using a one-pot thermal decomposition method, LiYF₄:Yb³⁺, Tm³⁺ UCNPs have demonstrated uses in drug delivery and photodynamic therapy, owing to their strong UV emissions that can induce reactions under NIR irradiation.^{133,138} Their square bipyramidal morphology with eight faces of equal surface energy aids in consistent

functionalization, further facilitating its potential uses. While this initial study introduced an activator concentration of 0.5% Tm^{3+} and was proven effective, the effect of activator concentration has not been examined further in LiYF_4 UCNPs. The Yb^{3+} dopant concentration of 25% was optimized to generate the strongest upconversion luminescence from the higher energy Tm^{3+} excited states ($^1\text{D}_2$ and $^3\text{P}_0$) with minimal quenching *via* energy migration.¹²⁵

Therefore, to evaluate the effect of activator concentration on $\text{LiYF}_4:\text{Yb}^{3+},\text{Tm}^{3+}$ UCNPs, nanoparticles were synthesized with a range of Tm^{3+} dopant concentrations, nominally from 0.1 – 0.5 mol%, with a constant Yb^{3+} concentration of 25 mol%.¹³⁹ Since the narrow range of Tm^{3+} concentrations varied by only 0.1%, ICP-MS was completed to determine the experimental dopant concentrations, shown in **Table 4.1**, and the subsequent analysis uses these values instead of their nominal concentrations.

Table 4.1 ICP-MS results for the experimental dopant concentrations of Yb^{3+} and Tm^{3+} in LiYF_4 UCNPs.

Ion	0.1% Tm^{3+}	0.2% Tm^{3+}	0.4% Tm^{3+}	0.5% Tm^{3+}
Y^{3+}	$71.1 \pm 3.55\%$	$72.2 \pm 3.60\%$	$71.7 \pm 3.58\%$	$73.8 \pm 3.72\%$
Tm^{3+}	$0.08 \pm 0.004\%$	$0.24 \pm 0.012\%$	$0.46 \pm 0.023\%$	$0.55 \pm 0.027\%$
Yb^{3+}	$28.8 \pm 1.44\%$	$27.6 \pm 1.38\%$	$27.9 \pm 1.40\%$	$25.7 \pm 1.44\%$

TEM micrographs of the four synthesized compositions are shown in **Figure 4.1a-d**, depicting the expected square bipyramidal morphology and similar size distributions (**Figure 4.1e**), ranging from 87.5 to 95.7 nm across the long axis. These similarities are necessary to assert that any changes in the upconversion luminescence are solely a consequence of the varying Tm^{3+} concentration. PXRD was completed as well, shown in **Figure 4.1f**, to confirm the expected tetragonal crystal phase with the $I4_1/a$ space group, consistent across all samples studied.¹⁴⁰

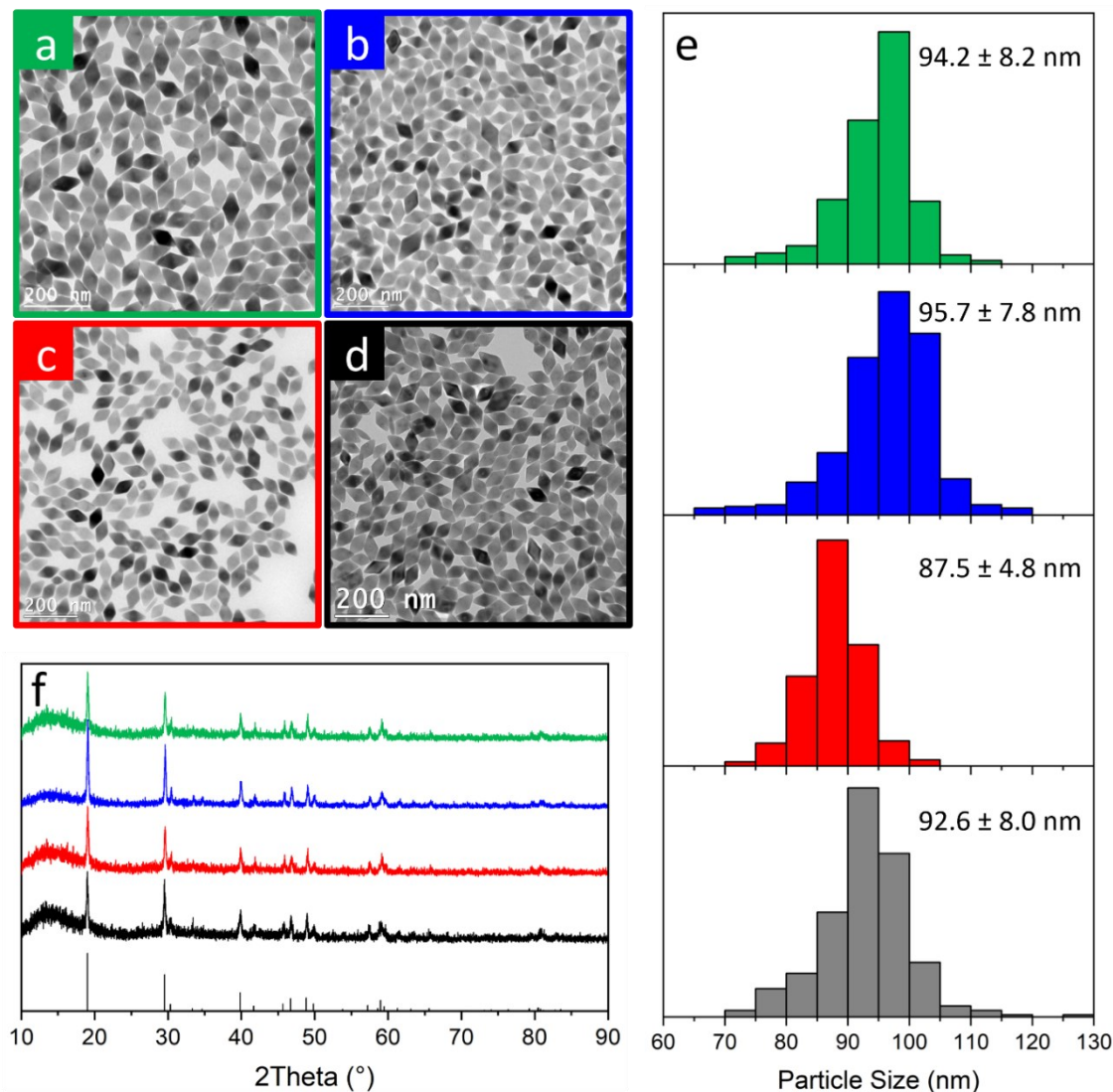


Figure 4.1 TEM micrographs of $\text{LiYF}_4:25\% \text{Yb}^{3+}, x\% \text{Tm}^{3+}$, where x is (a, \blacksquare) 0.08, (b, \blacksquare) 0.24, (c, \blacksquare) 0.46, and (d, \blacksquare) 0.55, with (e) the corresponding particle size distributions and (f) PXRD diffractograms (compared to the reference pattern PDF#77-0816 for tetragonal LiYF_4). Adapted from Reference 139 with permission from the Royal Society of Chemistry.

The upconversion emission spectra under 976 nm irradiation are presented in **Figure 4.2**, with the expected bands in the UV, visible, and NIR regions (recall the energy level diagram in **Figure 2.3**). It is immediately apparent that the emissions change relative intensity, with the UV and visible emissions decreasing while the NIR emission increases as a function of increasing Tm^{3+} concentration. Moreover, the maximum luminescence intensity in the UV and visible region is observed at 0.24% Tm^{3+} , which is about seven times brighter than the established 0.5% (experimentally 0.55%). This contrasts previous investigations into NaYF_4 UCNPs that conclude

the optimal concentration for the UV and visible emissions is 0.5 mol%.¹⁴¹ This discrepancy is justified by comparing the unit cells of LiYF₄ and NaYF₄ (Appendix 2) where the average interionic Y³⁺-Y³⁺ distance for LiYF₄ is approximately 5.16 Å, while in NaYF₄ this distance is 6.15 Å.^{142,143} This means, when the dopant concentrations are the same, Tm³⁺ ions in the LiYF₄ lattice are closer together and more likely to interact through CR mechanisms that nonradiatively depopulate the higher excited states (³P₀ and ¹D₂) in favor of the NIR emitting ³H₄ state. Thus, to specifically maximize the emission intensity of the UV and visible emissions, a lower concentration is necessary in the LiYF₄ host. However, decreasing the dopant concentration too much (0.08 mol%) results in too few Tm³⁺ ions in the nanoparticle lattice and all the luminescence intensities decrease considerably.

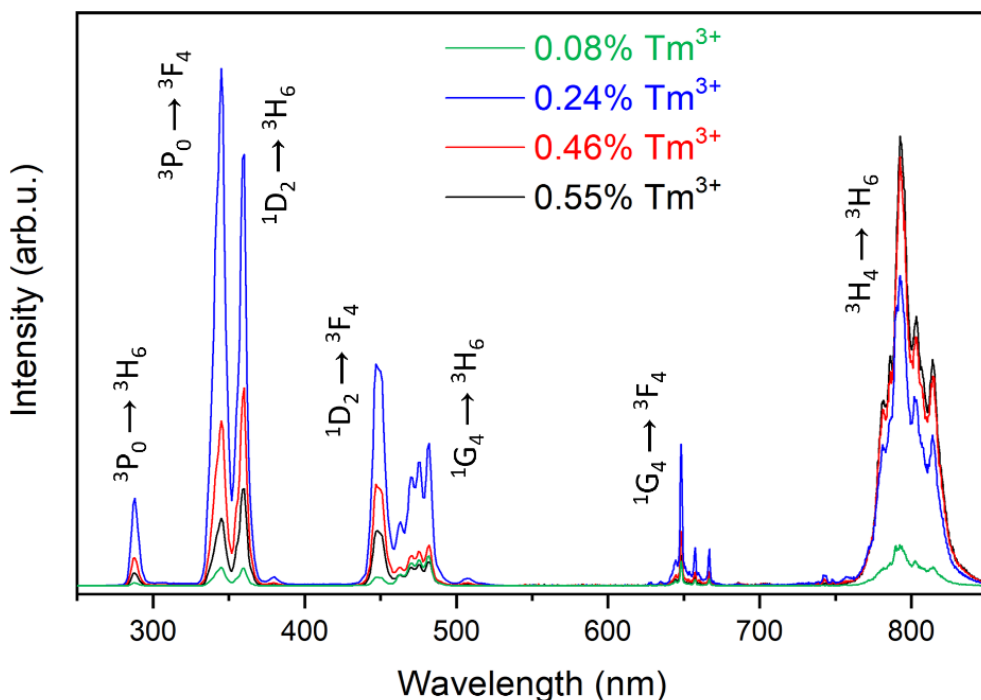


Figure 4.2 Upconversion emission spectra of LiYF₄:25%Yb³⁺,x%Tm³⁺, where x is (■) 0.08, (■) 0.24, (■) 0.46, and (■) 0.55, under 976 nm excitation. Reproduced from Reference 139 with permission from the Royal Society of Chemistry.

Since the emission spectra clearly show that the different radiative transitions of Tm³⁺ have maximal intensities at different activator concentrations, the mechanisms that populate and relax the various excited states need to be examined further. When normalizing the emission spectra to the transitions from the ¹G₄ excited state (responsible for the emissions at 475 and 650 nm), a

drastic change in emission intensity is observed between the 0.08% Tm^{3+} composition and the others, as shown in **Figure 4.3a**. In particular, the emission intensities from the $^1\text{D}_2$ and $^3\text{P}_0$ excited states decrease by over 80%, which suggests that the population of the $^1\text{D}_2$ excited state does not stem from ETU, but rather *via* constructive CR mechanisms. This is consistent with previous reports that establish CR mechanisms between the $^1\text{G}_4$ state and other excited states to populate the $^1\text{D}_2$ state, as illustrated in **Figure 4.3b**.^{144,145} Therefore, a dopant concentration of 0.08% spaces the Tm^{3+} ions too far apart, preventing these necessary mechanisms that are responsible for the strong UV and blue emissions.

In contrast to the population of the $^1\text{D}_2$ state, which relies on constructive CR mechanisms between Tm^{3+} ions, the $^3\text{P}_0$ excited state (responsible for the emissions at 288 and 345 nm) is known to be populated almost exclusively through ETU with Yb^{3+} , from the $^1\text{D}_2$ excited state.^{146,147} Therefore, when normalizing the emission spectra to the $^1\text{D}_2$ transitions (at 360 and 450 nm, presented in **Figure 4.4a**), the emission intensities from the $^3\text{P}_0$ excited state should be consistent across all concentrations if CR is not occurring. However, this is not the case; instead, the relative intensity of the emissions from the $^3\text{P}_0$ excited state decrease with increasing Tm^{3+} concentration, indicating nonradiative depopulation of this excited state *via* an undiscovered CR mechanism. Since the emission intensity of the $^3\text{H}_4 \rightarrow ^3\text{H}_6$ transition at 800 nm also increases considerably between the 0.08% and 0.24% Tm^{3+} UCNPs, it appears that a mechanism including the population of the $^1\text{D}_2$ and $^3\text{H}_4$ states at the expense of the $^3\text{P}_0$ excited state can be minimized at these lower Tm^{3+} concentrations. The proposed mechanism, depicting $^3\text{P}_0 + ^3\text{F}_4 \rightarrow ^1\text{D}_2 + ^3\text{H}_4$ in **Figure 4.4b**, is prominent above the 0.24% Tm^{3+} threshold, due to the high resonance between the excited states, resulting in considerable quenching of the 288 and 345 nm upconverted emissions with increasing Tm^{3+} concentration.

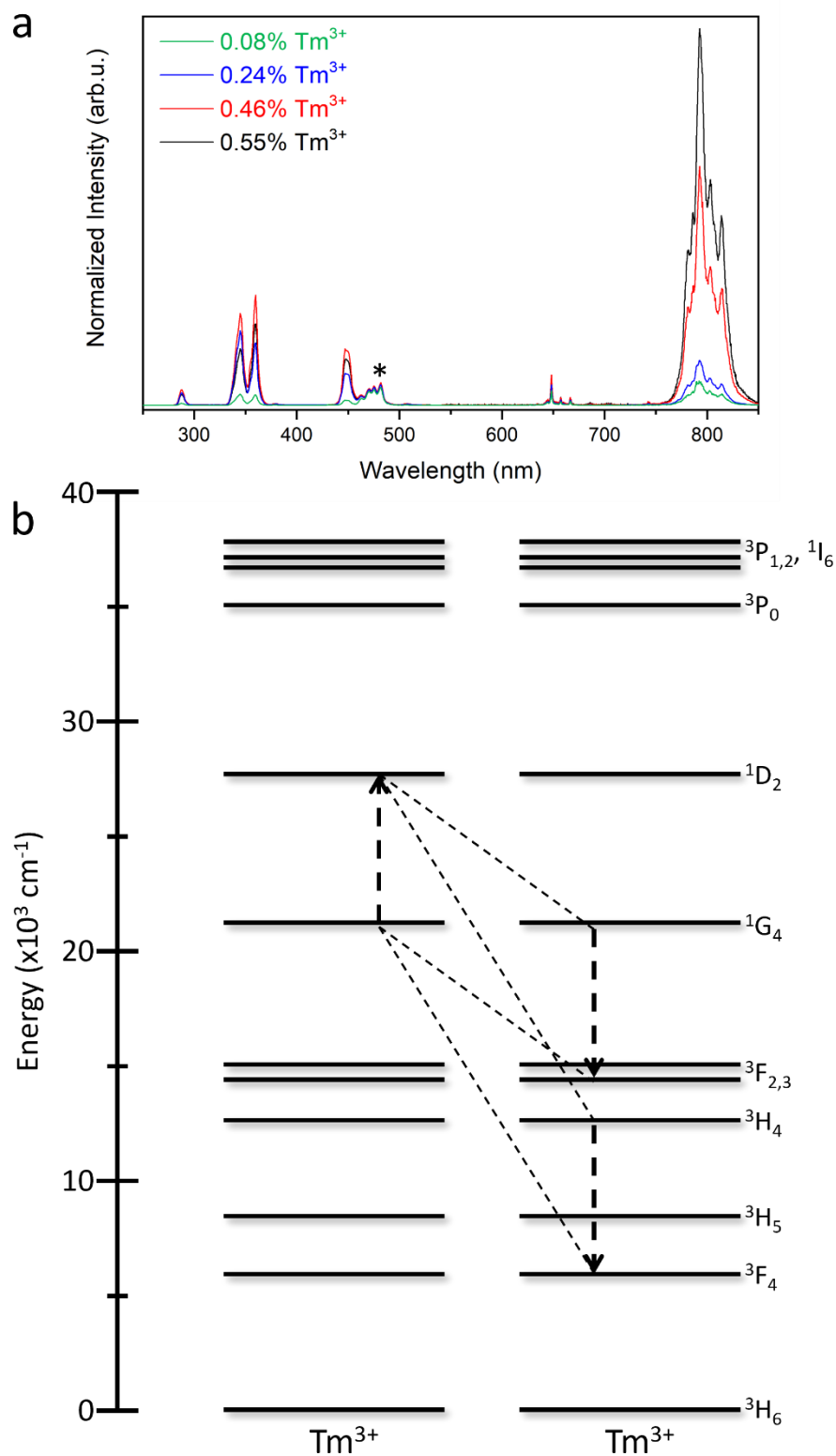


Figure 4.3 (a) Upconversion emission spectrum from Figure 4.2 normalized to the $^1\text{G}_4 \rightarrow ^3\text{H}_6$ transition, as indicated by the asterisk. (b) Energy level diagram depicting the CR mechanisms described in Reference 145.

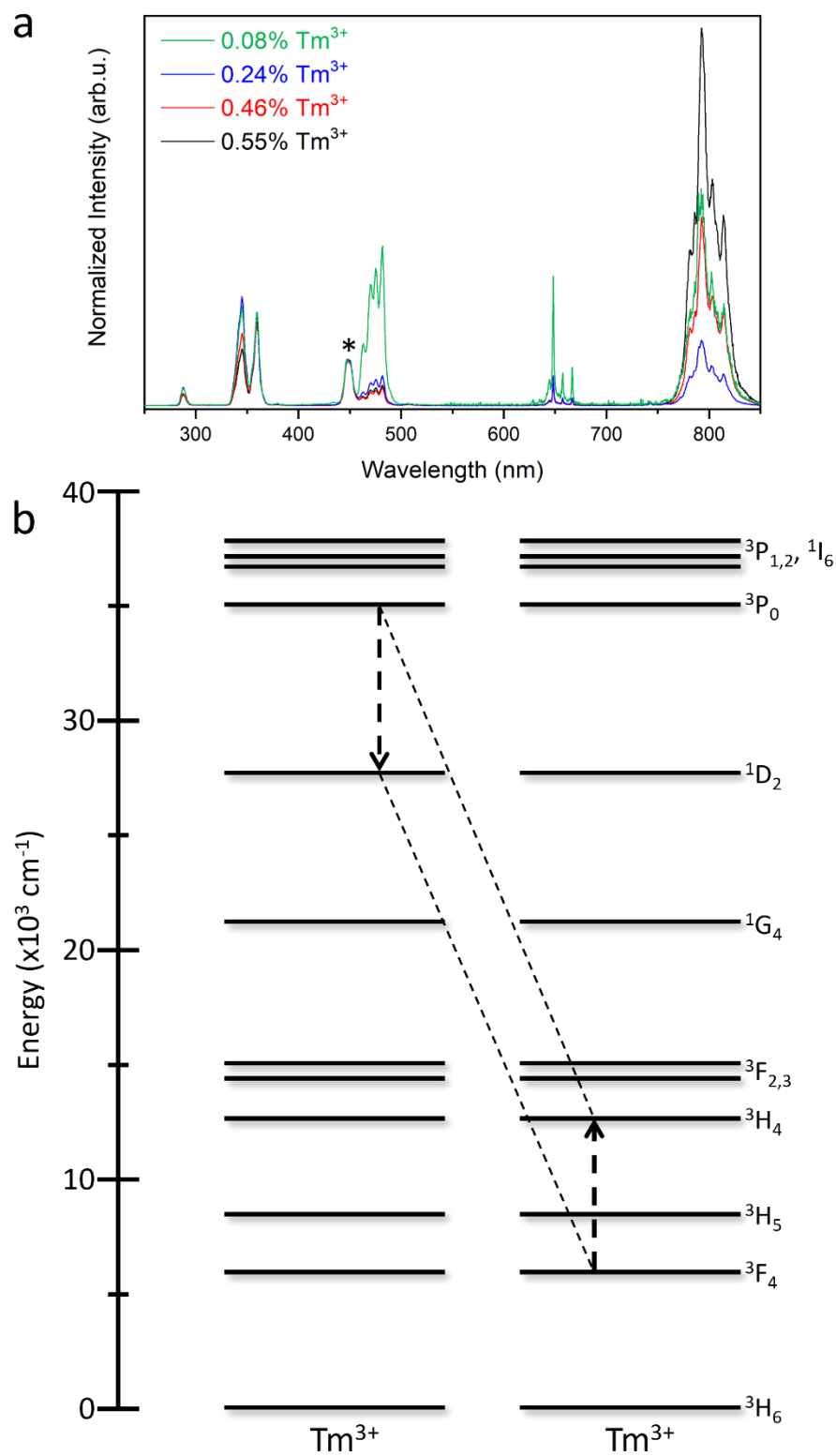


Figure 4.4 (a) Upconversion emission spectrum from Figure 4.2 normalized to the $^1\text{D}_2 \rightarrow ^3\text{F}_4$ transition, as indicated by the asterisk. (b) Energy level diagram depicting the proposed CR mechanism. Adapted from Reference 139 with permission from the Royal Society of Chemistry.

To further elucidate these mechanisms, luminescence lifetimes of the UCNPs with Tm^{3+} concentrations from 0.24 – 0.55% were measured, shown in **Figure 4.5**, with their corresponding decay times (fitted to a single exponential) in **Table 4.2**. As expected, with increasing Tm^{3+} concentration, the decay times shorten, indicating more efficient nonradiative energy transfer between activator ions. From 0.24% to 0.55% Tm^{3+} , the $^3\text{P}_0$ and $^1\text{D}_2$ excited state decay times shortened by 48.6% and 44.4%, respectively, while the $^1\text{G}_4$ and $^3\text{H}_4$ excited state decay times shortened by only 38.6% and 32.9%, respectively. The greater decrease in decay time from the $^3\text{P}_0$ excited state indicates the high susceptibility of this state to quenching, despite having the fastest excited state lifetime overall. Moreover, since the $^3\text{P}_0$ excited state is populated solely *via* ETU from the $^1\text{D}_2$ state, this greater decrease in the $^3\text{P}_0$ excited state decay time relative to the $^1\text{D}_2$ excited state indicates an increase in probability for CR that quenches the $^3\text{P}_0$ level to the $^1\text{D}_2$ level.

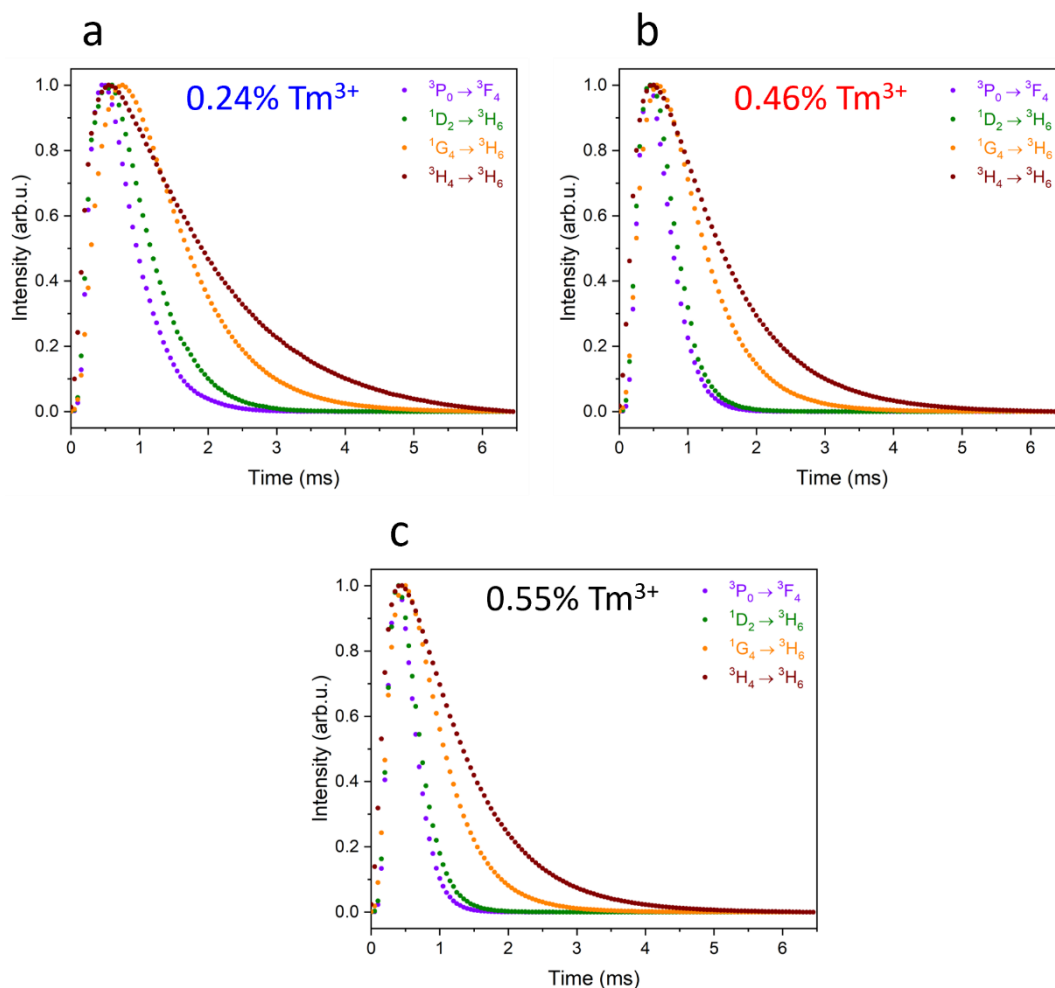


Figure 4.5 Upconversion lifetime profiles of $\text{LiYF}_4:25\%\text{Yb}^{3+}, x\%\text{Tm}^{3+}$, where x is (a) 0.24, (b) 0.46, and (c) 0.55, under pulsed 976 nm excitation. Adapted from Reference 139 with permission from the Royal Society of Chemistry.

Table 4.2 Single exponential fitting of the decay components in Figure 4.5.

Transition	Decay Time (μs)		
	0.24% Tm^{3+}	0.46% Tm^{3+}	0.55% Tm^{3+}
${}^3\text{P}_0 \rightarrow {}^3\text{F}_4$	619	387	318
${}^1\text{D}_2 \rightarrow {}^3\text{H}_6$	689	462	383
${}^1\text{G}_4 \rightarrow {}^3\text{H}_6$	1136	851	700
${}^3\text{H}_4 \rightarrow {}^3\text{H}_6$	1665	1223	1116

NIR emission spectra were recorded as well, to corroborate the results from the upconversion emission spectra and lifetimes, shown in **Figure 4.6**. The emissions at 1485 nm (${}^3\text{H}_4 \rightarrow {}^3\text{F}_4$) and 1730 nm (${}^3\text{F}_4 \rightarrow {}^3\text{H}_6$) increase with increasing Tm^{3+} concentration, matching the trend observed for the 800 nm transition in **Figure 4.2**. As expected, the ${}^3\text{H}_4 \rightarrow {}^3\text{F}_4$ emission trend matches the trend of the ${}^3\text{H}_4 \rightarrow {}^3\text{H}_6$ transition with changing Tm^{3+} concentration, since they originate from the same excited state. Interestingly, the ratio between the two NIR emissions also appears to change, with the emission at 1730 nm increasing relative to the emission at 1485 nm. This correlation is justified by a previously reported CR mechanism that favors the population of the ${}^3\text{F}_4$ excited state at the expense of the ${}^3\text{H}_4$ state (${}^3\text{H}_4 + {}^3\text{H}_6 \rightarrow {}^3\text{F}_4 + {}^3\text{F}_4$).¹⁴⁰ Therefore, with increasing Tm^{3+} concentration, the observed combination of CR mechanisms results in nonradiative depopulation of the ${}^3\text{P}_0$ excited state to ultimately populate the ${}^3\text{F}_4$ excited state, which manifests in weaker UV emissions and stronger NIR emissions.

Overall, due to the complexity of Tm^{3+} , which has many resonant excited states, the population dynamics responsible for the emissions in the UV, visible, and NIR regions are not fully understood, and maximizing the emission bands in any spectral region requires considerable attention and study. The work herein helps elucidate the (de)population mechanisms of the higher energy excited states, demonstrating that decreasing the Tm^{3+} concentration from the established 0.5% to 0.24% (nominally 0.2%) improves the emission intensities from the ${}^3\text{P}_0$ and ${}^1\text{D}_2$ excited state transitions. In the LiYF_4 nanoparticle host, this resulted in the emission intensities in the UV and blue spectral regions increasing by a factor of seven, making the resulting UCNPs considerably brighter and more viable in applications where these wavelengths are desired.

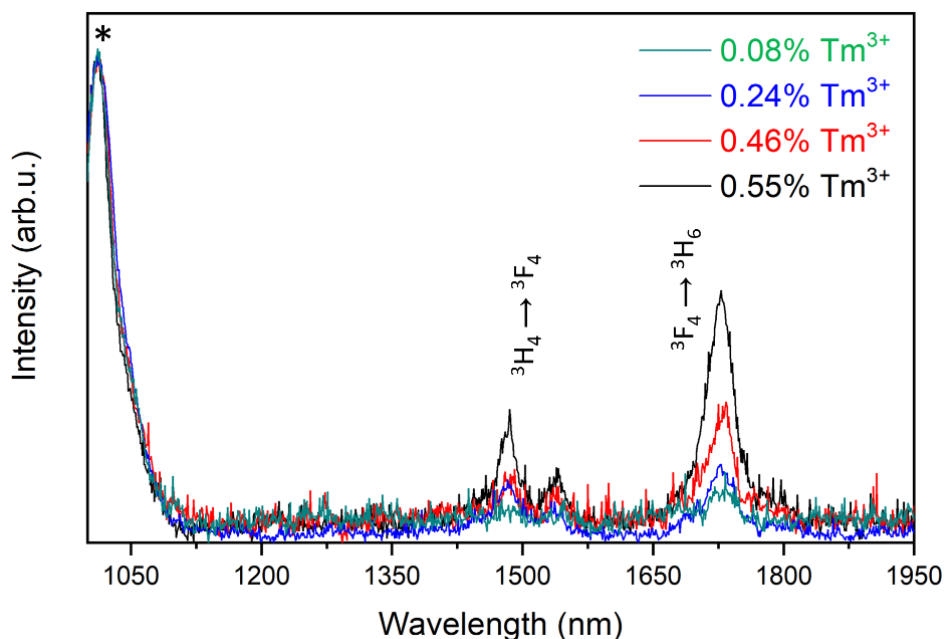


Figure 4.6 NIR emission spectrum of $\text{LiYF}_4:25\%\text{Yb}^{3+},x\%\text{Tm}^{3+}$, where x is (■) 0.08, (■) 0.24, (■) 0.46, and (■) 0.55, under 976 nm excitation. Spectra are normalized to the Yb^{3+} emission from the ${}^2\text{F}_{5/2} \rightarrow {}^2\text{F}_{7/2}$ transition at 1030 nm, indicated by an asterisk. Reproduced from Reference 139 with permission from the Royal Society of Chemistry.

4.1.1. Proof-of-Concept: NIR-Triggered Photoisomerization

With the newly optimized Tm^{3+} concentration for maximal UV emissions, the difference in upconversion intensities was evaluated *via* a photocatalysis experiment. $\text{LiYF}_4:25\%\text{Yb}^{3+},0.55\%\text{Tm}^{3+}$ and $\text{LiYF}_4:25\%\text{Yb}^{3+},0.24\%\text{Tm}^{3+}$ UCNPs were employed to upconvert 976 nm irradiation to UV light, which could then induce a *trans-cis* photoisomerization of 3-(4-phenylazophenoxy)propanol (azopropOH, **Figure 4.7a**). Due to its potential changes in shape, solubility and absorption properties, this azobenzene derivative has been demonstrated in drug delivery systems under UV irradiation, or NIR irradiation when in conjunction with $\text{LiYF}_4:25\%\text{Yb}^{3+},0.5\%\text{Tm}^{3+}$ UCNPs.^{133,148} While the *trans* isomer has a strong $\pi \rightarrow \pi^*$ absorption band in the UV region, centered around 342 nm, the *cis* isomer has an $n \rightarrow \pi^*$ absorption band in the blue spectral region, as observed in the absorption spectra in **Figure 4.7b**. This means that, while the UV bands from Tm^{3+} will enable the *trans-cis* isomerization, the blue emission bands may induce an isomerization back to the *trans* isomer. Since the UV:blue emission intensity ratio doubles when the Tm^{3+} dopant concentration is reduced from 0.55% to 0.24%, a shift in the equilibrium in favor of the *cis* isomer is expected upon irradiation.

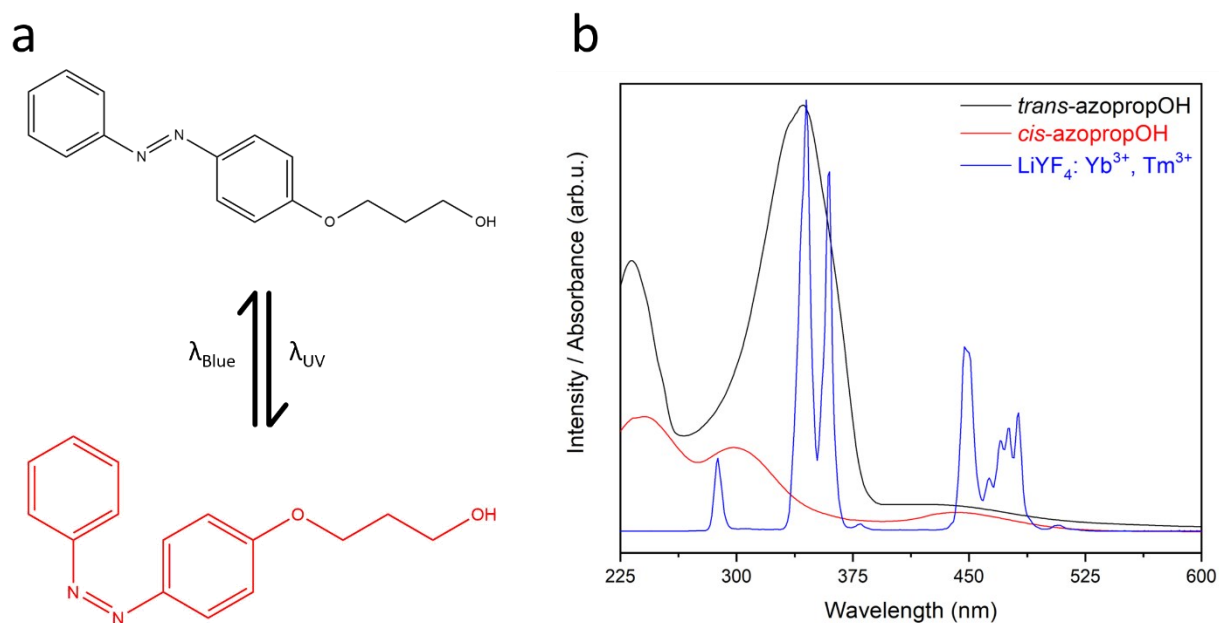


Figure 4.7 (a) Reaction scheme depicting the UV/blue-sensitized photoisomerization of azopropOH. (b) absorption spectra of the (■) *trans*- and (■) *cis*- isomers of azopropOH, overlapping the (■) upconversion emission spectrum of LiYF₄:25%Yb³⁺,0.24%Tm³⁺. Adapted from Reference 139 with permission from the Royal Society of Chemistry.

By evaluating the decrease in the $\pi \rightarrow \pi^*$ absorption band as a function of 976 nm irradiation, when the UCNPs are dispersed in solution with azopropOH, the difference in effectiveness can be observed. As shown in **Figure 4.8**, after 210 min of irradiation, there is negligible photoisomerization from the LiYF₄:25%Yb³⁺,0.55%Tm³⁺ nanoparticles, whereas the LiYF₄:25%Yb³⁺,0.24%Tm³⁺ composition induced a 20% conversion from the *trans* to the *cis* isomer. Since this observed photoisomerization is occurring when the UCNPs and azopropOH are simply dispersed in the same solution, it is expected to be greater in a system that functionalizes the nanoparticles with an azobenzene derivative. This improvement in azobenzene isomerization capabilities emphasizes the importance of properly understanding the population dynamics of Yb³⁺/Tm³⁺ co-doped UCNPs, hopefully highlighting the potential benefits in future studies on upconversion at the nanoscale.

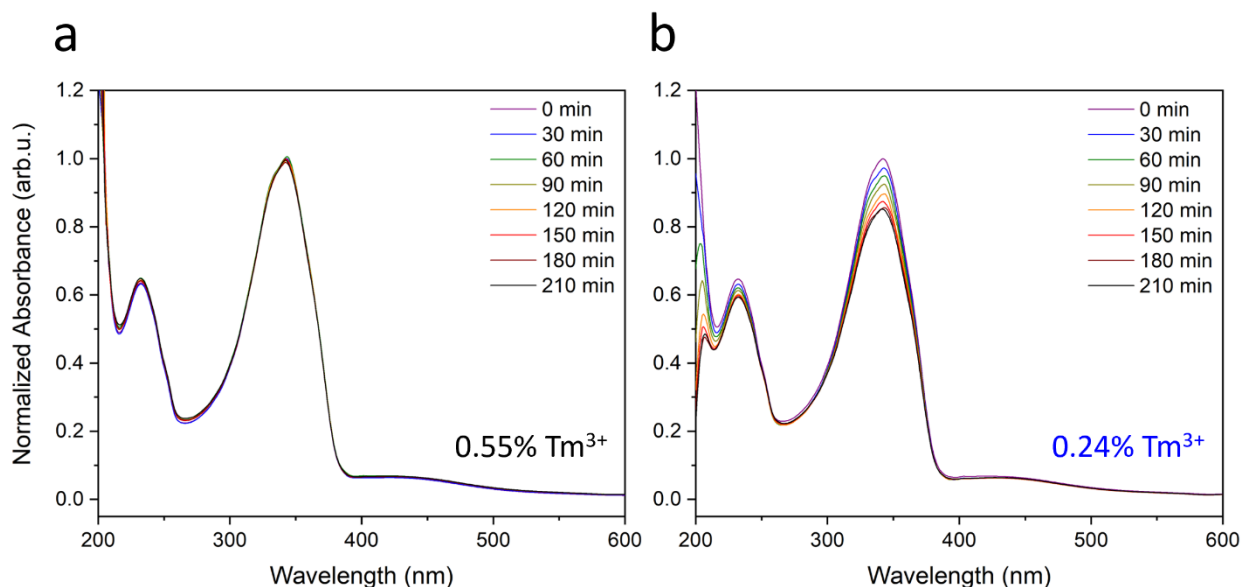


Figure 4.8 Absorption spectrum of *trans*-azopropOH after continuous 976 nm irradiation, in solution with $\text{LiYF}_4:25\% \text{Yb}^{3+}, x\% \text{Tm}^{3+}$ UCNPs, where x is (a) 0.55 and (b) 0.24. Reproduced from Reference 139 with permission from the Royal Society of Chemistry.

4.2. Effect of Activator Concentration on $\text{Ba}_{1-x}\text{Y}_x\text{F}_{2+x}:\text{Yb}^{3+}, \text{Tm}^{3+}$ UCNPs

The observations in Section 4.1 indicate that a shorter interionic distance between rare-earth sites in UCNPs can aid in populating specific Tm^{3+} excited states. This appears to be a consequence of higher Yb^{3+} dopant concentrations (exceeding 20 mol%), which harvests more incident photons and shifts the equilibrium of states to the UV emitting levels. However, as a trade-off, closer spacing between Tm^{3+} ions facilitates greater concentration quenching *via* CR mechanisms, thus requiring a lower dopant concentration to maximize the intensities of the UV and visible emissions. To explore this relationship further, the $\text{Ba}_{1-x}\text{Y}_x\text{F}_{2+x}$ host composition, with larger interionic spacing, was explored next.¹⁴⁹

The barium ternary fluoride hosts are scarce in the literature on UCNPs, likely due to the plethora of possible crystal phases and great uncertainty in nanoparticle morphology. This complicates their study and the reliability in their spectroscopic properties. With respect to the former concern, different synthesis conditions can crystallize this material into tetragonal BaYF_5 , orthorhombic Ba_2YF_7 , trigonal $\text{Ba}_4\text{Y}_3\text{F}_{17}$, monoclinic BaY_2F_8 , or cubic $\text{Ba}_{1-x}\text{Y}_x\text{F}_{2+x}$.^{129,150–152} Nevertheless, barium host UCNPs doped with Yb^{3+} and Tm^{3+} have demonstrated uses in NIR imaging, due to the strong emission band at 800 nm.¹⁵³

Following a previously established one-pot thermal decomposition method, with a 1:1 molar ratio of $\text{Ba}^{2+}:\text{Y}^{3+}$, the synthesized barium yttrium fluoride nanoparticles have an irregular morphology and are polydisperse, averaging around 15 nm, as observed in the TEM micrograph in **Figure 4.9**.¹²⁹ This inconsistency in morphology is likely due to increased agitation in the reaction solution. Above 280 °C, when the trifluoroacetate precursors begin to decompose, the barium acetylacetonate ligands protonate to form acetylacetone, which boils at 140 °C and causes the observed disruptions in the reaction solution.¹⁵⁴

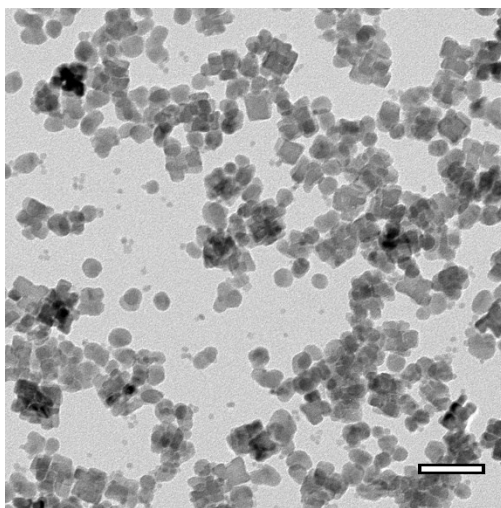


Figure 4.9 TEM micrograph of synthesized barium yttrium fluoride nanoparticles. Scale bar is set to 50 nm. Reprinted with permission from Reference 149. Copyright 2021 American Chemical Society.

Given the slew of potential crystal structures, and the polydispersity observed *via* TEM, high resolution PXRD was measured, shown in **Figure 4.10**. The resulting diffractogram was compared to the theoretical or reference patterns of cubic BaYF_5 , trigonal $\text{Ba}_4\text{Y}_3\text{F}_{17}$, and tetragonal BaYF_5 , all of which have similar diffraction patterns to the experimental results.^{155–157} Attempting to refine the diffractogram to the trigonal crystal phase was not possible, and extra signals present in the tetragonal reference pattern excludes this structure as well. Refinement of the diffractogram reflections to the cubic phase, with the space group Fm-3m , resulted in a lattice parameter of $a = 5.9073(3)$ Å. This confirmed that the synthesized nanoparticles possessed a cubic BaYF_5 crystal structure.

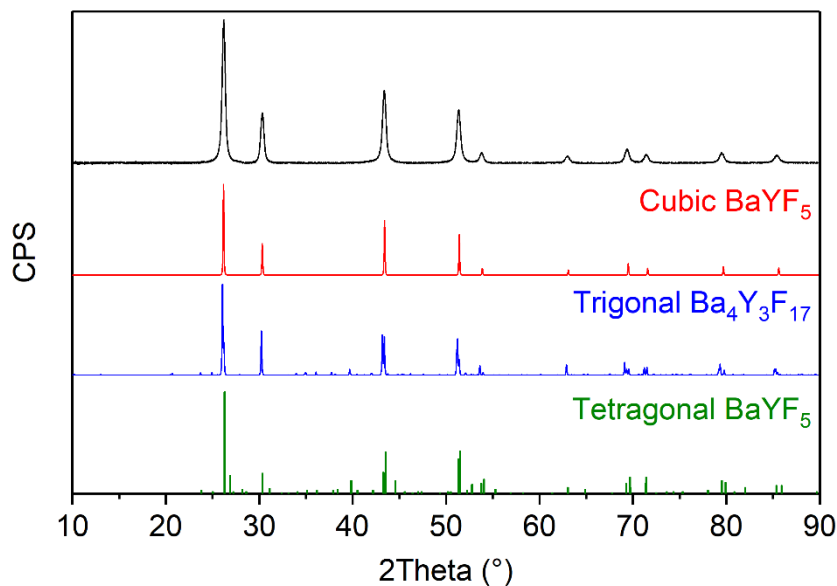


Figure 4.10 PXRD diffractogram of synthesized barium yttrium fluoride nanoparticles, as compared to the theoretical patterns of cubic BaYF₅ and trigonal Ba₄Y₃F₁₇, and reference pattern of tetragonal BaYF₅ (PDF#46-0039). Reprinted with permission from Reference 149. Copyright 2021 American Chemical Society.

Previous reports on the BaF₂-YF₃ system observe that the Ba_{1-x}Y_xF_{2+x} cubic structure is only possible when $x < 0.36$, transitioning to the trigonal phase at higher Y³⁺ ratios.¹⁵¹ Since this is inconsistent with the results herein (where $x = 0.50$), a series of nanoparticle compositions were synthesized, varying the Ba²⁺:Y³⁺ ratio from $x = 0.33$ to 0.80 (confirmed *via* ICP-MS in **Table 4.3**). PXRD measurements completed on these compositions are presented in **Figure 4.11a**, depicting the same reflections across the series, but with slightly higher 2θ values as x increases, due to the larger unit cell edge length as Ba²⁺ increasingly replaces Y³⁺. A Bragg's law analysis on these reflections was calculated using Equations 4.1 and 4.2:¹⁵⁸

$$\lambda = 2d(\sin\theta) \quad (4.1)$$

$$d = a/\sqrt{(h^2 + k^2 + l^2)} \quad (4.2)$$

Where λ is the X-ray wavelength (1.540598 Å for a Cu K_α source), d is the interatomic lattice spacing, θ is the reflection angle observed *via* PXRD, a is the unit cell edge length for a cubic crystal phase material, and hkl are Miller indices for the specific reflection. This provided a range of lattice parameter values from 5.766(2) to 5.96(1) Å as the value of x decreased, following a linear trend observed in **Figure 4.11b**, consistent with Vegard's Law.

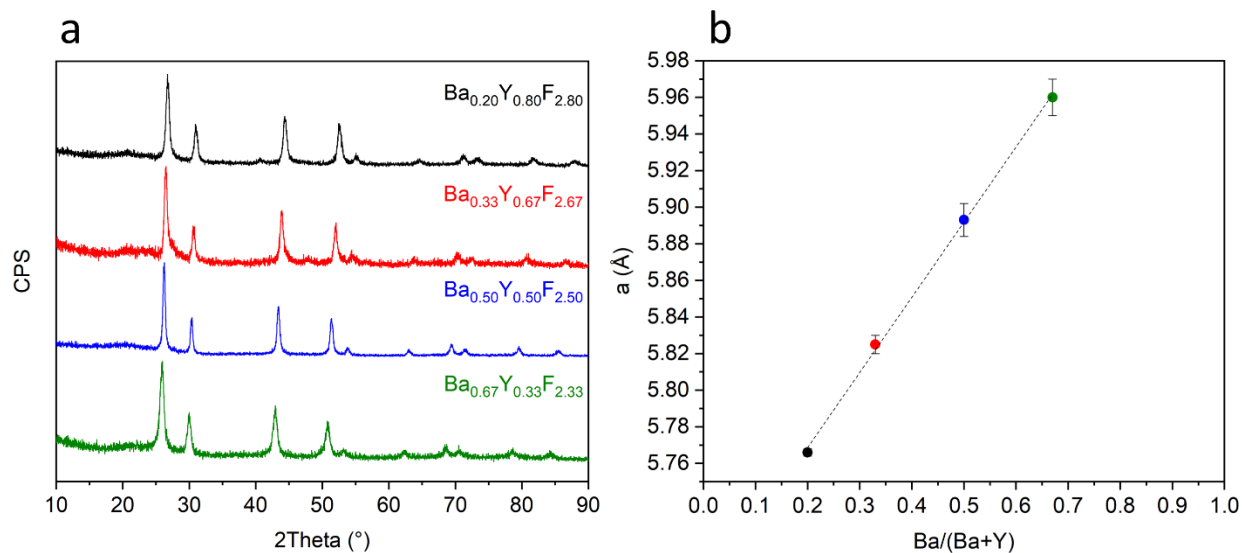


Figure 4.11 (a) PXRD diffractograms of $Ba_{1-x}Y_xF_{2+x}$ nanoparticles, where x is (■) 0.80, (■) 0.67, (■) 0.50, and (■) 0.33. (b) The calculated unit cell parameter a as a function of Ba^{2+} concentration, depicting a linear trend. Adapted with permission from Reference 149. Copyright 2021 American Chemical Society.

Table 4.3 ICP-MS results depicting the experimental $Ba^{2+}:Y^{3+}$ ratio to determine x in synthesized $Ba_{1-x}Y_xF_{2+x}$ nanoparticles.

Nominal x Value	Y^{3+} (mol)	Ba^{2+} (mol)	Experimental x Value
0.80	$4.62 \times 10^{-6} \pm 9.45 \times 10^{-8}$	$1.87 \times 10^{-6} \pm 2.42 \times 10^{-8}$	0.71 ± 0.12
0.67	$6.03 \times 10^{-5} \pm 6.55 \times 10^{-7}$	$3.71 \times 10^{-5} \pm 5.23 \times 10^{-7}$	0.62 ± 0.15
0.50	$5.73 \times 10^{-6} \pm 6.03 \times 10^{-8}$	$5.34 \times 10^{-6} \pm 6.40 \times 10^{-8}$	0.52 ± 0.10
0.33	$2.66 \times 10^{-6} \pm 2.48 \times 10^{-8}$	$6.10 \times 10^{-6} \pm 3.84 \times 10^{-8}$	0.30 ± 0.08
0.20	$1.48 \times 10^{-6} \pm 2.72 \times 10^{-8}$	$7.97 \times 10^{-6} \pm 4.55 \times 10^{-8}$	0.16 ± 0.07

These crystallography results reinforce the cubic phase UCNPs synthesized *via* the thermal decomposition protocol, contradicting previous investigations into the BaF_2 - YF_3 composition. The synthesis herein is completed at 300 °C, whereas the previous reported phase diagrams are obtained from melts above 800 °C. Therefore, it is likely that this synthesis approach does not provide sufficient energy to the system to order the cations towards the trigonal phase, as is reported. Rather the kinetically favored cubic phase remains, regardless of $Ba^{2+}:Y^{3+}$ ratio.

With this information confirmed, luminescent $Ba_{1-x}Y_xF_{2+x}$ nanoparticles were synthesized with a 1:1 ratio of $Ba^{2+}:Y^{3+}$ ($x = 0.5$), which had the highest synthesis yield and crystallinity

amongst the series. To probe the rare-earth site symmetry, BaYF₅:15%Eu³⁺ nanoparticles were synthesized, and the excitation and emission spectra were recorded, shown in **Figure 4.12a**. Emission bands in the visible region from the ⁵D_{1,0} → ⁷F_J were observed upon 355 nm irradiation, to induce the ⁵D₄ ← ⁷F₀ absorption. The magnetic dipole ⁵D₀ → ⁷F₁ transition at 591 nm is of particular interest, owing to its largely independent transition probability with respect to the electric field acting on the Eu³⁺ ion.⁹ In contrast, the hypersensitive electric dipole ⁵D₀ → ⁷F₂ transition, which is situated at 612 nm (only ≈580 cm⁻¹ away), is highly influenced by the crystal field. Therefore, the ratio between these two transitions can provide information on the symmetry of the Eu³⁺ site, with a larger ⁵D₀ → ⁷F₁ : ⁵D₀ → ⁷F₂ ratio characteristic of a high symmetry site, while a smaller ratio would be indicative of a low symmetry site. From the emission spectrum, the Eu³⁺ ions appear to be occupying a high symmetry environment, which corroborates the conclusions obtained *via* PXRD, since the cubic BaYF₅ crystal structure contains O_h site symmetry for the cation sites. If the nanoparticles possessed the trigonal Ba₄Y₃F₁₇ crystal structure, where the Eu³⁺ ions would occupy a site with C₁ symmetry, the emission from the ⁵D₀ → ⁷F₂ transition would have been more intense relative to the ⁵D₀ → ⁷F₁ transition.¹⁵⁹

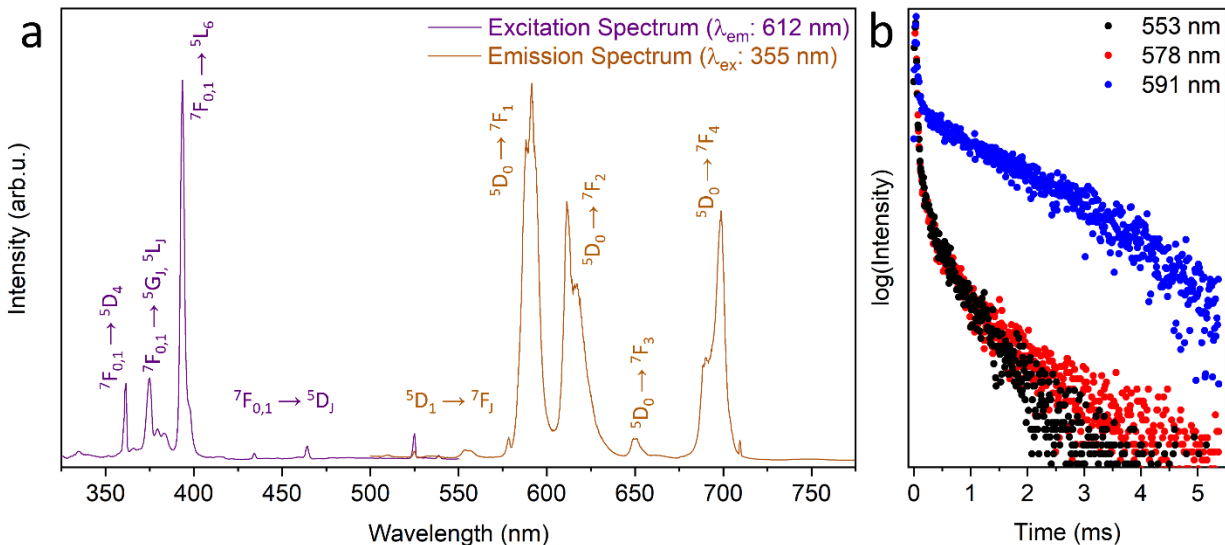


Figure 4.12 (a) Excitation (λ_{em} : 612 nm) and emission (λ_{ex} : 355 nm) spectra of BaYF₅:20%Eu³⁺ nanoparticles. (b) Luminescence lifetimes of BaYF₅:15%Eu³⁺ nanoparticles from emissions at (■) 553 nm (⁵D₁ → ⁷F₂), (■) 591 nm (⁵D₀ → ⁷F₁), and (■) 578 nm (⁵D₁ → ⁷F₃). Reprinted with permission from Reference 149. Copyright 2021 American Chemical Society.

An emission band appears at 578 nm, which could either be attributed to the ⁵D₁ → ⁷F₃ or the ⁵D₀ → ⁷F₀ transition, the latter of which could only be present in very low symmetry

environments (C_n , C_{nv} , or C_s).⁹ Should the observed emission be from the ${}^5D_0 \rightarrow {}^7F_0$ transition, the site occupied by the Eu^{3+} ions would be more difficult to determine. To alleviate this uncertainty, luminescence lifetimes of this emission were recorded and compared to the known ${}^5D_1 \rightarrow {}^7F_2$ (553 nm) and ${}^5D_0 \rightarrow {}^7F_1$ (591 nm) radiative transitions, shown in **Figure 4.12b**. Since the decay time profile of the emission band at 578 nm overlaps with the known 5D_1 emission band, it can be concluded that this unknown emission originates from the ${}^5D_1 \rightarrow {}^7F_3$ transition, which corroborates the O_h rare-earth site symmetry.

Normally, O_h symmetry is disadvantageous to lanthanide luminescence, owing to the centrosymmetric nature of the cation site that would minimize j-mixing. However, in the BaYF_5 host, the aliovalent substitution of the Ba^{2+} cations with Y^{3+} cations gives rise to interstitial anions required to compensate the charge imbalance, thus distorting the lattice of the host and lowering the site symmetry from native O_h symmetry. The unit cell for BaYF_5 illustrates this phenomenon, as observed in Appendix 2, by all the potential F^- sites within the seemingly simple cubic structure.

With a proper understanding of the BaYF_5 crystallography, UCNPs were synthesized with Yb^{3+} and Tm^{3+} as co-dopants. Similar to the study in Section 4.1, the concentration of Tm^{3+} was varied from 0.5 – 2.0%, with a constant 25% Yb^{3+} , to elucidate any relative changes in emission intensity. Upon 976 nm irradiation, the upconversion emission spectra in **Figure 4.13** possess all the expected Tm^{3+} emission bands, including the less frequently observed ${}^3F_{2,3} \rightarrow {}^3H_6$ transition. The $\text{BaYF}_5:25\%\text{Yb}^{3+}, 1.5\%\text{Tm}^{3+}$ UCNPs appear brightest for all the upconverted emissions, with all the compositions showing the strongest emission band at 800 nm (${}^3H_4 \rightarrow {}^3H_6$), and substantially weaker relative emission intensities from the 1D_2 and 3P_0 transitions.

Interestingly, the relative emission intensities from the different excited states are not consistent with varying activator concentration, as observed in **Figure 4.14**. Firstly, as the Tm^{3+} concentration increases, the relative intensity of the ${}^3P_0 \rightarrow {}^3F_4$ emission decreases relative to the ${}^1D_2 \rightarrow {}^3H_6$ emission. This can be justified using the CR mechanism established in Section 4.1, ${}^3P_0 + {}^3F_4 \rightarrow {}^1D_2 + {}^3H_6$, labelled CR1 in **Table 4.4**. As the concentration of Tm^{3+} increases and the ions get closer together, this mechanism becomes more prevalent and quenches the 3P_0 excited state in favor of the 1D_2 excited state, resulting in the observed trend in **Figure 4.14a**. Similarly, the $I({}^1G_4 \rightarrow {}^3H_6) / I({}^3H_4 \rightarrow {}^3H_6)$ ratio decreases with increasing Tm^{3+} content, observed in **Figure 4.14b**. This can be rationalized through a series of previously reported CR mechanisms (CR2-CR7 in

Table 4.4) which all depopulate the 1G_4 state in favor of the 3H_4 state, increasing in probability as the activator interionic spacing shortens.^{160,161}

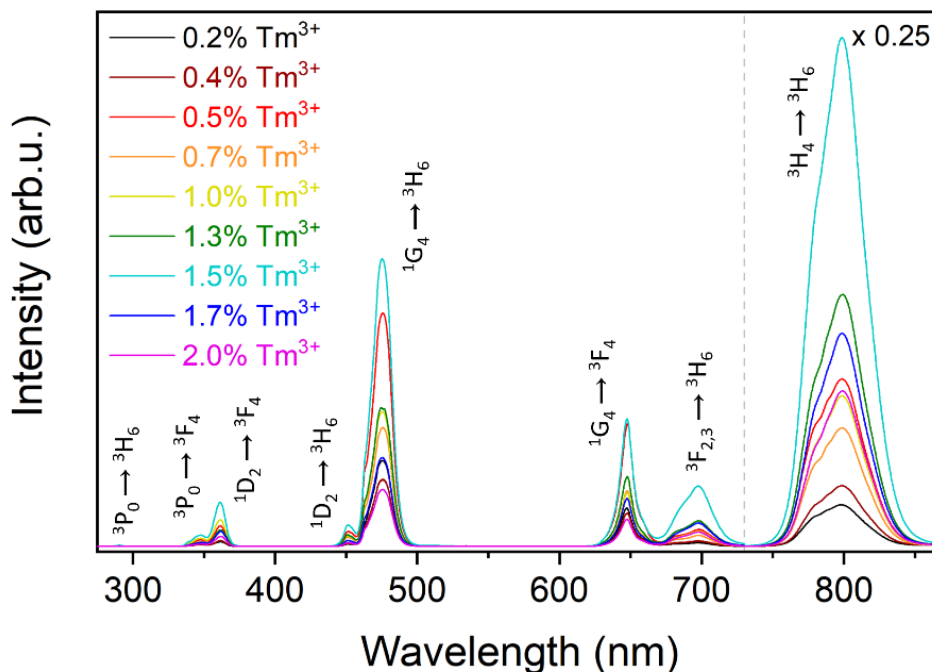


Figure 4.13 Upconversion emission spectra of $\text{BaYF}_5:25\%Yb^{3+}, x\%Tm^{3+}$, under 976 nm excitation, where x varies from 0.2 to 2.0. Reprinted with permission from Reference 149. Copyright 2021 American Chemical Society.

The $I(^1D_2 \rightarrow ^3F_4) / I(^1G_4 \rightarrow ^3H_6)$ ratio follows a different trend entirely, as observed in **Figure 4.14c**. This ratio increases as the Tm^{3+} concentration increases from 0.2 to 1.3%, but then decreases as the Tm^{3+} concentration increases further. The initial increase is likely due to the two CR mechanisms described in Section 4.1 (CR 8 and CR9 in **Table 4.4**, recall **Figure 4.3b**), increasing in probability as the Tm^{3+} distances shorten with increasing concentration.¹⁴⁵ These mechanisms favor the population of the 1D_2 excited state at the expense of the 1G_4 excited state, thus increasing the $I(^1D_2 \rightarrow ^3F_4) / I(^1G_4 \rightarrow ^3H_6)$ ratio. However, since this occurs simultaneously with the previously discussed depopulation of the 1G_4 state in favor of the lower energy states (recall **Figure 4.14b**), the population of the 1D_2 state becomes less probable between 0.7 and 1.3% Tm^{3+} , as observed by the change in slope. Beyond 1.3% Tm^{3+} , the depopulation of the 1D_2 state likely occurs *via* CR10, favoring the lower energy excited states.¹⁶² Since CR10 requires ions in the 1D_2 excited state to begin with, which is not likely at the lower dopant concentrations (as

observed by the weak 1D_2 emissions), this mechanism only becomes relevant when the Tm^{3+} concentration exceeds 1%.

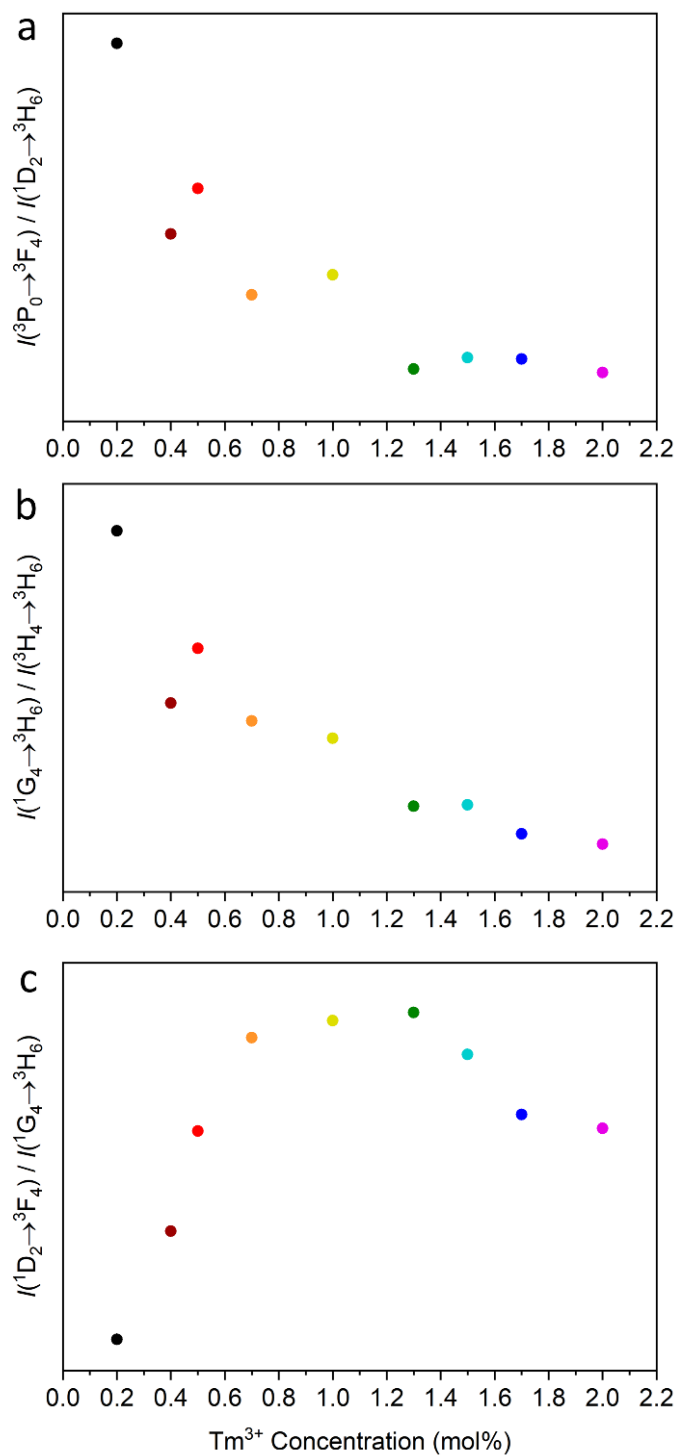


Figure 4.14 Ratios of integrated emission intensities from Figure 4.13 as a function of Tm^{3+} concentration, to infer their relative population: (a) $^3P_0 : ^1D_2$, (b) $^1G_4 : ^3H_4$, and (c) $^1D_2 : ^1G_4$. Reprinted with permission from Reference 149. Copyright 2021 American Chemical Society.

Table 4.4 Reported CR mechanisms between Tm³⁺ ions in nanoparticles.

Number	CR Mechanism	Reference
CR1	$^3P_0 + ^3F_4 \rightarrow ^1D_2 + ^3H_4$	139
CR2	$^1G_4 + ^3H_6 \rightarrow ^3H_5 + ^3H_4$	160
CR3	$^1G_4 + ^3H_6 \rightarrow ^3F_{2,3} + ^3F_4$	160
CR4	$^1G_4 + ^3H_5 \rightarrow ^3F_{2,3} + ^3F_{2,3}$	161
CR5	$^1G_4 + ^3F_4 \rightarrow ^3H_4 + ^3F_{2,3}$	161
CR6	$^1G_4 + ^3H_6 \rightarrow ^3H_4 + ^3H_5$	161
CR7	$^1G_4 + ^3H_6 \rightarrow ^3F_4 + ^3F_{2,3}$	161
CR8	$^1G_4 + ^3H_4 \rightarrow ^1D_2 + ^3F_4$	145
CR9	$^1G_4 + ^1G_4 \rightarrow ^1D_2 + ^3F_3$	145
CR10	$^1D_2 + ^3H_6 \rightarrow ^3H_4 + ^3F_3$	162

All the discussed CR mechanisms are facilitated *via* FRET, which is why shortening the interionic spacing between Tm³⁺ ions improves their probability. Additionally, the intrinsic decay time of an excited state involved in a CR mechanism also contributes to the FRET efficiency.⁵⁶ This means Tm³⁺ excited states with longer decay times are more susceptible to CR. To illustrate this, upconversion decay times of the most intense emissions, the $^1G_4 \rightarrow ^3H_6$ and $^3H_4 \rightarrow ^3H_6$ transitions at 475 and 802 nm, respectively, were recorded and plotted in **Figure 4.15**, with the corresponding single exponential decay times reported in **Table 4.5**. At the lowest dopant concentration studied (0.2% Tm³⁺), the excited state lifetime of the 1G_4 level is considerably longer than the 3H_4 level, alluding to the 1G_4 excited state having the longer intrinsic decay time. As the concentration of Tm³⁺ increases to 2 mol%, the decay time of the 1G_4 excited state shortens by about 49%, while the 3H_4 excited state lifetime only shortens by about 16%. This suggests that the 1G_4 excited state is far more sensitive to CR, in part due to its longer intrinsic lifetime which improves FRET efficiencies from this state, as well as the slew of possible mechanisms through which it may ET. This enhanced nonradiative relaxation of the 1G_4 state may contribute to the population of the lower energy excited states, thus enabling stronger NIR emissions.

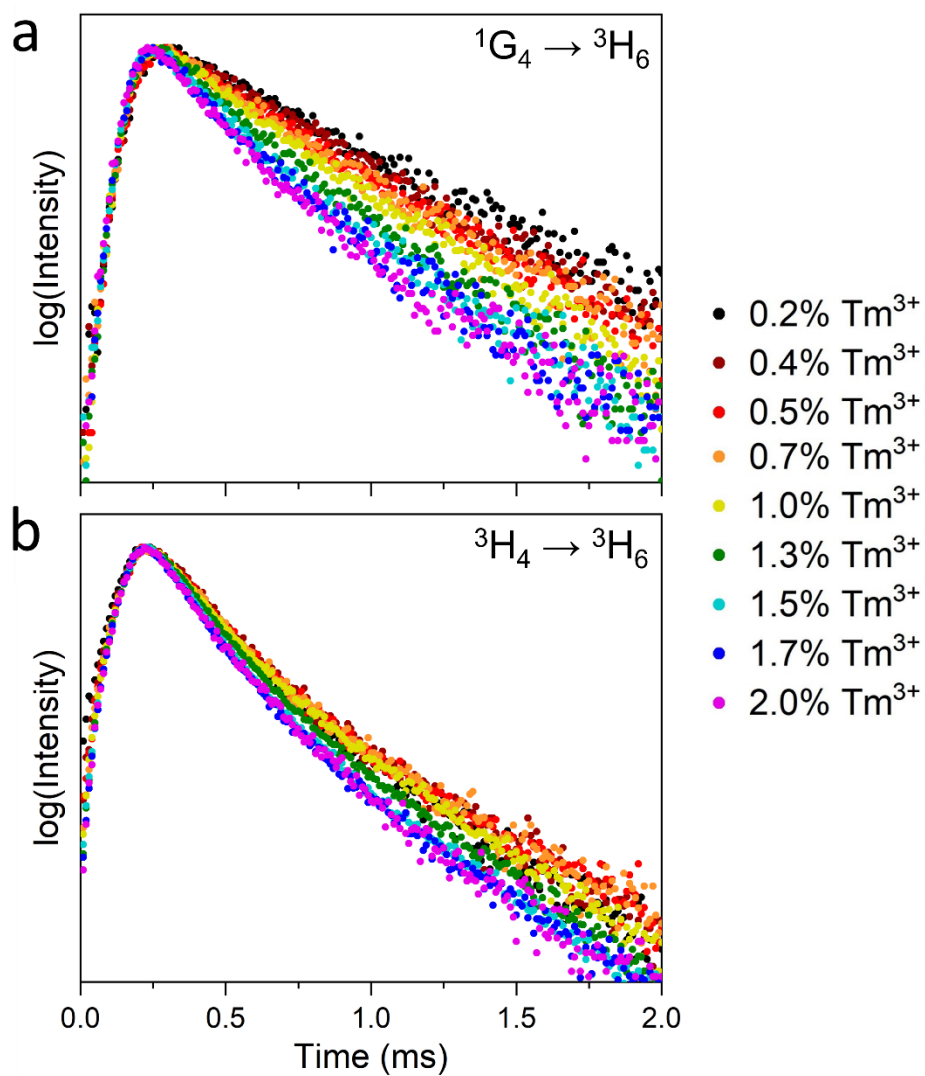


Figure 4.15 Upconversion lifetimes of the (a) $^1G_4 \rightarrow ^3H_6$ transition at 475 nm and (b) $^3H_4 \rightarrow ^3H_6$ transition at 802 nm from BaYF₅:25%Yb³⁺,x%Tm³⁺, under pulsed 976 nm excitation, where x varies from 0.2 to 2.0. Reprinted with permission from Reference 149. Copyright 2021 American Chemical Society.

Table 4.5 Single exponential decay times from the curves in Figure 4.15.

% Tm ³⁺	Decay Time (μ s)	
	¹ G ₄ \rightarrow ³ H ₆	³ H ₄ \rightarrow ³ H ₆
0.2	528 \pm 10	256 \pm 2
0.4	495 \pm 6	267 \pm 2
0.5	449 \pm 5	263 \pm 2
0.7	423 \pm 6	266 \pm 2
1.0	384 \pm 4	260 \pm 2
1.3	326 \pm 4	238 \pm 1
1.5	293 \pm 4	218 \pm 1
1.7	285 \pm 4	213 \pm 1
2.0	267 \pm 3	215 \pm 1

To assess the efficiency of the brightest BaYF₅:25%Yb³⁺,1.5%Tm³⁺ UCNP composition, upconversion QY measurements were completed as a function of excitation power density, focusing on the most intense ¹G₄ \rightarrow ³H₆ and ³H₄ \rightarrow ³H₆ transitions, shown in **Figure 4.16**. By focusing on excitation power densities from 0.3 to 4.8 W/cm², which are within one order of magnitude of the biologically acceptable 0.7 W/cm², the potential implications of this composition on bioimaging applications can be considered.¹⁶³ As expected, the ³H₄ \rightarrow ³H₆ emission at 802 nm has a higher QY than the ¹G₄ \rightarrow ³H₆ transition at 475 nm, sometimes exceeding two orders of magnitude. However, the sensitivity to power density appears to be greater in the ¹G₄ \rightarrow ³H₆ transition, which can be explained through the exponential relationship between upconversion efficiency and excitation power, as generalized by Equation 4.3:

$$I \propto P^n \quad (4.3)$$

Where I is the upconversion intensity, P is the excitation power density, and n is the number of incident photons required to populate the excited state responsible for that transition. Since populating the ³H₄ and ¹G₄ excited states require two and three incident photons, respectively, the emissions that originate from the ¹G₄ excited state will vary to a greater extent with changing excitation power densities.

QYs for the 802 nm emission range from 0.06 to 0.88%, which is comparable to other studied UCNP compositions in the literature.^{164–167} Given that these nanoparticles are smaller and lack additional functionalization (such as a core/shell structure) to improve the upconversion efficiency, this composition is proven as a potential alternative when the NIR emission is of interest. Interestingly, while the QY of the blue emission at 475 nm is lackluster at lower power densities ($3.4 \times 10^{-4}\%$ at 0.3 W/cm^2), the QY at higher power densities ($1.8 \times 10^{-2}\%$ at 4.8 W/cm^2) exceed previously reported values for this emission.^{164,166} This is likely due to the reduced efficiency of CR8 and CR9 in this host, which would populate the 1D_2 excited state at the expense of the 1G_4 state. Preventing these mechanisms allows more absorbed NIR photons to contribute to the emission at 475 nm, rather than upconvert further and populate the UV emitting levels; useful for applications that require this blue emission.

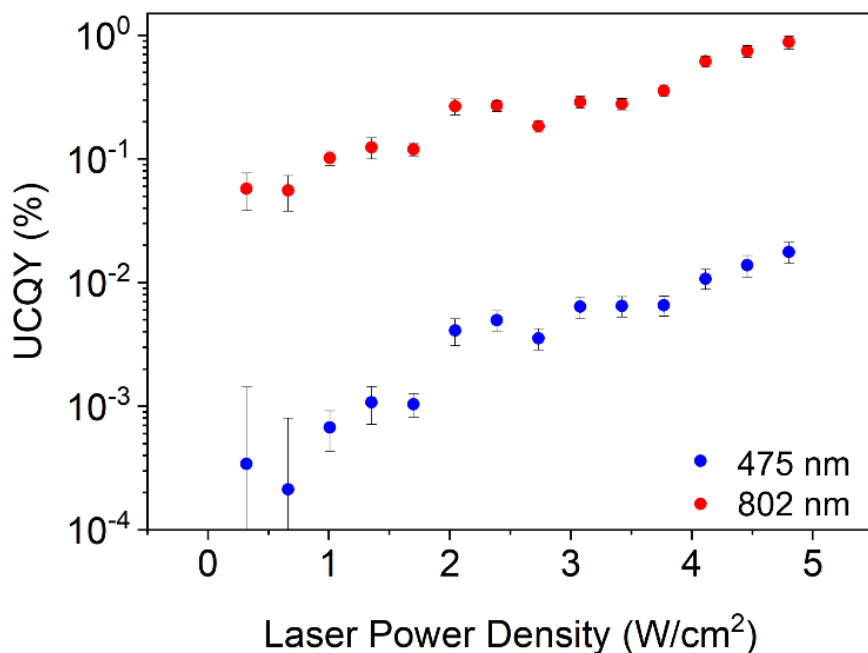


Figure 4.16 Upconversion QYs of the (■) $^1G_4 \rightarrow ^3H_6$ transition at 475 nm and (■) $^3H_4 \rightarrow ^3H_6$ transition at 802 nm from $\text{BaYF}_5:25\%Yb^{3+}, 1.5\%Tm^{3+}$, under 976 nm excitation. Reprinted with permission from Reference 149. Copyright 2021 American Chemical Society.

4.3. Effect of Host Composition on Yb³⁺,Tm³⁺ UCNPs

Under the same irradiation and detection conditions, relative upconversion intensities from nanoparticles of LiYF₄:25%Yb³⁺,0.2%Tm³⁺, NaGdF₄:20%Yb³⁺,1%Tm³⁺/NaGdF₄, and BaYF₅:25%Yb³⁺,1.5%Tm³⁺ were compared, shown in **Figure 4.17**. The dopant concentrations were chosen based on their established “ideal” concentrations, and the analysis strictly focused on relative intensities, due to differences in UCNP size and architecture.

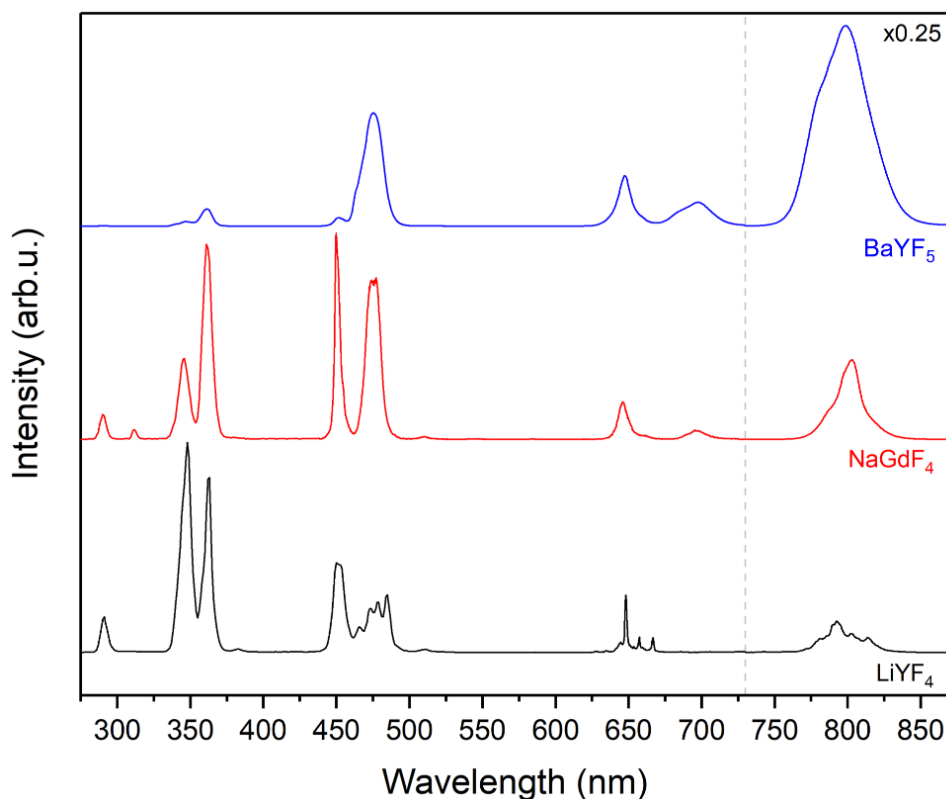


Figure 4.17 Upconversion emission spectra of (■) BaYF₅, (■) NaGdF₄, and (■) LiYF₄ UCNPs doped with Yb³⁺ and Tm³⁺, under 976 nm excitation. The NIR spectral region is scaled by x0.25. Reprinted with permission from Reference 149. Copyright 2021 American Chemical Society.

The observed differences in splitting for each transition are a consequence of the lanthanide site symmetry and coordination.⁷ The highest symmetry (O_h) in the BaYF₅ UCNPs results in the least splitting. The lower symmetry C_{3h} sites in the NaGdF₄ host results in a few split bands, whereas the lowest S₄ site symmetry in the LiYF₄ host results in a considerable number of discrete bands for each Tm³⁺ transition.^{168,169}

Focusing on the relative intensities between different compositions, the primary difference lies in the relatively weak emissions from the 1D_2 and 3P_0 transitions in BaYF₅, as compared to NaGdF₄ and LiYF₄. As discussed previously, since the interionic spacing between cation sites is longest in the BaYF₅ host, the potential constructive CR mechanisms that populate the 1D_2 excited state are minimized. This manifests in stronger emissions from the lower energy 1G_4 and 3H_4 levels. In contrast, destructive CR mechanisms that quench the higher energy excited states are minimized in the LiYF₄ UCNP, thus providing stronger emissions in the UV and visible spectral regions.

From this comparison, it becomes evident that one composition should not be considered universally optimal for any one application. For applications requiring strong UV emissions, the LiYF₄ host composition appears superior based on the UCNP studied herein. On a similar note, applications that exploit blue emissions should focus on the NaGdF₄ host, and applications that require NIR emissions should rely on the BaYF₅ host.

4.4. Proof-of-Concept: NIR Nanothermometry Using Upconversion Lifetimes

Over the last decade, the lanthanide luminescence community has started to focus on the study of nanothermometry applications using upconverting nanoparticles.^{170,171} With excitation and emission bands in the NIR biological windows, nanoparticles doped with certain lanthanides (or combinations thereof) can noninvasively measure the temperature of a local environment with high spatial resolution. This technique relies on changes in the rate of phonons with varying temperatures, since vibrational modes are Boltzmannian in nature and thus change with temperature, as calculated using Equation 4.4:²⁶

$$\langle n_s \rangle = \frac{1}{e^{\hbar\omega_s/kT} - 1} \quad (4.4)$$

Where $\langle n_s \rangle$ is the rate of phonons, ω_s is the energy of the phonon, k is the Boltzmann constant, and T is temperature. This manifests in changes in the ratio of emission bands from different excited states that can be bridged *via* phonons. When correlated back to a calibration curve, the temperature can be calculated.

The main limitation in such a technique is the uncertainty that arises when comparing the measurement to the calibration curve.¹⁷²⁻¹⁷⁴ Scattering from larger biomolecules and certain absorption bands (such as those of hemoglobin) can inadvertently change emission intensity ratios,

thus the observed spectra may not solely change as a function of temperature, but also as a function of environment.¹⁰⁸ Observing the lifetime of a single emission band mitigates this uncertainty, since the measurement would rely on the relative intensity of one transition and would not be affected by the fluctuation in transmittance with changing environments. This is facilitated by the changes in excited state decay rates with temperature, depicted in Equation 4.5:¹⁷⁵

$$\tau_{decay} = \frac{1}{k_r + k_{FRET} + k_{h.ph.} + k_{s.ph.}} \quad (4.5)$$

Where the decay time of an excited state (τ_{decay}) is inversely proportional to the radiative relaxation rate (k_r), the rate of nonradiative energy transfer (k_{FRET}), and the rate of relaxation *via* host and solvent phonons ($k_{h.ph.}$ and $k_{s.ph.}$, respectively). Since phonons are temperature dependent, as described in Equation 4.4, the excited state lifetime varies with temperature. Previous studies with lanthanide-doped photoluminescent nanothermometers with NIR emissions have illustrated the capabilities of such a technique.^{176,177}

From the results in Section 4.3, NIR upconversion luminescence from BaYF₅:Yb³⁺,Tm³⁺ would be optimal to demonstrate this technique with UCNPs. However, there are still concerns that must be addressed before they can be properly employed. The polydisperse nature of the synthesized nanoparticles hinders both their physical and spectroscopic properties, which need to be precise and reproducible to measure temperature with minimal errors. Therefore, the synthesis of BaYF₅ nanoparticles needs to be refined to obtain reliable, monodisperse UCNPs that can be employed in such a technique. Instead, core/shell NaYF₄:Yb³⁺,Tm³⁺/NaYF₄ nanoparticles were synthesized.¹⁷⁸ NaYF₄ has very similar physical and spectroscopic properties to NaGdF₄, and the addition of an inert shell aimed to minimize solvent quenching to enhance the upconversion luminescence intensity. To probe the influences that may affect the 800 nm upconversion emission lifetime with varying temperature, Tm³⁺ dopant concentrations of 1% and 2% were studied (with a constant 20% Yb³⁺). Relatively high Tm³⁺ concentrations enable greater population of the ³H₄ excited state and should therefore improve the 800 nm emission intensity. Additionally, 976 nm laser pulse widths of 200 μ s, 500 μ s, and 1 ms were used to ascertain differences in decay time with varying excitation irradiance. It is well documented that increasing the power of the excitation source, either directly or by prolonging the excitation pulse width, results in shorter upconversion decay times.^{179,180} This is effectively because greater excitation irradiance allows the ions to

achieve an equilibrium that favors the higher energy states, which is necessary for upconversion. Thus, when the excitation source ceases, the ions can emit. Under lower excitation powers, where the equilibrium favors lower energy excited states, ETU must continue to populate the emitting level even after the excitation source is turned off, consequently extending the observed lifetime. Finally, the UCNPs were dispersed in dimethylformamide (DMF) and water, two polar solvents with very different phonon energies, as observed by their infrared absorption spectra.^{181,182} Water has a strong, broad absorption band at approximately 3500 cm^{-1} characteristic of OH stretching vibrations, whereas the strongest vibrational absorption of DMF stems from the carbonyl stretch at about 1700 cm^{-1} . Each variable: activator concentration, excitation pulse width, and solvent, are expected to influence the decay times, and therefore the thermal sensitivities, of the ensuing measurements.

TEM micrographs of the synthesized core/shell nanoparticles are presented in **Figure 4.18a** and **b**, illustrating the similar size distributions and the slightly varying contrast between the core and shell. The emission spectra are shown in **Figure 4.18c**, centered on the emission at 800 nm, indicating an increased rate of concentration quenching that reduces the emission intensity for the UCNPs doped with 2% Tm^{3+} .

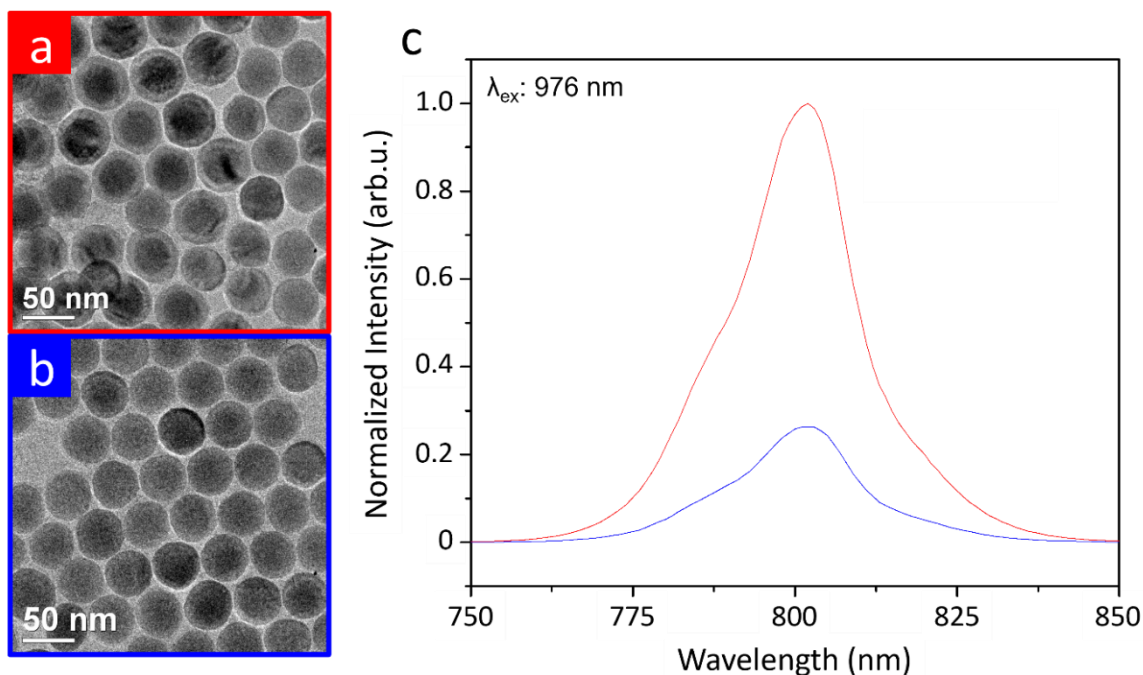


Figure 4.18 (a,b) TEM micrographs and (c) upconversion emission spectrum, under 976 nm excitation of core/shell $\text{NaYF}_4:20\%\text{Yb}^{3+},x\%\text{Tm}^{3+}/\text{NaYF}_4$, where x is (■) 1 and (■) 2. Reprinted with permission from Reference 178. Copyright 2021 American Chemical Society.

Upon pulsed 976 nm excitation, lifetimes of both compositions were recorded and shown in **Figure 4.19**, varying the solution temperature from 20 – 70 °C. This temperature range only slightly extends beyond what is biologically relevant.¹⁷⁶ The fastest 200 μs pulse width did not provide sufficient excitation energy to generate strong emissions, except for the 1% Tm³⁺-doped UCNPs in water. Regardless, in all the measurements, there is a clear decrease in lifetime of the 800 nm emission as the temperature of the solution is increased.

To analyze this change in lifetime, the decay portion of the lifetime profiles were fitted to a single exponential and plotted as a function of temperature in **Figure 4.20**. At first glance, it is possible to assume a linear trend, which leads to the initial thermal sensitivities reported in **Table 4.6**. However, since the electronic relaxation of an ion is considered to follow traditional rate laws, the change in decay time with temperature should also hold true to an Arrhenius-type fitting, as expressed in Equation 4.6:^{183,184}

$$\tau = \tau_0 / (1 + C e^{-\Delta E / (kT)}) \quad (4.6)$$

Where τ is the observed lifetime, τ_0 is the theoretical lifetime at 0 K, C is the quenching rate constant, and ΔE is the energy gap between the emitting level and the closest lower lying energy level (which is most likely to be populated *via* phonon quenching). From this fitting, a thermal sensitivity (S_R) could be calculated using Equation 4.7:

$$S_R = \tau \frac{C}{\tau_0} e^{-\Delta E / (kT)} \frac{\Delta E}{kT^2} \quad (4.7)$$

The values of S_R are similar to the thermal sensitivities calculated using a linear fit, indicating that the temperature range studied does in fact follow a linear trend.

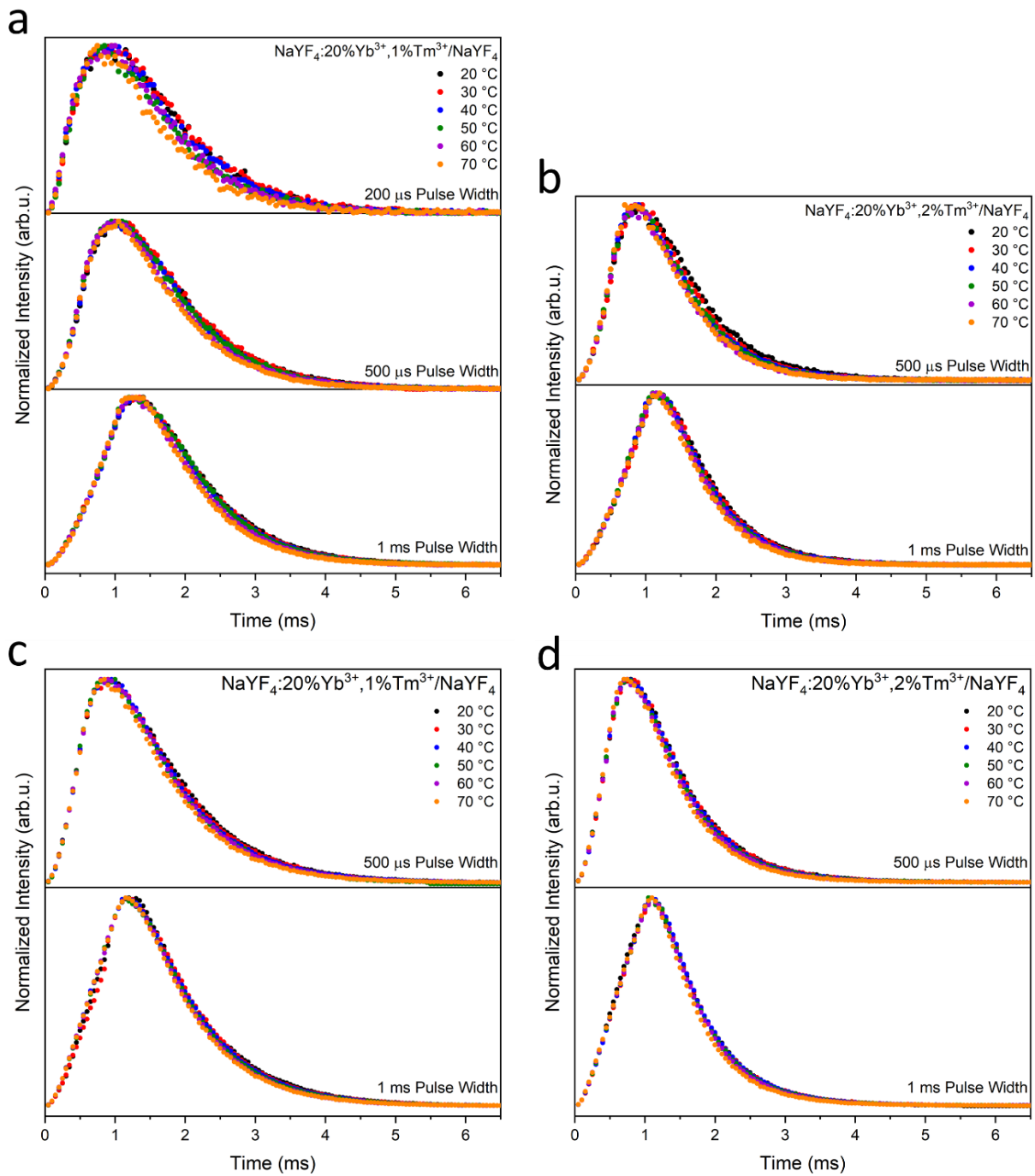


Figure 4.19 Upconversion lifetime profiles of $\text{NaYF}_4:20\% \text{Yb}^{3+}, x\% \text{Tm}^{3+}/\text{NaYF}_4$ under pulsed 976 nm excitation, where x is (a,c) 1 and (b,d) 2, dispersed in (a,b) water and (c,d) DMF. Reprinted with permission from Reference 178. Copyright 2021 American Chemical Society.

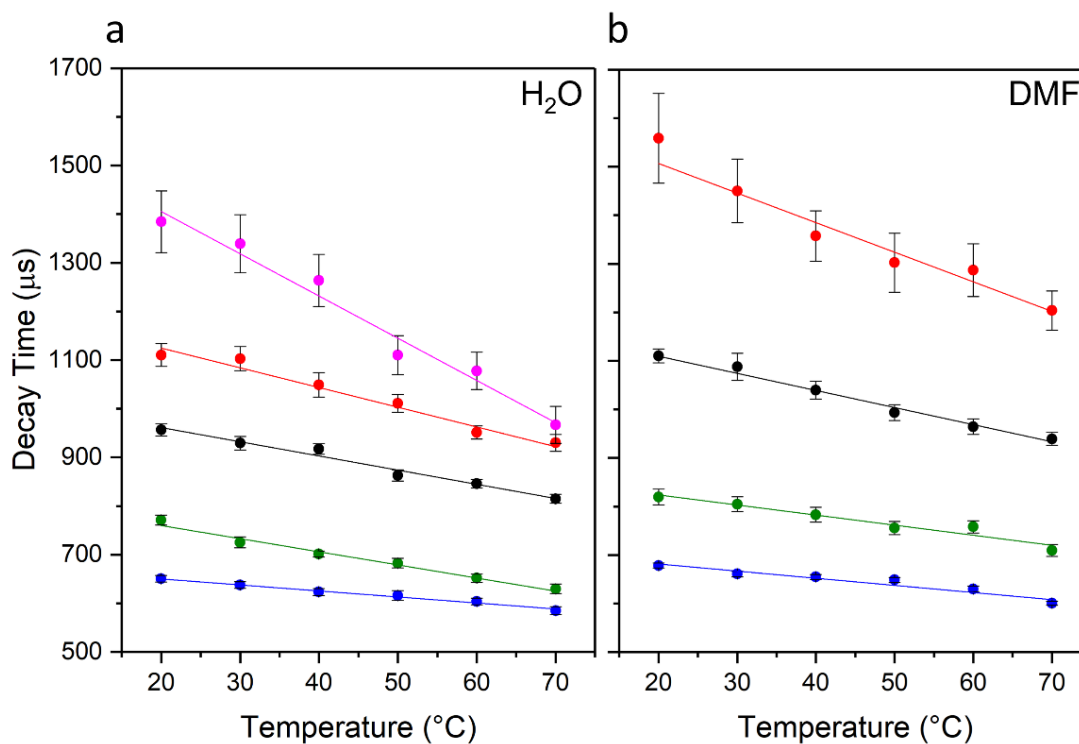


Figure 4.20 Single exponential decay times plotted as a function of temperature in (a) water and (b) DMF, from the lifetime profiles in Figure 4.19. 1% Tm^{3+} : (■) 200 μs , (■) 500 μs , (■) 1 ms, 2% Tm^{3+} : (■) 500 μs , (■) 1 ms. Reprinted with permission from Reference 178. Copyright 2021 American Chemical Society.

Table 4.6 Linear and Arrhenius fitting from the trends observed in Figure 4.20.

Solvent	Composition	Pulse Width	Max Thermal Sensitivity (%/K)	
			Linear Fit	Arrhenius Fit
H ₂ O	1% Tm^{3+}	200 μs	0.9	0.9
		500 μs	0.4	0.5
		1 ms	0.4	0.4
	2% Tm^{3+}	500 μs	0.4	0.4
		1 ms	0.2	0.2
		1 ms	0.2	0.2
DMF	1% Tm^{3+}	500 μs	0.5	0.5
		1 ms	0.4	0.3
		1 ms	0.4	0.3
	2% Tm^{3+}	500 μs	0.3	0.4
		1 ms	0.2	0.3
		1 ms	0.2	0.3

By observing the lifetimes in different solvents, the intention was to examine the role that solvent phonons play on thermal sensitivity. However, there is no apparent trend when comparing the temperature dependent decay times in water and DMF. The primary uncertainty here lies in the presence of an inert shell that, while beneficial to the upconversion luminescence intensity, physically separates the Tm^{3+} ions from the solvating shell, thus preventing solvent phonon quenching. This also suggests that the observed changes in decay time from the UCNPs as a function of temperature are more likely caused by phonon energies of the host lattice.

Since the UCNPs with 2% Tm^{3+} are subject to greater concentration quenching, the decay times are generally faster than the samples containing 1% Tm^{3+} . As mentioned in Section 1.3, the longer the donor lifetime, the greater potential for nonradiative relaxation *via* energy transfer, which includes phonon related quenching pathways. This is further proven here, where the longer decay times from the 1% Tm^{3+} -doped UCNPs make them more susceptible to phonon quenching, and thus change with a greater magnitude as a function of temperature. This indicates that the $\text{NaYF}_4:20\%\text{Yb}^{3+},1\%\text{Tm}^{3+}/\text{NaYF}_4$ UCNPs are superior in both luminescence intensity as well as thermal sensitivity, owing to less concentration quenching.

By irradiating the UCNPs with different pulse widths, the expected trend is observed where shorter pulse widths generate longer excited state lifetimes. However, with lower excitation powers, the upconversion efficiency is also weaker (recall the power dependence in Equation 4.3), which results in lower signal-to-noise ratios. This trade-off is observed clearly in **Figure 4.20**, where the measurements with the noisiest lifetime profiles, and therefore the highest uncertainty (fitting error), are the measurements with the greatest thermal sensitivity (greatest slope).

While the proof-of-concept herein demonstrates that upconversion lifetimes can be used as alternatives in nanothermometry, the thermal sensitivities are lackluster in comparison to traditional ratiometric techniques, by about one order of magnitude.¹⁷⁴ However, properly understanding the variables that influence this nanothermometric probe can lead to potential improvements.

Chapter 5. Tm³⁺ and Tb³⁺ co-doped Upconverting Nanoparticles

With the myriad of Tm³⁺ emissions that can be sensitized *via* ETU with Yb³⁺, there are many possibilities where they can be employed. One such prospect is to incorporate other luminescent ions and engineer multicolor-emitting UCNPs for applications including multiplexed imaging and information storage.^{115,185,186} By coupling Tm³⁺, which can emit UV light, with other lanthanides that are sensitized with UV light, these newly introduced ions can be excited and generate additional emissions under NIR excitation. One example of an ion with excitation bands between 350 and 360 nm is Tb³⁺, with relatively bright green emissions after excitation into the ⁵L_J excited states, depicted in **Figure 5.1**.¹⁸⁷ As discussed in Section 1.2.2, cooperative sensitization mechanisms can be achieved with Yb³⁺ and Tb³⁺, however their efficiencies are considerably lower than ETU. Therefore, sensitization through the UV emitting levels of Tm³⁺ can enhance the emission intensities of Tb³⁺ under NIR irradiation.

Previous investigations on triply-doped NaYF₄ microparticles with Yb³⁺, Tm³⁺, and Tb³⁺ have shown the characteristic green emissions of Tb³⁺ under NIR excitation, demonstrating the potential of such a system.¹⁸⁸ However, as established in Chapter 4, if the excitation of Tb³⁺ is achieved through the UV emissions of Tm³⁺, the LiYF₄ host composition would prove better for sensitizing Tb³⁺. When adding 15% Tb³⁺, which is reported as the optimal dopant concentration in NaYF₄, to LiYF₄:25%Yb³⁺,0.2%Tm³⁺ UCNPs, an almost

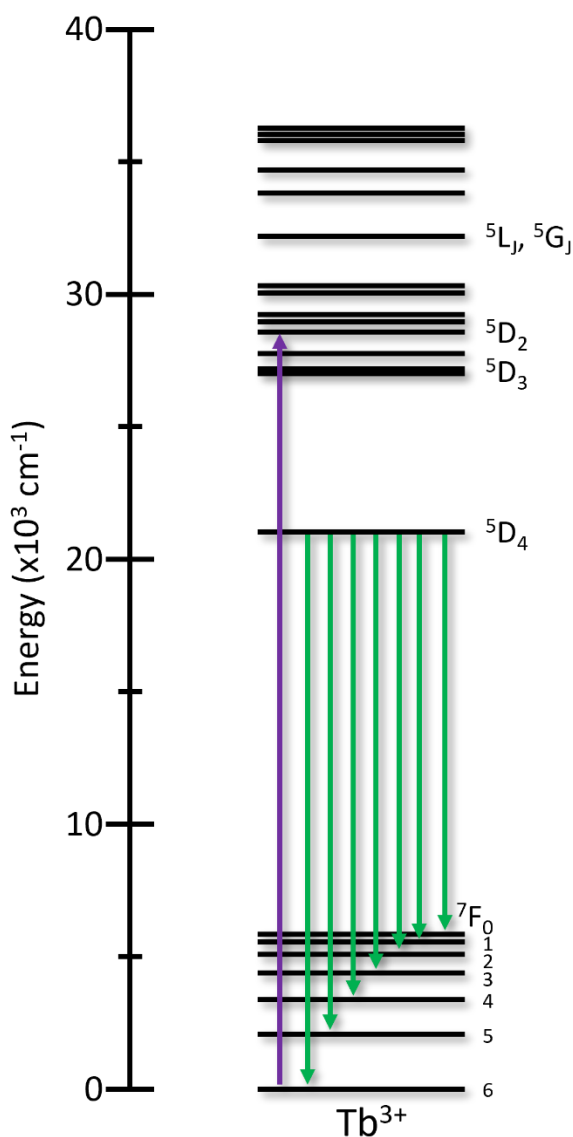


Figure 5.1 Tb³⁺ energy level diagram.

complete quenching of the Tm^{3+} upconverted emissions is observed and no Tb^{3+} emissions are present, as shown in **Figure 5.2a**.

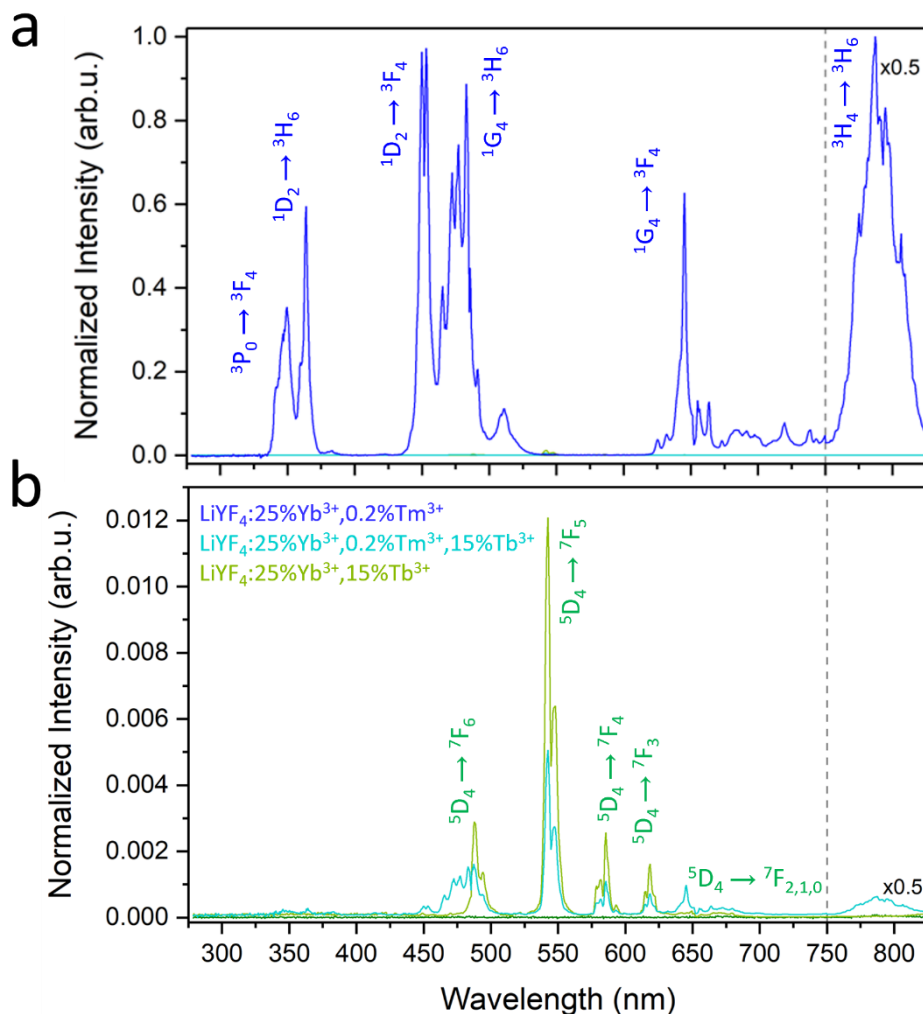


Figure 5.2 Upconversion emission spectra, under 976 nm excitation, of (■) $\text{LiYF}_4:25\%Yb^{3+}, 0.2\%Tm^{3+}$, (■) $\text{LiYF}_4:25\%Yb^{3+}, 0.2\%Tm^{3+}, 15\%Tb^{3+}$, and (■) $\text{LiYF}_4:25\%Yb^{3+}, 15\%Tb^{3+}$ nanoparticles at (a) full scale or (b) zoomed in along the intensity axis. Spectra are not intensity calibrated as a function of wavelength.

As shown in **Figure 5.2b**, which zooms in on the intensity axis of **Figure 5.2a**, Tb^{3+} emissions are present between 475 and 650 nm, characteristic of the $^5D_4 \rightarrow ^7F_J$ radiative transitions (**Figure 5.1**). Moreover, the Tm^{3+} emissions are observed as well, albeit 99% weaker than the UCNPs without Tb^{3+} . Unexpectedly, however, these emissions are weaker than LiYF_4 nanoparticles doped with only Yb^{3+} and Tb^{3+} . This indicates that the luminescence observed from the $\text{LiYF}_4:25\%Yb^{3+}, 15\%Tb^{3+}$ UCNPs is facilitated *via* cooperative sensitization, and the addition

of Tm^{3+} quenches the emission intensities rather than sensitizes them further.¹⁸⁹ This combination of results indicates that Tb^{3+} is quenching Tm^{3+} , and Tm^{3+} is quenching Tb^{3+} .

A previously reported ET mechanism from the Tb^{3+} emitting state to Tm^{3+} ($\text{Tb}^{3+}:^5\text{D}_4 + \text{Tm}^{3+}:^3\text{H}_6 \rightarrow \text{Tb}^{3+}:^7\text{F}_0 + \text{Tm}^{3+}:^3\text{F}_3$) may explain the observed quenching of the Tb^{3+} emissions with the addition of Tm^{3+} .¹⁹⁰ However, if this quenching mechanism was present, it would be observed regardless of the Tb^{3+} excitation pathway, whether that be *via* cooperative sensitization or direct excitation. Instead, this decrease in intensity is not observed under 355 nm irradiation, as shown in **Figure 5.3**, where the emissions from Tb^{3+} are the same intensity regardless of Tm^{3+} . This means the addition of Tm^{3+} is not quenching the radiative relaxation of the $^5\text{D}_4$ state, but rather preventing the population of the $^5\text{D}_4$ state. This likely means that the greater ET efficiency between Yb^{3+} and Tm^{3+} is preventing the cooperative sensitization of Tb^{3+} , and thus the decrease in the Tb^{3+} emission intensities is observed.

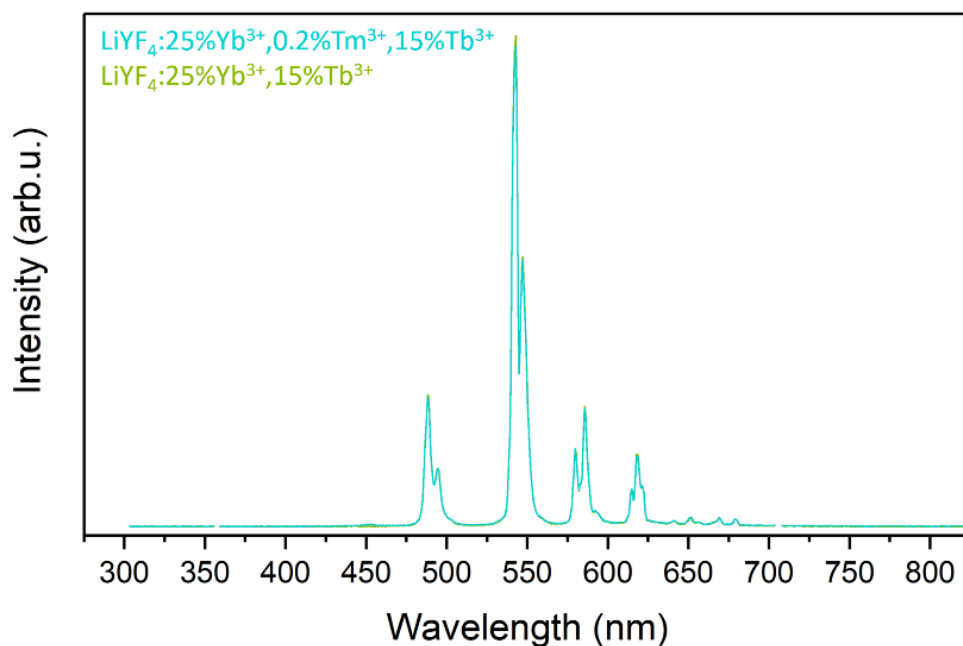


Figure 5.3 Photoluminescence emission spectra, under 355 nm excitation, of (■) $\text{LiYF}_4:25\%\text{Yb}^{3+},0.2\%\text{Tm}^{3+},15\%\text{Tb}^{3+}$ and (■) $\text{LiYF}_4:25\%\text{Yb}^{3+},15\%\text{Tb}^{3+}$ nanoparticles. Spectra are not intensity calibrated as a function of wavelength. The excitation source at 355 nm and the second order at 710 nm have been removed.

To justify the observed quenching of Tm^{3+} by the addition of Tb^{3+} , the NIR emission spectra were recorded under 976 nm excitation, as shown in **Figure 5.4a**. A decrease in intensity of the ${}^3\text{F}_4 \rightarrow {}^3\text{H}_6$ emission at ≈ 1700 nm is observed when Tb^{3+} is added, which is likely due to ET from the ${}^3\text{F}_4$ excited state of Tm^{3+} to the ${}^7\text{F}_0$ state of Tb^{3+} , as depicted in **Figure 5.4b**.¹⁸⁸ Since this almost completely quenches the population of the ${}^3\text{F}_4$ state of Tm^{3+} , which is the first step in the ETU process, subsequent ET to populate the higher energy levels cannot occur, which in turn prevents all the upconverted Tm^{3+} emissions.

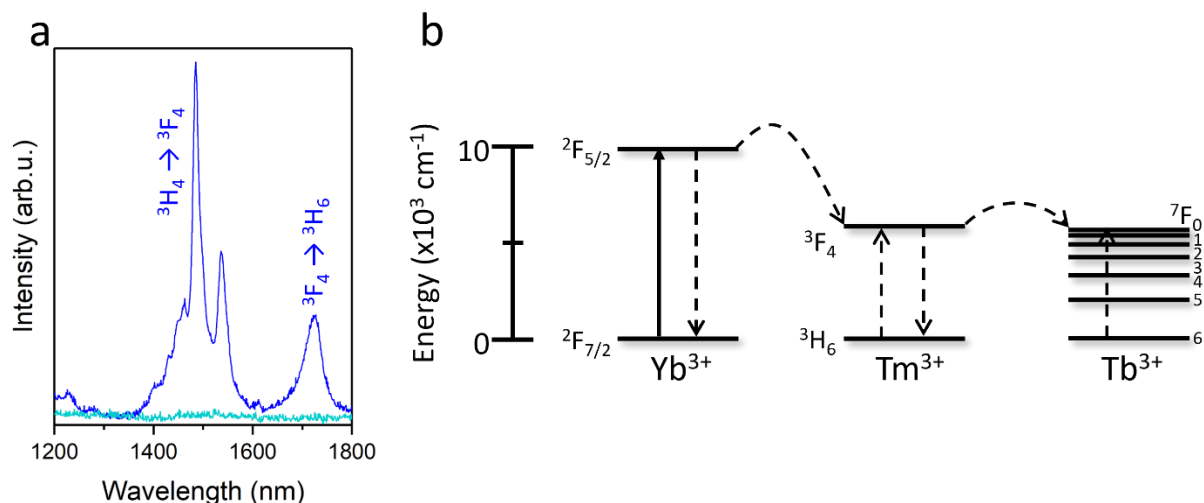


Figure 5.4 (a) NIR Luminescence spectra, under 976 nm excitation, of (■) $\text{LiYF}_4:25\%\text{Yb}^{3+}, 0.2\%\text{Tm}^{3+}$ and (■) $\text{LiYF}_4:25\%\text{Yb}^{3+}, 0.2\%\text{Tm}^{3+}, 15\%\text{Tb}^{3+}$ nanoparticles. (b) Energy level diagram depicting the ET process from excited Yb^{3+} to the lower excited states of Tb^{3+} .

Since the observed processes between Yb^{3+} , Tm^{3+} , and Tb^{3+} appear to inadvertently prevent any efficient upconversion luminescence, the sensitization of Tb^{3+} via Tm^{3+} upconversion luminescence needs to be addressed differently. Architecturally, by synthesizing core/shell nanoparticles, with Yb^{3+} and Tm^{3+} doped in the core to facilitate upconversion and Tb^{3+} in the shell to absorb the outgoing UV emissions, the intended system may still be realized. However, due to the limitations in core/shell synthesis of LiYF_4 nanoparticles at the time of this research, NaGdF_4 UCNPs were synthesized in its place, trading upconversion efficiency for reproducible and monodisperse core/shell nanoparticles.¹⁹¹

5.1. $\text{Tm}^{3+} \rightarrow \text{Tb}^{3+}$ ET Across Core/Shell Interface in NaGdF_4 UCNPs

To evaluate the ET efficiency across the core/shell interface in NaGdF_4 UCNPs, several dopant concentrations of Tb^{3+} in the shell were studied. By segregating the upconverting Yb^{3+} and Tm^{3+} ions in the core, and the Tb^{3+} ions in the shell, destructive ET mechanisms may be mitigated in such a way that the sensitization of Tb^{3+} still occurs through Tm^{3+} . TEM micrographs of core $\text{NaGdF}_4:49\%\text{Yb}^{3+},1\%\text{Tm}^{3+}$ and core/shell $\text{NaGdF}_4:49\%\text{Yb}^{3+},1\%\text{Tm}^{3+}/\text{NaGdF}_4:x\%\text{Tb}^{3+}$ are presented in **Figure 5.5a-d**, where x is 0, 10, and 20. A constant dopant concentration of 49% Yb^{3+} was used, owing to previous reports of improved relative intensities of the $^1\text{D}_2$ transitions.¹⁴⁴ The particle size distributions were calculated using these micrographs and are presented in **Figure 5.5e**. The core nanoparticles were consistently 8.9 ± 1.1 nm, with a shell thickness of approximately 6 nm across all compositions. ICP-MS measurements were completed to confirm the consistent dopant concentrations of Yb^{3+} and Tm^{3+} in the core and linear trend of Tb^{3+} concentration in the shell, shown in **Table 5.1**. These consistencies in UCNP size and composition were imperative to accurately study the Tb^{3+} population dynamics under NIR irradiation.

Table 5.1 ICP-MS results for the experimental composition of the NaGdF_4 core/shell UCNPs studied.

Ion	0% Tb^{3+}	10% Tb^{3+}	20% Tb^{3+}
Gd^{3+}	$87.50 \pm 0.47\%$	$81.06 \pm 5.76\%$	$73.79 \pm 3.98\%$
Tb^{3+}	$0.09 \pm 0.02\%$	$8.10 \pm 0.60\%$	$15.97 \pm 0.94\%$
Tm^{3+}	$0.26 \pm 0.02\%$	$0.25 \pm 0.02\%$	$0.24 \pm 0.03\%$
Yb^{3+}	$12.15 \pm 1.46\%$	$10.59 \pm 0.92\%$	$10.01 \pm 0.62\%$

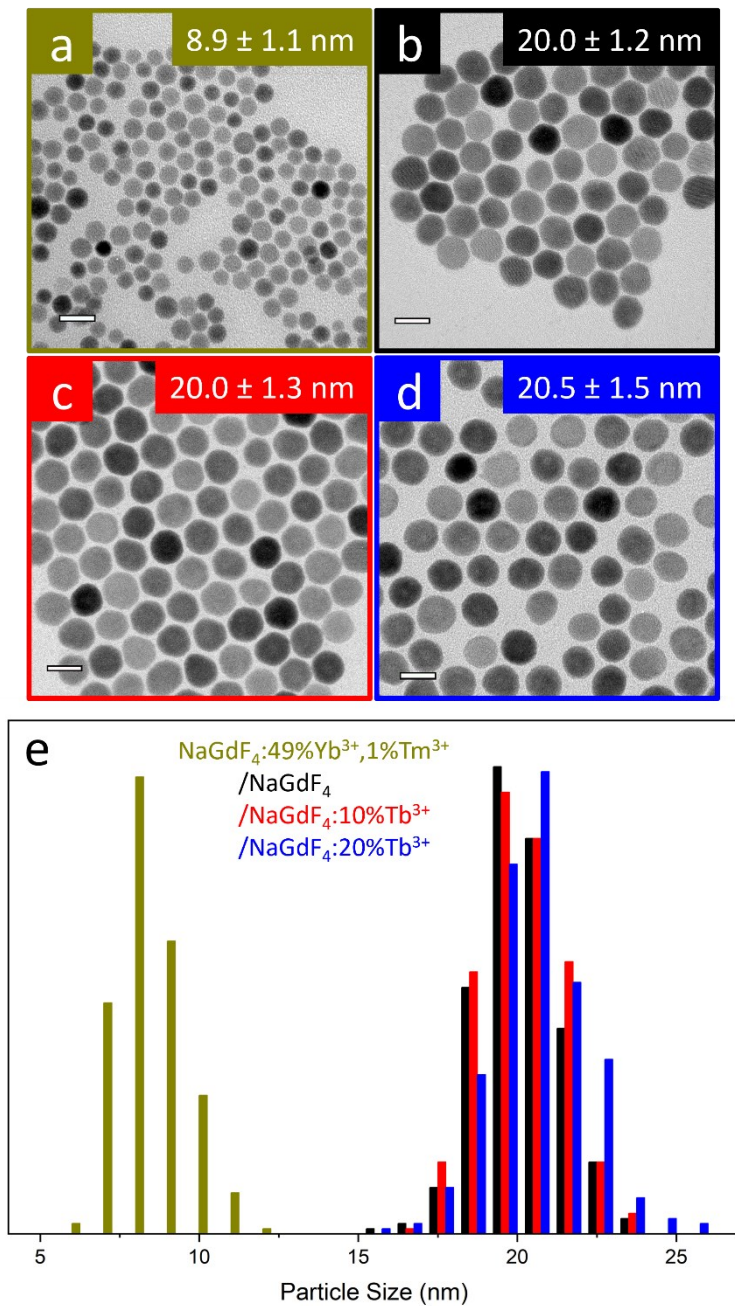


Figure 5.5 TEM micrographs of nanoparticles comprising (a, \blacksquare) core-only $\text{NaGdF}_4:49\% \text{Yb}^{3+}, 1\% \text{Tm}^{3+}$, (b, \blacksquare) core/shell $\text{NaGdF}_4:49\% \text{Yb}^{3+}, 1\% \text{Tm}^{3+} / \text{NaGdF}_4$, (c, \blacksquare) core/shell $\text{NaGdF}_4:49\% \text{Yb}^{3+}, 1\% \text{Tm}^{3+} / \text{NaGdF}_4:10\% \text{Tb}^{3+}$, and (d, \blacksquare) core/shell $\text{NaGdF}_4:49\% \text{Yb}^{3+}, 1\% \text{Tm}^{3+} / \text{NaGdF}_4:20\% \text{Tb}^{3+}$, with (e) the corresponding particle size distributions. Scale bars are set to 20 nm.

NaGdF_4 nanoparticles can crystallize in multiple phases, the two most common being the cubic and hexagonal structures.⁷⁴ Of these two phases, it is well established that the hexagonal structure facilitates more efficient lanthanide luminescence, due in part to its lower RE site

symmetry. To distinguish which crystal phases were synthesized herein, PXRD diffractograms were recorded, presented in **Figure 5.6a**, which depict reflections consistent with the hexagonal phase. However, the low signal-to-noise ratio raises uncertainty in the crystalline quality of the samples. This was attributed to the small sample quantity and the relatively small UCNP size that resulted in poor experimental reflection intensities. Thus, HAADF STEM micrographs were obtained, shown in **Figure 5.6b** and **c**. These high-resolution images confirm a high degree of crystallinity in the synthesized nanoparticles, including along the fringe of the core where the shell begins. Moreover, the individual lanthanide positions can be observed and identified using the superimposed theoretical P-6 crystal structure overlaid on the micrograph in **Figure 5.6c**, confirming the hexagonal phase.¹⁹²

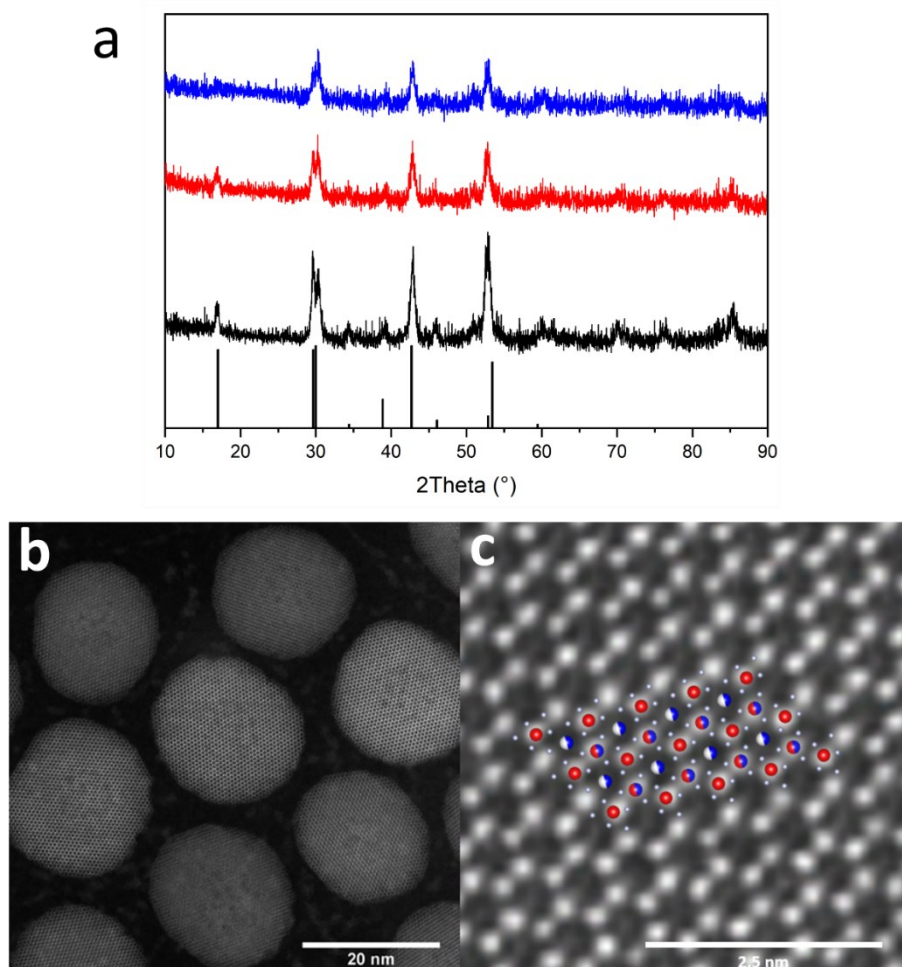


Figure 5.6 (a) PXRD diffractograms of core/shell UCNPs comprising (■) $\text{NaGdF}_4:49\% \text{Yb}^{3+}, 1\% \text{Tm}^{3+} / \text{NaGdF}_4$, (■) $\text{NaGdF}_4:49\% \text{Yb}^{3+}, 1\% \text{Tm}^{3+} / \text{NaGdF}_4:10\% \text{Tb}^{3+}$, and (■) $\text{NaGdF}_4:49\% \text{Yb}^{3+}, 1\% \text{Tm}^{3+} / \text{NaGdF}_4:20\% \text{Tb}^{3+}$, compared to the reference pattern for hexagonal phase NaGdF_4 (PDF#27-0699). (b,c) HAADF STEM micrographs of $\text{NaGdF}_4:49\% \text{Yb}^{3+}, 1\% \text{Tm}^{3+} / \text{NaGdF}_4:20\% \text{Tb}^{3+}$ UCNPs, overlapping the theoretical lattice structure of hexagonal NaGdF_4 with space group P-6.

As expected, under 976 nm irradiation, the characteristic Tm^{3+} emissions are observed, as shown in **Figure 5.7**. Importantly, the emission bands from the $\text{Tb}^{3+} {}^5\text{D}_4 \rightarrow {}^7\text{F}_j$ transitions are also observed. When increasing the Tb^{3+} dopant concentration, the upconverted emissions of Tm^{3+} decrease in intensity, indicative of ET processes that depopulates the Tm^{3+} excited states in favor of sensitizing Tb^{3+} . However, increasing the Tb^{3+} concentration from 10% to 20% results in no apparent increase in the Tb^{3+} emission intensities, indicating that exceeding this dopant concentration is resulting in concentration quenching, likely *via* EM to surface defects or quenching centers prevalent in the shell of the UCNPs.

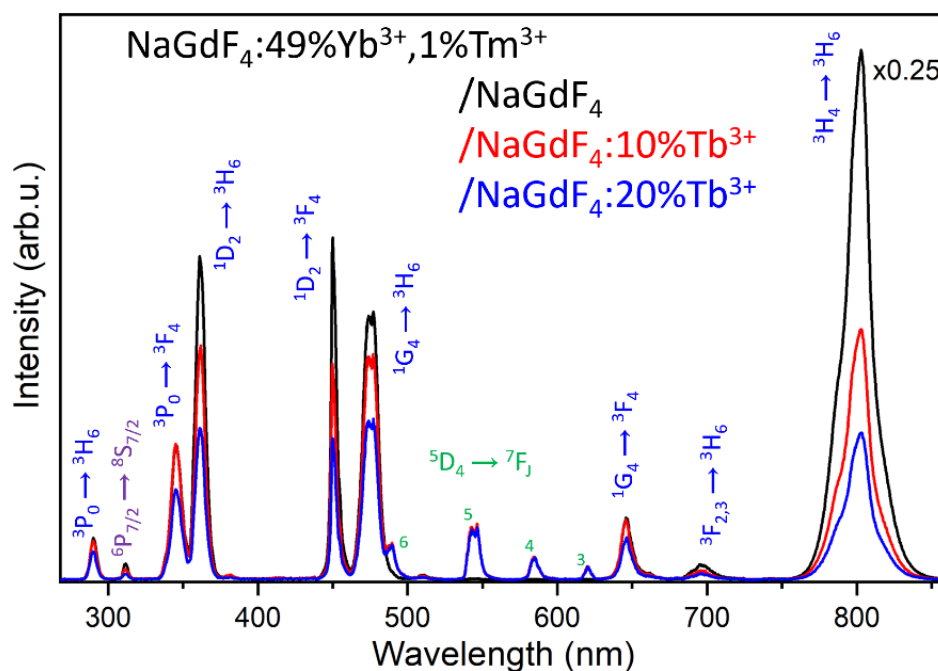


Figure 5.7 Upconversion emission spectra, under 976 nm excitation, of (■) $\text{NaGdF}_4:49\%\text{Yb}^{3+}, 1\%\text{Tm}^{3+}/\text{NaGdF}_4$, (■) $\text{NaGdF}_4:49\%\text{Yb}^{3+}, 1\%\text{Tm}^{3+}/\text{NaGdF}_4:10\%\text{Tb}^{3+}$, and (■) $\text{NaGdF}_4:49\%\text{Yb}^{3+}, 1\%\text{Tm}^{3+}/\text{NaGdF}_4:20\%\text{Tb}^{3+}$ core/shell nanoparticles.

Since the NaGdF_4 host composition possesses Gd^{3+} ions, an emission band is also present at 312 nm, corresponding to the ${}^6\text{P}_{7/2} \rightarrow {}^8\text{S}_{7/2}$ radiative transition of Gd^{3+} . Since the energy gap of this transition is very high ($>30000 \text{ cm}^{-1}$) and is not susceptible to quenching effects, the weak relative intensity is indicative of a weak excitation of Gd^{3+} into the ${}^6\text{P}_{7/2}$ level. This can be confirmed *via* excitation spectroscopy, presented in **Figure 5.8a**, which shows Gd^{3+} excitation bands between 270 – 280 nm (${}^6\text{I}_J \leftarrow {}^8\text{S}_{7/2}$) and 305 – 320 nm (${}^6\text{P}_J \leftarrow {}^8\text{S}_{7/2}$). Neither of these bands

overlap the Tm^{3+} upconverted emission at 290 nm from the ${}^3\text{P}_0 \rightarrow {}^3\text{H}_6$ transition, indicating that the sensitization of Gd^{3+} is phonon-assisted, and therefore inefficient.

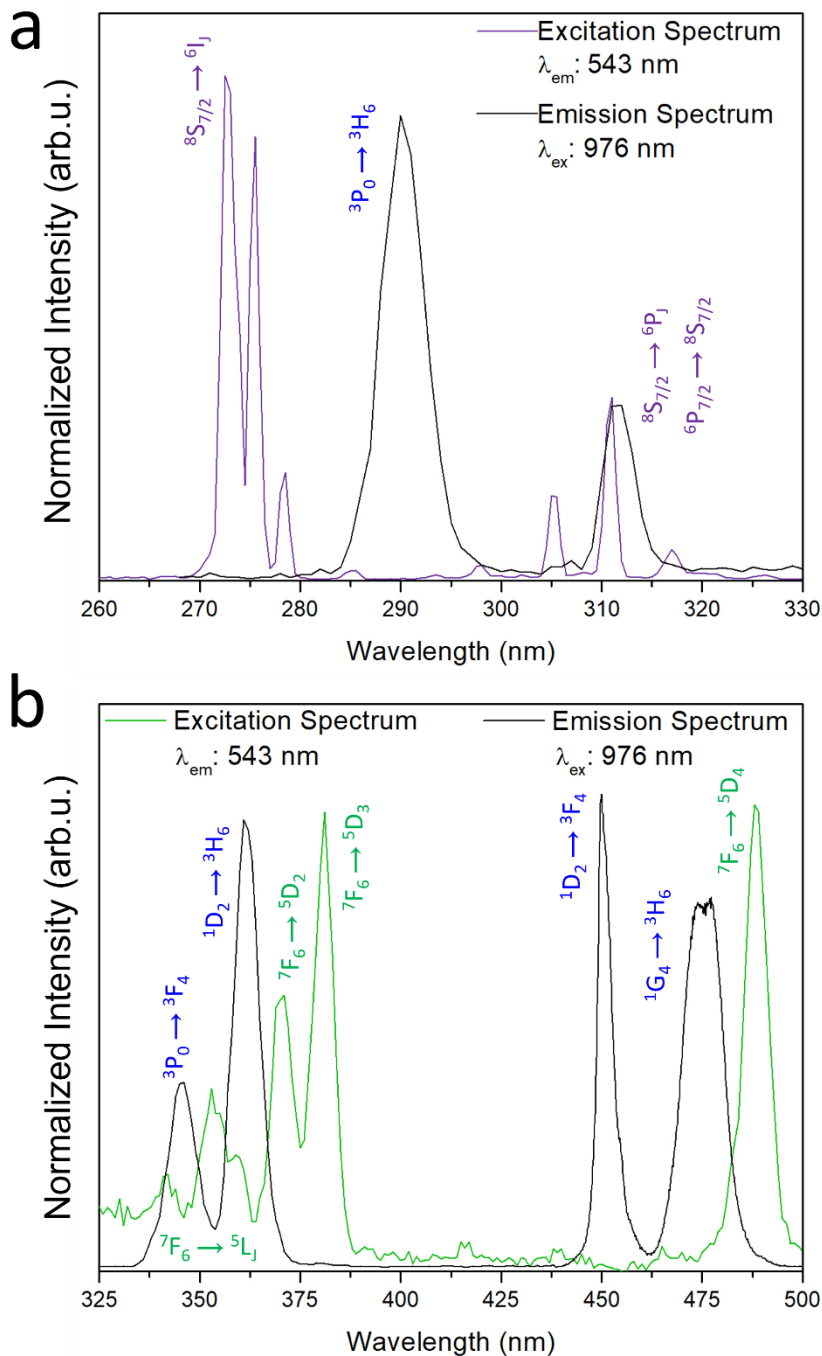


Figure 5.8 Excitation spectra of $\text{NaGdF}_4:49\% \text{Yb}^{3+}, 1\% \text{Tm}^{3+} / \text{NaGdF}_4:20\% \text{Tb}^{3+}$ core/shell nanoparticles ($\lambda_{\text{em}}: 543 \text{ nm}$) overlapping the upconversion emission spectra recorded in Figure 5.7, depicting the excitation bands of (a) Gd^{3+} and (b) Tb^{3+} . Excitation spectra are not intensity calibrated as a function of wavelength.

It is interesting to note that previous reports on this UCNP composition have concluded that the excitation of Tb^{3+} in the shell is facilitated *via* EM from excited Gd^{3+} ions across the core/shell interface.¹⁹³ However, this evidently cannot be the sole population mechanism, since the Gd^{3+} emission at 312 nm is weaker than the observed Tb^{3+} emissions. Instead, it is far more probable that the excitation of Tb^{3+} occurs *via* ET from excited Tm^{3+} ions in the core, as depicted by the Tb^{3+} excitation spectrum presented in **Figure 5.8b**. The excitation bands of Tb^{3+} in the UV spectral region ($^5\text{L}_J, ^5\text{D}_J \leftarrow ^7\text{F}_6$) and between 475 – 500 nm ($^5\text{D}_4 \leftarrow ^7\text{F}_6$) overlap with the emission bands of Tm^{3+} in the UV ($^3\text{P}_0 \rightarrow ^3\text{F}_4, ^1\text{D}_2 \rightarrow ^3\text{H}_6$) and blue ($^1\text{G}_4 \rightarrow ^3\text{H}_6$) spectral regions. When Tm^{3+} and Tb^{3+} were co-doped in the core-only LiYF_4 host, since there was almost complete depopulation of the $^3\text{F}_4$ excited state of Tm^{3+} , ET from these higher energy transitions would not be possible.

In contrast to the previous spectroscopic results in **Figure 5.2**, where Tb^{3+} and Tm^{3+} were distributed throughout the core-only lattice, the spatial separation of Tm^{3+} in the core and Tb^{3+} in the shell facilitates the emissions of both ions. This separation minimizes nonradiative ET from the lower energy excited states of Tm^{3+} , which was observed to quench the entire upconversion process. However, this would also decrease potential nonradiative ET from the higher energy Tm^{3+} excited states. Therefore, the upconversion lifetimes of the Tm^{3+} emissions at 345 ($^3\text{P}_0 \rightarrow ^3\text{F}_4$), 450 ($^1\text{D}_2 \rightarrow ^3\text{F}_4$) and 475 ($^1\text{G}_4 \rightarrow ^3\text{H}_6$) nm were recorded to evaluate the efficiency of nonradiative ET, presented in **Figure 5.9**. The corresponding single exponential decay times are listed in **Table 5.2**, with the change in decay time corresponding to E_{FRET} between Tm^{3+} and Tb^{3+} (as described in Section 1.3). The different integrated intensities from **Figure 5.7** were calculated as well, to evaluate the total energy transfer efficiency (E_{ET}) from Tm^{3+} to Tb^{3+} .

As expected, increasing the Tb^{3+} dopant concentration in the shell results in shorter Tm^{3+} decay times from the $^1\text{D}_2$ and $^1\text{G}_4$ transitions, which is consistent with the observed decrease in upconversion emission intensities. However, the differences in decay time are less than the differences in integrated intensity. This indicates that, while $\text{Tm}^{3+} \rightarrow \text{Tb}^{3+}$ FRET is occurring, radiative ET is more efficient and therefore accounts for a greater percentage of the total sensitization of Tb^{3+} . Similarly, the decay time for the $^3\text{P}_0 \rightarrow ^3\text{F}_4$ transition does not change at all with Tb^{3+} concentration, indicating that any ET from this state is strictly radiative.

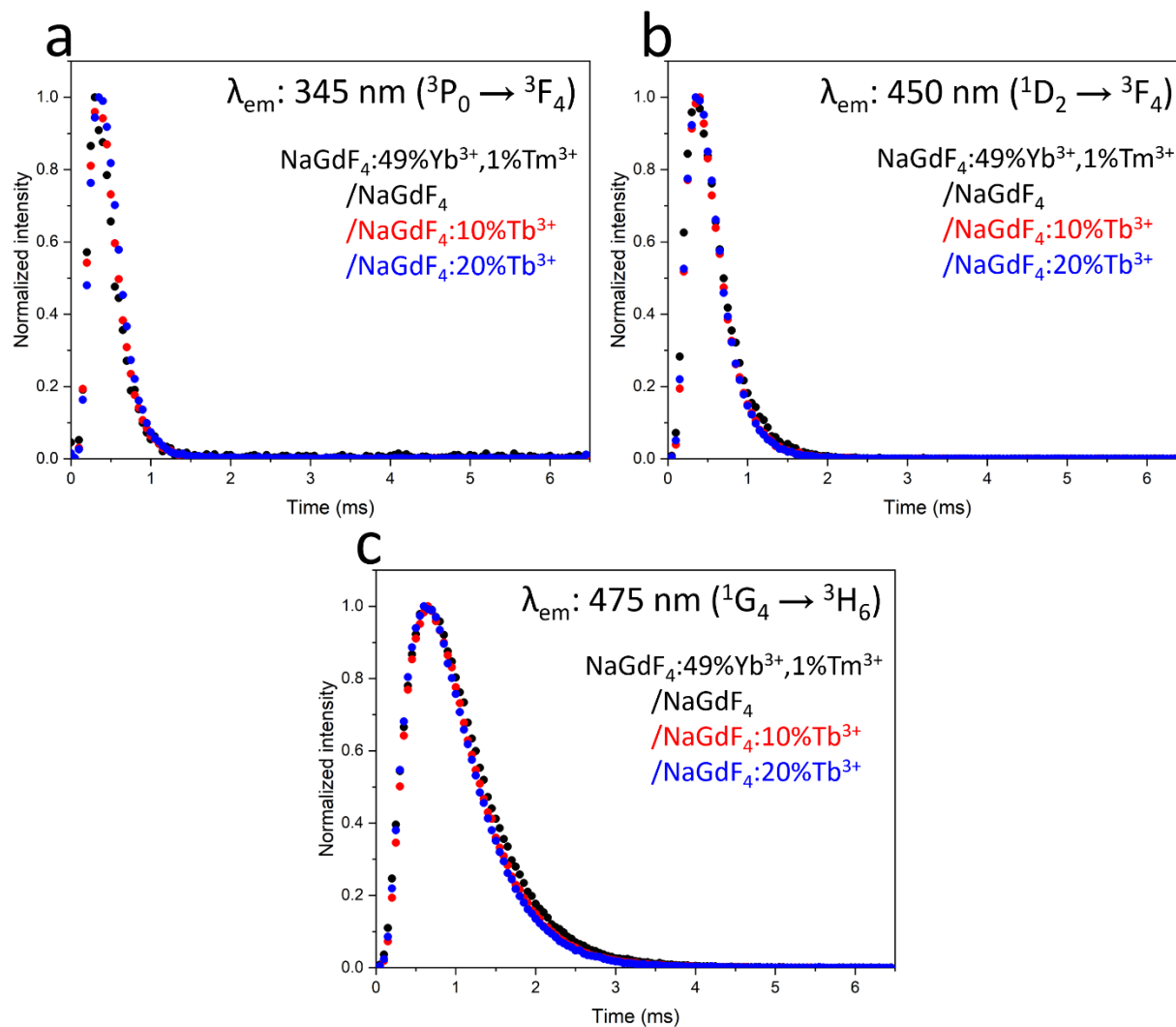


Figure 5.9 Upconversion lifetimes, under pulsed 976 nm excitation, of NaGdF₄:49%Yb³⁺,1%Tm³⁺/NaGdF₄:x%Tb³⁺ core/shell nanoparticles, where x is (■) 0, (■) 10, and (■) 20. Emissions were observed from the (a) ³P₀ → ³F₄, (b) ¹D₂ → ³F₄, and (c) ¹G₄ → ³H₆ transitions of Tm³⁺.

The greatest ET efficiency (both nonradiative and radiative) originates from the Tm³⁺ ¹D₂ → ³H₆ transition of Tm³⁺ at 360 nm, depicted in **Figure 5.10**, which has the greatest spectral overlap with the excitation bands of Tb³⁺. Lesser contributions from the Tm³⁺ ³P₀ and ¹G₄ excited states are observed, consistent with their weaker spectral overlap with Tb³⁺.

Table 5.2 Upconversion decay times and corresponding energy transfer efficiencies derived from Figure 5.7 and Figure 5.9.

		Transition		
		${}^3P_0 \rightarrow {}^3F_4$	${}^1D_2 \rightarrow {}^3F_4$	${}^1G_4 \rightarrow {}^3H_6$
0% Tb³⁺	Decay Time	218 μ s	320 μ s	696 μ s
10% Tb³⁺	E_{ET}	3.2%	32.9%	11.6%
	Decay Time	215 μ s	286 μ s	630 μ s
	E_{FRET}	$1.5 \pm 2.2\%$	$10.8 \pm 1.2\%$	$9.5 \pm 2.0\%$
20% Tb³⁺	E_{ET}	33.7%	55.7%	38.9%
	Decay Time	221 μ s	272 μ s	617 μ s
	E_{FRET}	$-1.3 \pm 2.7\%$	$15.0 \pm 0.9\%$	$11.3 \pm 2.0\%$

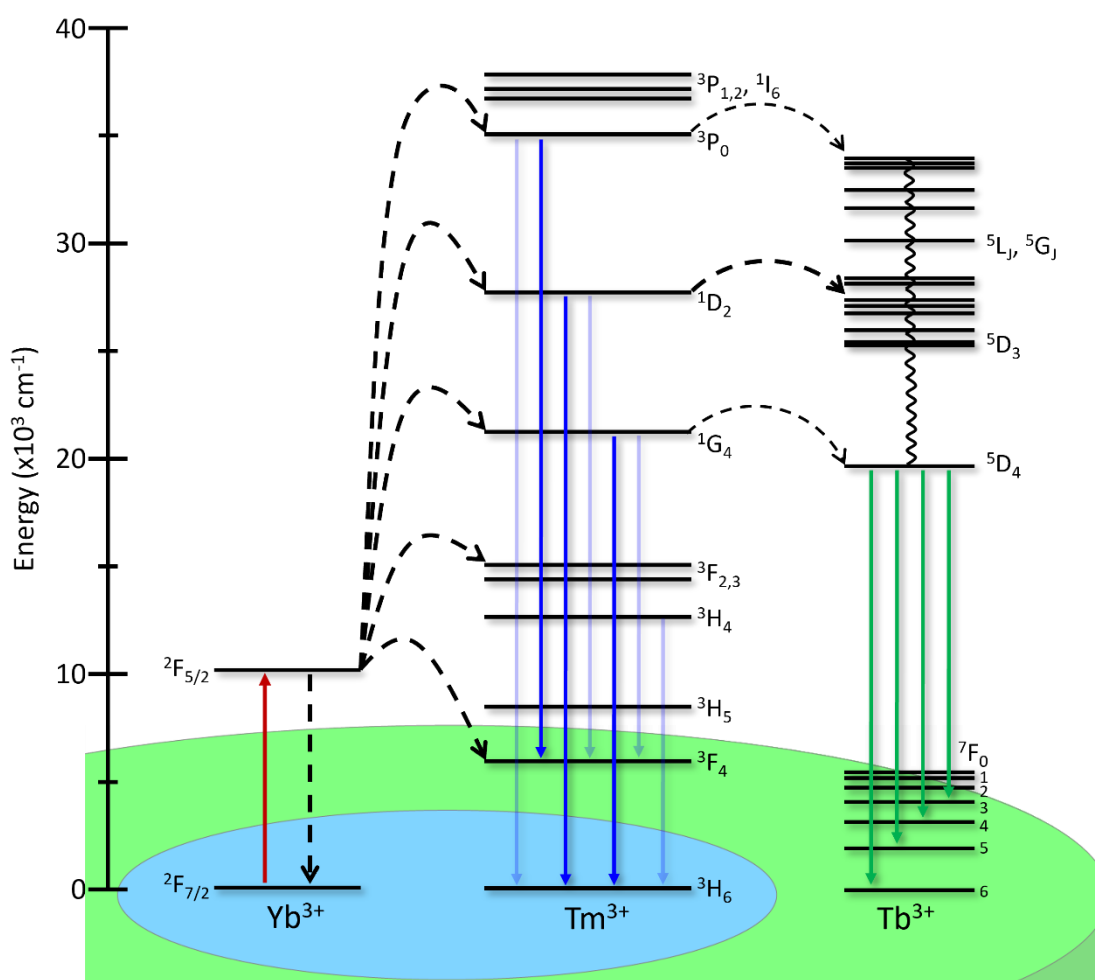


Figure 5.10 Energy level diagram depicting the ET mechanisms from Tm³⁺ to Tb³⁺ across the core/shell interface.

An interesting observation is the decreasing intensity of the 803 nm emission (${}^3\text{H}_4 \rightarrow {}^3\text{H}_6$) with increasing Tb^{3+} concentration. This is inconsistent with the proposed population mechanisms described above. Increasing the Tb^{3+} concentration shortens the ${}^3\text{H}_4$ excited state lifetime as well, as observed in **Figure 5.11a**. These findings could not be due to ET from Tm^{3+} in the ${}^3\text{H}_4$ excited state to Tb^{3+} , as no resonant excited states are present. Instead, it is most likely a shift in the equilibrium of Tm^{3+} excited states that enables this decrease in intensity. As depicted in **Figure 5.11b**, since the ${}^1\text{D}_2$ excited state is depopulated to excite the ${}^5\text{L}_J$ levels of Tb^{3+} , the efficiency of the ${}^1\text{G}_4 + {}^3\text{H}_4 \rightarrow {}^1\text{D}_2 + {}^3\text{F}_4$ CR mechanism (CR8 from Chapter 4), which populates the ${}^1\text{D}_2$ excited state, increases as compensation.¹⁴⁵ Furthermore, a depopulation of the ${}^1\text{D}_2$ state *via* ET to Tb^{3+} also prevents the CR mechanism: ${}^1\text{D}_2 + {}^3\text{H}_6 \rightarrow {}^3\text{H}_4 + {}^3\text{F}_3$ (CR10 from Chapter 4), which would populate the ${}^3\text{H}_4$ excited state at the expense of the ${}^1\text{D}_2$ excited state.¹⁶² A decrease in efficiency of this mechanism inadvertently decreases the population of the ${}^3\text{H}_4$ state, thus quenching the emission at 803 nm.

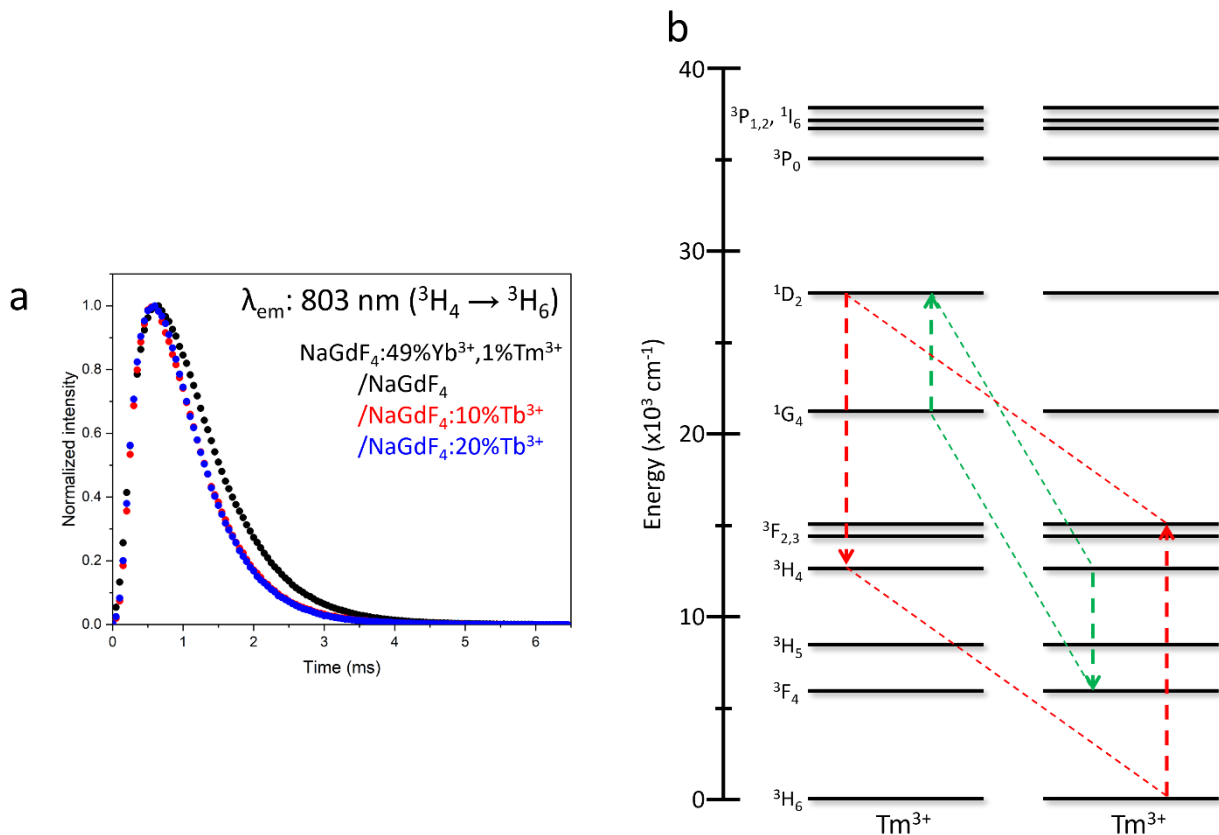


Figure 5.11 (a) Upconversion luminescence lifetime of the ${}^3\text{H}_4 \rightarrow {}^3\text{H}_6$ transition of Tm^{3+} , under pulsed 976 nm excitation, of NaGdF₄:49%Yb³⁺,1%Tm³⁺/NaGdF₄:x%Tb³⁺ core/shell nanoparticles, where x is (■) 0, (■) 10, and (■) 20. (b) Energy level diagram depicting the indirect depopulation of the ${}^3\text{H}_4$ state of Tm^{3+} through CR mechanisms influenced by ET to Tb^{3+} .

As a final consideration, cooperative sensitization may also contribute to the emissions from Tb^{3+} under NIR irradiation, as was observed in $\text{LiYF}_4:\text{Yb}^{3+},\text{Tb}^{3+}$ UCNPs in **Figure 5.2**. However, when Tm^{3+} is omitted from the NaGdF_4 core composition, no upconversion luminescence was observed, as shown in **Figure 5.12**. This excludes the potential cooperative sensitization mechanism and reinforces the observed radiative and nonradiative $\text{Tm}^{3+} \rightarrow \text{Tb}^{3+}$ ET as the principal sensitization mechanisms, predominantly through the $^1\text{D}_2$ excited state.

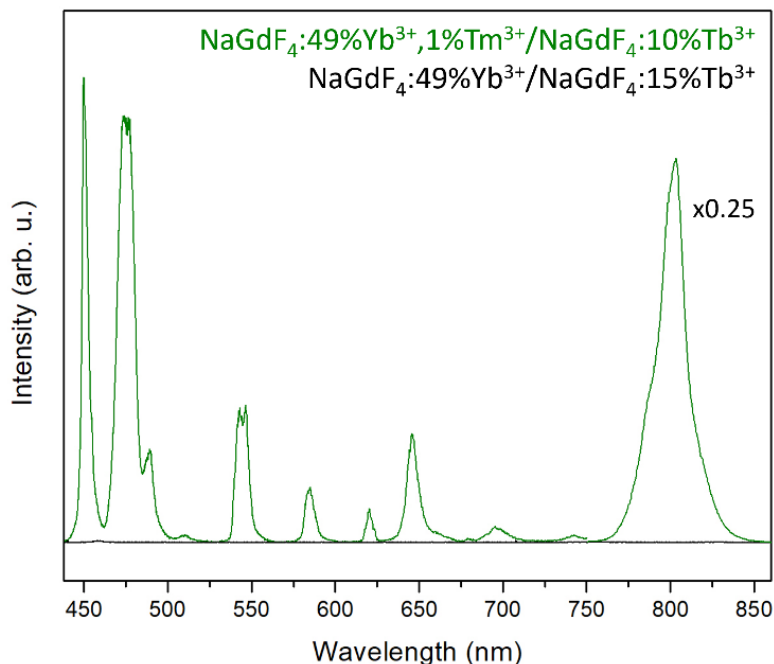


Figure 5.12 Upconversion luminescence spectra, under 976 nm excitation, of core/shell nanoparticles comprising (■) $\text{NaGdF}_4:49\%\text{Yb}^{3+},1\%\text{Tm}^{3+}/\text{NaGdF}_4:10\%\text{Tb}^{3+}$ and (■) $\text{NaGdF}_4:49\%\text{Yb}^{3+}/\text{NaGdF}_4:15\%\text{Tb}^{3+}$.

5.2. Proof-of-Concept: Time-Resolved Color Tuning for Particle Velocimetry

Since the blue Tm^{3+} emissions at 450 and 475 nm are not fully quenched when sensitizing Tb^{3+} , both the blue emissions of Tm^{3+} and the green Tb^{3+} emissions are present under 976 nm excitation. With simultaneous emissions in the blue and green spectral regions, there are many possible applications that can benefit from multiplexed luminescence. An advantageous property of these ions is their substantially different excited state lifetimes. As observed in **Figure 5.13a**, the decay time of the Tm^{3+} emission at 450 nm is in the hundreds of microseconds, while the emission from Tb^{3+} at 543 nm is in the milliseconds. This is facilitated primarily by the longer

intrinsic excited state lifetime of Tb^{3+} , which separates the observed luminescence lifetimes by over one order of magnitude.^{145,194} Moreover, by isolating the Tb^{3+} in the shell of the synthesized UCNPs and restricting its sensitization to mostly radiative ET from Tm^{3+} , the Tm^{3+} emissions are allowed to fully decay radiatively, which indirectly further prolongs the observed lifetimes of Tb^{3+} . This allows for temporal separation of the two emission colors during pulsed NIR excitation, which can be observed individually when gating the signal acquisition. The photographs in **Figure 5.13b** and the time-resolved emission spectra in **Figure 5.13c** enable the visualization of this phenomenon, where the samples appear blue during irradiation, and slowly change to green when the excitation source has ceased, since the Tm^{3+} emissions decay long before Tb^{3+} emissions.

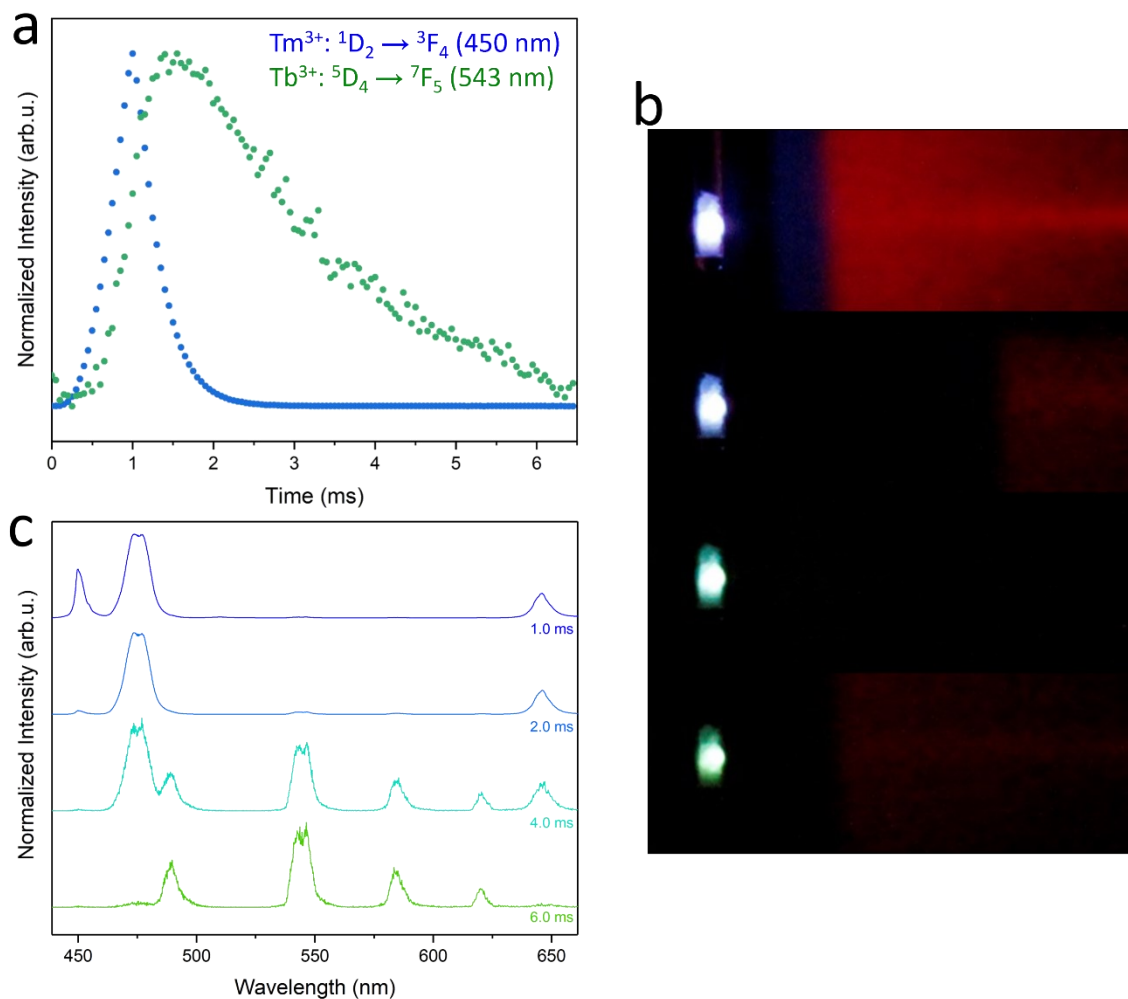


Figure 5.13 (a) Upconversion luminescence lifetimes of the Tm^{3+} and Tb^{3+} emissions at 450 and 543 nm, respectively, (b) digital photographs, and (c) normalized time-resolved emission spectra of core/shell $\text{NaGdF}_4:49\%\text{Yb}^{3+},1\%\text{Tm}^{3+}/\text{NaGdF}_4:20\%\text{Tb}^{3+}$ UCNPs under pulsed 976 nm excitation.

A practical application of these UCNPs is in particle velocimetry, which measures the velocity of particles suspended in a flowing dispersion as a means of measuring the velocity of the fluid itself. A traditional particle velocimetry technique is particle imaging velocimetry (PIV), which takes images of luminescent particles under double-pulsed excitation, where the time between pulses and travelled distance of individual particles is correlated to a velocity.¹⁹⁵ The limitations to this technique include the necessity for dilute samples, high-speed imaging and modeling algorithms. More recently, ratiometric emissions from UCNPs have been explored, where different velocities expose the nanoparticles to different excitation times, thus changing their relative intensity.¹⁹⁶ However, these methods require external calibration, which is most often impractical when replicating the experimental conditions.

By exploiting UCNPs with an internal calibration that can be imaged using traditional photography, particle velocimetry could be achieved without the limitations present in the more conventional approaches. To demonstrate this, the $\text{NaGdF}_4:49\% \text{Yb}^{3+}, 1\% \text{Tm}^{3+} / \text{NaGdF}_4:20\% \text{Tb}^{3+}$ UCNPs were dispersed in toluene, and the solution was flowed through microcapillaries of varying internal diameters and flow rates, to explore the versatility of the technique.¹⁹⁷ The 976 nm laser is positioned such that the UCNPs are excited upon entering the viewing window. They then continue through the remainder of the capillary as their luminescence intensity decays, shown in the photographs in **Figure 5.14a**.

The expected parabolic emission profile is characteristic of laminar flow, which is necessary for accurate solution velocity measurements.¹⁹⁸ The emission intensity profile can then be quantified as a function of distance, as presented in **Figure 5.14b**, and correlated to the lifetime profile presented in **Figure 5.13a**, to determine the velocity of the solution.

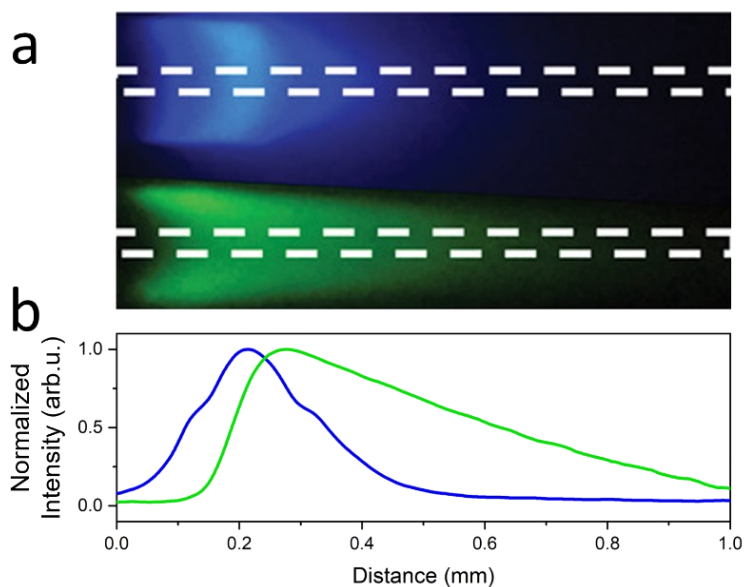


Figure 5.14 (a) Digital photographs and (b) intensity profiles in a rectangular area of flowing UCNPs in a microcapillary, obtained using a blue and green bandpass filter.

As discussed in Section 4.4, when the excitation pulse width is varied, the lifetime profiles of lanthanide excited state emissions change as well. This is true for both Tm^{3+} and Tb^{3+} , as observed in **Figure 5.15**, where a longer pulse width results in a shorter luminescence decay time. This is problematic for the velocimetry measurements since a change in solution velocity will change how long the UCNPs remain within the laser beam path. For example, if the flow velocity through a microcapillary is slower, the nanoparticles passing through the beam path will remain within it for longer, effectively increasing the “pulse width”. With a longer pulse width, the lifetime profile will shorten, and the experimental flow velocity will appear faster than the actual flow velocity. This discrepancy between the experimental and theoretical particle velocities would need to be accounted for using an external control, thus minimizing its potential use as compared to ratiometric techniques.

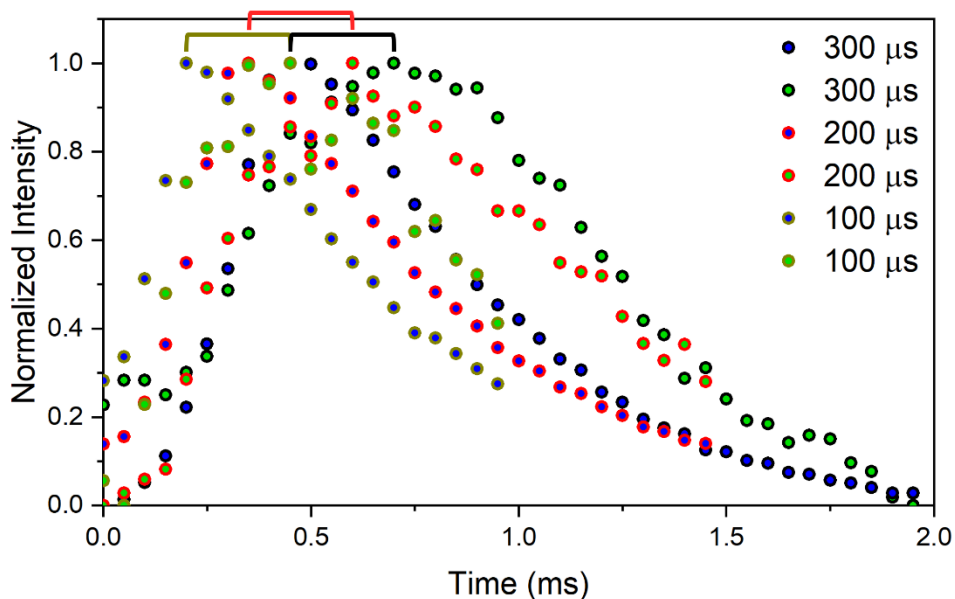


Figure 5.15 Upconversion luminescence lifetimes of the (■) Tm^{3+} emission at 450 nm and the (■) Tb^{3+} emission at 543 nm of $\text{NaGdF}_4:49\%\text{Yb}^{3+}, 1\%\text{Tm}^{3+}/\text{NaGdF}_4:20\%\text{Tb}^{3+}$ core/shell UCNPs, under 976 nm excitation pulse widths of (■) 100, (■) 200, and (■) 300 μs . Brackets above each lifetime profile depict the same $252 \pm 10 \mu\text{s}$ time delay between maxima.

Instead of correlating the entire emission profiles as a function of distance and time, where this source of variability would need to be accounted for, the maxima can be exploited instead. Since the sensitization of Tb^{3+} is almost exclusively through ET from Tm^{3+} , the changing excitation pulse width will affect Tb^{3+} and Tm^{3+} equally. Therefore, the emission maxima of Tb^{3+} always occurs with a constant delay after the emission maxima of Tm^{3+} , regardless of decay time

and pulse width. As expected, this is observed in **Figure 5.15**, where a time difference of $252 \pm 10 \mu\text{s}$ is always present between the maximum intensity of the Tm^{3+} blue and Tb^{3+} green emissions, for all excitation pulse widths.

With this known time difference between the Tm^{3+} and Tb^{3+} emission maxima, measuring the particle velocity could be achieved. Photographs of the UCNPs flowing through capillaries with an internal diameter of 75, 100, and 150 μm were recorded at different flow rates, shown in **Figure 5.16a**. These images were processed through ImageJ to determine which pixels are the brightest for the blue emission of Tm^{3+} and the green emission of Tb^{3+} , and the distance between them was calculated. Since this distance corresponds to a time interval of $252 \pm 10 \mu\text{s}$, a velocity was obtained and plotted in **Figure 5.16b**. The minimum flow rate was chosen such that the distance between the maximum blue and green emissions were well-resolved (meaning they do not occur on the same pixel), while the maximum flow rate was the fastest the UCNPs could travel through the capillary while still possessing a sufficient signal-to-noise ratio that could be imaged (meaning the luminescence was not too dim). The theoretical velocities were then calculated using Equation 5.1:¹⁹⁸

$$v_p(x, 0) = u(x, 0) = 2\langle u_{avg} \rangle = 2Q/A \quad (5.1)$$

when $x \gg x_E$

Where v_p is the particle velocity and u is the axial fluid velocity. When the solution follows conventional laminar flow and the particles are flowing at the same velocity as the solvent (meaning there are minimal drag forces), this can be approximated as twice the average axial velocity (u_{avg}), which is calculated using the known flow rate (Q) and capillary cross-section area (A).

The measured particle velocities range between 30 and 500 mm/s, depending on the capillary diameter and flow rate input, with deviations from the theoretical values that average between 3.25% and 5.61%. These results indicate a very promising alternative velocimetry technique, as the experimental flow velocities match the theoretically calculated values with high precision and minimal errors. Since this technique can be imaged using a standard digital camera and does not require external calibration, the results herein demonstrate a method that is more easily achievable, cost-effective, and user-friendly in both an academic and industrial setting.

While knowledge of the nanoparticle composition and dynamics is required ahead of time, they are expected to be consistent across batches of synthesized UCNPs.

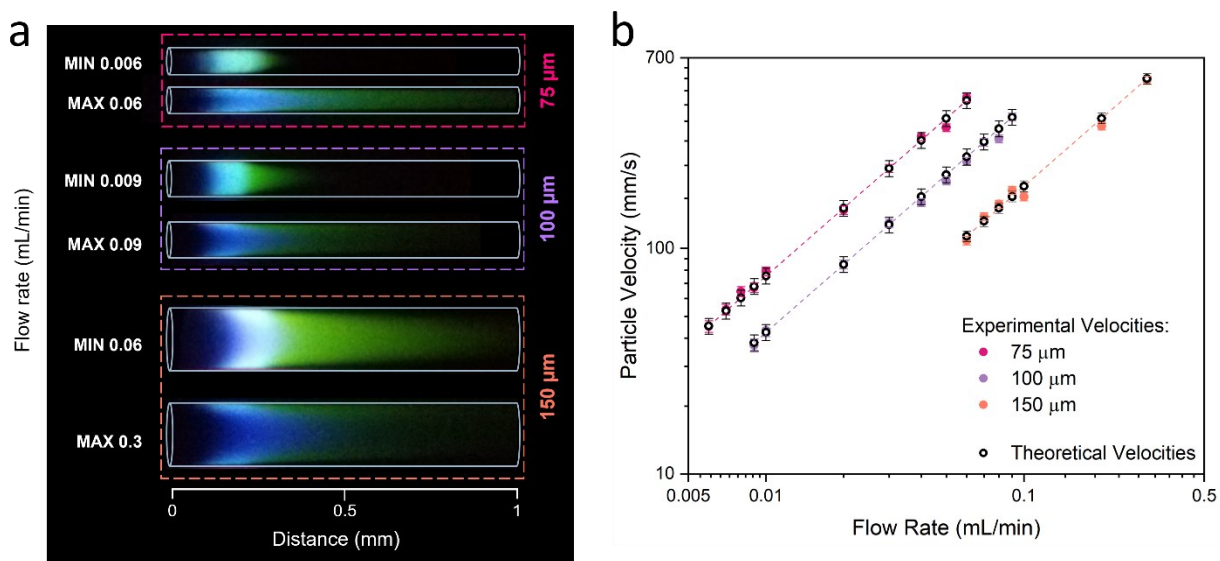


Figure 5.16 (a) Digital photographs of $\text{NaGdF}_4:49\% \text{Yb}^{3+}, 1\% \text{Tm}^{3+} / \text{NaGdF}_4:20\% \text{Tb}^{3+}$ core/shell UCNPs in toluene, flowing through microcapillaries of varying internal diameters and flow rates. (b) Experimental particle velocities, compared to the theoretical values calculated using Equation 5.1 and the known flow rate.

Chapter 6. Er³⁺-doped and Ho³⁺-doped Upconverting Nanoparticles

UCNPs doped with Er³⁺ or Ho³⁺, when co-doped with Yb³⁺ as a sensitizer, have characteristic green and red emissions under 976 nm irradiation.¹⁹⁹ While the ETU process is similar between the two systems (recall **Figure 2.1** and **2.2**), it is well known that the upconversion efficiency of Ho³⁺ is considerably lower than Er³⁺. This has been partially explained by greater phonon relaxation of the emitting levels of Ho³⁺, since the lower lying levels are closer in energy than in Er³⁺.²⁰⁰ However, with the perception that Ho³⁺ is simply a weaker version of Er³⁺, little to no effort has been made to further understand its limitations or possible uses.

6.1. Spectroscopy of Yb³⁺,Er³⁺ and Yb³⁺,Ho³⁺ Co-doped LiYF₄ UCNPs

To evaluate the differences in spectroscopic properties of Er³⁺ and Ho³⁺, LiYF₄ nanoparticles were synthesized, with Yb³⁺ as the sensitizer.²⁰¹ Firstly, LiYF₄:Yb³⁺,Er³⁺ UCNPs were synthesized with varying sensitizer concentration. Since previous findings established 25% Yb³⁺ to be optimal in LiYF₄, while studies on Er³⁺-doped NaREF₄ UCNPs tend to use 18-20% Yb³⁺, nanoparticles with both sensitizer dopant concentrations were synthesized, with a constant 2% Er³⁺.^{125,202} The TEM micrographs are shown in **Figure 6.1**, indicating that a higher Yb³⁺ dopant concentration results in slightly smaller nanoparticles. This is likely a consequence of the smaller Yb³⁺ ionic radius, relative to Y³⁺, which shortens the LiREF₄ unit cell parameters with increasing concentration, in turn shortening the dimensions of the synthesized nanoparticles.²⁰³

Under 976 nm excitation, the characteristic Er³⁺ bands are present at 525, 550, and 650 nm, from the ²H_{11/2} → ⁴I_{15/2}, ⁴S_{3/2} → ⁴I_{15/2}, ⁴F_{9/2} → ⁴I_{15/2} transitions, respectively, as shown in **Figure 6.2a**. Despite the previous findings that concluded 25% Yb³⁺ enhanced the upconversion process in LiYF₄:Yb³⁺,Tm³⁺ UCNPs, this was not the case when Er³⁺ is the activator. Rather, the nanoparticle composition with an Yb³⁺ concentration of 18% was brighter for all emission wavelengths. Increasing the sensitizer concentration to 25% likely increased back-transfer from Er³⁺ to Yb³⁺, in turn quenching the Er³⁺ emissions.²⁰⁴ Since the resonance between the excited states of Er³⁺ and Yb³⁺ is greater than the resonance between the states of Tm³⁺ and Yb³⁺, such back-transfer mechanisms are not as likely with Tm³⁺ as an activator.

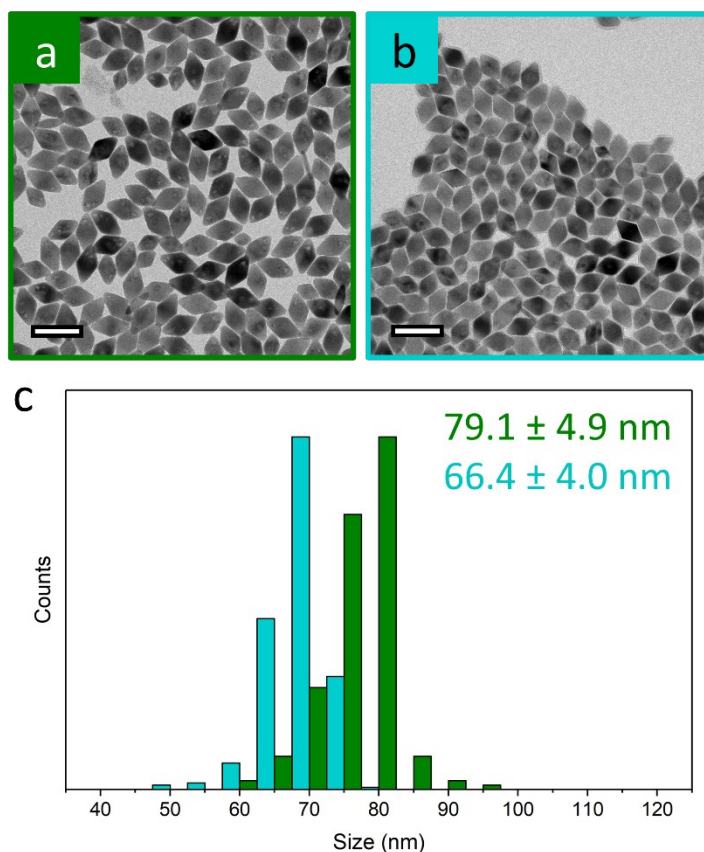


Figure 6.1 TEM micrographs of (a, ■) $\text{LiYF}_4:18\%\text{Yb}^{3+},2\%\text{Er}^{3+}$ and (b, ■) $\text{LiYF}_4:25\%\text{Yb}^{3+},2\%\text{Er}^{3+}$ UCNPs, with (c) their corresponding particle size distributions. Scale bars are set to 100 nm. Adapted with permission from Reference 201. Copyright 2023 American Chemical Society.

Interestingly, the emission intensity of the ${}^4\text{S}_{3/2} \rightarrow {}^4\text{I}_{15/2}$ transition at 550 nm quenches by about 70% with increasing sensitizer concentration, whereas the other upconverted emissions only dim by about 40%. This is in agreement with a previously reported back-transfer mechanism: $\text{Er}^{3+}:{}^4\text{S}_{3/2} + \text{Yb}^{3+}:{}^2\text{F}_{7/2} \rightarrow \text{Er}^{3+}:{}^4\text{I}_{13/2} + \text{Yb}^{3+}:{}^2\text{F}_{5/2}$, which increases in probability with increasing Yb^{3+} concentration, resulting in increased nonradiative depopulation of the ${}^4\text{S}_{3/2}$ excited state.²⁰⁴ The upconversion decay time of the 550 nm emission, shown in **Figure 6.2b**, shortens by about 46%, corroborating this increase in nonradiative ET from Er^{3+} to Yb^{3+} .

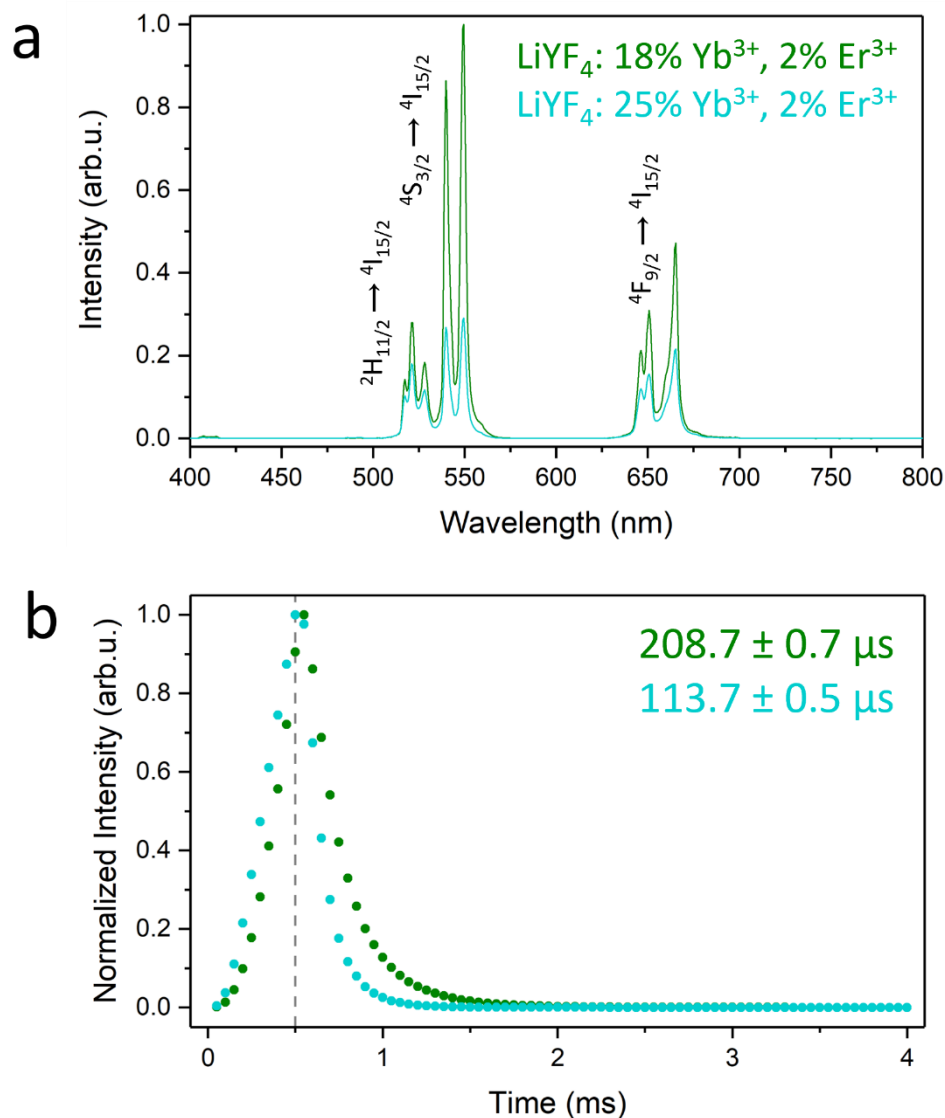


Figure 6.2 (a) Upconversion emission spectra under continuous wave 976 nm excitation, and (b) luminescence lifetimes under pulsed 976 nm excitation, of (■) LiYF₄:18%Yb³⁺,2%Er³⁺ and (■) LiYF₄:25%Yb³⁺,2%Er³⁺ UCNPs. Adapted with permission from Reference 201. Copyright 2023 American Chemical Society.

In a similar investigation to that of Section 4.1, the effect of decreasing the Ho³⁺ activator concentration below the established 1 mol% was studied.²⁰⁵ TEM micrographs of the synthesized nanoparticles are presented in **Figure 6.3a-c**, showing a similar size distribution (**Figure 6.3d**) for samples doped with 0.25, 0.5, and 1%Ho³⁺. From the upconversion emission spectra shown in **Figure 6.4a**, decreasing the activator concentration only has adverse effects on the intensity of the $^5F_4 \rightarrow ^5I_8$, $^5S_2 \rightarrow ^5I_8$, and $^5F_5 \rightarrow ^5I_8$ radiative transitions at 535, 540, and 650 nm, respectively. The upconversion lifetimes were recorded as well, shown in **Figure 6.4b**, indicating that the brightest

$\text{LiYF}_4:20\%\text{Yb}^{3+},1\%\text{Ho}^{3+}$ UCNPs also has the fastest excited state decay time. This indicates that, as expected, decreasing the Ho^{3+} concentration decreases the probability for nonradiative concentration quenching mechanisms by increasing the spacing between dopant ions. However, doing so also decreases the number of activator ions, which ultimately decreases the upconversion luminescence intensities despite slightly increased concentration quenching.

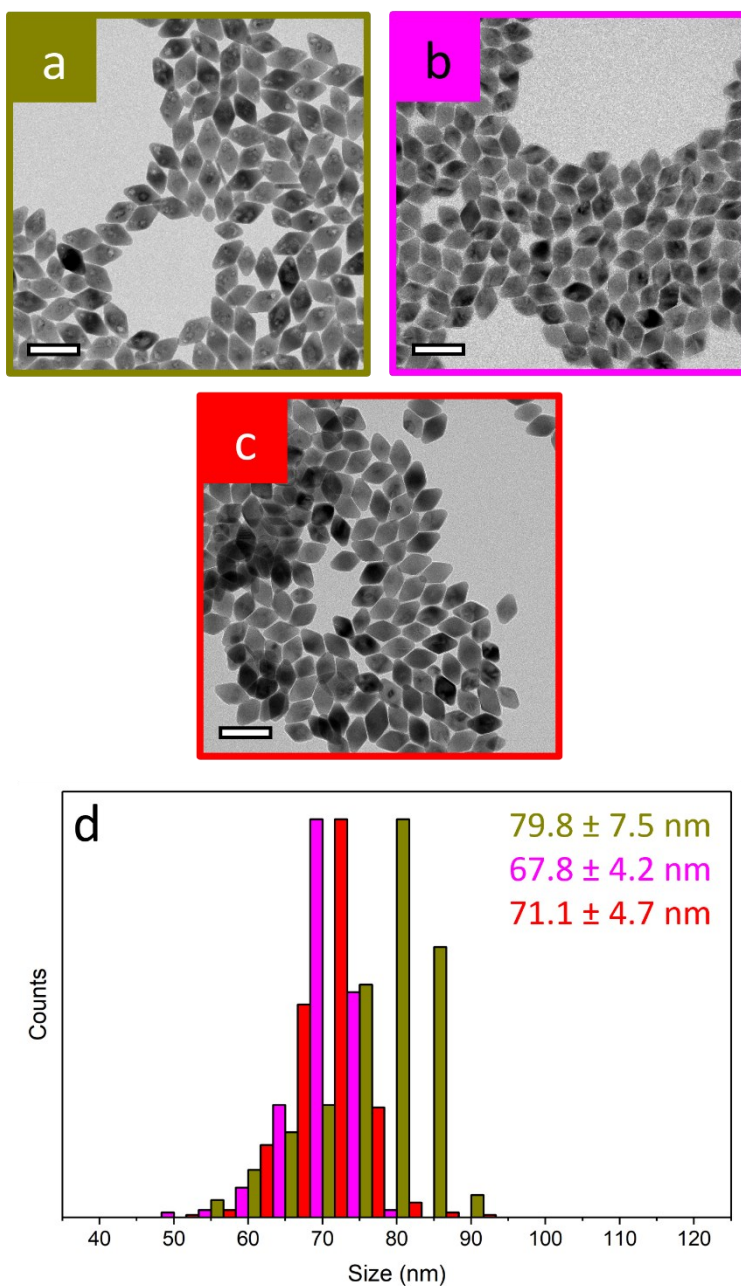


Figure 6.3 TEM micrographs of $\text{LiYF}_4:20\%\text{Yb}^{3+},x\%\text{Ho}^{3+}$ UCNPs, where x is (a, \blacksquare) 1, (b, \blacksquare) 0.5, and (c, \blacksquare) 0.25, with their (d) corresponding particle size distributions. TEM scale bars are set to 100 nm. Adapted with permission from Reference 201. Copyright 2023 American Chemical Society.

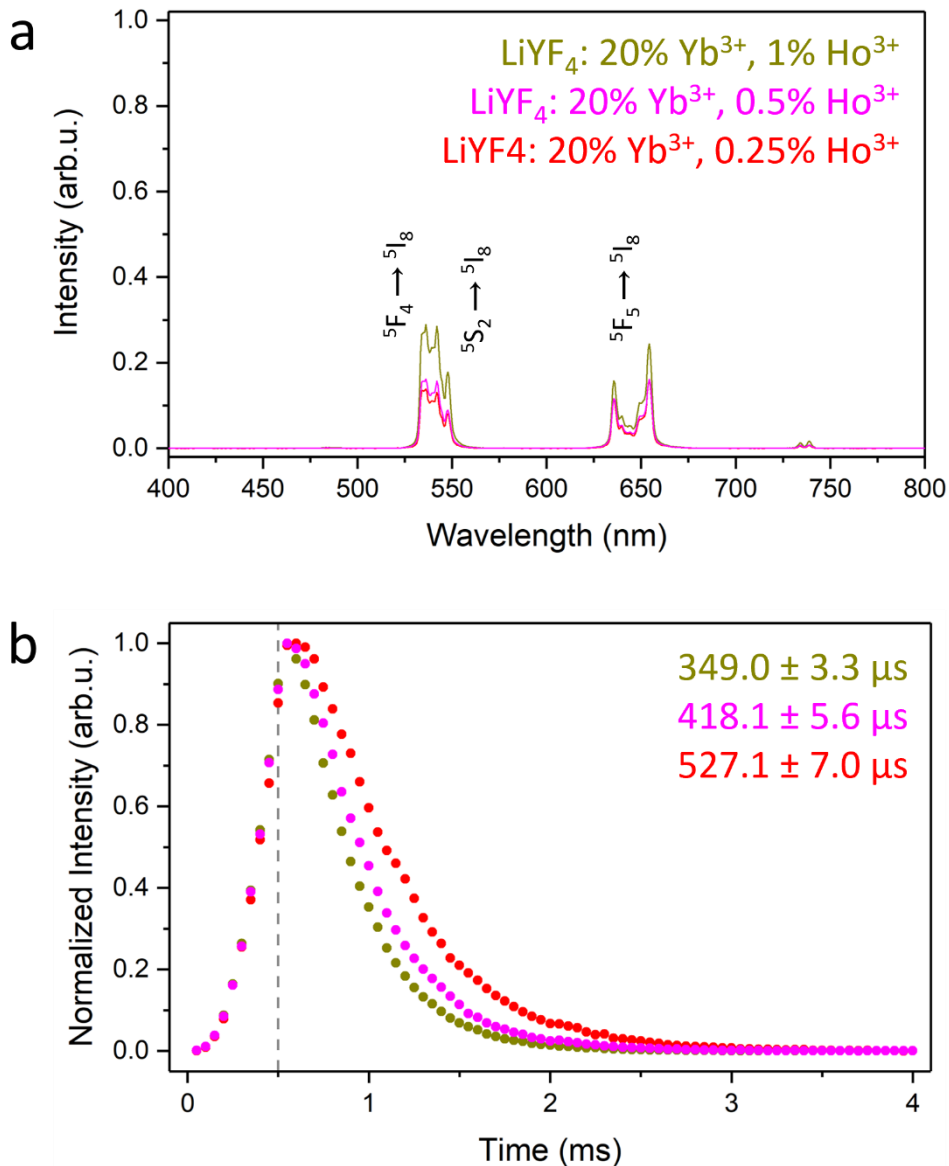


Figure 6.4 (a) Upconversion emission spectra under continuous wave 976 nm excitation, and (b) luminescence lifetimes under pulsed 976 nm excitation. Emission spectra in (a) are normalized to the intensity in Figure 6.2a. Adapted with permission from Reference 201. Copyright 2023 American Chemical Society.

When comparing the brightest LiYF₄:18%Yb³⁺,2%Er³⁺ and LiYF₄:20%Yb³⁺,1%Ho³⁺ UCNP compositions, the Er³⁺ emitting nanoparticles are about three times brighter. Previous investigations into the intrinsic properties of these ions (in LaF₃) conclude that all the emitting transitions of Ho³⁺ have higher transition probabilities than Er³⁺, as reported in **Table 6.1**.^{206,207} This means that the weaker Ho³⁺ emissions originate from inefficient ETU populating the excited states, rather than a quenching of the excited states. This is likely due to slightly less resonance between the excited states of Ho³⁺ and Yb³⁺, as compared to Yb³⁺ and Er³⁺. Moreover, since ETU

in Yb³⁺,Er³⁺ co-doped UCNPs is more efficient, more activator ions can be doped into the nanoparticles, which then facilitates greater CR or EM mechanisms and in turn shortens the experimentally observed lifetime of Er³⁺, relative to Ho³⁺, despite the higher transition probabilities.²⁰⁸

Table 6.1 Transition probabilities of Er³⁺ and Ho³⁺, reported in LaF₃ from Reference 206 and 207.

Er ³⁺		Ho ³⁺	
Transition	Probability (s ⁻¹)	Transition	Probability (s ⁻¹)
² H _{11/2} → ⁴ I _{15/2} (525 nm)	1220	⁵ F ₄ → ⁵ I ₈ (535 nm)	2310
⁴ S _{3/2} → ⁴ I _{15/2} (550 nm)	662	⁵ S ₂ → ⁵ I ₈ (540 nm)	1210
⁴ F _{9/2} → ⁴ I _{15/2} (650 nm)	468	⁵ F ₅ → ⁵ I ₈ (650 nm)	1280

6.2. Proof-of-Concept: Covert Information Storage Using Time-Resolved

Imaging

Since the turn of the millennium, the ubiquity of digital media has made security technologies increasingly important, and there has become a major need for developing strategies to encode complex information in a secure manner. Printing information that only the intended end-user is capable of processing is pivotal to the manufacturing and distribution of goods, products, and documentation. As a means of encoding such information, the use of UCNPs in printed information storage devices has been studied since 2012, generating QR codes or other printed patterns that can only be observed under NIR irradiation.¹¹⁴ As the technology has developed, printing multiple overlapping patterns using UCNPs with different emission wavelengths has allowed for more complex information storage with inherent anti-counterfeiting capabilities.^{116,209} With overlapping luminescent patterns, a bandpass filter is required to isolate one set of information from the rest, providing an internal encryption method. However, since bandpass filters are readily available, more complicated methods are needed to further secure the stored information.

Taking advantage of the temporal domain using lanthanide-doped nanoparticles can improve the covert nature of printed information by complicating the detection methodology.²¹⁰

By exploiting different UCNP compositions that emit at the same wavelengths but with different excited state lifetimes, the printed information can be covered and only detected under pulsed excitation. This can be achieved by printing the “pattern” with a nanoparticle composition that emits for longer, and “masking” it with a faster-emitting composition at the same wavelength. Only once the excitation source has ceased and the luminescence from the mask has fully decayed can the pattern be imaged. Moreover, since the emissions from both the pattern and mask fully decay within milliseconds, which is beyond what is observable by the naked eye, only with prior knowledge of the compositions and their decay times can the information be decrypted and interpreted.²¹¹

6.2.1. Photoluminescent Nanoparticles

To establish the capabilities of this technique, nanoparticle compositions that can emit under direct UV excitation were studied first, with an order of magnitude between the luminescence decay times of the pattern and mask. Eu^{3+} is one of the most commonly used luminescent lanthanide ions, owing to its efficient red emission bands that are exploited in various industries.²² These bands are also characterized by relatively long decay times, sometimes exceeding several milliseconds, due to the large energy gap between the emitting $^5\text{D}_0$ state and the lower energy $^7\text{F}_J$ states, as depicted in **Figure 6.5**. Therefore, $\text{LiYF}_4:20\%\text{Eu}^{3+}$ photoluminescent nanoparticles were synthesized to print the pattern.

CsMnCl_3 perovskite nanoparticles were synthesized to print the mask, owing to their characteristic band gap emission centered at 650 nm that decays in the hundreds of microseconds.²¹² A difference of one order of magnitude between the emission decay times of the pattern and mask is sufficient to allow clear imaging of the Eu^{3+} luminescence once the emission from the perovskite composition has decayed, using a conventional digital camera. TEM micrographs of both compositions are shown in **Figure 6.6a** and **b**, depicting the expected square bipyramidal and hexagonal-like morphologies for the $\text{LiYF}_4:20\%\text{Eu}^{3+}$ and CsMnCl_3 nanoparticle compositions, respectively. The PXRD diffractograms were recorded as well, shown in **Figure 6.6c** and **d**, confirming the tetragonal and trigonal crystal phases, respectively.

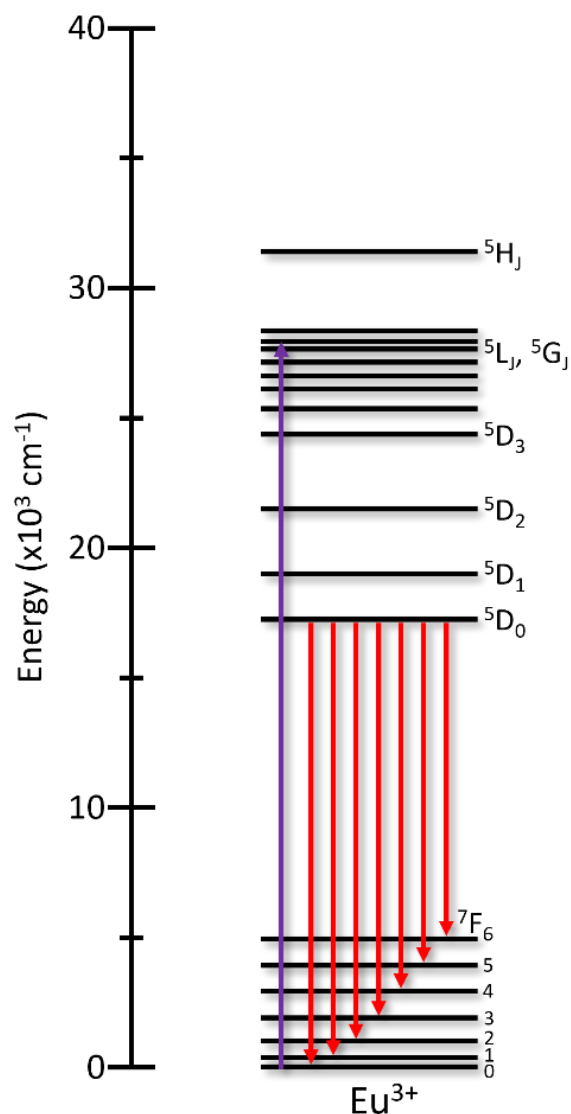


Figure 6.5 Eu³⁺ energy level diagram.

Under direct 355 nm irradiation, the expected Eu³⁺ emission bands from the ${}^5D_0 \rightarrow {}^7F_{1-4}$ transitions were observed, as shown in **Figure 6.7a**, spanning 575 – 700 nm. These emissions are completely overlapped by the broad emission band from the CsMnCl₃ nanoparticles, which spans 550 to 800 nm. As observed under pulsed excitation, the Eu³⁺ emissions have a decay time of almost 10 ms, while the perovskite emissions decay in approximately 100 μ s, as plotted in **Figure 6.7b**. Surprisingly, there appears to be a slight delay in the Eu³⁺ emissions, as shown in the time-resolved spectra in **Figure 6.7c**, which is unusual for direct photoluminescence. Typically, direct excitation of the higher excited states of an activator ion would not result in a rise time, since the

emitting level is populated almost instantaneously. However, since 355 nm excitation populates the higher energy 5L_1 levels, which requires many internal conversion steps *via* phonon relaxations to populate the emitting 5D_0 level of Eu^{3+} , this slight delay is observed. While not expected, this improves the separation in lifetime between the prospective pattern and mask when printing these nanoparticle compositions.

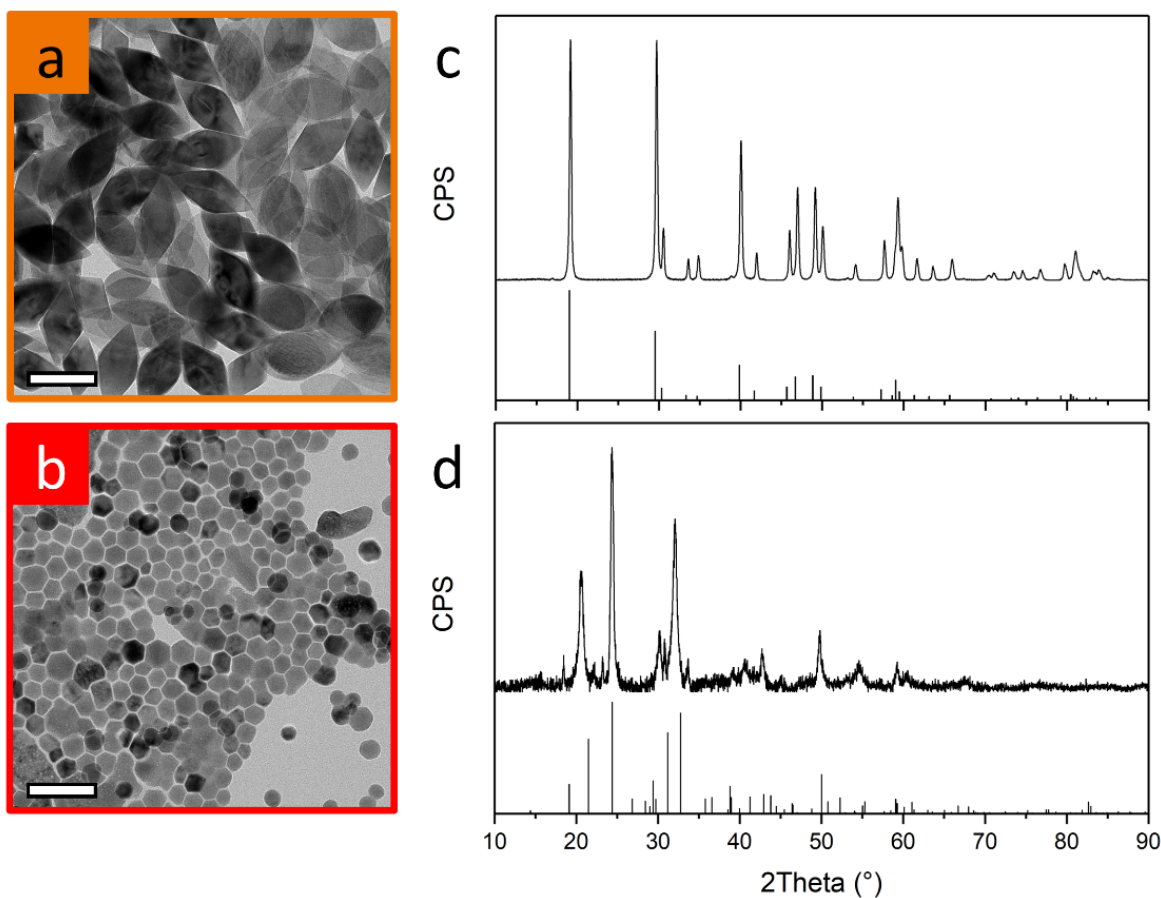


Figure 6.6 (a,b) TEM micrographs and (c,d) PXRD diffractograms of (a,c, ■) $\text{LiYF}_4:20\%\text{Eu}^{3+}$ and (b,d, ■) CsMnCl_3 photoluminescent nanoparticles. Diffractograms are compared to reference patterns for LiYF_4 (PDF#077-0816) and CsMnCl_3 (PDF#070-1324). Scale bars are set to 100 nm. Adapted with permission from Reference 201. Copyright 2023 American Chemical Society.

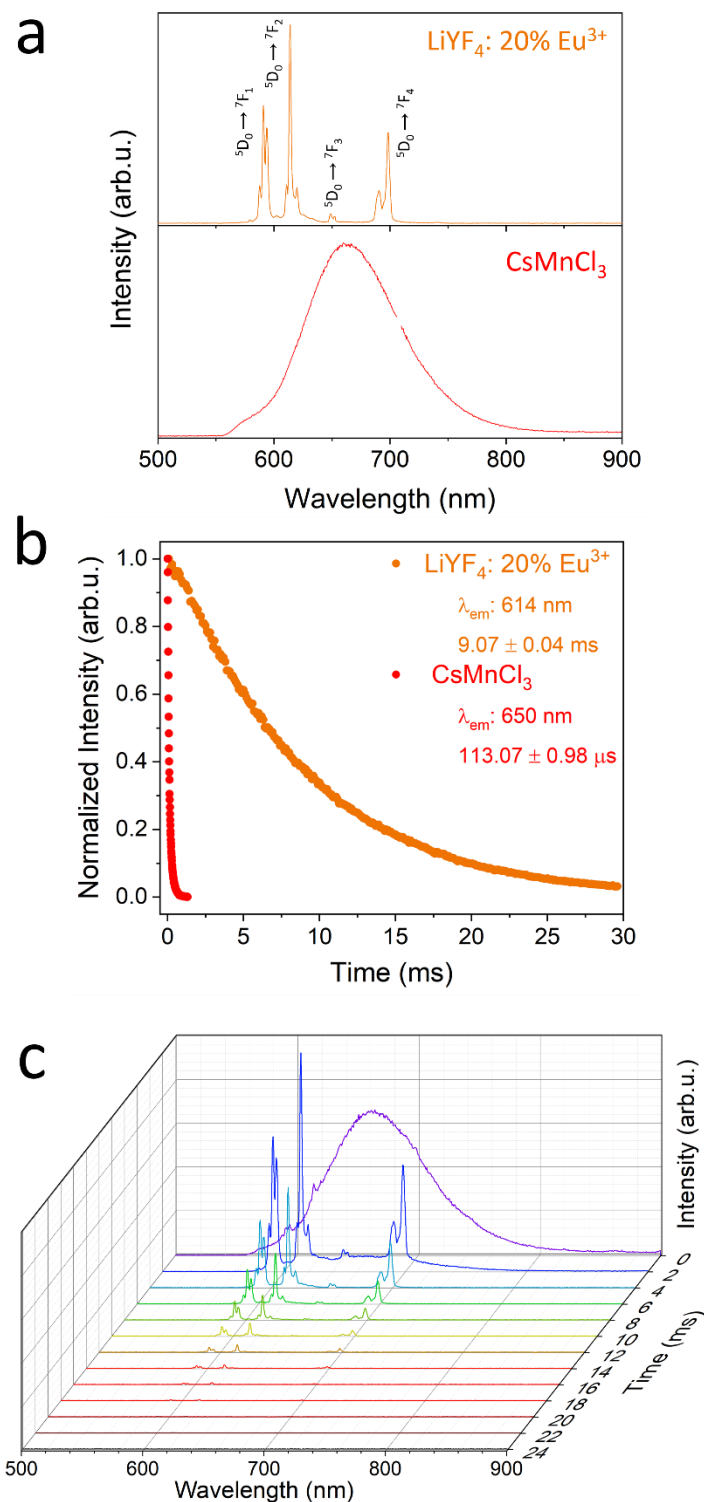


Figure 6.7 (a) Photoluminescence emission spectra and (b) luminescence lifetimes under pulsed 355 nm excitation of (■) $\text{LiYF}_4:20\% \text{Eu}^{3+}$ and (■) CsMnCl_3 nanoparticles. (c) Time-resolved emission spectra under pulsed 355 nm excitation of both nanoparticle compositions combined into a single sample capillary. Adapted with permission from Reference 201. Copyright 2023 American Chemical Society.

Inks were produced by dispersing each nanoparticle composition in a 10% v/v solution of methyl benzoate in toluene, to improve the solvent viscosity. These prints were completed by drop casting the solutions on standard borosilicate glass slides, using a template made from masking tape. The pattern, which consisted of “Eu”, was printed using the $\text{LiYF}_4:20\%\text{Eu}^{3+}$ nanoparticle ink and was then completely covered using the CsMnCl_3 ink. As shown in **Figure 6.8a**, under ambient lighting, no pattern could be distinguished, since the opaque CsMnCl_3 ink covers the printed pattern. Similarly, under 355 nm irradiation (**Figure 6.8b**), since the CsMnCl_3 band gap emission is stronger than the forbidden Eu^{3+} emissions, the entire print is brightly illuminated, and no pattern is visible. Only once the excitation source has ceased, and the CsMnCl_3 emissions are allowed to fully decay, can the lingering Eu^{3+} emissions be imaged for a few milliseconds, as shown in **Figure 6.8c**. This demonstrates the potential to exploit the longer luminescence lifetimes of lanthanide ions and take advantage of the temporal dimension to encode information, rather than just the two spatial dimensions in print.

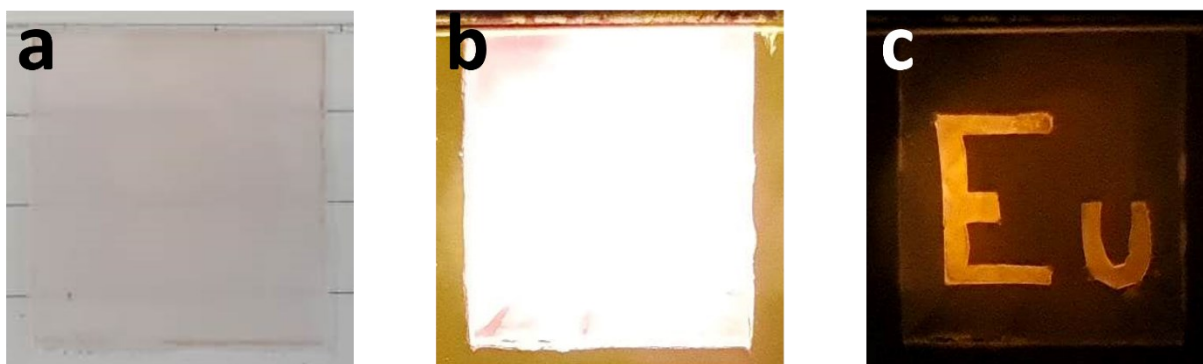


Figure 6.8 Digital photographs of the completed print consisting of $\text{LiYF}_4:20\%\text{Eu}^{3+}$ nanoparticles forming the “Eu” symbol, masked using CsMnCl_3 nanoparticles, under (a) ambient lighting, (b) pulsed 355 nm excitation when the source is on, and (c) pulsed 355 nm excitation when the source has turned off and the emission from the CsMnCl_3 nanoparticles decays. Reprinted with permission from Reference 201. Copyright 2023 American Chemical Society.

6.2.2. Upconverting Nanoparticles

With the confirmed capabilities of this technique, the Er^{3+} and Ho^{3+} -doped UCNPs established in Section 5.1 were explored next, using NIR excitation instead of UV excitation. These ions are ideal since they possess overlapping emission bands in the green (525-560 nm) and red (650 nm) spectral regions. Moreover, relying on lower energy excitation avoids the possible

fluorescence of the substrate, such as paper, allowing for more versatile printing. The $\text{LiYF}_4:18\%\text{Yb}^{3+},2\%\text{Er}^{3+}$ UCNPs were brightest and had a faster luminescence lifetime than the Ho^{3+} -doped UCNPs, and therefore employed as the masking composition. However, the difference in decay time with the brightest Ho^{3+} emitting nanoparticles ($\text{LiYF}_4:20\%\text{Yb}^{3+},1\%\text{Ho}^{3+}$) was not sufficient to generate the pattern. Therefore, larger nanoparticles of $\text{LiYF}_4:20\%\text{Yb}^{3+},0.5\%\text{Ho}^{3+}$ were synthesized in an attempt to lengthen the upconversion lifetime, with the corresponding TEM micrograph in **Figure 6.9**. By lowering the dopant concentration, possible CR mechanisms between the Ho^{3+} ions were reduced, and increasing the nanoparticle size minimizes surface quenching, by decreasing the surface-area-to-volume ratio. Both approaches manifest in a longer excited state lifetime, aiding in the temporal separation between the emissions of Ho^{3+} and Er^{3+} .

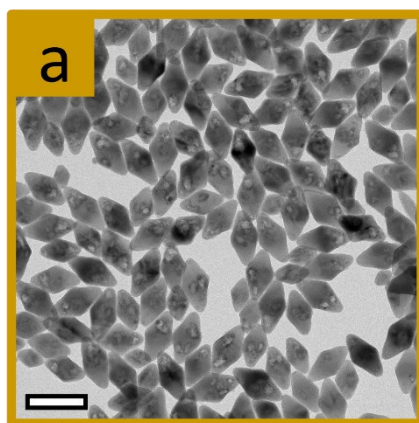


Figure 6.9 TEM micrograph of $\text{LiYF}_4:20\%\text{Yb}^{3+},0.5\%\text{Ho}^{3+}$ UCNPs. Scale bar is set to 100 nm. Adapted with permission from Reference 201. Copyright 2023 American Chemical Society.

To print these UCNPs on standard paper through a conventional office printer, the nanoparticles must be hydrophilic. Therefore, a ligand exchange protocol was completed to replace the as-synthesized oleate-capping ligand with citrate.^{128,135} After the ligand exchange was completed, the upconversion emission spectra were recorded again, shown in **Figure 6.10a**. While all the emission bands are still present, it is evident that the green-to-red emission ratios have decreased for both compositions. This is likely a consequence of either the acidic conditions in the ligand exchange protocol, which increased the prevalence of surface defects, or the newly introduced hydroxyl functional groups from the citrate ligand. Both of these changes manifest in greater phonon quenching effects that depopulate the green emitting states in favor of the red emitting states, thus decreasing the green-to-red emission ratio.¹²⁸ These increased quenching

effects also shorten the decay times of all the observed emission bands, as shown under pulsed 976 nm excitation in **Figure 6.10b**. However, there is still a difference between the longest emission of Er^{3+} , which is approximately 200 μs , and the longest emission of Ho^{3+} , which is approximately 700 μs . This indicates that the two compositions may still be used to generate a time-resolved encrypted information system.

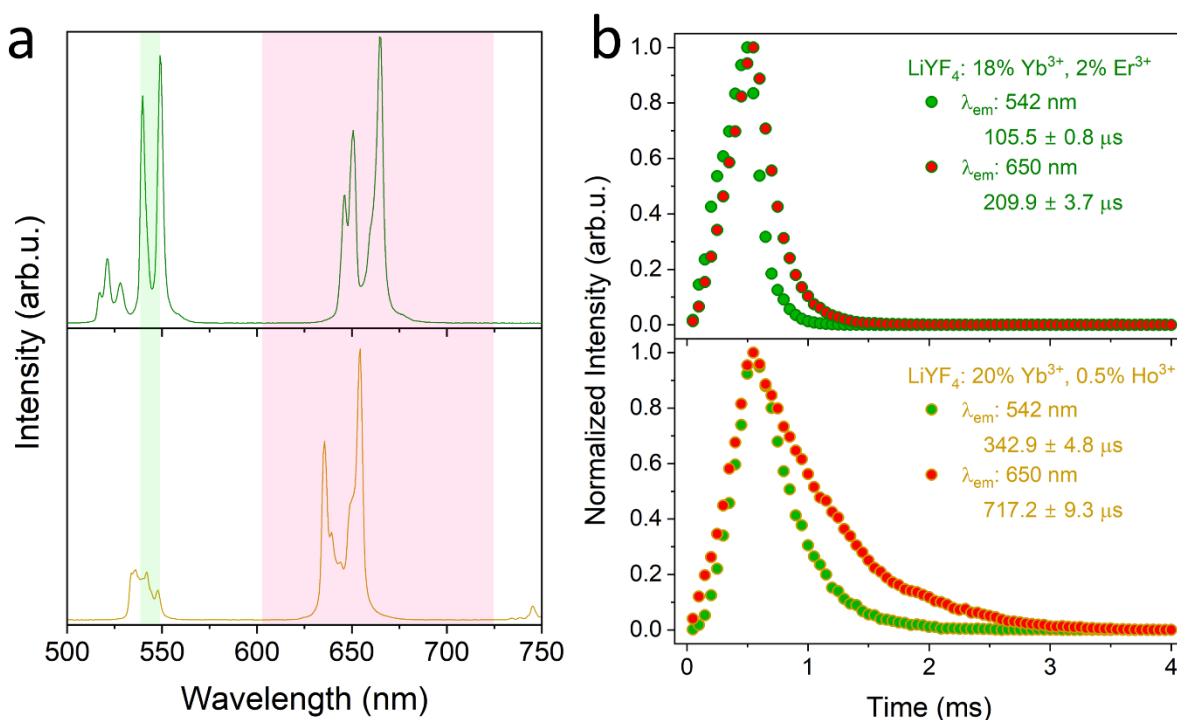


Figure 6.10 (a) Upconversion emission spectra under continuous wave 976 nm excitation and (b) luminescence lifetimes under pulsed 976 nm excitation of citrate-capped (■) $\text{LiYF}_4:18\%\text{Yb}^{3+}, 2\%\text{Er}^{3+}$ and (■) $\text{LiYF}_4:20\%\text{Yb}^{3+}, 0.5\%\text{Ho}^{3+}$ UCNPs. Shaded regions in (a) correspond to the green and red bandpass filtered used in the digital photographs of Figure 6.11. Reprinted with permission from Reference 201. Copyright 2023 American Chemical Society.

The citrate-capped nanoparticles were then dispersed in a 70:30 ethylene glycol:water solution, loaded into a printer cartridge, and printed onto standard paper. The print consisted of a QR code using two layers of the $\text{LiYF}_4:20\%\text{Yb}^{3+}, 0.5\%\text{Ho}^{3+}$ UCNPs, masked using two layers of the $\text{LiYF}_4:18\%\text{Yb}^{3+}, 2\%\text{Er}^{3+}$ UCNPs with the shorter lifetime. By using a QR code, the effectiveness of the system could be evaluated by how easily the code can be imaged using a standard QR code reader.

Under continuous wave irradiation, shown in **Figure 6.11a**, the pattern is slightly visible through the mask. This is most likely a consequence of the overlapping four layers of the pattern

and mask, whereas the pattern only contains two layers, resulting in slightly different luminescence intensities between them. Similarly, when using either a green or red bandpass filter, the pattern appears slightly through the mask, as shown in **Figure 6.11b** and **c**, respectively. Regardless, there is not enough contrast between the pattern and mask to process the QR code using a scanner.

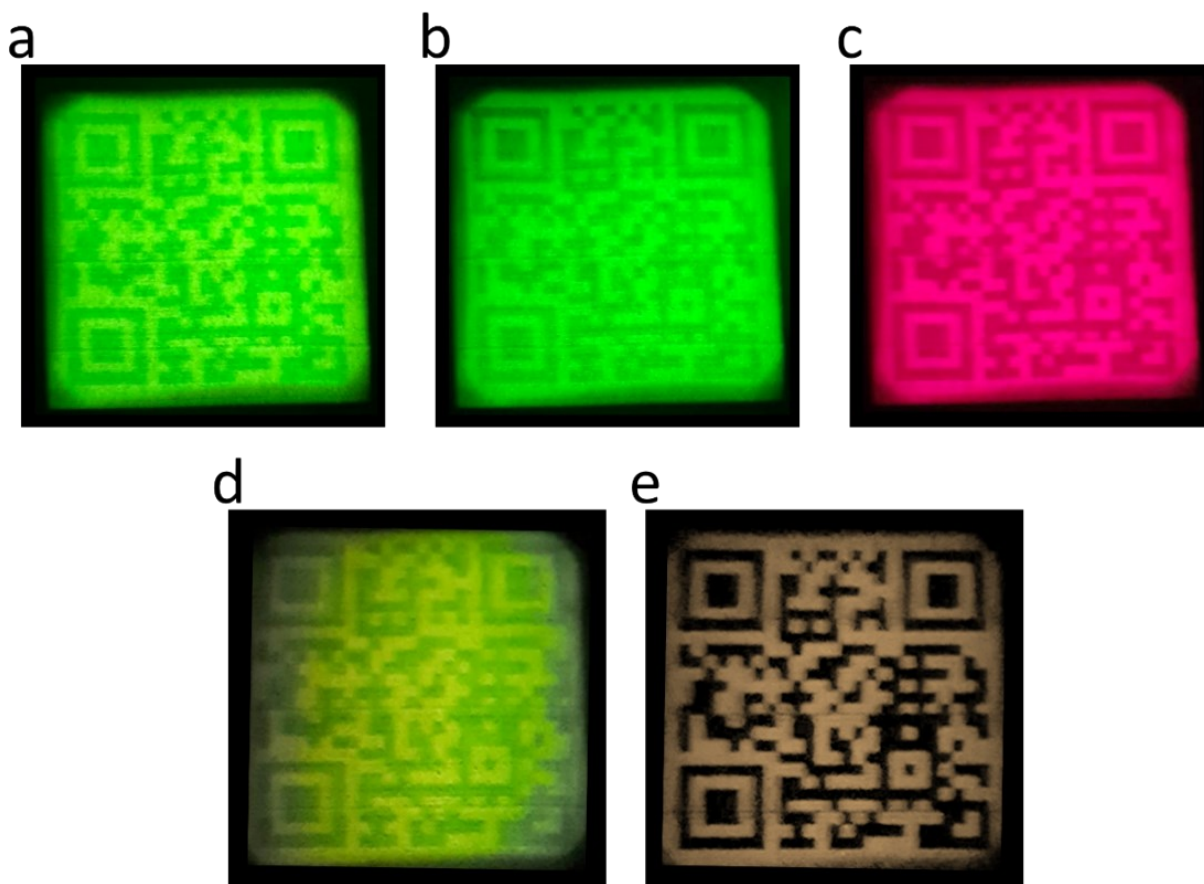


Figure 6.11 Digital photographs consisting of a QR code printed using $\text{LiYF}_4:20\%\text{Yb}^{3+},0.5\%\text{Ho}^{3+}$ UCNP, masked with $\text{LiYF}_4:18\%\text{Yb}^{3+},2\%\text{Er}^{3+}$ UCNP. Print was illuminated under continuous wave 976 nm excitation (a) without a filter or using a (b) green or (c) red bandpass filter. Print was illuminated under pulsed 976 nm excitation and imaged (d) during excitation or (e) after excitation has ceased and the emissions from the $\text{LiYF}_4:18\%\text{Yb}^{3+},2\%\text{Er}^{3+}$ UCNP fully decay. The image in (e) is brightness adjusted. Reprinted with permission from Reference 201. Copyright 2023 American Chemical Society.

During pulsed excitation, when the 976 nm excitation source is on, the print appears similar to the print under continuous wave irradiation, as shown in **Figure 6.11d**. However, the perceived color is slightly more yellow, owing to the lower power density of pulsed excitation which further decreases the green-to-red ratio of both compositions. Only once the excitation source is turned off, and the Er^{3+} emissions are allowed to fully decay, is the Ho^{3+} -emitting QR code illuminated

alone, shown in **Figure 6.11e**. The color appears brown owing to the dim red emission of Ho^{3+} with a slight contribution from the weaker green emission. This image can be recorded using a QR code scanner, taking the user to the Concordia.ca homepage.

This approach to covert information storage takes advantage of the forbidden nature of lanthanide luminescence, which lengthens the excited state lifetimes and produces emissions that emit up to several milliseconds after the excitation source has ceased. By exploiting this temporal dimension, only those who have prior knowledge of the printed compositions can record and interpret the information.

Chapter 7. Eu^{3+} -doped Radioluminescent Nanoparticles

As discussed in Section 2.1., the trends and influences on bulk scale radioluminescent materials do not necessarily translate at the nanoscale, owing to the complex interactions between ionizing radiation and nanoparticles.⁹³ This results in uncertainties in which material compositions will perform adequately at the nanoscale and can be implemented in various applications.^{44,213} One such class of RLNPs with demonstrated uses as X-ray storage phosphors and in X-ray mediated photodynamic therapy are the lanthanide-doped ternary fluorides, due in part to their chemical stability, radiation hardness, low cytotoxicity, and potential for functionalization.^{45,123}

While lanthanide-doped ternary fluorides show promise as RLNPs, the scientific community has not focused much attention on their study and possible implications. This contrasts with the overwhelming research on lanthanide-doped ternary fluorides as UCNPs. Therefore, to take indirect advantage of the research explored on upconversion, the nanoparticle properties known to dictate the upconversion efficiency were explored, to elucidate their influence on the radioluminescence efficiency.²¹⁴

7.1. Effect of Material Density on $\text{LiREF}_4:\text{Eu}^{3+}$ RLNPs

As depicted in Equation 1.2., the density of a material plays a substantial role in its ability to attenuate X-ray photons, which is necessary to initiate the radioluminescence process.⁴⁷ Similarly, a larger Z_{eff} increases X-ray attenuation, thus improving the luminescence output. To evaluate the magnitude of these influences, LiREF_4 nanoparticles doped with Eu^{3+} were synthesized using a previously established thermal decomposition synthesis.¹²⁵ Synthesizing nanoparticles with the lightest alkali metal, Li^+ , allows for the greatest difference in the material density and Z_{eff} when varying the RE cation. The host RE ions used were the spectroscopically silent Y^{3+} and Lu^{3+} , due to the larger and lighter Y^{3+} ion relative to Lu^{3+} , which provided a substantial change in material density and Z_{eff} .²⁰³ Moreover, the band-gap of these compositions always remains between 11 and 11.5 eV.¹²¹ This is paramount since differences in the material band-gap will also change the number of generated electron/hole pairs, another variable which influences the radioluminescence process.⁴⁹ Eu^{3+} was employed as the luminescent center throughout this investigation, owing to its versatile and characteristic red emissions, as demonstrated in Chapter 4 and Chapter 6. A constant activator dopant concentration of 20 mol%

was chosen, due to previous investigations into NaGdF₄ RLNPs; which will be investigated further in Section 7.2.²¹⁵

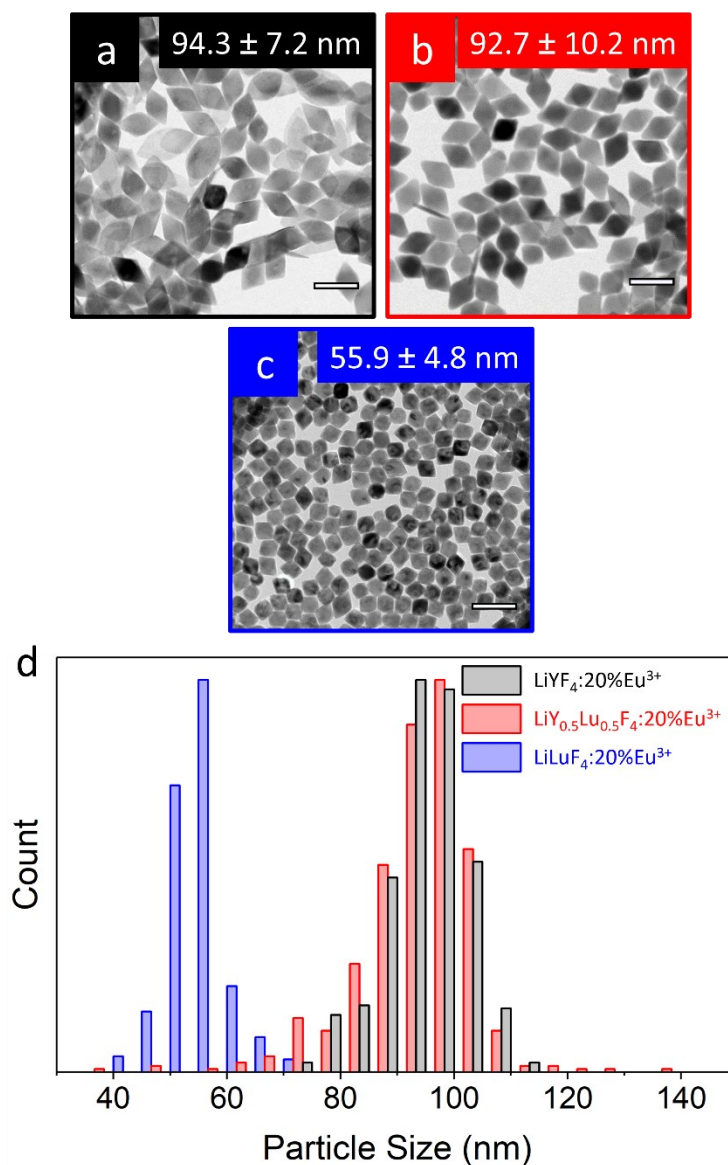


Figure 7.1 TEM micrographs of (a,■) LiYF₄:20%Eu³⁺, (b,■) LiY_{0.5}Lu_{0.5}F₄:20%Eu³⁺, and (c,■) LiLuF₄:20%Eu³⁺ nanoparticles, with (d) their corresponding particle size distributions. Scale bars are set to 100 nm. Reprinted with permission from Reference 214. Copyright 2022 American Chemical Society.

TEM micrographs of the synthesized LiYF₄, LiLuF₄, and LiY_{0.5}Lu_{0.5}F₄ nanoparticles, doped with 20% Eu³⁺, are presented in **Figure 7.1a-c**. As synthesized, they possess the same square bipyramidal morphology across all samples. Interestingly, the LiLuF₄:Eu³⁺ nanoparticles possess a smaller nanoparticle size than the other compositions, as plotted in **Figure 7.1d**, owing

to a difference in aspect ratio between the short and long axes. It is speculated that this is due to increased nucleation of the LiLuF₄ nanoparticles during synthesis, leading to less potential for growth from the remaining monomers present in the reaction solution. While changing the synthesis conditions could have produced more consistent nanoparticle sizes to match the other compositions, doing so would also change the degree of crystallinity or defect density in a manner that cannot be quantified easily.^{74,216,217} Therefore, the luminescence of the different nanoparticles was studied as is, taking into consideration the differences in size in the ensuing analysis.

The tetragonal crystal phase of each nanoparticle composition was confirmed *via* PXRD, as shown in **Figure 7.2**, where all the reflections shift slightly due to changes in unit cell size. The unit cell parameters were extracted from the diffractograms and used to calculate the experimental material densities, as well as the Z_{eff} , presented in **Table 7.1**. The least dense LiYF₄:20%Eu³⁺ nanoparticles had a density of about 4.2 g/cm³, while the densest LiLuF₄:20%Eu³⁺ composition was about 6.0 g/cm³, a difference of approximately 42%. These are similar to the density of more common radioluminescent materials, such as Y₃Al₅O₁₂ (4.6 g/cm³) and Lu₃Al₅O₁₂ (6.7 g/cm³).^{218,219} A difference in Z_{eff} of approximately 67% was also calculated between the LiYF₄:20%Eu³⁺ and LiLuF₄:20%Eu³⁺ compositions.

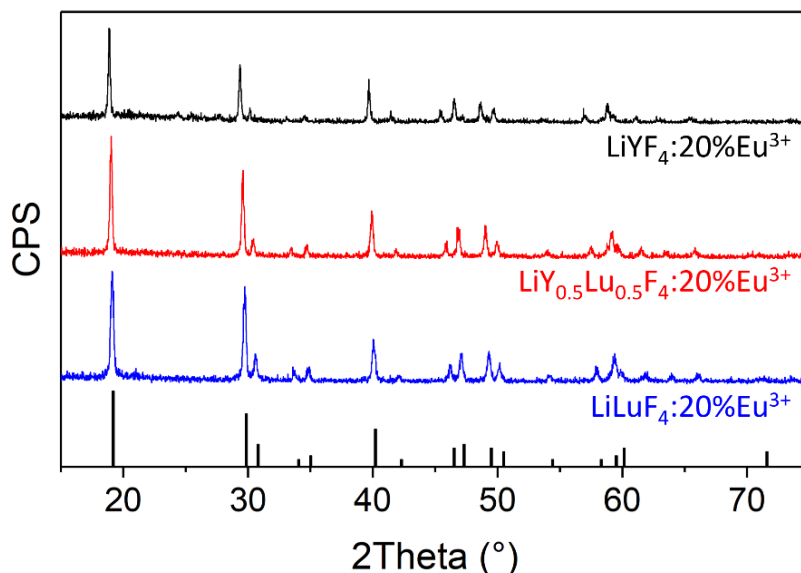


Figure 7.2 PXRD diffractograms of (■) LiYF₄:20%Eu³⁺, (■) LiY_{0.5}Lu_{0.5}F₄:20%Eu³⁺, and (■) LiLuF₄:20%Eu³⁺ nanoparticles, compared to the reference pattern for LiLuF₄ (PDF#027-1251). Reprinted with permission from Reference 214. Copyright 2022 American Chemical Society.

Table 7.1 Unit cell parameters and Z_{eff} calculations for the synthesized RLNP compositions.

Composition	a (Å)	c (Å)	V (Å ³)
LiYF₄:20%Eu³⁺	5.1789(12)	10.796(6)	289.56(7)
LiY_{0.5}Lu_{0.5}F₄:20%Eu³⁺	5.1583(13)	10.695(4)	284.56(9)
LiLuF₄:20%Eu³⁺	5.1310(13)	10.621(4)	279.62(9)
Composition		ρ (g/cm ³)	Z_{eff}
LiYF₄:20%Eu³⁺		4.232(1)	20.925
LiY_{0.5}Lu_{0.5}F₄:20%Eu³⁺		5.111(2)	32.268
LiLuF₄:20%Eu³⁺		6.019(2)	34.953

With the different RLNPs established, the radioluminescence emission spectra were recorded under X-ray excitation, shown in **Figure 7.3**. All the characteristic Eu³⁺ emission bands from the ⁵D₀ → ⁷F_J transitions were observed, increasing in relative intensity as a function of material density by about 45%. While this trend was anticipated, it is not confirmed if this is a consequence of increasing attenuation and/or a change in the radioluminescence efficiency (recall Equation 1.4). Therefore, the theoretical X-ray attenuation was calculated using the NIST database “X-ray Form Factor, Attenuation, and Scattering Tables” (**Figure 7.4a**), the emission spectrum of the X-ray excitation source (**Figure 7.4b**), and Equation 1.3, with the resulting relative X-ray attenuation presented in **Table 7.2**.²²⁰ Interestingly, a difference of less than 2% was calculated between the lightest LiYF₄:Eu³⁺ and the heaviest LiLuF₄:Eu³⁺ RLNPs, which is certainly not sufficient to increase the radioluminescence intensity by 45%. Therefore, there must be an increase in the radioluminescence efficiency with increasing material density and Z_{eff} .

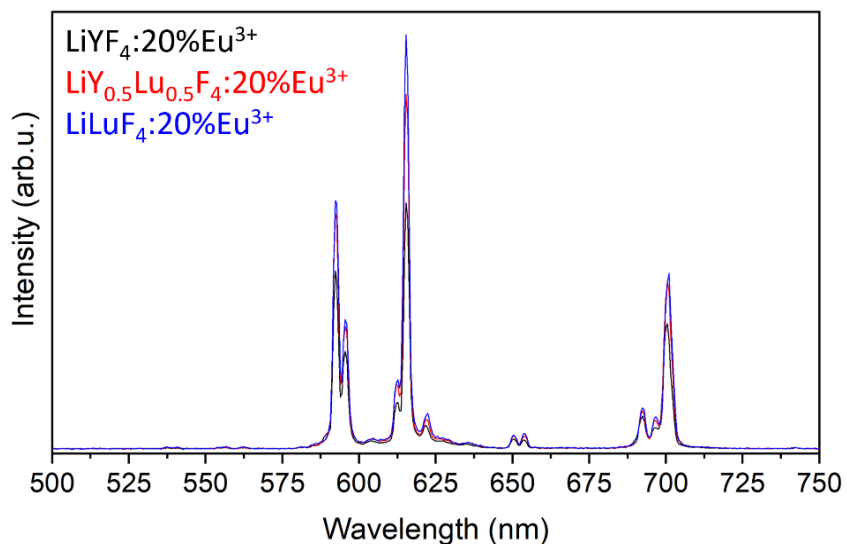


Figure 7.3 Radioluminescence emission spectra, under X-ray excitation, of (■) $\text{LiYF}_4:20\%\text{Eu}^{3+}$, (■) $\text{LiY}_{0.5}\text{Lu}_{0.5}\text{F}_4:20\%\text{Eu}^{3+}$, and (■) $\text{LiLuF}_4:20\%\text{Eu}^{3+}$ nanoparticles. Reprinted with permission from Reference 214. Copyright 2022 American Chemical Society.

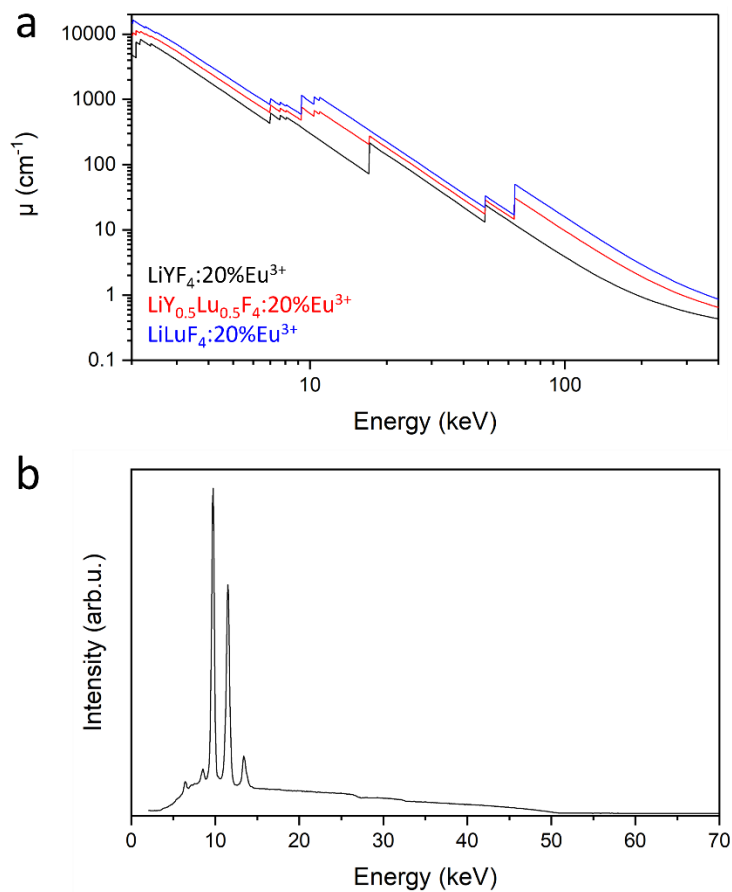


Figure 7.4 (a) Linear attenuation coefficient of each nanoparticle composition and (b) the Mini-X X-ray source emission spectrum. Reprinted with permission from Reference 214. Copyright 2022 American Chemical Society.

Table 7.2 Theoretical transmitted X-ray energy of each nanoparticle composition, using Figure 7.4 and Equation 1.3.

Composition	I_0 (arb.u.)	I_x (arb.u.)	Rel.
	802471		
LiYF₄:20%Eu³⁺		11740	1.00
LiY_{0.5}Lu_{0.5}F₄:20%Eu³⁺		6459	1.01
LiLuF₄:20%Eu³⁺		3293	1.01

As a control experiment to evaluate the relative efficiency of the different compositions, all doped with the same 20% Eu³⁺, photoluminescence emission spectra were recorded under 355 nm irradiation, as shown in **Figure 7.5**. These results directly correlate to the quantum efficiency of the luminescence centers, thus providing a relative comparison of Q in Equation 1.4. Intriguingly, the photoluminescence intensity decreases with increasing material density and Z_{eff} , an inverted trend to the radioluminescence intensity recorded previously. This is likely a consequence of the closer spacing of the RE ions in the smaller unit cells of LiLuF₄, resulting in greater nonradiative interactions between Eu³⁺ ions and thus a decrease in luminescence intensity, as discussed in Chapter 4. This implies that the observed increase in radioluminescence efficiency must be due to an increase in conversion efficiency or host-to-activator ET efficiency, despite a decrease in activator efficiency. The conversion efficiency, β , which describes the generation of electron/hole pairs from absorbed X-ray energy can be calculated using Equation 7.1:⁴⁹

$$\beta = \xi_{min}/\xi \quad (7.1)$$

Where ξ_{min} and ξ are the minimum and average energies required to produce a single electron/hole pair, respectively. These values can be calculated using Equation 7.2 and 7.3, respectively:

$$\xi_{min} = E_i + \langle E_{kin}^e \rangle + \langle E_{kin}^h \rangle \quad (7.2)$$

$$\xi = E_i \frac{3 + K}{2 - K[1 - e^{-1/K}]} \quad (7.3)$$

Where E_i is the ionization energy (approximately 1.5x the band-gap energy of the material), $\langle E_{kin} \rangle$ is the average kinetic energy of the generated electron (e) or hole (h), and K is the energy loss fraction from phonon quenching. Since the studied RLNPs possess similar band-gap energies, and are synthesized using identical protocols, it is presumed that these variables do not change greatly between compositions. Therefore, the observed increase in radioluminescence efficiency with increasing material density and Z_{eff} must be the result of greater ET between the recombining electron/hole pairs of the nanomaterial lattice and the Eu^{3+} dopant ions. This is possibly due to the closer spacing of the ions in the smaller LiLuF_4 unit cells, decreasing the Eu^{3+} quantum efficiency but ultimately improving the overall radioluminescence efficiency of the $\text{LiLuF}_4:20\%\text{Eu}^{3+}$ RLNPs.

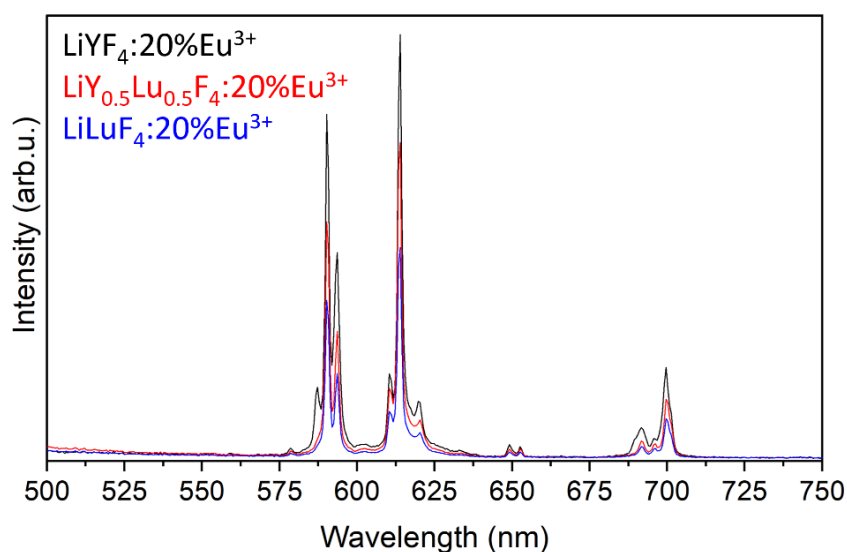


Figure 7.5 Photoluminescence emission spectra, under 355 nm excitation, of (■) $\text{LiYF}_4:20\%\text{Eu}^{3+}$, (■) $\text{LiY}_{0.5}\text{Lu}_{0.5}\text{F}_4:20\%\text{Eu}^{3+}$, and (■) $\text{LiLuF}_4:20\%\text{Eu}^{3+}$ nanoparticles. Reprinted with permission from Reference 214. Copyright 2022 American Chemical Society.

7.2. Effect of Activator Concentration on $\text{LiLuF}_4:\text{Eu}^{3+}$ RLNPs

Previous studies using Eu^{3+} -doped RLNPs in X-ray imaging elect to employ 15-20 mol% Eu^{3+} , which have been optimized beforehand *via* photoluminescence.^{122,215} However, it is not conclusive that the brightest nanoparticles under direct UV excitation will also perform best under excitation with ionizing radiation. Furthermore, the sensitivity of radioluminescence to dopant concentration has also not been well established in lanthanide-doped ternary fluoride nanoparticles, unlike the exhaustive concentration studies on upconversion luminescence, which

are known to be highly sensitive to deviations in dopant concentrations. Therefore, this was evaluated by varying the Eu^{3+} dopant concentration between 10 – 30 mol% in the LiLuF_4 host.

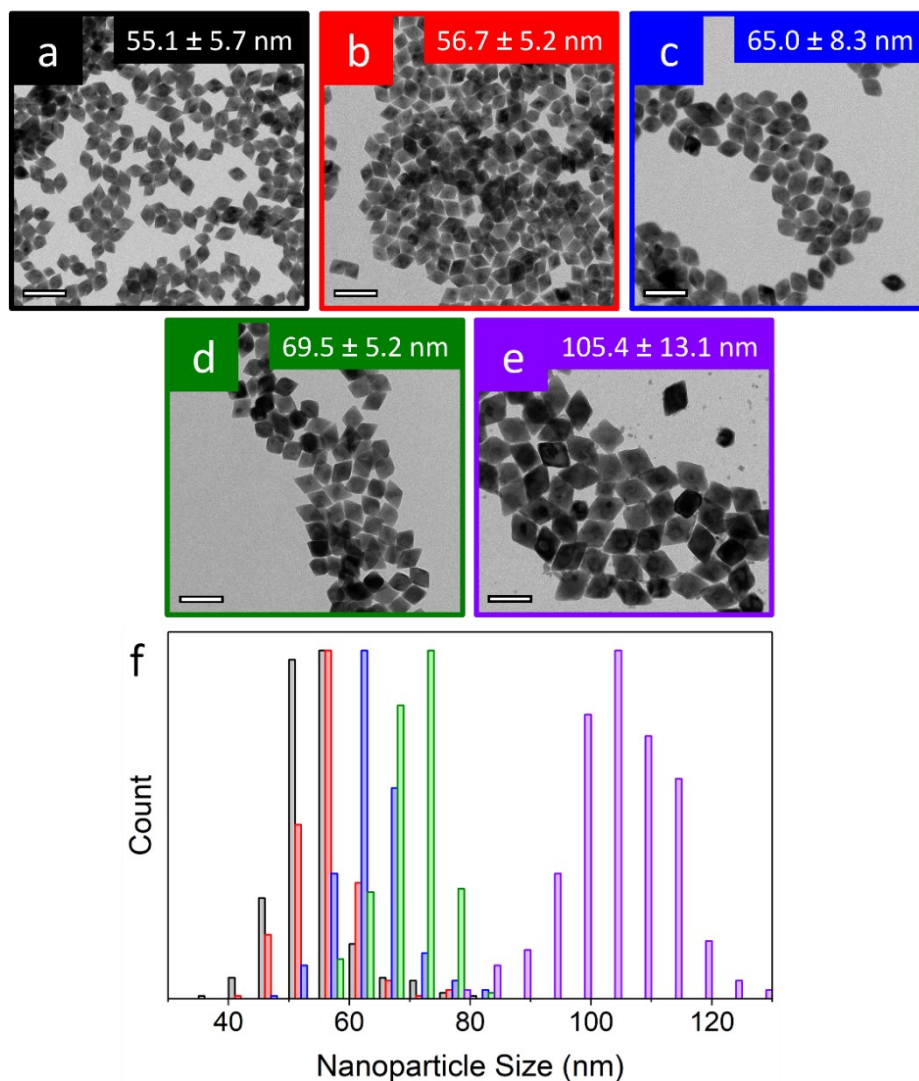


Figure 7.6 TEM micrographs of $\text{LiLuF}_4:x\%\text{Eu}^{3+}$ nanoparticles, where x is (a, ■) 10, (b, ■) 15, (c, ■) 20, (d, ■) 25, and (e, ■) 30, with (f) their corresponding particle size distributions. Scale bars are set to 100 nm. Reprinted with permission from Reference 214. Copyright 2022 American Chemical Society.

TEM micrographs in the synthesized nanoparticles are presented in **Figure 7.6a-e**, which increase in size with increasing Eu^{3+} concentration, as shown in the size distribution in **Figure 7.6f**. This result is likely not due to the Eu^{3+} cation being larger than Lu^{3+} , since the increase in nanoparticle size far exceeds the difference in ionic radius (Eu^{3+} : 1.066 Å, Lu^{3+} : 0.977 Å).²⁰³ Instead, with increasing Eu^{3+} concentration, the formation of more favorable LiEuF_4 unit cells increases in prevalence, relative to LiLuF_4 unit cells.²²¹ This results in more efficient nanoparticle

growth during the synthesis process, thus generating larger particles that must be taken into consideration when evaluating the emission spectra that follow.

Under X-ray excitation, the resulting radioluminescence emission spectra are presented in **Figure 7.7a**, following a traditional concentration study. An initial increase in Eu^{3+} emission intensity is observed as the activator concentration increases, due to a greater number of Eu^{3+} ions in the RLNP lattice. This is followed by a decrease in intensity when the dopant concentration exceeds 20%, due to increased EM processes which depopulates the Eu^{3+} emitting state.

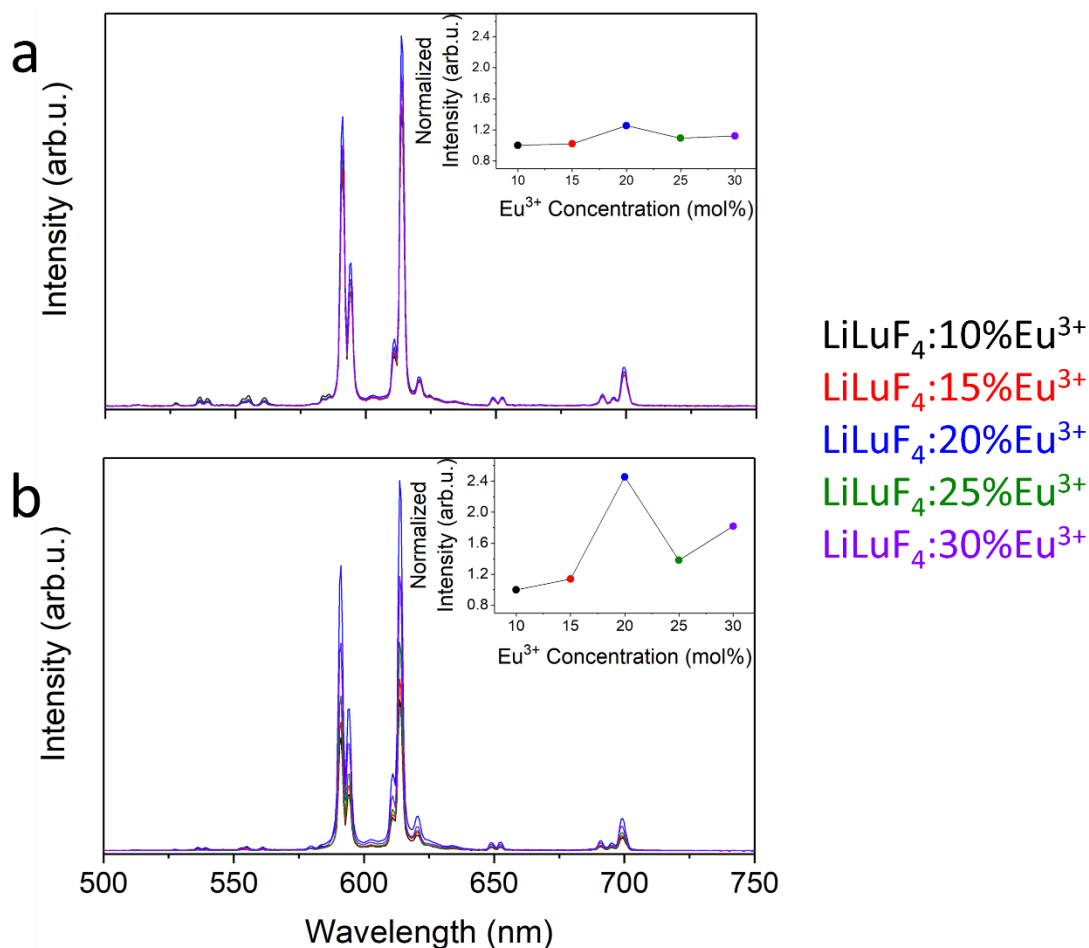


Figure 7.7 (a) Radioluminescence emission spectra under X-ray excitation, and (b) photoluminescence emission spectra under 355 nm excitation of $\text{LiLuF}_4:x\%\text{Eu}^{3+}$ nanoparticles, where x is (■) 10, (■) 15, (■) 20, (■) 25, and (■) 30. Insets correspond to the integrated intensity of each spectrum, normalized to the weakest $\text{LiLuF}_4:10\%\text{Eu}^{3+}$ RLNPs. Reprinted with permission from Reference 214. Copyright 2022 American Chemical Society.

This same trend is observed under direct UV excitation, as presented in **Figure 7.7b**. However, the $\text{LiLuF}_4:30\%\text{Eu}^{3+}$ RLNPs slightly increase in photoluminescence intensity, likely due

to the considerably larger nanoparticle size. This is corroborated by recording the luminescence lifetimes plotted in **Figure 7.8**. With increasing Eu^{3+} concentration, the probability of nonradiative quenching *via* EM increases, thus shortening the decay time. However, at 30% Eu^{3+} , the luminescence decay time increases, indicating fewer quenching pathways despite the higher dopant concentration. This means the increase in nanoparticle size is reducing the probability for surface defects to nonradiatively depopulate the excited states of Eu^{3+} , and consequently the photoluminescence intensity increases.

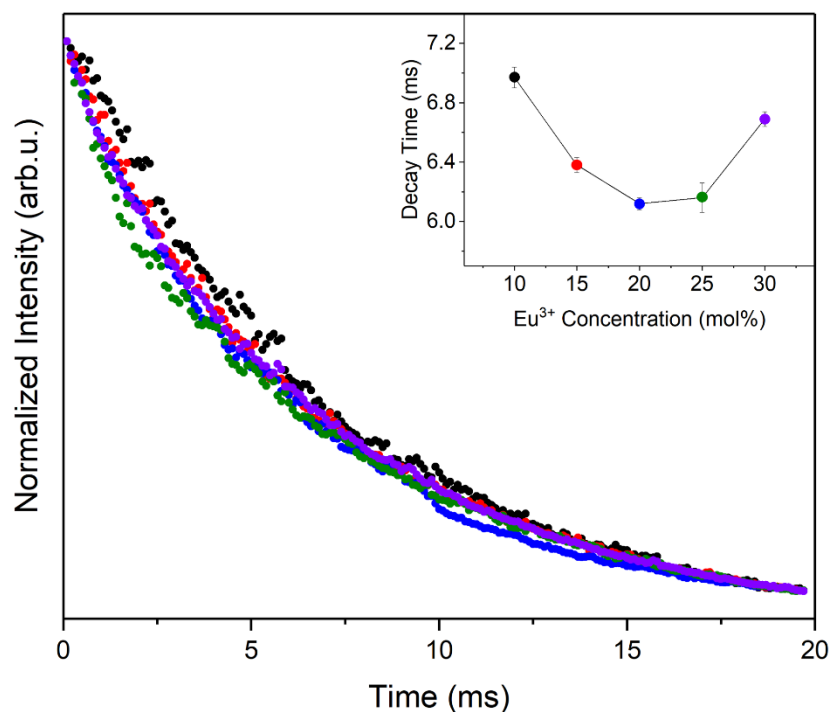


Figure 7.8 Photoluminescence lifetimes recorded under pulsed 355 nm excitation of $\text{LiLuF}_4:x\%\text{Eu}^{3+}$ nanoparticles, where x is (■) 10, (■) 15, (■) 20, (■) 25, and (■) 30. Reprinted with permission from Reference 214. Copyright 2022 American Chemical Society.

Surprisingly, when comparing the relative intensities of the same nanoparticle compositions under UV and X-ray excitation, the sensitivity to dopant concentration is very different. The difference in photoluminescence intensity between the weakest (10% Eu^{3+}) and brightest (20% Eu^{3+}) compositions is greater than double, whereas the radioluminescence intensities only differ by approximately 25% between these compositions. The difference in material density is only about 2% across these compositions, which rules out any influences discussed in Section 7.1. Therefore, it is possible this insensitivity to dopant concentration under excitation with ionizing radiation is the result of the indirect electron/hole recombination processes

which occur at higher energies, circumventing the more typical quenching mechanisms that occur when directly populating the Eu^{3+} excited states *via* UV excitation.

To determine if these results are consistent across activator ions, LiLuF_4 nanoparticles doped with Dy^{3+} and Sm^{3+} were synthesized. These ions were chosen due to their excitation and emission dynamics which are similar to Eu^{3+} under UV excitation. The resulting radioluminescence spectra, photoluminescence spectra, and photoluminescence lifetimes were recorded and presented in **Figure 7.9** and **7.10**, respectively.

As expected, both Dy^{3+} and Sm^{3+} exhibit maximal luminescence intensities at lower dopant concentrations than Eu^{3+} , owing to greater CR mechanisms that quench their emitting $^4\text{F}_{9/2}$ and $^4\text{G}_{5/2}$ excited states, respectively.^{222,223} However, the trends observed in both the photoluminescence and radioluminescence emission spectra are inconsistent with those observed for Eu^{3+} . In the case of Dy^{3+} -doped LiLuF_4 nanoparticles, while the same sensitivity to dopant concentration was observed, the ideal Dy^{3+} dopant concentration is not the same when irradiating the nanoparticles with UV light or X-rays. This has been reported previously and attributed to the indirect excitation that stems from electron/hole recombination on the Dy^{3+} luminescent centers.²²⁴ In the case of Sm^{3+} -doped LiLuF_4 nanoparticles, the sensitivity to dopant concentration is greater during X-ray irradiation than UV excitation, directly contrasting the results observed with Eu^{3+} and Dy^{3+} . These discrepancies are likely the result of the complex mechanisms that populate the luminescent center excited states. For example, the host-to-activator ET efficiency (S) which is poorly understood, and possible interactions with the 4f-5d excitation bands of the lanthanide ions, which further complicate the pathways through which the lanthanide activator ions are excited into their 4f excited states. In any case, the results herein indicate that the radioluminescence sensitivity to dopant concentration is both activator and host specific, and must be studied on a case-by-case basis. This is corroborated with other concentration studies on RLNPs doped with Eu^{3+} , Dy^{3+} , or Sm^{3+} , but in different host compositions, which do not correlate with the spectroscopic results herein.^{215,225,226}

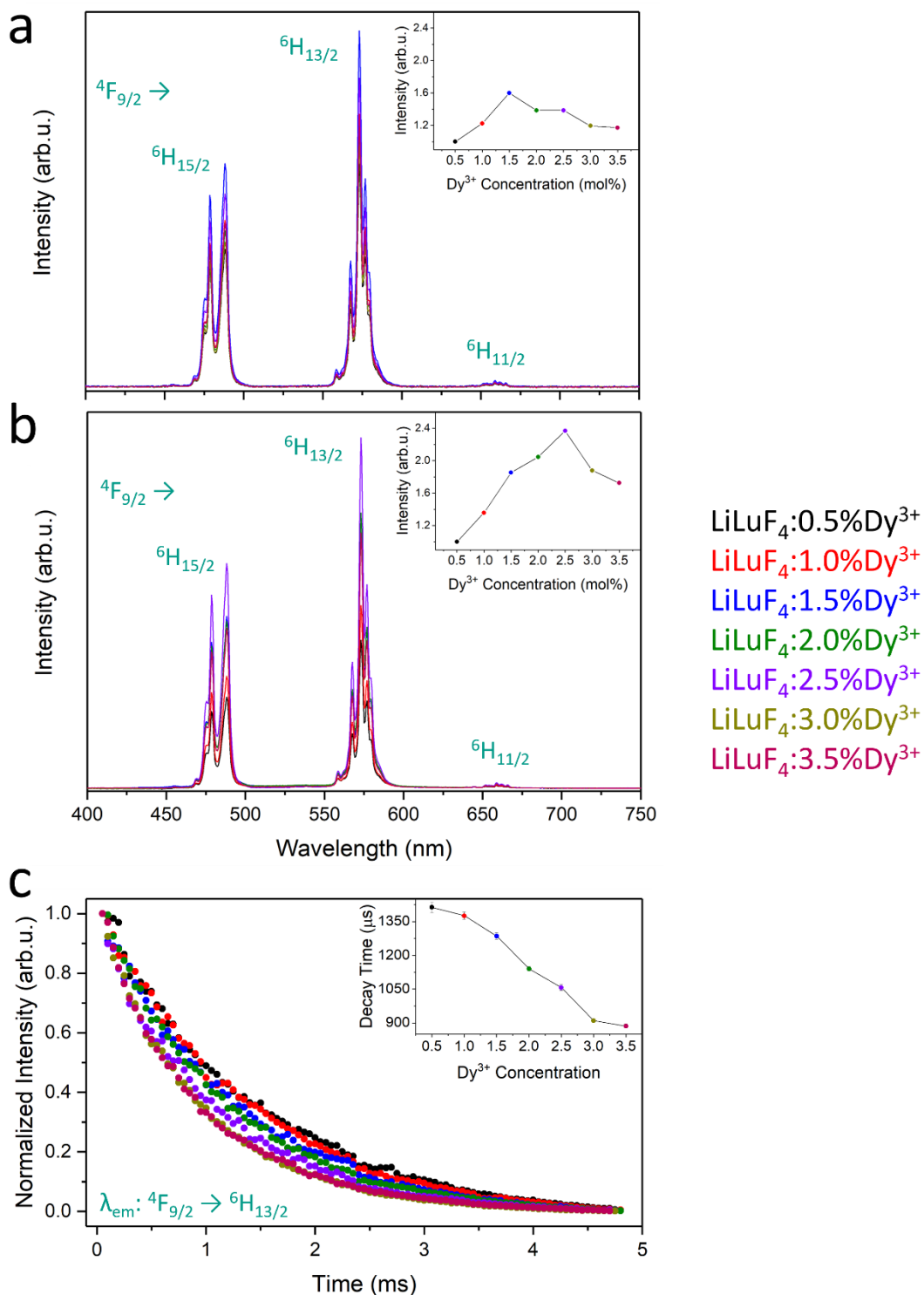


Figure 7.9 (a) Radioluminescence emission spectra under X-ray excitation, (b) photoluminescence emission spectra under 355 nm excitation, and (c) luminescence lifetimes under pulsed 355 nm excitation, of LiLuF₄:x%Dy³⁺ nanoparticles, where x is (■) 0.5, (■) 1.0, (■) 1.5, (■) 2.0, (■) 2.5, (■) 3.0, and (■) 3.5. Reprinted with permission from Reference 214. Copyright 2022 American Chemical Society.

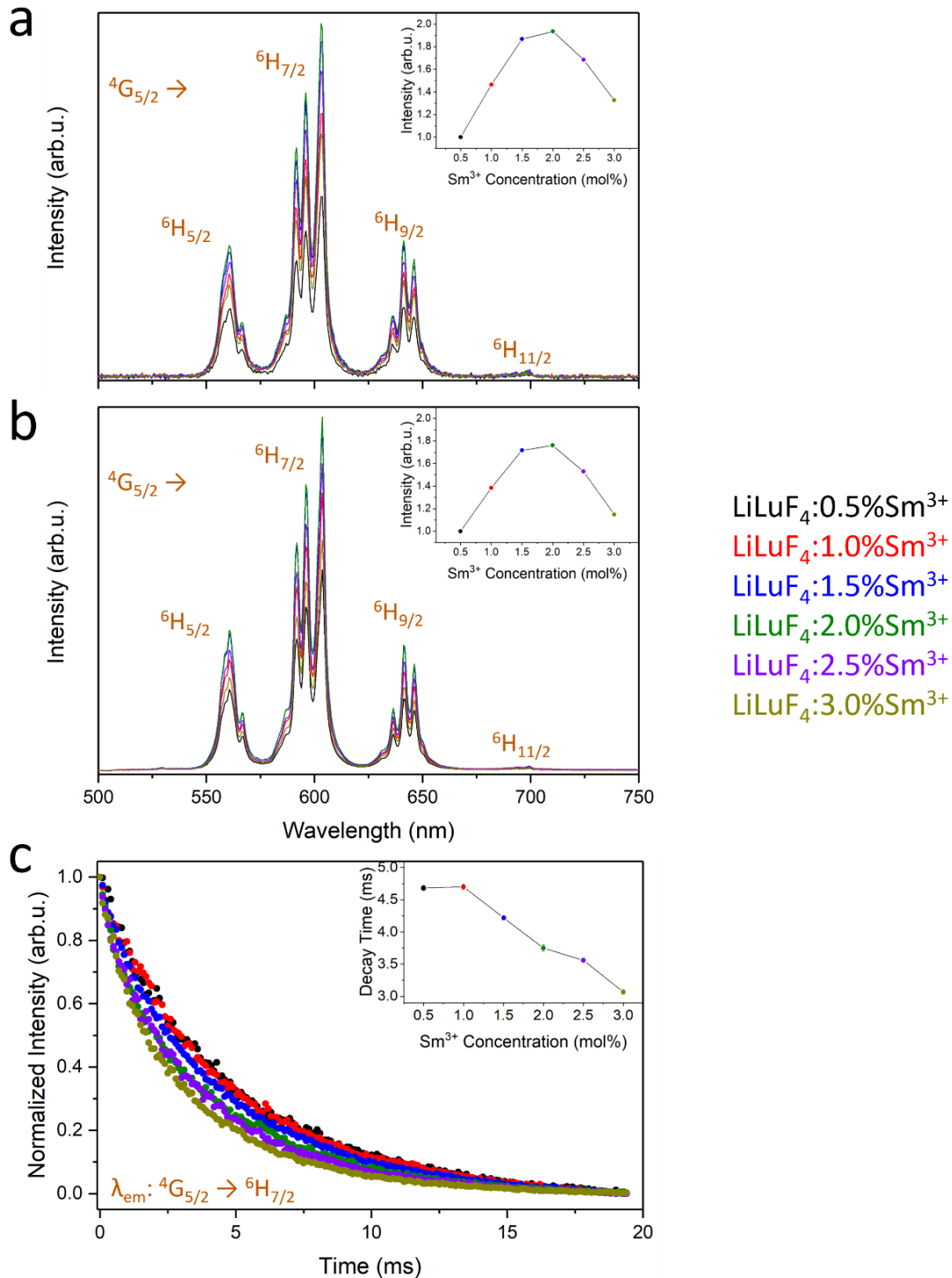


Figure 7.10 (a) Radioluminescence emission spectra under X-ray excitation, (b) photoluminescence emission spectra under 355 nm excitation, and (c) luminescence lifetimes under pulsed 355 nm excitation, of LiLuF₄:x%Sm³⁺ nanoparticles, where x is (■) 0.5, (■) 1.0, (■) 1.5, (■) 2.0, (■) 2.5, and (■) 3.0. Reprinted with permission from Reference 214. Copyright 2022 American Chemical Society.

7.3. Effect of Adding a Gd³⁺ Sensitizer to LiLuF₄:Eu³⁺ RLNPs

Upconversion luminescence is enhanced by several orders of magnitude with the addition of a sensitizer *via* ETU.³⁴ This is due in part to the improved absorption capability of a material doped with a sensitizer ion, since increasing the activator concentration will result in concentration quenching *via* nonradiative processes such as CR and EM. In a similar approach, the addition of a sensitizer ion in RLNPs can also perhaps improve the luminescence efficiency by increasing the number of recombination centers that can excite a spectroscopically active ion, without increasing the activator ion itself and thus increasing concentration quenching effects.

In Eu³⁺-doped materials, under UV excitation, the addition of Gd³⁺ as a sensitizer is well established. This has been demonstrated through quantum cutting (QC), where one higher energy photon is converted into two lower energy photons. Specifically, a single Gd³⁺ ion excited into the ⁶G_J levels can ET to Eu³⁺ through two independent mechanisms, thus generating two emitted photons from Eu³⁺.²²⁷ The first ET step (Gd³⁺:⁶G_J + Eu³⁺:⁷F₁ → Gd³⁺:⁶P_J + Eu³⁺:⁵D₀) is followed by a second ET process (ET from the ⁶P_{7/2} level of Gd³⁺ to the higher energy states of Eu³⁺), sequentially. Therefore, it is postulated that adding Gd³⁺ to LiLuF₄:Eu³⁺ RLNPs will introduce a new luminescent center that can be excited *via* host-to-activator ET (recall *S* from Equation 1.4). The excited Gd³⁺ ions can then facilitate QC to further sensitize the Eu³⁺ dopant ions, increasing the luminescence output.

LiLuF₄:10%Gd³⁺,20%Eu³⁺ nanoparticles were synthesized to test this hypothesis, as increasing the overall dopant concentration beyond 30% resulted in polydisperse nanoparticles. To assess the radioluminescence capabilities of Gd³⁺ independently, which is necessary to demonstrate its sensitizing capabilities, a control of LiLuF₄:10%Gd³⁺ nanoparticles were synthesized as well. TEM micrographs of these RLNPs, including a sample of LiLuF₄:20%Eu³⁺, are shown in **Figure 7.11**, which once again demonstrates an inconsistency in size, as discussed in Section 7.2. This is taken into consideration in the spectroscopic analysis that ensues.

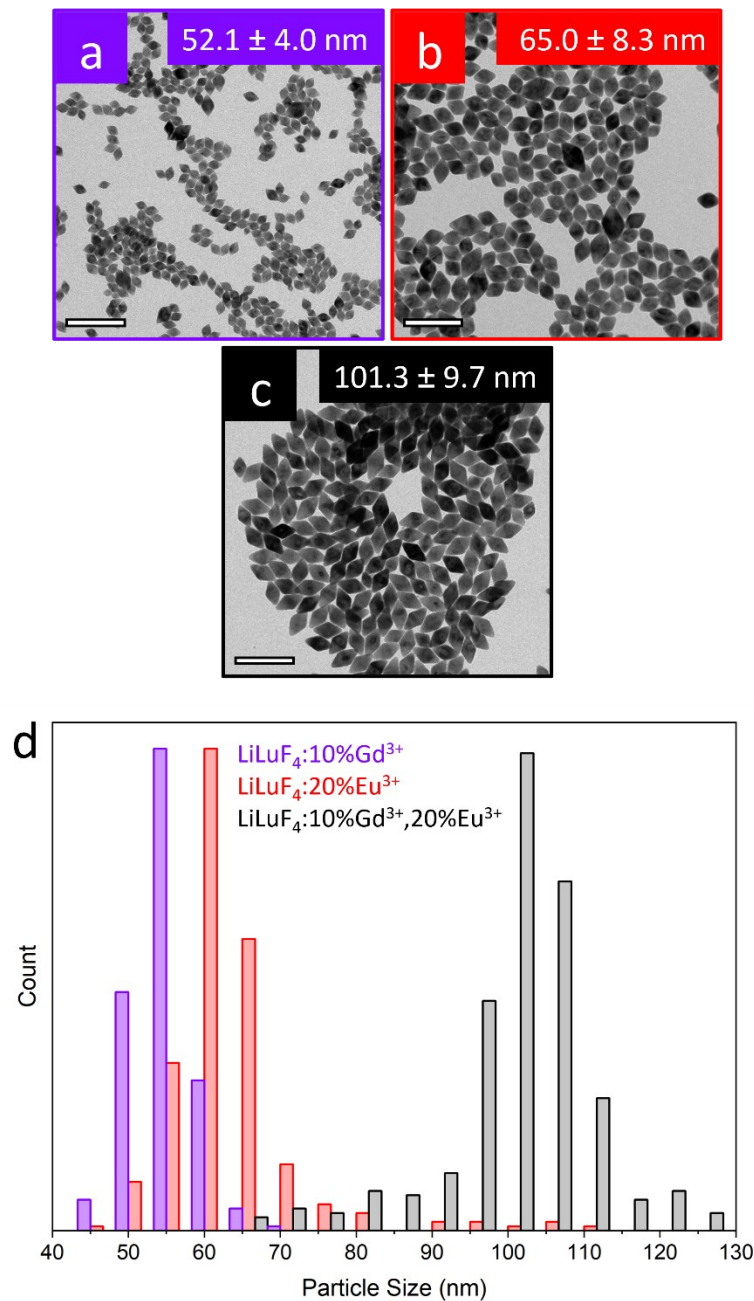


Figure 7.11 TEM micrographs of (a) LiLuF₄:10%Gd³⁺, (b) LiLuF₄:20%Eu³⁺, and (c) LiLuF₄:10%Gd³⁺,20%Eu³⁺ nanoparticles, with (d) their corresponding size distributions. TEM scale bars set to 200 nm. Reprinted with permission from Reference 214. Copyright 2022 American Chemical Society.

Under X-ray irradiation, the radioluminescence spectra of the LiLuF₄:10%Gd³⁺ control RLNPs displayed the characteristic Gd³⁺ emissions at 314 nm and between 575 and 650 nm, from the ⁶P_{7/2} → ⁸S_{7/2} and the ⁶G_J → ⁶P_J transitions, respectively, as shown in **Figure 7.12a**. With the addition of Eu³⁺, shown in **Figure 7.12b**, the Gd³⁺ emission intensities decrease considerably,

indicating ET from Gd^{3+} to Eu^{3+} . Moreover, the Eu^{3+} emission intensities increase by approximately 25%, suggesting sensitization from Gd^{3+} . However, since there is a substantial increase in nanoparticle size, it is unclear if this enhancement is attributed to the sensitization effect from Gd^{3+} or a minimization of quenching effects in the larger nanoparticles. To establish which of these properties is contributing to the enhanced Eu^{3+} emissions, the ${}^5D_1 \rightarrow {}^7F_J$ transitions are inspected (the inset in **Figure 7.12b**). If the brighter Eu^{3+} luminescence was a consequence of increasing size, all the Eu^{3+} emissions would be enhanced, including the 5D_1 transitions. However, since this is not the case, and only the ${}^5D_0 \rightarrow {}^7F_J$ emissions increase in intensity, it can be concluded that the enhancement is due to sensitization from Gd^{3+} .

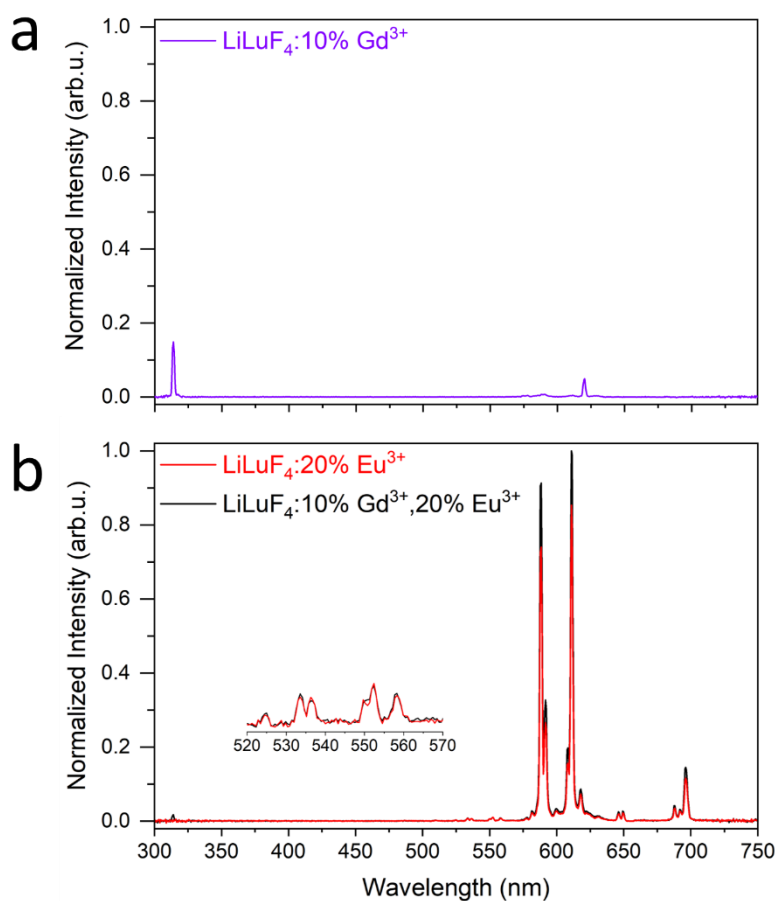


Figure 7.12 Radioluminescence emission spectra, under X-ray excitation, of (a, ■) $LiLuF_4:10\%Gd^{3+}$, (b, ■) $LiLuF_4:20\%Eu^{3+}$, and (b, ■) $LiLuF_4:10\%Gd^{3+},20\%Eu^{3+}$ RLNPs. Adapted with permission from Reference 214. Copyright 2022 American Chemical Society.

The initial intention of adding Gd^{3+} as a sensitizer was to increase the number of recombination sites, which would improve the ET efficiency from the generated electron/hole pairs of the host to the spectroscopically active Eu^{3+} and Gd^{3+} ions. However, if this was the case, the ${}^5\text{D}_1 \rightarrow {}^7\text{F}_J$ transitions of Eu^{3+} would also increase in intensity, as the second QC step from Gd^{3+} populates the higher energy ${}^5\text{H}_J$ levels of Eu^{3+} , which then relax nonradiatively into both the ${}^5\text{D}_1$ and ${}^5\text{D}_0$ states. Instead, as depicted in **Figure 7.13**, it appears that the same number of recombination events is occurring, but a percentage of these are occurring on the newly introduced Gd^{3+} ions instead of the Eu^{3+} ions. These excited Gd^{3+} ions then undergo QC with Eu^{3+} , populating one ion into the higher energy states (like a Eu^{3+} being excited normally), and populating one ion directly into the ${}^5\text{D}_0$ excited state. This means that the enhancement gained from each excited Gd^{3+} ion is only one Eu^{3+} ion in the ${}^5\text{D}_0$ excited state, exhibiting an enhancement of only the ${}^5\text{D}_0 \rightarrow {}^7\text{F}_J$ transitions.

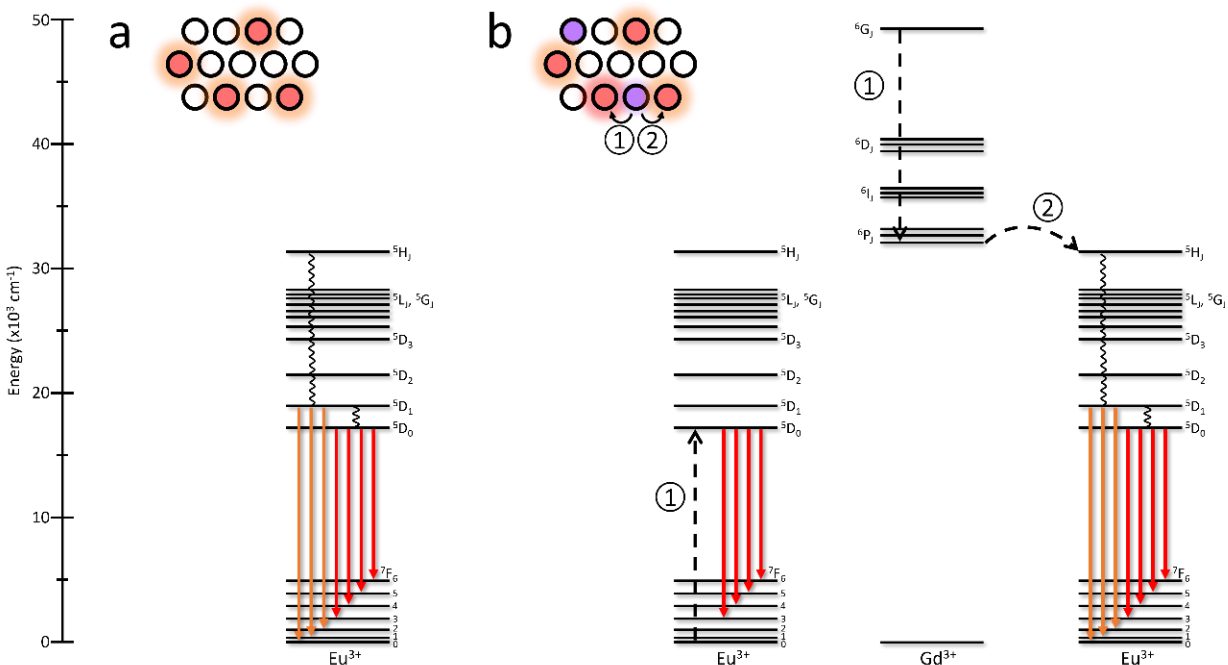


Figure 7.13 Schematic representation of the population dynamics of Eu^{3+} (a) excited solely *via* electron/hole recombination or (b) through QC with Gd^{3+} .

Since the Gd^{3+} emissions are relatively weak under ionizing radiation in this nanoparticle composition, their capacity to sensitize and improve the Eu^{3+} radioluminescence emissions is

limited. Furthermore, since the Gd^{3+} ions also influence the growth of the synthesized nanoparticles, it is unlikely that such an approach is beneficial for the long-term implementation of Eu^{3+} -doped $LiLuF_4$ RLNPs. However, these results indicate that the number of recombination events is not a limitation to the activator ion, but rather a property of the host composition itself.

7.4. Influence of Nanoparticle Architecture on $LiLuF_4:Eu^{3+}$ RLNPs

Due to the susceptibility of surface-related quenching effects in UCNPs, the adoption of core/shell architectures has been widely successful in improving their upconversion efficiency.^{228–230} It remains unclear, however, if such architectures would also improve the luminescence efficiency of RLNPs, since the host lattice is what drives the radioluminescence process. For example, electron/hole pairs generated in the shell may not recombine on a luminescence center in the core. Moreover, the relatively large energy gap between the emitting 5D_0 excited state of Eu^{3+} and the lower lying 7F_J levels is greater than 12000 cm^{-1} , reducing its vulnerability to phonon quenching pathways. Therefore, core/shell $LiLuF_4$ nanoparticles were synthesized to probe this strategy and evaluate its effectiveness on the radioluminescence intensities.

The established $LiLuF_4:20\%Eu^{3+}$ composition was synthesized as the core, with a shell of $LiLuF_4:20\%Eu^{3+}$ to act as a control composition that is subject to all the same synthetic parameters as the other shells. Undoped $LiLuF_4$ was grown as an inert shell with a slightly higher density and Z_{eff} than the core, and a shell of $LiLuF_4:10\%Y^{3+}$ was grown as a composition with a consistent density throughout. As calculated in **Figure 7.14**, using the reference patterns of $LiYF_4$, $LiEuF_4$, and $LiLuF_4$, a dopant concentration of 10 mol% Y^{3+} mimics the material density and Z_{eff} of $LiLuF_4:20\%Eu^{3+}$, thus eliminating this variable as a possible influence on the radioluminescence intensities.

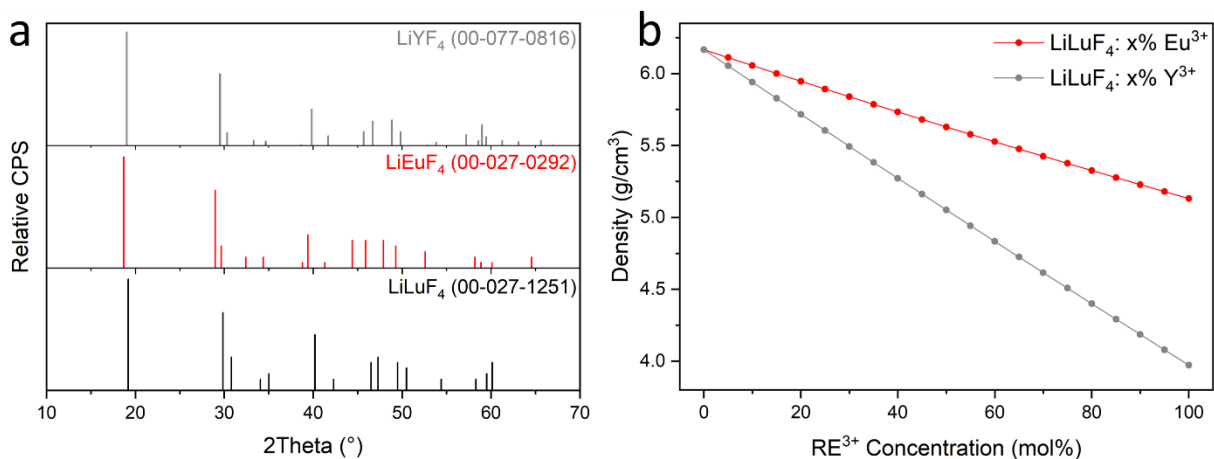


Figure 7.14 (a) Reference PXRD patterns for (■) LiYF₄ (PDF#77-0816), (■) LiEuF₄ (PDF#27-0292), and (■) LiLuF₄ (PDF#27-1251), used to calculate (b) the theoretical material densities as a function of Y³⁺ or Eu³⁺ dopant concentration. Reprinted with permission from Reference 214. Copyright 2022 American Chemical Society.

From the TEM micrographs shown in **Figure 7.15a-e**, a 14 nm shell was added to all the RLNPs, sufficiently thick to prevent all surface-related quenching on the Eu³⁺ dopant ions in the core.^{231–233} This was further validated by recording the photoluminescence lifetimes, plotted in **Figure 7.15f**. The core LiLuF₄:20%Eu³⁺ (7.18 ± 0.03 ms) and core/shell LiLuF₄:20%Eu³⁺/LiLuF₄:20%Eu³⁺ nanoparticles (7.89 ± 0.03 ms) possess the fastest excited state lifetime, due to quenching effects acting on Eu³⁺ ions near the surface. Since the larger core/shell nanoparticles have a smaller surface-area-to-volume ratio, fewer activator ions are subject to these quenching effects, resulting in a slightly longer decay time. The core/shell LiLuF₄:20%Eu³⁺/LiLuF₄ (9.49 ± 0.08 ms) and core/shell LiLuF₄:20%Eu³⁺/LiLuF₄:10%Y³⁺ nanoparticles (9.78 ± 0.08 ms) have longer excited state lifetimes since the Eu³⁺ ions are only present in the core, protected from surface quenching. Since the unit cell of the LiLuF₄ shell is smaller than the LiLuF₄:20%Eu³⁺ core, a slight lattice mismatch at the core/shell interface likely introduced defects that minimally shortened the excited state decay time of this composition.

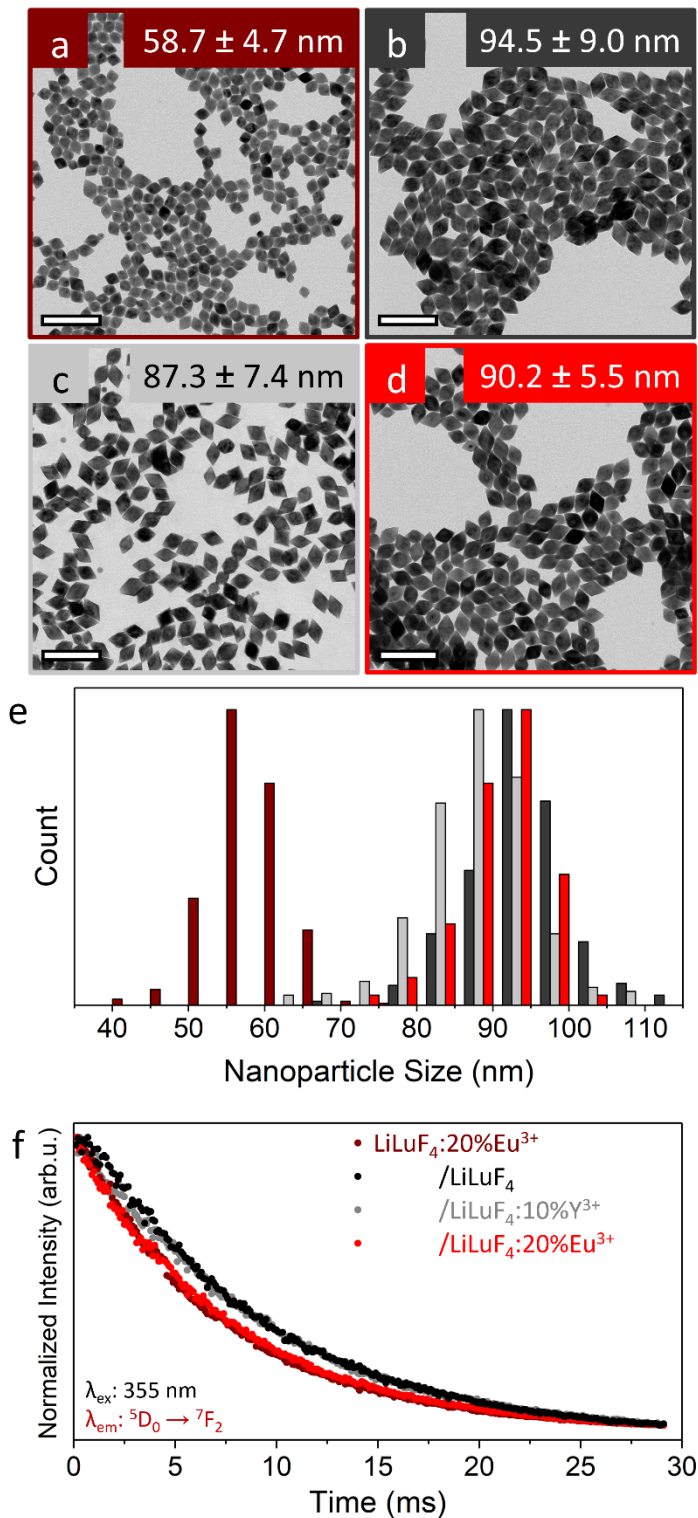


Figure 7.15 TEM micrographs of (a, \blacksquare) core-only LiLuF₄:20%Eu³⁺, (b, \blacksquare) core/shell LiLuF₄:20%Eu³⁺/LiLuF₄, (c, \blacksquare) core/shell LiLuF₄:20%Eu³⁺/LiLuF₄:10%Y³⁺, and (d, \blacksquare) core/shell LiLuF₄:20%Eu³⁺/LiLuF₄:20%Eu³⁺ nanoparticles, with their corresponding (e) particle size distributions and (f) photoluminescence lifetimes under pulsed 355 nm excitation. Scale bars are set to 200 nm. Reprinted with permission from Reference 214. Copyright 2022 American Chemical Society.

Under direct UV excitation, the core-only $\text{LiLuF}_4:20\%\text{Eu}^{3+}$ and core/shell $\text{LiLuF}_4:20\%\text{Eu}^{3+}/\text{LiLuF}_4:20\%\text{Eu}^{3+}$ control RLNPs have very similar photoluminescence intensities (+3%), as shown in **Figure 7.16a**. This indicates that the change in size has only a slight effect on the luminescence efficiency of the Eu^{3+} dopant ions, as calculated in **Table 7.3**. Interestingly, under X-ray excitation (**Figure 7.16b**), a decrease in radioluminescence intensity of almost 30% was observed for the core/shell $\text{LiLuF}_4:20\%\text{Eu}^{3+}/\text{LiLuF}_4:20\%\text{Eu}^{3+}$ control RLNPs relative to the core-only nanoparticles. This was attributed to the formation of a radial gradient during the shell growth synthesis, forcing the majority of the Eu^{3+} ions closer to the center of the nanoparticles and distancing them from the surface where the electron/hole pairs are generated.^{234,235}

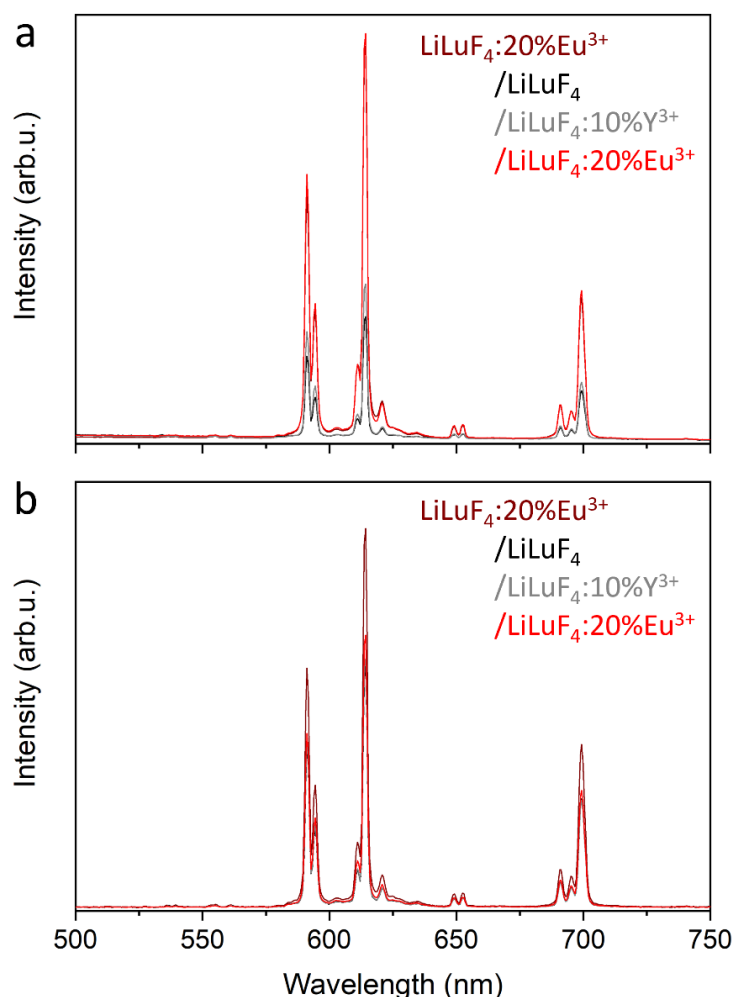


Figure 7.16 (a) Photoluminescence emission spectra under 355 nm excitation, and (b) radioluminescence emission spectra under X-ray excitation of (a, ■) core-only $\text{LiLuF}_4:20\%\text{Eu}^{3+}$, (b, ■) core/shell $\text{LiLuF}_4:20\%\text{Eu}^{3+}/\text{LiLuF}_4$, (c, ■) core/shell $\text{LiLuF}_4:20\%\text{Eu}^{3+}/\text{LiLuF}_4:10\%\text{Y}^{3+}$, and (d, ■) core/shell $\text{LiLuF}_4:20\%\text{Eu}^{3+}/\text{LiLuF}_4:20\%\text{Eu}^{3+}$ nanoparticles. Reprinted with permission from Reference 214. Copyright 2022 American Chemical Society.

Table 7.3 Relative luminescence intensity and Eu^{3+} efficiency of the studied nanoparticle compositions, using the calculated differences in volume occupied by the core and shell.

Photoluminescence			
Composition	Core/Shell (vol%)	Relative Intensity	Relative Intensity/Eu^{3+}
$\text{LiLuF}_4:20\%\text{Eu}^{3+}$	100/N/A	1.00	1.00
/LiLuF_4	24/76	0.31	1.29
/$\text{LiLuF}_4:10\%\text{Y}^{3+}$	30/70	0.40	1.32
/$\text{LiLuF}_4:20\%\text{Eu}^{3+}$	28/72	1.03	1.03
Radioluminescence			
Composition		Relative Intensity	Relative Intensity/Eu^{3+}
$\text{LiLuF}_4:20\%\text{Eu}^{3+}$		1.00	1.00
/LiLuF_4		0.64	2.67
/$\text{LiLuF}_4:10\%\text{Y}^{3+}$		0.65	2.14
/$\text{LiLuF}_4:20\%\text{Eu}^{3+}$		0.72	0.72

With the addition of either inert shell composition, LiLuF_4 or $\text{LiLuF}_4:10\%\text{Y}^{3+}$, the photoluminescence intensities of the core/shell RLNPs decreased by over 50%. Since the Eu^{3+} ions are only in the core of the nanoparticles, the addition of the undoped shell effectively dilutes the number of activator ions present in the powder samples. When calculating the luminescence intensity relative to this difference in Eu^{3+} content, a $\approx 30\%$ increase in relative efficiency is observed. This means that, while the addition of an inert shell minimizes quenching effects on the Eu^{3+} ions, the shell itself reduces the number of Eu^{3+} ions in a given volume, thus decreasing the overall luminescence intensity. This is also the case under ionizing radiation, where the radioluminescence intensities of the core/shell RLNPs decreased by over 30%, despite an increase in relative efficiency of the Eu^{3+} ions by more than double. Moreover, as expected, the RLNPs with the denser LiLuF_4 shell are over 25% more efficient than those with the $\text{LiLuF}_4:10\%\text{Y}^{3+}$ shell, indicating an increase in material density improves the radioluminescence process, corroborating the findings in Section 7.1.

These results indicate that, while the addition of a shell improves the efficiency of the activator ions doped in the core, the shell material itself is excessively diluting the number of activator ions in the given volume, thus decreasing the luminescence output. While this does not

prove effective in Eu^{3+} -doped LiLuF_4 RLNPs, other activator/host combinations that are more susceptible to phonon quenching may benefit from core/shell architecture to enhance the radioluminescence intensity.

Chapter 8. Conclusions and Future Directions

8.1. Conclusions

The field of lanthanide-doped luminescent nanoparticles has focused primarily on application-based research, mostly due to the incredible phenomenon of upconversion which has garnered considerable attention over the last few decades. Furthermore, lanthanide-doped radioluminescent nanomaterials have also piqued the interest of the scientific community in applications that employ ionizing radiation. However, despite all their demonstrated uses, commercial implementation has not yet been achieved. This is due in part to a lackluster understanding of the population and relaxation dynamics that facilitate lanthanide luminescence, especially at the nanoscale, hindering their luminescence efficiencies and output. Therefore, the studies herein aimed to elucidate (de)population mechanisms of lanthanides doped into ternary fluoride nanoparticles, with the intention of enhancing their luminescence intensities. Furthermore, improving our knowledge of the dynamics of lanthanide ions may enable us to take advantage of the temporal dimension in a variety of applications.

8.1.1. Lanthanide Luminescence Mechanisms and Optimizations

Nanoparticles co-doped with Yb^{3+} and Tm^{3+} were synthesized first, to evaluate the effect of host composition and dopant concentration on the upconversion process, under 976 nm irradiation. By studying LiYF_4 UCNPs with an activator concentration between 0.08 and 0.55 mol%, the effect of various known CR mechanisms was quantified, and a new CR mechanism that depopulates the higher energy $^3\text{P}_0$ excited state was established. This mechanism ($^3\text{P}_0 + ^3\text{F}_4 \rightarrow ^1\text{D}_2 + ^3\text{H}_4$) becomes prevalent above 0.24% Tm^{3+} , resulting in a decrease in intensity of the UV emissions at 290 and 345 nm. Therefore, the ideal activator dopant concentration of 0.24% Tm^{3+} (nominally 0.2%) was established as the most efficient for the UV and blue upconverted emissions in LiYF_4 UCNPs.

In an analogous investigation, BaYF_5 UCNPs were synthesized with an activator concentration ranging from 0.2 – 2.0 mol%. This host composition was observed to possess brighter relative intensities in the NIR region, in contrast to the LiYF_4 UCNPs. Corroborated with previously reported CR mechanisms, nonradiative relaxation of the higher energy $^3\text{P}_0$ and $^1\text{D}_2$

excited states was observed, which favored the population of the 3H_4 excited state responsible for the NIR emission at 800 nm. This was observed in combination with a lack of population into the 1D_2 excited state, due to the larger interionic spacing between Tm^{3+} ions, further enabling the lower energy upconverted emissions at 475 and 800 nm.

When comparing different host compositions, lower symmetry of the lanthanide cation site results in increased population of the higher energy excited states through greater j-mixing. Similarly, higher site symmetry facilitates upconverted emissions in the NIR region by minimizing subsequent ETU steps. Overall, these results indicate that careful consideration in the choice of host and dopant concentration is necessary for co-doped Yb^{3+} and Tm^{3+} UCNPs, since only certain radiative transitions may be needed in a given application.

One commonly employed strategy to improve UCNPs is core/shell architectures, to change the spacing between dopant ions with either co-dopants or the nanoparticle environment. However, the type of interactions between ions in the core and shell are studied with little attention to detail. Therefore, $NaGdF_4$ nanoparticles doped with Yb^{3+} and Tm^{3+} in the core and Tb^{3+} in the shell were synthesized, to quantify the ET mechanisms across the core/shell interface. The results herein indicate that, once sensitized *via* 976 nm irradiation, the ET from Tm^{3+} in the core to Tb^{3+} in the shell occurred primarily through a radiative mechanism from the 1D_2 excited state into the 5L_1 excited states. A lesser contribution from nonradiative ET was observed, as well as ET from the 1G_4 and 3P_0 levels through both radiative and nonradiative processes.

With the extensive amount of research focused on upconversion luminescence at the nanoscale, significantly fewer studies are completed on radioluminescence at the nanoscale, despite its potential. Therefore, Eu^{3+} -doped RLNPs were synthesized, and considerations commonly developed for UCNPs were explored under ionizing radiation. Firstly, the effect of host material density and Z_{eff} was explored by synthesizing $LiYF_4$, $LiY_{0.5}Lu_{0.5}F_4$, and $LiLuF_4$ nanoparticles doped with Eu^{3+} . While there was no evident improvement in X-ray attenuation as anticipated, it was elucidated that the ET efficiency between the host and the luminescence centers increases with density and Z_{eff} . Secondly, the effect of Eu^{3+} dopant concentration was explored, confirming an ideal concentration of 20 mol% Eu^{3+} that is consistent with photoluminescence experiments. However, under X-ray excitation, the influence of dopant concentration on luminescence intensity was minimal, only varying by 25%, compared to direct UV excitation, with

intensities that varied by over 100%. Furthermore, these results are inconsistent with those found for other activator ions, such as Dy^{3+} and Sm^{3+} , indicating that the influence of dopant concentration on radioluminescence intensity is activator/host specific. Thirdly, the addition of Gd^{3+} as a possible sensitizer ion was explored, owing to its ability to QC with Eu^{3+} . Interestingly, it was observed that the number of recombination events does not change despite more luminescence centers. Therefore, no considerable improvements in luminescence intensity were observed with the addition of a sensitizer ion. Finally, the effect of core/shell architectures was evaluated, to minimize quenching effects that may act on the Eu^{3+} ions. While there were observed improvements in the efficiency of Eu^{3+} , the addition of shell material occupied excess volume and minimized the overall luminescence output. This indicates that the large energy gap between the $^5\text{D}_0$ and lower energy $^7\text{F}_J$ levels of Eu^{3+} is not susceptible to quenching effects, thus the addition of a shell was not an effective strategy to improving the Eu^{3+} radioluminescence intensities.

8.1.2. Demonstrated Applications Using Luminescence Lifetimes

As demonstrated throughout this thesis when elucidating energy transfer mechanisms, the main purpose of measuring luminescence lifetimes is to gain information on nonradiative ET between two spectroscopically active species. However, since the lanthanide excited state lifetimes can exceed several milliseconds, the prolonged luminescence after excitation has ceased can also be explored in a variety of time-resolved applications.

Traditional spectroscopic nanothermometry uses the ratio between different thermally linked excited states to measure temperature, relative to an external control. However, since the emissions lie at different wavelengths, scattering and absorption processes may differ depending on the localization of the nanoparticle probe, adding uncertainty to the technique. By relying on the relative intensity of a single emission wavelength, these concerns are mitigated. Phonon quenching of lanthanide excited states relies on the vibrational modes of the nanoparticle lattice or surrounding environment, which increase in prevalence with increasing temperature. Therefore, the decay time of the Tm^{3+} excited states are indirectly affected by a change in temperature. By recording the upconversion decay time between 20 and 70 °C under pulsed 976 nm excitation, the thermal sensitivity of the $^3\text{H}_4 \rightarrow ^3\text{H}_6$ transition at 800 nm was measured. While the results exhibit thermal sensitivities weaker than conventional ratiometric techniques, the potential to use such an approach was demonstrated, without the aforementioned limitations.

With the known difference in excited state lifetime of the emitting levels of Tm^{3+} and Tb^{3+} , imaging the emissions at different points in time during pulsed excitation will change the perceived color of a UCNP sample. Therefore, core/shell NaGdF_4 nanoparticles doped with Yb^{3+} and Tm^{3+} in the core and Tb^{3+} in the shell were photographed under pulsed excitation, demonstrating a change in color from blue to green post-excitation. If the nanoparticles are in motion, the excited state lifetime can also be correlated to a distance traveled. This means they can be exploited in particle velocimetry, using multiple emission wavelengths as an internal control. This technique was investigated using microcapillaries from 75 to 150 μm in internal diameter, flowing a solution of UCNPs at different rates. The experimental velocities, when compared to their theoretical values, exhibited accurate results with minimal errors, illustrating a promising alternative to conventional PIV, without limitations in data interpretation and sample concentration.

While different excited state lifetimes can change the perceived emission color of UCNPs with time, different luminescent species with overlapping emission colors can also possess different excited state lifetimes. This can be exploited in printed information storage devices, where a pattern printed using a longer decaying nanoparticle composition can be masked using a different nanoparticle composition that emits at the same wavelength, but decays faster. This was demonstrated using UV-sensitized $\text{LiYF}_4:\text{Eu}^{3+}$ and CsMnCl_3 , where a printed symbol could only be observed after the excitation source has turned off, and the faster decaying CsMnCl_3 nanoparticles fully emitted. Similarly, under NIR irradiation, a QR code printed using $\text{LiYF}_4:\text{Yb}^{3+},\text{Ho}^{3+}$ nanoparticles could only be processed using a code scanner when the emissions from a $\text{LiYF}_4:\text{Yb}^{3+},\text{Er}^{3+}$ nanoparticle mask had fully decayed. By taking advantage of the temporal dimension, an added level of anti-counterfeiting capabilities was demonstrated in print, requiring prior knowledge of the luminescence dynamics to decrypt.

In summary, the forbidden nature of 4f-4f lanthanide luminescence is often considered a limitation in its applicable use, due to weak luminescence efficiencies. However, this also prolongs their emissions after excitation has ceased, sometimes exceeding several milliseconds. By exploiting such a phenomenon, the temporal dimension can be utilized, extending the applicability of lanthanide luminescence at the nanoscale.

8.2. Future Directions

While the work presented herein aimed to further the understanding of population dynamics and luminescence mechanisms of various lanthanide ions in nanomaterials, there are still many uncertainties that need to be addressed. The comparison of different host compositions co-doped with Yb^{3+} and Tm^{3+} was limited to relative intensities, owing to differences in nanoparticle sizes and architecture. To properly evaluate the difference in efficiency as a function of solely host composition, nanoparticles of different ternary fluorides need to have similar sizes and must be synthesized using the same reaction conditions. This could be achieved by varying synthetic parameters that have minimal effects on the crystallinity while still having control over the size of the nanoparticles. These could include the oleic acid:octadecene ratio, reaction solution stir rate, or reagent concentrations. This would minimize changes in crystallinity and surface defects while maintaining some degree of control over the size of the synthesized UCNPs. Moreover, the dopant concentrations of both the sensitizer and activator must be calculated such that the average interionic spacing between the ions is the same across compositions, despite their differences in unit cell size. Only once these conditions are met can a comparison of absolute upconversion efficiency be studied.

The conclusions from the radioluminescence studies of Eu^{3+} -doped LiLuF_4 nanoparticles appeared to only hold true to this specific combination of host and dopant, as substituting the activator for Dy^{3+} or Sm^{3+} resulted in different and even contrasting effects. Therefore, the effect of material density and Z_{eff} , sensitizer addition, or core/shell architecture must also be explored with other host compositions (such as NaLuF_4 or BaLuF_5) and activator ions (including Pr^{3+} and Tb^{3+}). Moreover, all the radioluminescence studies herein were completed using the same 50 kVp X-ray source. Different sources of ionizing radiation, such as gamma rays, electrons, or higher energy X-rays, will interact with the nanoparticles differently, and can have future implications in detectors for space or medical imaging, among others.

The different proof-of-concepts presented in this thesis aim to demonstrate the versatility of lanthanide luminescence, by taking advantage of the prolonged excited state lifetimes of the forbidden 4f-4f transitions. Therefore, approaches can be taken to improve their feasibility in a practical setting.

To enhance the thermal sensitivity of the ${}^3\text{H}_4 \rightarrow {}^3\text{H}_6$ transition of Tm^{3+} for nanothermometry, efforts must be taken to lengthen the decay time of this excited state. By prolonging the lifetime of the ${}^3\text{H}_4$ excited state, the susceptibility to phonon-related quenching effects will increase, thus improving its variability with temperature. This could include decreasing the Tm^{3+} dopant concentration, even if it is slightly detrimental to the upconversion luminescence intensity. Moreover, while an inert shell improved the luminescence intensity, it also minimized the interactions with the solvent, which are necessary to influence the lifetime with temperature. Nanoparticles without an inert shell, or perhaps an inert core/active shell composition (such as $\text{NaYF}_4/\text{NaYF}_4:\text{Yb}^{3+},\text{Tm}^{3+}$) will enhance the interactions between the activator ions and the surrounding solvent molecules, possibly increasing the thermal sensitivity as the phonon relaxation rate increases with temperature.

Particle velocimetry using lanthanide-doped core/shell nanoparticles proved a promising alternative to conventional PIV techniques. However, there were limitations in the minimum and maximum flow rates that could accurately be quantified. By enhancing the luminescence intensity of the overall UCNP composition, the detection limit of the different emission wavelengths as a function of distance could be lowered. This may be achieved using core/shell LiYF_4 UCNPs, which have notably brighter Tm^{3+} UV emissions and will therefore sensitize Tb^{3+} more effectively. Similarly, by prolonging the luminescence lifetime of the longer transition, slower flow rates can be measured since the distance between the maxima of both emissions will separate further. By decreasing the Tb^{3+} concentration, EM processes that are likely shortening the Tb^{3+} excited state lifetimes will be minimized, in turn allowing for a slower flow rate to be accurately measured.

Finally, the covert nature of multiple overlapping nanoparticle compositions for information storage was demonstrated, taking advantage of the temporal dimension. However, there were slight inconsistencies that must be addressed to improve the feasibility of this printing technique. By interlacing the printed pattern and mask, rather than overlapping the two compositions, the QR code could be fully hidden during continuous wave excitation, since there would not be more nanoparticles printed where the four layers overlap and luminesce brighter than the pattern, which only consisted of two layers. Furthermore, while the emissions of Er^{3+} and Ho^{3+} are similar, there are slight differences in their emission bands, which can allow for sophisticated bandpass filters to isolate one band and identify the pattern without pulsed excitation. By

exploiting a single activator ion, such as Er^{3+} only, the pattern and mask would truly possess the same emissions bands. Varying the dopant concentration or exploiting different nanoparticle architectures (core-only vs core/shell) would influence the relaxation processes differently and thus change their upconversion emission lifetimes.

References

- 1 N. N. Greenwood and A. Earnshaw, Eds., in *Chemistry of the Elements*, Butterworth-Heinemann, Oxford, 2nd edn., 1997, pp. 1227–1249.
- 2 S. Cotton, *Lanthanide and Actinide Chemistry*, John Wiley & Sons Ltd, Chichester, 2006.
- 3 J.-C. G. Bünzli and I. McGill, *Ullmann's Encycl. Ind. Chem.*, 2018, 1–53.
- 4 T. Wallington, A. Sherman, M. Everson, F. Field, R. Roth and R. Kirchain, *SAE Int. J. Mater. Manuf.*, 2012, **5**, 473–477.
- 5 R. Won, *Nat. Mater.*, 2010, **9**, S13.
- 6 G. Rayner-Canham and T. Overton, *Descriptive Inorganic Chemistry*, W. H. Freeman, New York, 6th edn., 2014.
- 7 S. Hufner, *Optical Spectra of Transparent Rare Earth Compounds*, Academic Press, 1978.
- 8 J.-C. G. Bünzli and S. V. Eliseeva, in *Lanthanide Luminescence*, eds. P. Hänninen and H. Härmä, Springer Berlin, Heidelberg, Heidelberg, 2010, vol. 7, pp. 1–45.
- 9 K. Binnemans, *Coord. Chem. Rev.*, 2015, **295**, 1–45.
- 10 A. J. Freeman and R. E. Watson, *Phys. Rev.*, 1962, **127**, 2058–2075.
- 11 J. G. Bünzli, *Inorganica Chim. Acta*, 1987, **139**, 219–222.
- 12 G. H. Dieke and H. M. Crosswhite, *Appl. Opt.*, 1963, **2**, 675.
- 13 G. L. Miessler, P. J. Fischer and D. A. Tarr, *Inorganic Chemistry*, Pearson, London, 5th edn., 2014.
- 14 M. T. Berry, M. F. Reid and F. S. Richardson, *J. Chem. Phys.*, 1986, **84**, 2917–2925.
- 15 R. Naccache, Concordia University, 2012.
- 16 P. A. Tanner and C. K. Duan, *Coord. Chem. Rev.*, 2010, **254**, 3026–3029.
- 17 O. Deutschbein, *Ann. Phys.*, 1939, **428**, 183–188.
- 18 X. Qin, X. Liu, W. Huang, M. Bettinelli and X. Liu, *Chem. Rev.*, 2017, **117**, 4488–4527.
- 19 H. Terraschke and C. Wickleder, *Chem. Rev.*, 2015, **115**, 11352–11378.
- 20 V. Mahalingam, R. Naccache, F. Vetrone and J. A. Capobianco, *Chem. - A Eur. J.*, 2009, **15**, 9660–9663.
- 21 M. H. V. Werts, *Sci. Prog.*, 2005, **88**, 101–131.
- 22 G. Tessitore, G. A. Mandl, S. L. Maurizio, M. Kaur and J. A. Capobianco, *RSC Adv.*, 2023, **13**, 17787–17811.
- 23 G. K. Moortgat and A. R. Ravishankara, in *Encyclopedia of Atmospheric Sciences*, eds. G. R. North, J. Pyle and F. Zhang, Academic Press, Cambridge, 2nd edn., 2015, pp. 370–379.

- 24 J. R. Lakowicz, Ed., *Principles of Fluorescence Spectroscopy*, Springer, New York, 2006.
- 25 D. L. Pavia, G. M. Lampman, G. S. Kriz and J. R. Vyvyan, *Introduction to Spectroscopy*, Cengage Learning, Stamford, 5th edn., 2001.
- 26 R. K. Pathria and P. D. Beale, in *Statistical Mechanics*, Elsevier, 2011, pp. 179–229.
- 27 R. J. Mears, L. Reekie, I. M. Jauncey and D. N. Payne, *Electron. Lett.*, 1987, **23**, 1026–1028.
- 28 S. V. Eliseeva and J.-C. G. Bünzli, *New J. Chem.*, 2011, **35**, 1165–1176.
- 29 J. F. Suyver and A. Meijerink, *Chem. Weekbl.*, 2002, **98**, 12–13.
- 30 N. Bloembergen, *Phys. Rev. Lett.*, 1959, **2**, 84–85.
- 31 F. Auzel, *J. Lumin.*, 1990, **45**, 341–345.
- 32 Y. Guyot, H. Manaa, J. Y. Rivoire, R. Moncorgé, N. Garnier, E. Descroix, M. Bon and P. Laporte, *Phys. Rev. B*, 1995, **51**, 784–799.
- 33 F. E. Auzel, *Proc. IEEE*, 1973, **61**, 758–786.
- 34 H. Zhang, L. P. Tu and X. M. Liu, in *Upconverting Nanoparticles: Perspectives, Synthesis, and Applications*, ed. C. Altavilla, CRC Press, Boca Raton, 2017, pp. 19–36.
- 35 M. Haase and H. Schäfer, *Angew. Chemie Int. Ed.*, 2011, **50**, 5808–5829.
- 36 S. Magne, Y. Ouerdane, M. Druetta, J. P. Goure, P. Ferdinand and G. Monnom, *Opt. Commun.*, 1994, **111**, 310–316.
- 37 P. Goldner, F. Pellé, D. Meichenin and F. Auzel, *J. Lumin.*, 1997, **71**, 137–150.
- 38 G. M. Salley, R. Valiente and H. U. Güdel, *Phys. Rev. B*, 2003, **67**, 134111.
- 39 V. V. Ovsyankin, in *Spectroscopy of Crystals Containing Rare Earth Ions*, eds. A. A. Kaplyanskii and R. M. McFarlane, 1st edn., 1987, vol. 21, pp. 343–480.
- 40 G. Sun, Y. Xie, Y. Wang, G. A. Mandl, S. L. Maurizio, H. Zhang, X. Ottenwaelder, J. A. Capobianco and L. Sun, *Angew. Chemie Int. Ed.*, 2023, **62**, e202304591.
- 41 G. Blasse and B. C. Grabmaier, *Luminescent Materials*, Springer Berlin, Heidelberg, Heidelberg, 1994.
- 42 E. B. Podgoršak, *Radiation Physics for Medical Physicists*, Springer Cham, Cham, 3rd Ed., 2016.
- 43 A. J. Wojtowicz, *Acta Phys. Pol. A*, 1999, **95**, 165–178.
- 44 P. Lecoq, *Nucl. Instruments Methods Phys. Res. Sect. A Accel. Spectrometers, Detect. Assoc. Equip.*, 2016, **809**, 130–139.
- 45 G. A. Mandl, F. Vettier, G. Tessitore, S. L. Maurizio, K. Bietar, U. Stochaj and J. A. Capobianco, *ACS Appl. Bio Mater.*, 2023, **6**, 2370–2383.
- 46 G. A. Mandl, Concordia University, 2023.

- 47 E. B. Podgorsak, *Radiation Oncology Physics: A Handbook for Teachers and Students*, Vienna, 2005.
- 48 M. H. McKetty, *RadioGraphics*, 1998, **18**, 151–163.
- 49 A. Lempicki, A. J. Wojtowicz and C. Brecher, in *Wide-Gap Luminescent Materials: Theory and Applications*, ed. S. R. Rotman, Springer US, Boston, MA, 1997, pp. 235–301.
- 50 S. J. Duclos, C. D. Greskovich, R. J. Lyons, J. S. Vartuli, D. M. Hoffman, R. J. Riedner and M. J. Lynch, *Nucl. Instruments Methods Phys. Res. Sect. A Accel. Spectrometers, Detect. Assoc. Equip.*, 2003, **505**, 68–71.
- 51 M. Kokubun, K. Abe, Y. Ezoe, Y. Fukazawa, S. Hong, H. Inoue, T. Itoh, T. Kamae, D. Kasama, M. Kawaharada, N. Kawano, K. Kawashima, S. Kawasoe, Y. Kobayashi, J. Kotoku, M. Kouda, A. Kubota, G. M. Madejski, K. Makishima, T. Mitani, H. Miyasaka, R. Miyawaki, K. Mori, M. Mori, T. Murakami, M. M. Murashima, K. Nakazawa, H. Niko, M. Nomachi, M. Ohno, Y. Okada, K. Oonuki, G. Sato, M. Suzuki, H. Takahashi, I. Takahashi, T. Takahashi, K. Tamura, T. Tanaka, M. Tashiro, Y. Terada, S. Tominaga, S. Watanabe, K. Yamaoka, T. Yanagida and D. Yonetoku, *IEEE Trans. Nucl. Sci.*, 2004, **51**, 1991–1996.
- 52 C. M. Pepin, P. Bérard, A.-L. Perrot, C. Pépin, D. Houde, R. Lecomte, C. L. Melcher and H. Dautet, *IEEE Trans. Nucl. Sci.*, 2004, **51**, 789–795.
- 53 J. E. Grove, C. C. Cheung, M. Kerr, L. J. Mitchell, B. F. Phlips, R. S. Woolf, E. A. Wulf, M. S. Briggs, C. A. Wilson-Hodge, D. Kocevski and J. Perkins, *Instrum. Methods Astrophys.*
- 54 L. J. Mitchell, B. F. Phlips, R. S. Woolf, T. T. Finne and W. N. Johnson, in *UV, X-Ray, and Gamma-Ray Space Instrumentation for Astronomy XXI*, SPIE, 2019, vol. 11118, pp. 122–139.
- 55 M. A. Omary and H. H. Patterson, *Encycl. Spectrosc. Spectrom.*, 2017, 636–653.
- 56 T. Förster, *Ann. Phys.*, 1948, **437**, 55–75.
- 57 D. L. Dexter, *J. Chem. Phys.*, 1953, **21**, 836–850.
- 58 N. J. Turro, *Modern Molecular Photochemistry*, University Science Books, Sausalito, 1991.
- 59 R. A. Hewes and J. F. Sarver, *Phys. Rev.*, 1969, **182**, 427.
- 60 T. Miyakawa and D. L. Dexter, *Phys. Rev. B*, 1970, **1**, 2961.
- 61 F. W. Ostermayer, J. P. van der Ziel, H. M. Marcos, L. G. Van Uitert and J. E. Geusic, *Phys. Rev. B*, 1971, **3**, 2698.
- 62 G. Blasse, *Recl. des Trav. Chim. des Pays-Bas*, 1986, **105**, 143–149.
- 63 F. Vetrone, J.-C. Boyer, J. A. Capobianco, A. Speghini and M. Bettinelli, *Chem. Mater.*, 2003, **15**, 2737–2743.

- 64 L. Cademartiri and G. A. Ozin, *Concepts of Nanochemistry*, Wiley-VCH, 2009.
- 65 K. D. Sattler, Ed., *Handbook of Nanophysics: Nanoparticles and Quantum Dots*, CRC Press, Boca Raton, 2011.
- 66 R. Nussinov and C. Alemán, *Phys. Biol.*, 2006, **3**, E01.
- 67 R. P. Feynman, in *Engineering and Science*, California Institute of Technology, 1960, pp. 22–36.
- 68 K. E. Drexler, *Proc. Natl. Acad. Sci. U. S. A.*, 1981, **78**, 5275–5278.
- 69 S. Chahal, J.-R. Macairan, N. Yousefi, N. Tufenkji and R. Naccache, *RSC Adv.*, 2021, **11**, 25354–25363.
- 70 H. Li, X. Wang, D. Huang and G. Chen, *Nanotechnology*, 2019, **31**, 072001.
- 71 G. A. Mandl, G. Tessitore, S. L. Maurizio and J. A. Capobianco, in *Luminescent Materials*, De Gruyter, 2023, pp. 155–184.
- 72 R. Naccache, Q. Yu and J. A. Capobianco, *Adv. Opt. Mater.*, 2015, **3**, 482–509.
- 73 V. K. LaMer and R. H. Dinigar, *J. Am. Chem. Soc.*, 1950, **72**, 4847–4854.
- 74 H.-X. Mai, Y.-W. Zhang, R. Si, Z.-G. Yan, L.-D. Sun, L.-P. You and C.-H. Yan, *J. Am. Chem. Soc.*, 2006, **128**, 6426–6436.
- 75 W. Ostwald, *Zeitschrift für Phys. Chemie*, 1897, **22U**, 289–330.
- 76 A. Zunger and O. I. Malyi, *Chem. Rev.*, 2021, **121**, 3031–3060.
- 77 A. H. Wilson, *The Theory of Metals*, Cambridge University Press, Cambridge, 2nd edn., 1953.
- 78 J. A. Capobianco, G. Prevost, P. P. Proulx, P. Kabro and M. Bettinelli, *Opt. Mater. (Amst)*, 1996, **6**, 175–184.
- 79 J. A. Capobianco, P. P. Proulx, M. Bettinelli and F. Negrisolò, *Phys. Rev. B*, 1990, **42**, 5936–5944.
- 80 M. Naftaly and A. Jha, *J. Appl. Phys.*, 2000, **87**, 2098–2104.
- 81 F. Vetrone, J. C. Boyer, J. A. Capobianco, A. Speghini and M. Bettinelli, *Nanotechnology*, 2003, **15**, 75.
- 82 R. Vijayakumar and X. Huang, *J. Mater. Sci. Mater. Electron.*, 2019, **30**, 4196–4202.
- 83 F. Wang and X. Liu, *J. Am. Chem. Soc.*, 2008, **130**, 5642–5643.
- 84 G. Tessitore, G. A. Mandl, M. G. Brik, W. Park and J. A. Capobianco, *Nanoscale*, 2019, **11**, 12015–12029.
- 85 S. Rahim, M. H. Hasim, M. T. M. Ayob, I. A. Rahman, K. A. M. Salleh and S. Radiman, *Mater. Res.*, 2020, **22**, 20190383.
- 86 D. R. Cooper, J. A. Capobianco and J. Seuntjens, *Nanoscale*, 2018, **10**, 7821–7832.

- 87 J.-C. Boyer, F. Vetrone, L. A. Cuccia and J. A. Capobianco, *J. Am. Chem. Soc.*, 2006, **128**, 7444–7445.
- 88 J. Zhou, S. Wen, J. Liao, C. Clarke, S. A. Tawfik, W. Ren, C. Mi, F. Wang and D. Jin, *Nat. Photonics*, 2018, **12**, 154–158.
- 89 F. Vetrone, R. Naccache, V. Mahalingam, C. G. Morgan and J. A. Capobianco, *Adv. Funct. Mater.*, 2009, **19**, 2924–2929.
- 90 S. Wilhelm, M. Kaiser, C. Würth, J. Heiland, C. Carrillo-Carrion, V. Muhr, O. S. Wolfbeis, W. J. Parak, U. Resch-Genger and T. Hirsch, *Nanoscale*, 2015, **7**, 1403–1410.
- 91 A. N. Belsky, R. A. Glukhov, I. A. Kamenskikh, P. Martin, V. V. Mikhailin, I. H. Munro, C. Pedrini, D. A. Shaw, I. N. Shpinkov and A. N. Vasil'ev, *J. Electron Spectros. Relat. Phenomena*, 1996, **79**, 147–150.
- 92 V. Vistovskyy, Y. Chornodolskyy, A. Gloskovskii, S. Syrotyuk, T. Malyi, M. Chylyi, P. Zhmurin, A. Gektin, A. Vasil'ev and A. Voloshinovskii, *Radiat. Meas.*, 2016, **90**, 174–177.
- 93 J. Y. Jung, G. A. Hirata, G. Gundiah, S. Derenzo, W. Wrasidlo, S. Kesari, M. T. Makale and J. McKittrick, *J. Lumin.*, 2014, **154**, 569–577.
- 94 A. Gnach, T. Lipinski, A. Bednarkiewicz, J. Rybka and J. A. Capobianco, *Chem. Soc. Rev.*, 2015, **44**, 1561–1584.
- 95 E. Hemmer, P. Acosta-Mora, J. Méndez-Ramos and S. Fischer, *J. Mater. Chem. B*, 2017, **5**, 4365–4392.
- 96 A. Shalav, B. S. Richards, T. Trupke, K. W. Krämer and H. U. Güdel, *Appl. Phys. Lett.*, 2005, **86**, 013505.
- 97 W. Wu, J. Yuan, S. Dong and J. Hao, *ACS Cent. Sci.*, 2021, **7**, 1611–1621.
- 98 A. R. N. Bastos, C. D. S. Brites, P. A. Rojas-Gutierrez, R. A. S. Ferreira, R. L. Longo, C. DeWolf, J. A. Capobianco and L. D. Carlos, *Nanoscale*, 2020, **12**, 24169–24176.
- 99 J. F. Suyver, J. Grimm, M. K. Van Veen, D. Biner, K. W. Krämer and H. U. Güdel, *J. Lumin.*, 2006, **117**, 1–12.
- 100 A. Speghini, M. Pedroni, N. Zaccheroni and E. Rampazzo, in *Upconverting Nanoparticles: Perspectives, Synthesis, and Applications*, ed. C. Altavilla, CRC Press, Boca Raton, 2017, pp. 37–68.
- 101 F. Wang and X. Liu, *Chem. Soc. Rev.*, 2009, **38**, 976–989.
- 102 Z. Wang and A. Meijerink, *J. Phys. Chem. C*, 2018, **122**, 26298–26306.
- 103 G. Tessitore, G. A. Mandl, S. L. Maurizio and J. A. Capobianco, in *Modern Applications of Lanthanide Luminescence*, Springer, Cham, 2021, pp. 1–36.
- 104 M. Nyk, R. Kumar, T. Y. Ohulchanskyy, E. J. Bergey and P. N. Prasad, *Nano Lett.*, 2008, **8**, 3834–3838.

- 105 T. Sabri, P. D. Pawelek and J. A. Capobianco, *ACS Appl. Mater. Interfaces*, 2018, **10**, 26947–26953.
- 106 E. V. Khaydukov, K. E. Mironova, V. A. Semchishen, A. N. Generalova, A. V. Nechaev, D. A. Khochenkov, E. V. Stepanova, O. I. Lebedev, A. V. Zvyagin, S. M. Deyev and V. Y. Panchenko, *Sci. Rep.*, 2016, **6**, 35103.
- 107 M. M. Dcona, Q. Yu, J. A. Capobianco and M. C. T. Hartman, *Chem. Commun.*, 2015, **51**, 8477–8479.
- 108 Y. T. Lim, S. Kim, A. Nakayama, N. E. Stott, M. G. Bawendi and J. V. Frangioni, *Mol. Imaging*, 2003, **2**, 50–64.
- 109 Y. F. Wang, G. Y. Liu, L. D. Sun, J. W. Xiao, J. C. Zhou and C. H. Yan, *ACS Nano*, 2013, **7**, 7200–7206.
- 110 W. Shao, G. Chen, A. Kuzmin, H. L. Kutscher, A. Pliss, T. Y. Ohulchanskyy and P. N. Prasad, *J. Am. Chem. Soc.*, 2016, **138**, 16192–16195.
- 111 M. Kaur, G. A. Mandl, S. L. Maurizio, G. Tessitore and J. A. Capobianco, *Nanoscale Adv.*, 2022, **4**, 608–618.
- 112 S. Hao, Y. Shang, D. Li, H. Ågren, C. Yang and G. Chen, *Nanoscale*, 2017, **9**, 6711–6715.
- 113 L. Wang and J. Yu, in *Interface Science and Technology*, Academic Press, Cambridge, 2023, vol. 35, pp. 1–52.
- 114 J. M. Meruga, W. M. Cross, P. S. May, Q. Luu, G. A. Crawford and J. J. Kellar, *Nanotechnology*, 2012, **23**, 395201.
- 115 J. M. Meruga, A. Baride, W. Cross, J. J. Kellar and P. S. May, *J. Mater. Chem. C*, 2014, **2**, 2221–2227.
- 116 Y. Lu, J. Zhao, R. Zhang, Y. Liu, D. Liu, E. M. Goldys, X. Yang, P. Xi, A. Sunna, J. Lu, Y. Shi, R. C. Leif, Y. Huo, J. Shen, J. A. Piper, J. P. Robinson and D. Jin, *Nat. Photonics*, 2014, **8**, 32–36.
- 117 C. D. S. Brites, P. P. Lima, N. J. O. Silva, A. Millán, V. S. Amaral, F. Palacio and L. D. Carlos, *Nanoscale*, 2012, **4**, 4799–4829.
- 118 E. Saïdi, B. Samson, L. Aigouy, S. Volz, P. Löw, C. Bergaud and M. Mortier, *Nanotechnology*, 2009, **20**, 115703.
- 119 Y. Liu, W. Chen, S. Wang and A. G. Joly, *Appl. Phys. Lett.*, 2008, **92**, 43901.
- 120 X. Ou, X. Qin, B. Huang, J. Zan, Q. Wu, Z. Hong, L. Xie, H. Bian, Z. Yi, X. Chen, Y. Wu, X. Song, J. Li, Q. Chen, H. Yang and X. Liu, *Nature*, 2021, **590**, 410–415.
- 121 G. A. Mandl, D. Van Der Heggen, D. R. Cooper, J. J. Joos, J. Seuntjens, P. F. Smet and J. A. Capobianco, *Nanoscale*, 2020, **12**, 20759–20766.
- 122 C. Sun, G. Pratx, C. M. Carpenter, H. Liu, Z. Cheng, S. S. Gambhir and L. Xing, *Adv. Mater.*, 2011, **23**, H195–H199.

- 123 D. Van der Heggen, D. R. Cooper, M. Tesson, J. J. Joos, J. Seuntjens, J. A. Capobianco and P. F. Smet, *Nanomaterials*, 2019, **9**, 1127.
- 124 F. Maddalena, L. Tjahjana, A. Xie, Arramel, S. Zeng, H. Wang, P. Coquet, W. Drozdowski, C. Dujardin, C. Dang and M. D. Birowosuto, *Crystals*, 2019, **9**, 88.
- 125 V. Mahalingam, F. Vetrone, R. Naccache, A. Speghini and J. A. Capobianco, *Adv. Mater.*, 2009, **21**, 4025–4028.
- 126 H.-W. Chien, M.-T. Tsai, C.-H. Yang, R.-H. Lee and T.-L. Wang, *RSC Adv.*, 2020, **10**, 35600–35610.
- 127 D. Liu, X. Xu, Y. Du, X. Qin, Y. Zhang, C. Ma, S. Wen, W. Ren, E. M. Goldys, J. A. Piper, S. Dou, X. Liu and D. Jin, *Nat. Commun.*, , DOI:10.1038/ncomms10254.
- 128 N. Bogdan, F. Vetrone, G. A. Ozin and J. A. Capobianco, *Nano Lett.*, 2011, **11**, 835–840.
- 129 F. Vetrone, V. Mahalingam and J. A. Capobianco, *Chem. Mater.*, 2009, **21**, 1847–1851.
- 130 H. Xiao, B. Liu, L. Qiu, G. Li, G. Zhang, D. Huang, Y. Zhao, C. Yang, F. Jiang, P. Dang, H. Lian, Z. Cheng and J. Lin, *Angew. Chemie Int. Ed.*, 2022, **61**, e202115136.
- 131 D. Louër and M. Louër, *J. Appl. Crystallogr.*, 1972, **5**, 271–275.
- 132 M. L. Taylor, R. L. Smith, F. Dossing and R. D. Franich, *Med. Phys.*, 2012, **39**, 1769–1778.
- 133 G. A. Mandl, P. A. Rojas-Gutierrez and J. A. Capobianco, *Chem. Commun.*, 2018, **54**, 5847–5850.
- 134 T. Blumenthal, J. Meruga, P. S. May, J. Kellar, W. Cross, K. Ankireddy, S. Vunnam and Q. N. Luu, *Nanotechnology*, 2012, **23**, 185305.
- 135 Y. Ren, J. G. Rosch, M. R. Landry, H. Winter, S. Khan, G. Pratz and C. Sun, *Biomater. Sci.*, 2021, **9**, 496–505.
- 136 Y. Li, R. Wang, Y. Xu, W. Zheng and Y. Li, *Inorg. Chem.*, 2018, **57**, 8012–8018.
- 137 Z.-X. Li, F.-B. Shi, T. Zhang, H.-S. Wu, L.-D. Sun and C.-H. Yan, *Chem. Commun.*, 2011, **47**, 8109–8111.
- 138 Q. Yu, E. M. Rodriguez, R. Naccache, P. Forgione, G. Lamoureux, F. Sanz-Rodriguez, D. Scheglmann and J. A. Capobianco, *Chem. Commun.*, 2014, **50**, 12150–12153.
- 139 S. L. Maurizio, G. Tessitore, G. A. Mandl and J. A. Capobianco, *Nanoscale Adv.*, 2019, **1**, 4492–4500.
- 140 A. Braud, S. Girard, J. L. Doualan, M. Thuau, R. Moncorgé and A. M. Tkachuk, *Phys. Rev. B*, 2000, **61**, 5280–5292.
- 141 M. Kraft, C. Würth, E. Palo, T. Soukka and U. Resch-Genger, *Methods Appl. Fluoresc.*, 2019, **7**, 024001.
- 142 A. Grzechnik, K. Syassen, I. Loa, M. Hanfland and J. Y. Gesland, *Phys. Rev. B*, 2002, **65**,

- 104102.
- 143 A. Grzechnik, P. Bouvier, M. Mezouar, M. D. Mathews, A. K. Tyagi and J. Köhler, *J. Solid State Chem.*, 2002, **165**, 159–164.
- 144 B. S. Cao, J. L. Wu, Z. Q. Feng and B. Dong, *Mater. Chem. Phys.*, 2013, **142**, 333–338.
- 145 P. Villanueva-Delgado, K. W. Krämer, R. Valiente, M. de Jong and A. Meijerink, *Phys. Chem. Chem. Phys.*, 2016, **18**, 27396–27404.
- 146 G. Wang, W. Qin, J. Zhang, J. Zhang, Wangyan, C. Cao, L. Wang, G. Wei, P. Zhu and R. Kim, *J. Phys. Chem. C*, 2008, **112**, 12161–12167.
- 147 C. Cao, W. Qin, J. Zhang, Y. Wang, P. Zhu, G. Wang, G. Wei, L. Wang and L. Jin, *J. Fluor. Chem.*, 2008, **129**, 204–209.
- 148 P. A. Rojas-Gutierrez, S. Bhuckory, C. Mingoies, N. Hildebrandt, C. DeWolf and J. A. Capobianco, *ACS Appl. Nano Mater.*, 2018, **1**, 5345–5354.
- 149 S. L. Maurizio, G. Tessitore, K. W. Krämer and J. A. Capobianco, *ACS Appl. Nano Mater.*, 2021, **4**, 5301–5308.
- 150 X. Chuai, D. Zhang, D. Zhao, K. Zheng, C. He, F. Shi, L. Wang, H. Chen and W. Qin, *Mater. Lett.*, 2011, **65**, 2368–2370.
- 151 P. P. Fedorov, M. N. Mayakova, S. V. Kuznetsov, V. V. Voronov, R. P. Ermakov, K. S. Samarina, A. I. Popov and V. V. Osiko, *Mater. Res. Bull.*, 2012, **47**, 1794–1799.
- 152 B. P. Sobolev, *The rare earth trifluorides: The high temperature chemistry of the rare earth trifluorides*, Institute for Catalan Studies, Barcelona, 2000.
- 153 Z. Liu, E. Ju, J. Liu, Y. Du, Z. Li, Q. Yuan, J. Ren and X. Qu, *Biomaterials*, 2013, **34**, 7444–7452.
- 154 T. P. Melia and R. Merrifield, *J. Appl. Chem.*, 1969, **19**, 79–82.
- 155 A. M. Golubev, A. K. Ivanov-shits, V. I. Simonov, B. P. Sobolev, N. I. Sorokin and P. P. Fedorov, *Solid State Ionics*, 1990, **37**, 115–121.
- 156 M. Kieser and O. Greis, *Zeitschrift für Anorg. und Allg. Chemie*, 1980, **469**, 164–171.
- 157 B. A. Maksimov, K. Solans, A. P. Dudka, E. A. Genkina, M. Font-Badria, I. I. Buchinskaya, A. A. Loshmanov, A. M. Golubev, V. I. Simonov, M. Font-Altava and B. P. Sobolev, *Crystallogr. Reports*, 1996, **41**, 50–57.
- 158 C. Suryanarayana and M. G. Norton, *X-Ray Diffraction: A Practical Approach*, Springer US, New York, 1998.
- 159 J. Grube and G. Krieke, *J. Lumin.*, 2018, **203**, 376–384.
- 160 M. Misiak, K. Prorok, B. Cichy, A. Bednarkiewicz and W. Stręk, *Opt. Mater. (Amst.)*, 2013, **35**, 1124–1128.
- 161 B. Tian, J. Zhao, Y. Tian, X. Li, J. Zhang, J. Sun, R. Hua and B. Chen, *J. Nanosci.*

- Nanotechnol.*, 2015, **15**, 281–289.
- 162 D.-C. Yu, R. Martín-Rodríguez, Q.-Y. Zhang, A. Meijerink and F. T. Rabouw, *Light Sci. Appl.*, 2015, **4**, e344–e344.
- 163 American National Standard Z136.1-2014.
- 164 M. S. Meijer, P. A. Rojas-Gutierrez, D. Busko, I. A. Howard, F. Frenzel, C. Würth, U. Resch-Genger, B. S. Richards, A. Turshatov, J. A. Capobianco and S. Bonnet, *Phys. Chem. Chem. Phys.*, 2018, **20**, 22556–22562.
- 165 G. Chen, J. Shen, T. Y. Ohulchanskyy, N. J. Patel, A. Kutikov, Z. Li, J. Song, R. K. Pandey, H. Agren, P. N. Prasad and G. Han, *ACS Nano*, 2012, **6**, 8280–8287.
- 166 B. Purohit, D. Amans, Y. Guyot, B. Mahler, M. F. Joubert, C. Dujardin, S. Daniele, G. Ledoux and S. Mishra, *Mater. Today Chem.*, 2020, **17**, 100326.
- 167 X. Huang, L. Xiong, L. Yu, X. Gao and X. Qiu, *Inorg. Chem.*, 2020, **59**, 7752–7760.
- 168 M. Karbowiak, J. Cichos and C. Rudowicz, *Polyhedron*, 2016, **105**, 42–48.
- 169 P. Huang, W. Zheng, D. Tu, X. Shang, M. Zhang, R. Li, J. Xu, Y. Liu and X. Chen, *Adv. Sci.*, 2019, **6**, 1802282.
- 170 E. C. Ximendes, U. Rocha, T. O. Sales, N. Fernández, F. Sanz-Rodríguez, I. R. Martín, C. Jacinto and D. Jaque, *Adv. Funct. Mater.*, 2017, **27**, 1702249.
- 171 O. A. Savchuk, J. J. Carvajal, P. Haro-Gonzalez, M. Aguiló and F. Díaz, *J. Alloys Compd.*, 2018, **746**, 710–719.
- 172 L. Labrador-Páez, M. Pedroni, A. Speghini, J. García-Solé, P. Haro-González and D. Jaque, *Nanoscale*, 2018, **10**, 22319–22328.
- 173 Y. Shen, J. Lifante, N. Fernández, D. Jaque and E. Ximendes, *ACS Nano*, 2020, **14**, 4122–4133.
- 174 A. Bednarkiewicz, J. Drabik, K. Trejgis, D. Jaque, E. Ximendes and L. Marciniak, *Appl. Phys. Rev.*, 2021, **8**, 011317.
- 175 H. Toratani, T. Izumitani and H. Kuroda, *J. Non. Cryst. Solids*, 1982, **52**, 303–313.
- 176 M. Tan, F. Li, N. Cao, H. Li, X. Wang, C. Zhang, D. Jaque and G. Chen, *Small*, 2020, **16**, 2004118.
- 177 X. Qiu, Q. Zhou, X. Zhu, Z. Wu, W. Feng and F. Li, *Nat. Commun.*, 2020, **11**, 1–9.
- 178 M. E. Raab, S. L. Maurizio, J. A. Capobianco and P. N. Prasad, *J. Phys. Chem. B*, 2021, **125**, 13132–13136.
- 179 D. R. Gamelin and H. U. Gudel, in *Transition Metal and Rare Earth Compounds*, Springer, Berlin, Heidelberg, 2001, pp. 1–56.
- 180 D. J. Gargas, E. M. Chan, A. D. Ostrowski, S. Aloni, M. V. P. Altoe, E. S. Barnard, B. Sanii, J. J. Urban, D. J. Milliron, B. E. Cohen and P. J. Schuck, *Nat. Nanotechnol.*, 2014,

- 9, 300–305.
- 181 U.S. Secretary of Commerce, Water, <https://webbook.nist.gov/cgi/cbook.cgi?ID=C7732185&Type=IR-SPEC&Index=1>, (accessed 20 December 2023).
- 182 U.S. Secretary of Commerce, Formamide, N,N-dimethyl-, <https://webbook.nist.gov/cgi/cbook.cgi?ID=C68122&Type=IR-SPEC&Index=2>, (accessed 20 December 2023).
- 183 C. K. Duan, A. Meijerink, R. J. Reeves and M. F. Reid, *J. Alloys Compd.*, 2006, **408–412**, 784–787.
- 184 F. Li, J. Cai, F. F. Chi, Y. Chen, C. Duan and M. Yin, *Opt. Mater. (Amst.)*, 2017, **66**, 447–452.
- 185 H. S. Mader, P. Kele, S. M. Saleh and O. S. Wolfbeis, *Curr. Opin. Chem. Biol.*, 2010, **14**, 582–596.
- 186 M. B. Liisberg, S. Lahtinen, A. B. Sloth, T. Soukka and T. Vosch, *J. Am. Chem. Soc.*, 2021, **143**, 19399–19405.
- 187 J. Yang, L. Song, X. Wang, J. Dong, S. Gan and L. Zou, *Dalt. Trans.*, 2018, **47**, 1294–1302.
- 188 X. Xue, M. Thitsa, T. Cheng, W. Gao, D. Deng, T. Suzuki and Y. Ohishi, *Opt. Express*, 2016, **24**, 26307–26321.
- 189 K. Prorok, A. Bednarkiewicz, B. Cichy, A. Gnach, M. Misiak, M. Sobczyk and W. Strek, *Nanoscale*, 2014, **6**, 1855–1864.
- 190 M. Bettinelli and G. Ingletto, *J. Lumin.*, 1989, **43**, 115–119.
- 191 G. Tessitore, S. L. Maurizio, T. Sabri and J. A. Capobianco, *Angew. Chemie Int. Ed.*, 2019, **58**, 9742–9751.
- 192 A. Aebischer, M. Hostettler, J. Hauser, K. W. Krämer, T. Weber, H. U. Güdel and H.-B. Bürgi, *Angew. Chemie Int. Ed.*, 2006, **45**, 2802–2806.
- 193 F. Wang, R. Deng, J. Wang, Q. Wang, Y. Han, H. Zhu, X. Chen and X. Liu, *Nat. Mater.*, 2011, **10**, 968–973.
- 194 A. Aebischer, F. Gumy and J.-C. G. Bünzli, *Phys. Chem. Chem. Phys.*, 2009, **11**, 1346–1353.
- 195 J. S. Park, C. K. Choi and K. D. Kihm, *Exp. Fluids*, 2004, **37**, 105–119.
- 196 H. Huang, F. Huang, L. Lin, Z. Feng, Y. Cheng, Y. Wang and D. Chen, *ACS Appl. Mater. Interfaces*, 2019, **11**, 46379–46385.
- 197 G. Tessitore, S. L. Maurizio, T. Sabri, C. D. Skinner and J. A. Capobianco, *Adv. Mater.*, 2020, **32**, 2002266.
- 198 A. Kolin, *Am. J. Phys.*, 1953, **21**, 619–620.

- 199 G. Chen, H. Qiu, P. N. Prasad and X. Chen, *Chem. Rev.*, 2014, **114**, 5161–5214.
- 200 G. Liu, *Chem. Soc. Rev.*, 2015, **44**, 1635–1652.
- 201 S. L. Maurizio, A. Clermont-Paquette, R. Naccache and J. A. Capobianco, *ACS Appl. Nano Mater.*, 2023, **6**, 21496–21502.
- 202 J. F. Suyver, J. Grimm, K. W. Krämer and H. U. Güdel, *J. Lumin.*, 2005, **114**, 53–59.
- 203 R. D. Shannon, *Acta Crystallogr. Sect. A*, 1976, **32**, 751–767.
- 204 P. Du, L. Luo and J. Su Yu, *Part. Part. Syst. Charact.*, 2018, **35**, 1700416.
- 205 X. P. Chen, W. J. Zhang and Q. Y. Zhang, *Phys. B Condens. Matter*, 2011, **406**, 1248–1252.
- 206 M. J. Weber, *Phys. Rev.*, 1967, **157**, 262–272.
- 207 M. J. Weber, B. H. Matsinger, V. L. Donlan and G. T. Surratt, *J. Chem. Phys.*, 1972, **57**, 562–567.
- 208 A. Kumar Singh, S. B. Rai and A. Rai, *Prog. Cryst. Growth Charact. Mater.*, 2006, **52**, 99–106.
- 209 N. M. Sangeetha, P. Moutet, D. Lagarde, G. Sallen, B. Urbaszek, X. Marie, G. Viau and L. Ressler, *Nanoscale*, 2013, **5**, 9587–9592.
- 210 M. Tan, F. Li, X. Wang, R. Fan and G. Chen, *ACS Nano*, 2020, **14**, 6532–6538.
- 211 L. E. Humes, T. A. Busey, J. C. Craig and D. Kewley-Port, *Attention, Perception, Psychophys.*, 2009, **71**, 860–871.
- 212 L. Q. Guan, S. Shi, X. W. Niu, S. C. Guo, J. Zhao, T. M. Ji, H. Dong, F. Y. Jia, J. W. Xiao, L. D. Sun and C. H. Yan, *Adv. Sci.*, 2022, **9**, 2201354.
- 213 M. L. McConnell, in *The WSPC Handbook of Astronomical Instrumentation*, World Scientific Publishing, Singapore, 2021, pp. 27–50.
- 214 S. L. Maurizio, G. A. Mandl, M. D. Long and J. A. Capobianco, *Chem. Mater.*, 2022, **34**, 10123–10132.
- 215 L. Sudheendra, G. K. Das, C. Li, D. Stark, J. Cena, S. Cherry and I. M. Kennedy, *Chem. Mater.*, 2014, **26**, 1881–1888.
- 216 D. Pominova, I. Romanishkin, V. Proydakova, S. Kuznetsov, P. Grachev, A. Ryabova, N. Tabachkova, P. Fedorov and V. Loschenov, *Methods Appl. Fluoresc.*, 2022, **10**, 024005.
- 217 Y. Cheroura, Z. Smara, A. Potdevin, D. Boyer, A. Chafa, O. Ziane and R. Mahiou, *Mater. Res. Bull.*, 2020, **125**, 110809.
- 218 R. Fedyk, D. Hreniak, W. Łojkowski, W. Strek, H. Matysiak, E. Grzanka, S. Gierlotka and P. Mazur, *Opt. Mater. (Amst.)*, 2007, **29**, 1252–1257.
- 219 N. Wagner, B. Herden, T. Dierkes, J. Plewa and T. Jüstel, *J. Eur. Ceram. Soc.*, 2012, **32**, 3085–3089.

- 220 C. T. Chantler, K. Olsen, R. A. Dragoset, J. Chang, A. R. Kishore, S. A. Kotochigova and D. S. Zucker, X-Ray Form Factor, Attenuation, and Scattering Tables | NIST, <https://dx.doi.org/10.18434/T4HS32>, (accessed 18 May 2022).
- 221 R. E. Thoma, G. D. Brunton, R. A. Penneman and T. K. Keenan, *Inorg. Chem.*, 1970, **9**, 1096–1101.
- 222 M. E. Alvarez-Ramos, *J. Lumin.*, 2021, **233**, 117874.
- 223 M. Yamaga, H. Uno, S. Tsuda, J.-P. R. Wells and T. P. J. Han, *J. Lumin.*, 2012, **132**, 1608–1617.
- 224 J. Kaewkhao, N. Wantana, S. Kaewjaeng, S. Kothan and H. J. Kim, *J. Rare Earths*, 2016, **34**, 583–589.
- 225 M. Shoaib, R. Rajaramakrishna, G. Rooh, N. Chanthima, H. J. Kim, C. Saiyasombat, R. Botta, N. Nuntawong, S. Kothan and J. Kaewkhao, *Opt. Mater. (Amst.)*, 2020, **109**, 110322.
- 226 J. Tang, L. Luo, W. Li, J. Wang and P. Du, *Opt. Mater. (Amst.)*, 2021, **120**, 111463.
- 227 R. T. Wegh, H. Donker, K. D. Oskam and A. Meijerink, *Science (80-.)*, 1999, **283**, 663–666.
- 228 C. Homann, L. Krukewitt, F. Frenzel, B. Grauel, C. Würth, U. Resch-Genger and M. Haase, *Angew. Chemie Int. Ed.*, 2018, **57**, 8765–8769.
- 229 Z. L. Wang, Z. W. Quan, P. Y. Jia, C. K. Lin, Y. Luo, Y. Chen, J. Fang, W. Zhou, C. J. O'Connor and J. Lin, *Chem. Mater.*, 2006, **18**, 2030–2037.
- 230 T. Grzyb, P. Kamiński, D. Przybylska, A. Tymiński, F. Sanz-Rodríguez and P. Haro Gonzalez, *Nanoscale*, 2021, **13**, 7322–7333.
- 231 M. I. Saleh, B. Rühle, S. Wang, J. Radnik, Y. You and U. Resch-Genger, *Sci. Rep.*, 2020, **10**, 19318.
- 232 Y. Wang, K. Liu, X. Liu, K. Dohnalová, T. Gregorkiewicz, X. Kong, M. C. G. Aalders, W. J. Buma and H. Zhang, *J. Phys. Chem. Lett.*, 2011, **2**, 2083–2088.
- 233 F. Carl, L. Birk, B. Grauel, M. Pons, C. Würth, U. Resch-Genger and M. Haase, *Nano Res.*, 2021, **14**, 797–806.
- 234 X. Xu, C. Clarke, C. Ma, G. Casillas, M. Das, M. Guan, D. Liu, L. Wang, A. Tadich, Y. Du, C. Ton-That and D. Jin, *Nanoscale*, 2017, **9**, 7719–7726.
- 235 D. Hudry, D. Busko, R. Popescu, D. Gerthsen, A. M. M. Abeykoon, C. Kübel, T. Bergfeldt and B. S. Richards, *Chem. Mater.*, 2017, **29**, 9238–9246.
- 236 A. Grzechnik, K. Friese, V. Dmitriev, H.-P. Weber, J.-Y. Gesland and W. A. Crichton, *J. Phys. Condens. Matter*, 2005, **17**, 763–770.
- 237 M. Gunaseelan, S. Yamini, G. A. Kumar, C. Santhosh and J. Senthilselvan, *Mater. Res. Bull.*, 2018, **107**, 366–378.

238 J. Goodyear and D. J. Kennedy, *Acta Crystallogr. Sect. B*, 1973, **29**, 744–748.

Appendix 2: Nanomaterial Crystallography

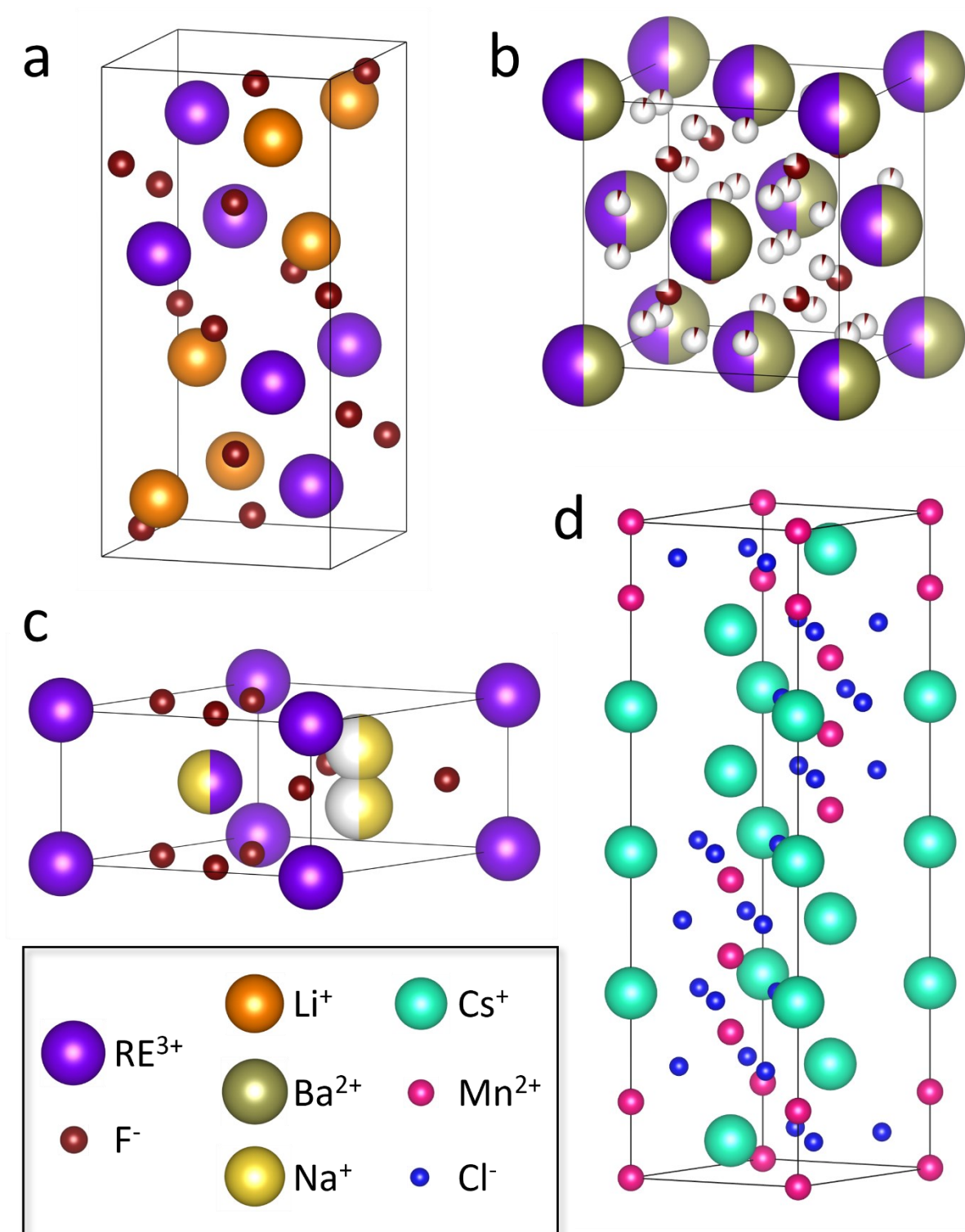


Figure X2 Unit cells for (a) tetragonal LiREF_4 ^{142,236}, (b) cubic BaREF_5 ²³⁷, (c) hexagonal NaREF_4 ¹⁴³, and (d) trigonal CsMnCl_3 ²³⁸.